Freie Universität Berlin

Ultrafast Energy Flow and Structural Changes in Nanoscale Heterostructures

Thomas Vasileiadis

Berlin 2019

Dissertation

zur Erlangung des Grades eines

Doktors der Naturwissenschaften

am Fachbereich Physik

der Freien Universität Berlin

This work has been performed between October 2014 and April 2019 in the Max-Planck and ERC research group 'Structural and Electronic Surface Dynamics' under the supervision of Dr. Ralph Ernstorfer and in the facilities of the Physical Chemistry department (Director: Prof. Martin Wolf) at the Fritz Haber Institute of the Max Planck Society.

The data of this work are stored and secured in the group drives of the 'Structural and Electronic Surface Dynamics' group in the Fritz Haber Institute and they can be made available upon request. The MD trajectories and the electron microscopy images of the size-selected nanoclusters can become available by the corresponding collaborators (Prof. V. Mavrantzas and Prof. R.E. Palmer, respectively).

The work of the author and the contributions of his collaborators are clearly stated.

Thomas Vasileiadis

Berlin, May 2019.

Erstgutachter: Dr. Ralph Ernstorfer

Zweitgutachter: Prof. Dr. Katharina J. Franke

Datum der Disputation: 22.07.2019

Contents

Abstract

A central goal of nanotechnology is the precise construction of nanoscale heterostructures with optimized chemical, physical or biological functionalities. It is known that function stems from structure but, in addition, function always involves nonequilibrium conditions and energy flow. The central topic of this thesis is the ultrafast energy flow in nanoscale heterostructures and how this energy flow drives ultrafast structural changes. The main experimental technique of this work is femtosecond electron diffraction, which probes the lattice response to electronic excitations. The nanoscale heterostructures contain metallic (Au) nanostructures of well-defined 0D or 2D morphology, supported on 2D substrates. In photoexcited heterostructures, thermal equilibrium is restored by electron-lattice interactions, within each component, and electronic and vibrational coupling across their interface. A newly developed model of ultrafast energy flow is used to measure the microscopic couplings, like electron-phonon coupling and interfacial vibrational coupling in nanoscale heterostructures using the observed Debye-Waller dynamics. Ultrafast energy flow in supported metallic nanostructures can initiate a rich variety of real-space motions like anharmonic lattice expansion and surface premelting, which manifest as distinct and quantifiable observables in reciprocal-space. These phenomena have been studied for Au nanoclusters on amorphous thin-film substrates. Au nanoclusters are found to exhibit ultrafast surface premelting at atypically low lattice temperatures and pronounced electron-lattice nonequilibrium conditions. Femtosecond electron diffraction is mostly used to study ultrafast motions related with phonons but in ultrasmall nanocrystals a new observable arises: the motion of the phonons' frame of reference, meaning the crystal itself. This has been demonstrated for Au nanoclusters attached on graphene using femtosecond electron diffraction experiments, molecular dynamics and electron diffraction simulations. The substrate has a significant effect on the energy flow and the structural motions of ultrasmall, adsorbed nanostructures and, inversely, metallic nanostructures can alter fundamental properties of semiconducting substrates. Surface decoration with plasmonic, quasi-2D nanoislands of Au sensitizes WSe_2 to sub-band-gap photons, causes nonlinear lattice heating and accelerates electron-phonon equilibration times. Conclusively, nanoscale heterostructures have a rich variety of nonequilibrium phenomena that affect their structure at ultrafast timescales. Ultrafast diffractive probes, like femtosecond electron diffraction, can provide a detailed, quantitative understanding of this relationship.

Kurzfassung

In dieser Doktorarbeit wird der ultraschnelle Energietransfer in nanoskaligen Heterostrukturen sowie die dadurch verursachten ultraschnellen Strukturänderungen untersucht. Die wichtigste Methode dieser Arbeit ist Femtosekunden-Elektronenbeugung. Diese Methode untersucht die Reaktion des Kristallgitters auf elektronische Anregung. Die Heterostrukturen bestehen aus Gold-Nanostrukturen mit wohldefinierten 0D oder 2D Strukturen, die auf 2D Substraten aufgebracht sind. In mit Licht angeregten Heterostrukturen wird das thermische Gleichgewicht durch Elektron-Phonon-Kopplung in den einzelnen Materialien sowie durch elektronische und phononische Kopplung zwischen den Materialien wiederhergestellt. Ein neu eingeführtes Modell für ultraschnellen Energietransfer wird verwendet, um die ultraschnellen Veränderungen der Gittertemperatur zu beschreiben. Das Modell ermöglicht es, aus der gemessenen Debye-Waller-Dynamik mikroskopische Größen wie Elektron-Phonon-Kopplung und Phonon-Phonon-Kopplung an der Grenzfläche der nanoskaligen Heterostrukturen zu extrahieren. Ultraschneller Energietransfer in metallischen Nanostrukturen können eine Vielzahl an Veränderungen im Kristallgitter hervorrufen, z.B. Gitterausdehnung und Schmelzen der Kristalloberfläche. Diese Veränderungen gemessen werden, für 0D Gold Nanostrukturen die auf 2D Substraten aufgebracht sind. Au-Nanocluster zeigen ultraschnelles Schmelzen der Kristalloberfläche bei außergewöhnlich niedrigen Gittertemperaturen und ausgeprägtem Nichtgleichgewichtszustand zwischen Elektronen und Gitter. Femtosekunden Elektronen Beugung ist eine Methode, die am häufigsten bei der Untersuchung durch Phonen induzierter ultraschneller Bewegungen von Atomen Anwendung findet. In ultrakleinen Nanokristallen stellt sich aber ein neue Herausforderung dar: der Referenzrahmen der Bewegung der Phononen, was der Kristall selber ist. Demonstriert wurde das für Gold 0D Nanostructuren, die auf Graphen. Das Substrat hat einen signifikanten Einfluss auf den Energiefluss und die strukturelle Bewegung von ultrakleinen, adsorbierten Nanostrukturen und in inverser Weise können metallische Nanostrukturen due fundamentalen Eigenschafter halbleitender Proben verändern. Wenn WSe_2 mit plasmonische quasi-2D Gold-Nanoinseln bedeckt wird, ändern sich dessen Eigenschaften so, dass Photonen unterhalb der Bandlücke absorbiert werden können. Die resultierende Erwärmung des Gitters folgt einem nichtlinearen Zusammenhang mit der Fluenz des einkoppelnden Lasers und die Elektron-Gitter Relaxationszeit ist reduziert.

Chapter 1. Introduction

1.1 Energy flow and structural changes in nonequilibrium states

A central concept in all branches of physics, chemistry and biology that deal with large amounts of particles is thermodynamic equilibrium. In thermodynamics, equilibrium and nonequilibrium are described in terms of how energy is shared among the numerous, microscopic degrees of freedom. In thermodynamic equilibrium, the energy is stored equally in all microscopic degrees of freedom. In nonequilibrium states the various microscopic degrees of freedom can have different energy contents. All interesting physical phenomena, for instance the ones that take place in devices, chemical reactions or biological systems, occur in nonequilibrium conditions. Nonequilibrium states have a finite lifetime, since microscopic couplings are eventually restoring thermodynamic equilibrium. Measuring microscopic couplings in solid state systems is one of the central objectives of the current work. This introductory section discusses in more detail the ideas of equilibrium and nonequilibrium in condensed-matter systems and motivates the development of time-resolved experimental techniques.

Ground state structure of solids. The macroscopic properties of solids originate from the structure and interactions of their microscopic building blocks: the electrons and the nuclei. In crystalline solids, atoms are distributed on periodic lattices. Due to the lattice periodicity, electronic and nuclear motions are both governed by wavefunctions ($\Psi(\vec{r})$) of the form [1]:

$$\Psi(\vec{r}) = e^{i\vec{k}\cdot\vec{r}} u_k(\vec{r}) \,, \qquad \text{R 1.1}$$

where $\vec{k}$ is the crystal momentum. This mathematical expression (Bloch state) describes a plane wave ($e^{i\vec{k}\cdot\vec{r}}$) that is modulated by the lattice periodicity ($u_k(\vec{r})$). Using relationship (R 1.1) and the expressions for the electromagnetic interactions of electrons and nuclei (Hamiltonian), it is possible to derive relationships between the energies and the crystal momenta of electrons in solids (electronic band structure). A similar procedure can be carried out for the nuclear motions (vibrations) and in this case the quasiparticle excitation is termed phonon. The predicted electronic and vibrational states are populated according to the Fermi-Dirac and Bose-Einstein statistics, respectively. In thermodynamic equilibrium, both electrons and phonons are characterized by a single temperature.

The ground-state structure of solids, and the statistical assumptions related with thermodynamic equilibrium, can explain several properties of materials [2]. The electronic band structure can be used to categorize solids as conducting, semiconducting or insulating and, in addition, it can tell if a solid is absorbing or transparent at a given wavelength of light. The phononic band structures of materials can be used to understand their elastic properties, heat capacities, and speed of sound. Driven by the necessity of categorizing solids and selecting them for various technological applications, scientists have developed a plethora of theoretical and experimental techniques for studying ground-state properties.

From the theory perspective, an important example is density functional theory (DFT). In its most basic form, DFT is inherently connected with the ground state structure of materials [3]. Regarding experimental mapping of band structures in equilibrium, some examples are static photoemission spectroscopy [4] for electrons and inelastic neutron scattering [5] for phonons. In addition, several optical spectroscopies can study electronic transitions and phonons in equilibrated, condensed matter systems. Here only few are mentioned that probe lattice dynamics. These are the Infrared, Brillouin and Raman spectroscopies [6] that measure the energy of long-wavelength phonons in a large variety of materials.

Electron-lattice nonequilibrium. Characterization of a material requires a detailed knowledge of the ground-state structure properties. However, the ground state description is incomplete once the material is used for a certain function. The various electronic and phononic states can be assigned a unique temperature only in perfect thermodynamic equilibrium. In a functional material some nonequilibrium conditions among its building blocks will always arise. In essence, function is always accompanied by some form of nonequilibrium.

The simplest example is related with electrical conduction in metals. In metals, static electric fields set the electrons in motion but there is no direct interaction between the electric field and the phonons. Electrons get accelerated from the external electric field, gain energy and scatter on the lattice and on defects. The inelastic scattering events produce phonons. This is the well-known phenomenon of Joule heating. Generation of excited charge carriers and subsequent emission of phonons takes place also when the external electric field is that of a laser pulse or other form of light. In semiconductors,

when the photon energy is sufficient, light excites electrons in the conduction band (holes in the valence band), which then interact with phonons and cause lattice heating. Obviously, such phenomena are very important for electronics and opto-electronics. Thus, it is essential to develop experimental techniques that quantify the strength of electron-phonon interactions.

The general importance of electron-lattice interactions can be made clear by a close inspection of the relationship R 1.1. The nuclear positions enter the general form of the electronic wavefunction and hence electrons and phonons are always coupled. Having accurate knowledge of electron-lattice interactions can be beneficial even for a refined view of the ground state itself. One important example is superconductivity. Superconductivity (BCS-type) is a ground-state property and it arises due to attractive interactions among electrons that are mediated by phonons [7] (electron-phonon coupling). The connection between thermal relaxation of electrons in metals and superconductivity is discussed in the theoretical work of Philip B. Allen [8].

Structural changes in solid-state systems. As mentioned before, the electronic and phononic band structures in equilibrium can be used to categorize materials. Yet, the recent ability to study materials at ultrafast timescales has revealed that even the band structure itself [9] and the entire atomic arrangement [10] can change for a brief period of time. Moreover, using the electronic band structure in equilibrium, to categorize a material as metallic or insulating, might be a problematic concept in some nonequilibrium conditions. For instance, several insulating materials have been found to transform into metals for a brief period of time [11], [12].

The electronic structure of materials can change at ultrafast timescales and, since electrons make up the chemical bonds between the atoms, the atomic positions will also be affected. The phononic band structure of a material in equilibrium can be used to predict its stiffness and other properties related with atomic vibrations. Interestingly, in conditions far from thermodynamic equilibrium, the vibrational properties of materials can change. For instance, Au can get harder [13] and Bi can get softer [14] when the electrons are much hotter than the lattice. These are only few of the many examples where conclusions drawn from equilibrium experiments and theories become invalid in nonequilibrium conditions. The current work deals with ultrafast changes of the atomic structure of materials with nanoscale dimensions.

Nonequilibrium in chemical phenomena. Being able to observe nonequilibrium states is important for physical processes in solids but also for a wide range of phenomena encountered in molecular physics and chemistry. Perhaps the most important example for chemistry is the so-called intermediate state, or the activated complex as described in the work of Eyring [15]. In the description of Eyring every chemical reaction pathway is crossing a short-living, nonequilibrium atomic arrangement called the activated complex. In nonequilibrium states an excess amount of energy can be transiently stored in specific microscopic degrees of freedom. This situation is similar with the thermal fluctuations described by Eyring. Nonequilibrium states can be triggered at a selected time by an external stimulus, like pulses of light, current or heat, opening up the way for numerous, interesting, time-resolved experiments and laser-based applications. The ability to observe in real-time the transition from chemical reactants, to activated complexes and final chemical products is a novel, fertile field for experimentalists [16]. Some recent works in this direction have dealt with motions and transformations of Carbon rings and chains [17], CF_3I molecules [18] and catalytic oxidation of CO [19] on ultrafast timescales.

1.2 Time-resolved investigations of solids

In view of the previous discussion, there are two important aspects of nonequilibrium phenomena in solid-state physics and chemistry. First, it is important to know how energy flows among the various microscopic degrees of freedom. Second, nonequilibrium conditions and energy flow can trigger structural transformations. This section introduces the experimental procedures that can be followed in order to address these points.

The periodic lattice of crystalline solids and the electronic and phononic band-structures are accessible with several experimental techniques. All experiments involve scattering of some type of radiation from the investigated solid-state system. When the used radiation is continuous, scattering experiments are most appropriate for studying the ground-state structure of materials. In close to equilibrium conditions it is possible to measure coupling between subsystems, for instance electron-phonon coupling, through the energy (frequency) broadening of the investigated electronic [20] or phononic [21] states. The main drawback of this approach is that several types of coupling can contribute to the

observed spectral broadening. This makes difficult to acquire an accurate microscopic description based solely on spectroscopic data.

For the purpose of measuring microscopic couplings and observing nonequilibrium states, the scattered radiation is ideally pulsed in order to record time-dependent snapshots of the system. The pulse duration needs to be shorter than the characteristic lifetime and interactions of nonequilibrium states. Assuming that electronic and phononic states lie in the eV ($1\,eV \cong 1.6 \cdot 10^{-19}\,J$) and meV energy-range, respectively, and from the Heisenberg uncertainty principle ($\Delta E \cdot \Delta t \geq h$), the lifetime of nonequilibrium states and interactions can be as short as picoseconds ($1\,ps \cong 10^{-12}\,s$) and femtoseconds ($1\,fs \cong 10^{-15}\,s$). Electronic circuits that record, transfer and store data are not sufficiently fast for real-time measurements of electron-lattice interactions. Instead, the pulses of the probing radiation need to be used in a stroboscopic, pump-probe manner. Pump-probe experiments use an intense 'pump' pulse (usually a laser pulse) to initiate some nonequilibrium dynamics and a weaker 'probe' pulse to study the transient, nonequilibrium states. The probing pulses can be electrons or electromagnetic waves ranging from THz to X-rays. According to the probe, the excited material can be studied by means of diffraction, microscopy or spectroscopy. The pump-probe principle is explained in more detail in **Chapter 2**.

Equation R 1.1 and the relevant discussion, made clear that all properties of crystalline solids are connected with their crystal structure. For this reason, a useful objective is to study the crystal structure of materials in equilibrium and nonequilibrium conditions. One of the main techniques for studying crystal structures is diffraction. The first diffraction experiments used X-rays and were reported by Walter Friedrich, Paul Knipping and Max Laue in 1912 [22]. Diffraction with electrons was first shown in 1927 by George Paget Thomson, Clinton Joseph Davisson and Lester Halbert Germer [23]. The transition from structural characterization with continuous streams of electrons, to studies of structural dynamics with pulses of electrons, was achieved in 1982 by Steve Williamson and Gerard Mourou [24]. These early, time-resolved diffraction experiments investigated phase transitions with a time-resolution that was in the order of picoseconds.

In time-resolved investigations, the solid is considered as a collection of interacting subsystems. Interactions strengths, or coupling constants, are then extracted with time-dependent equations that describe energy flow between the subsystems and fit some of

the observables. The three major subsystems of a solid are the electrons, the spins and the phonons (**figure 1.1**). Certain time-resolved techniques are mostly sensitive in the response of only one subsystem. The use of these techniques simplifies the interpretation of the observed dynamics. For example, time-resolved diffraction is sensitive to the lattice dynamics [25], [26], time-resolved photoemission is sensitive to the electron dynamics [9], [27] and time-resolved magneto-optic Kerr effect is mostly sensitive to the spin dynamics [28]. If the nonequilibrium conditions trigger some structural change, time-resolved diffraction can detect it in the most direct way.

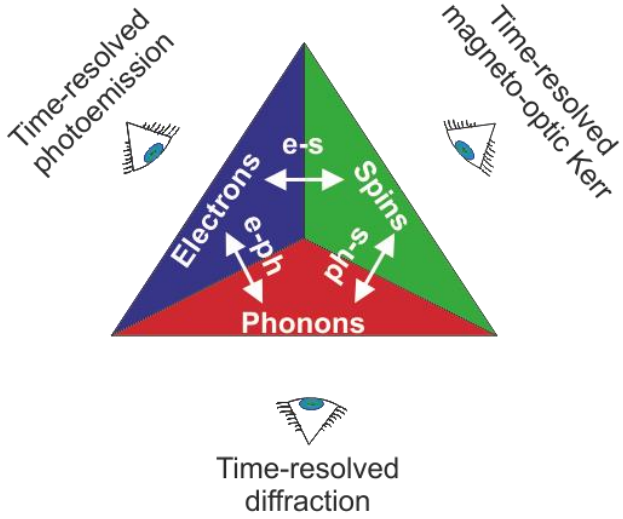

Figure 1.1: The subsystems of a solid, their interactions and examples of experimental techniques. The most simple, dynamic picture of a solid contains electrons, phonons and spins coupled with each other. Arrows with notations e-ph, ph-s and e-s stand for electron-phonon, phonon-spin (spin-lattice) and electron-spin (spin-orbit) interactions respectively. Certain time-domain techniques can selectively probe excitations in one of the three subsystems. In the case of the lattice (phonons) such a technique is time-resolved diffraction. *Adapted from reference* [29].

1.3 The case of nanostructures

Since the establishment of solid-state physics, the first diffraction and the first time-resolved diffraction experiments, the materials of technological interest have greatly evolved. The present work is concentrated on the case of nanomaterials or nanostructures.

Nanostructures are spatially confined solids with at least one of their dimensions ranging between one and one hundred nanometers (1 nm=10^{-9} m) [30], [31]. A nanostructure can be strongly confined in some dimensions of space and very extended in the other directions of space. From this point of view, the nanostructures are also termed low-dimensional materials. Some examples are (i) 0D nanostructures (confinement in all directions) like nanoclusters, (ii) 1D nanostructures like nanowires (iii) and 2D nanostructures like graphene (a two-dimensional layer of sp^2 Carbon atoms). Another important aspect of nanostructures is that, due to their small volume, the percentage of atoms that are located close to surface is drastically enhanced compared to bulk materials (high surface-to-volume ratio). For experiments and applications, nanostructures are deposited on various substrates hence the corresponding samples are practically, always heterogeneous. Nanostructures can posse several interesting functionalities, very different than their bulk counterparts.

One of the first who envisioned the use of nanostructures in technological applications (nanotechnology) was Richard Feynman. Feynman introduced the concept of nanotechnology in his famous lecture “There's Plenty of Room at the Bottom” in 1959. In view of the developments in microelectronics and electron microscopy, Feynman gave another lecture in 1984 titled “Tiny machines”, in which he proposed the use of small clusters of Au, containing ~100 atoms, for information storage. Likely, information storage was used as an illustrative example and many more interesting aspects aroused. In the lecture “Tiny machines”, some member of the audience questioned the durability of nanomaterials in realistic conditions. If nanomaterials are delicate arrangements of few atoms, can they withstand external perturbations?

The initial answer to this question was based on the ground-state description of materials. Atoms in nanostructures, as in molecules and crystals, have short-range order and this order is not affected by thermal fluctuations, providing that the temperature is not too high. Yet, all interesting functionalities occur in nonequilibrium conditions where the

temperature is an ill-defined quantity. Oppositely to thermal states, which have universal characteristics, nonequilibrium states depend on various factors like the external stimulus that initiates them, the chemical environment and more. Due to the complexity of nonequilibrium states the durability of nanomaterials cannot be judged by a single number, meaning the temperature, and it is necessary to examine the nonequilibrium interactions that arise when the nanostructure performs a certain function. Some nonequilibrium interactions will take place within the nanostructure, for instance electron-phonon interactions. Since the nanostructures are small and surface effects are important, interactions with neighboring materials should also play an important role.

In order to observe nanostructures one needs to exploit radiation with De Broglie wavelength much smaller than their characteristics size ($\lambda << 1$ nm) and large scattering cross-section with matter; the most convenient being electrons. The Au nanoclusters, used by Feynman as a model system in nanotechnology, have been extensively studied with transmission electron microscopy (TEM) and, interestingly, they were found to be highly mobile and fragile systems. Au nanoclusters can exhibit structural changes induced by electron-irradiation [32], [33]. Electron microscopy has also revealed that atoms on the surface of nanoclusters are in constant, diffusive motion [34]. In nanoclusters, surface roughening and surface melting occur at temperatures lower than the melting point of their bulk counterparts [35]. Apart from Au, interesting order-disorder transitions have been observed in many nanomaterials, for instance Bi nanoparticles [36].

Figure 1.2 illustrates the structural instabilities of confined, metallic systems. The four charts show four snapshots of a single Au nanocluster recorded with a scanning transmission electron microscope (Reproduced with permission from Professor Richard Palmer, Swansea University, and Dawn Foster, Birmingham University). From these images it becomes obvious that the atoms of nanoclusters are extremely mobile. Occasionally, the atoms form hexagonal patterns, parallel lines, zig-zag structures or completely random fluctuations. The surface is very rough and atoms are occasionally detaching from the nanocluster.

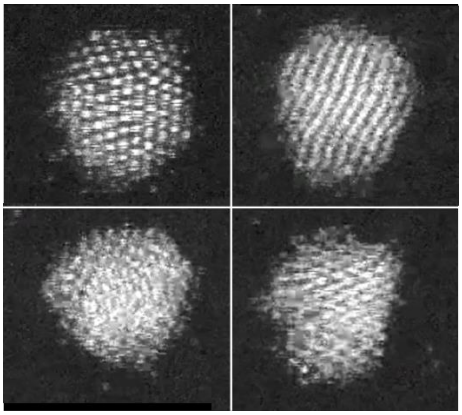

Figure 1.2: Four snapshots of a single Au nanocluster observed in the electron microscope. The atoms of the nanocluster are highly mobile and form short-living patterns such as hexagonal arrangements, parallel lines, zig-zag structures, surface imperfections and completely random fluctuations. *Credits: Professor Richard Palmer, Swansea University, and Dawn Foster, Birmingham University, reproduced with permission.*

How fast can these motions be? The Debye temperature of Au nanoclusters of similar size is in the order of 149 K [37]. The Debye frequency $v_m = k_B\Theta_D/h = 3\,THz$ corresponds to a period of 300 fs. This means that in order to resolve atomic motions in Au nanoclusters the instrumental time-resolution needs to be 300 fs or less. The time-resolution of *in situ* TEM setups is in the order of milliseconds. Instead, the required time-resolution can be achieved by time-resolved electron diffraction [38]. In order to cope with the multifarious instabilities that are encountered in nanoscale systems, the main experimental technique employed here is time-resolved electron diffraction with time-resolution in the order of 100 femtoseconds.

1.4 Applications and nonequilibrium phenomena in nanostructures

The general statement that functionalities are accompanied by nonequilibrium physics is now clarified for some of the most frequent applications of nanostructures. A brief review of nanostructures' applications is useful in order to narrow down the objectives and to maximize the impact of the present work.

Electronics and optoelectronics. Perhaps one of the most promising application of nanostructures is the miniaturization of electrical circuits [39]. One example is the

envisioned 2D transistor made from atomically thin layers of different materials [40]. For an efficient design, construction and control of spatially confined electrical circuits, it is essential to know how electrons and phonons interact and how they are transmitted through the various interfaces [41], [42]. Nanostructures are also useful for optoelectronic applications. One example is nano-antennas made of nanoscale Au and graphene [43] and ultrathin WSe_2 on nanostructured Au with enhanced fluorescence [44]. Again, ultrafast energy flow is playing an important role in order to understand how energy is transferred from the laser field to all the microscopic subsystems of the material.

Plasmonics. Experiments and applications that exploit metallic nanostructures to enhance light-matter interactions are termed plasmonics [45], [46]. Plasmonic nanostructures are usually made of noble metals like Au or Ag. Due to spatial confinement, the free charge carriers in plasmonic nanostructures can oscillate in phase with an external electromagnetic field and the structure is acting as a nano-antenna [46]. In the vicinity of the nano-antenna (near-field) the electromagnetic forces are enhanced. The near-field enhancement can be exploited in several applications. Neighboring nano-antennas can become coupled and transmit energy and information in space [47], [48]. Other applications include the local enhancement of light-matter interactions for detection of single molecules by spectroscopic methods [49]. However, light-induced heating of plasmonic nanostructures can easily result in irreversible, structural and morphological changes [50], which is a limiting factor for practical applications.

Femtochemistry. In the vicinity of metallic nanostructures, the enhanced density of electromagnetic energy and the generation of excited charge carriers can drive chemical reactions like dissociation of molecules [51]. Such applications belong to the field of femtochemistry. Femtochemistry deals with chemical reactions that are driven by light at ultrafast timescales [52]. Once again, ultrafast energy flow is important in order to understand the ultrafast damping of plasmonic oscillations and their transformation into hot electrons and eventually phonons. Electron-phonon interactions are competing processes for the electron-adsorbate interaction and hence they play an important role in femtochemical reactions [52], [53].

Catalysis. Beyond laser-based methods, metallic nanostructures are often used in chemistry as highly efficient catalysts for specific reactions [54]. One important and widely studied case is the catalytic transformation of the hazardous CO to the less

dangerous CO_2, using Au nanostructures on TiO_2 [55], [56]. Although catalysis is largely explored with static techniques (techniques with a minimum time-resolution of milliseconds or seconds), nonequilibrium conditions are obviously playing a role, based on the ideas of Eyring mentioned in **section 1.1**. Charge transfer is an essential part of catalysis [57] and photo-catalysis [58] with small, metallic nanostructures on semiconducting substrates and thus electron-lattice and nanostructure-substrate interactions are important. Catalytic chemical reactions can result in the generation of hot electrons [59]. Hot electrons are also encountered in laser-based experiments and their lifetime is limited by electron-phonon interactions. From this point of view, time-resolved, laser-based experiments might be proven useful for an in-depth understanding of surface chemical reactions and catalytic properties.

Beyond electrons, ultrafast motions of atoms are also crucial for the performance of catalysts. In catalysis, motions of surface atoms and imperfections play a dual role. On the one hand, diffusion of surface atoms leads to sintering [60] and inhibits catalytic activity [55], [56]. On the other hand, mobile surface atoms [61] and surface vacancies [62] are promoting the catalytic activity. Catalytic active sites are associated with atomic diffusion processes that occur in the picosecond timescale [61]. The exact role of atomic motions in catalysts is a very interesting and open subject.

Motions of supported nano-objects. Nanostructure on surfaces can translate and rotate in the picosecond timescale. In order to investigate translational and rotational diffusion or ballistic transport the usual model system is Au nanoclusters on graphene and graphite [63]–[65]. Translational and rotational diffusion of nanoclusters on surfaces is important for bottom-up synthesis of nanostructures, epitaxial growth [64] and sintering of nanocatalysts [60]. So far, there are no studies, to the best of the author's knowledge, which examined if such real-space motions produce reciprocal-space observables that are accessible by ultrafast diffractive probes.

Thermoelectrics. Solid-state systems with nanoscale heterogeneities are also used for thermoelectrics. Thermoelectric devices generate electricity in the presence of a temperature gradient. Various reports have shown that nanostructuring can enhance the performance of thermoelectrics [66]–[68]. The enhanced performance might be due to decreased, lattice-thermal-conductivity in systems with nanoscale heterogeneities [69]. Electron-phonon interactions and transmission of phonons across interfaces come again

into play, strengthening further the technological impact of time-resolved techniques that can probe interfacial energy flow, for instance time-resolved diffraction [70].

Solar cells and solar catalysts. Decorating the surface of a semiconductor with metallic nanostructures can enhance the light-induced generation of excited carriers. Metallic nanostructures can modify the properties of semiconducting surfaces mainly by hot electron injection [53] and plasmonic coupling [71]. These phenomena might be applied to photocatalysis [58], for instance water-splitting by visible light [72], and photovoltaics [73] for clean energy production.

1.5 State of the art and methodology of the present work

The applications mentioned in the previous section have some common, crucial aspects. First, all nanomaterials for practical applications are heterogeneous and, often, the support is playing a very active role. Second, most applications involve metal / semiconductor interfaces. Third, ultrafast energy flow is crucial and, sometimes, it can trigger structural changes. In view of these three points, the present section reviews the state of the art, regarding time-resolved diffraction studies of heterogeneous, nanoscale metal / semiconductor systems and, finally, it presents the methodology of the present work.

Time-resolved electron diffraction has been used to observe various nonequilibrium lattice motions, for instance, coherent oscillations [74], [75] and phase transitions [76], [77]. Morevoer, time-resolved electron diffraction can be used to quantify the coupling strength between electrons and phonons (see [78] and references therein). So far, time-resolved electron diffraction was mostly applied on homogeneous elements and compounds. Fewer studies are focused on the role of heterogeneity on the observed structural dynamics. Some recent examples are the works of Sokolowski-Tinten *et al.* [79], Pudell *et al.* [80] and Witte *et al.* [81]. The amount of time-resolved diffraction studies that deal with spatially confined solids (1-10 nm) is also limited. Ruan *et al.* [82] have studied Au nanoparticles, with a radius of 2 nm, in conditions close to melting. Frigge et al. studied atomic wires of In on a Si surface [10], [76]. Witte *et al.* studied few monolayer thick Pb on Si [81]. Other studies include Bi nanoparticles (10-20 nm) by

Esmail *et al*. [83], GaAs quantum dots (11-46 nm) by Vanacore *et al.* [84] and PbSe quantum dots (5-6 nm) by Wang *et al.* [85].

The present work aims to advance the field with comparative studies of prototypical nanoscale heterostructures. In all cases, the one component of the heterostructure is a solid with strong spatial confinement. The role of heterogeneity is studied in detail by depositing the same nanostructures on different substrates with membrane-like morphology (two-dimensional, 2D substrates). The nanostructures are either spatially confined in all directions of space (0D nanostructures), or only vertical to the substrate (2D nanostructures). All nanostructures are made of a simple metal (Au) and all substrates are semiconducting. Nanoscale metal/semiconductor heterostructures are prototypical systems for electronic and optoelectronic [43], [53], catalytic [55] and photocatalytic [51] applications. The synthesis of the metallic nanostructures has been carried out with modern physicochemical methods like size- and shape-selected synthesis of nanoclusters [86] and deposition on thin-films and layered crystals [87] (**Chapters 3, 4** & **5**) or epitaxial growth on layered crystals (**Chapter 6**).

1.6 Structure of the thesis

The present work reports time-resolved electron diffraction studies of prototypical:

(i) 0D metal / 2D semiconductor heterostructures,
(ii) 2D metal / 2D semiconductor heterostructures.

Any structural motion is driven by energy flow among the microscopic subsystems. For all investigated systems the author have modelled the microscopic energy flow taking into account heterogeneity. These models include:

(i) Intrinsic interactions for each material (*e.g.* electron-phonon coupling),
(ii) Extrinsic interactions between materials (*e.g.* interfacial phonon transmission).

The next step is to examine under which circumstances nonequilibrium conditions change the crystal structure and the morphology of nanostructures. The various lattice motions and structural changes that have been observed are summarized as follows:

(i) Lattice expansion of 0D nanostructures,

(ii) Partial surface melting of 0D nanostructures,

(iii) Rotational motions of 0D nanostructures,

(iv) Modified structural dynamics of 2D semiconducting crystals induced by surface-decoration with 2D metals.

In more detail, **Chapter 2** of the thesis introduces the femtosecond electron diffraction, the main experimental technique used by the author. In addition, it explains the various physical phenomena that are investigated and the theoretical and computational methods that were employed.

Chapters 3 deals with the ultrafast structural dynamics, in response to electronic excitations, in heterostructures composed of Au_{923} nanoclusters (0D) on thin-film substrates (2D) with the use of femtosecond electron diffraction. In photo-excited, supported nanoclusters thermal equilibrium is restored through intrinsic heat flow, between their electrons and their lattice, and extrinsic heat flow between the nanoclusters and their substrate. For an in-depth understanding of this process, the two-temperature model have been modified for 0D/2D heterostructures and used to describe energy flow among the various subsystems, to quantify interfacial coupling constants, and to elucidate the role of the optical and thermal substrate properties.

In **Chapter 4**, various forms of atomic motion, such as thermal expansion and lattice disordering, are studied through their distinct and quantifiable reciprocal-space observables. The anharmonicity of the interatomic potential leads to lattice expansion, which becomes evident as a shift of diffraction peaks to lower scattering angles. The effective lattice temperature, probed by the Debye-Waller effect, together with the observed lattice expansion, are used to measure the expansion coefficient of photo-excited nanoclusters. In addition, when lattice heating of Au nanoclusters is dominated by intrinsic heat flow, a reversible disordering of atomic positions occurs, which is absent when heat is injected as hot substrate-phonons. The present analysis indicates that hot electrons can distort the lattice of nanoclusters, even if the lattice temperature is below the equilibrium threshold for surface pre-melting. Based on simple considerations, the effect is interpreted as activation of surface diffusion due to modifications of the potential energy surface at high electronic temperatures. The chapter is concluded with a discussion of the implications of such a process in structural changes during surface chemical reactions.

In **Chapter 5**, femtosecond electron diffraction is combined with molecular dynamics and electron diffraction simulations to study size-selected Au nanoclusters on few-layer graphene. The dynamics of diffraction peaks' intensities reveal that the nanoclusters exhibit ultrafast, constrained rotations in addition to atomic vibrations. The crystallinity of the substrate is imposing a preferred orientation of the nanoclusters' lattices in equilibrium. The nanoclusters' orientation becomes evident from their electron diffraction pattern. Ultrashort laser pulses are then used to induce vibrational and rotational excitation of the nanoclusters and the resulting, time-dependent diffraction patterns are probed with femtosecond electron diffraction. Rotational motions of nanoclusters are impulsively excited, *i.e.* on the timescale of electron-phonon relaxation, and therefore participate in the overall non-equilibrium dynamics of nanoscale heterostructures. The chapter concludes with modelling of the ultrafast energy flow in atomic vibrations and nanocluster librations and comparison of their energetic contributions.

Chapter 6 is devoted to the study of quasi-2D nanoislands of Au on the layered semiconductor WSe_2. It is found that the Au nanolattices have an epitaxial relationship with the underlying WSe_2 surface. Before proceeding with the time-resolved experiments, the heterostructure is studied in detail with electron microscopy, linear optical absorption and angle-resolved photoemission spectroscopy. Femtosecond electron diffraction is then used to study intrinsic and extrinsic energy flow in the heterostructure. The main finding of this work is that the semiconducting WSe_2 can be excited at ultrafast timescales even with photons that are within its optical gap, providing that its surface is decorated by Au. The resulting lattice heating is distinctively faster than what has been observed previously for resonant excitation of pure WSe_2. Moreover, lattice heating follows a clear, nonlinear relationship with the energy input from the incident laser pulse. These results are a strong indication that electronic excitations in WSe_2, mediated by plasmons and electrons of Au nanostructures, have very different nature than electronic excitations caused by photons.

Chapter 2. Experimental & computational methods

This chapter explains the experimental and computational methods that were employed by the author of this work. The introduction on the working principle of femtosecond electron diffraction (FED) contains some practical information and conceptual insights in order to assist the growing number of new members and external users that employ the apparatus for their scientific interests. The initial experimental apparatus has been designed and constructed by Dr. Lutz Waldecker, in collaboration with Dr. Roman Bertoni and under the supervision of Dr. Ralph Ernstorfer [29], [38]. In the frame of the current doctoral thesis, the setup was moved in a clean-room facility and partially redesigned to increase its stability and to implement a new laser system with non-linear optics that allow pumping with various photon energies. Other changes included a modified design of the magnetic lens manipulator and cooling, a new geometry for pump-probe experiments, where the sample is tilted, and various modifications in the UHV chamber and the non-linear optics. Finally, it should be mentioned that **Chapters 3, 4** and **5** have mostly used the original design and **Chapter 6** the upgraded one.

2.1 Femtosecond electron diffraction

This work employs time-resolved, high-energy, electron diffraction with a temporal resolution in the order of 100 fs (1 fs=10^{-15} s) [38]. Due to its temporal resolution, the technique is termed femtosecond electron diffraction (FED). FED makes use of the photoelectric effect to produce ultrashort pulses of electrons using ultrashort pulses of photons. The ultrafast lattice dynamics of crystalline materials can then be recorded in a 'pump' (with photons) and 'probe' (with diffracted electrons) principle that is shown in **figure 2.1**.

The pulses of photoelectrons are accelerated by an electric voltage, enter the field-free area and get diffracted by the lattice. The arrival of the electrons on the sample occurs at selected time-delays ($\delta\tau$) relatively to the arrival of an ultrashort laser pulse. Both the laser pulse and the electrons arrive at nearly normal incidence on the sample. The signal of several thousand diffraction patterns is integrated for each time-delay using an electron

camera. The diffraction pattern that is finally recorded corresponds to a snapshot of the average atomic positions at time $\delta\tau$ after photoexcitation. The uncertainty in determining the time-delay stems from the finite pulse duration of electrons and photons. In FED, the main limiting factor of temporal resolution is the electron pulse duration. The recipe for FED, shown in **figure 2.1**, has three main ingredients: the laser pulses, the photoelectron pulses and the device that guides the electrons and records the diffraction patterns. These elements are separately described in the three following sections.

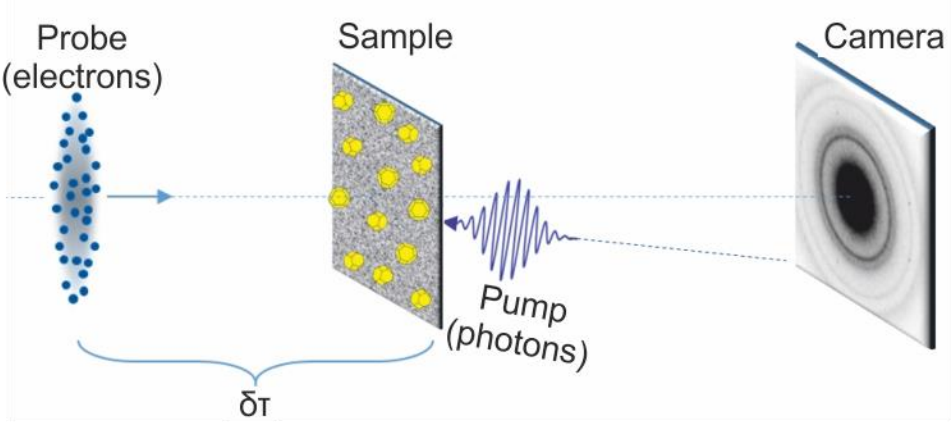

Figure 2.1: Schematic illustration of the pump-probe principle in FED. An electron pulse (probe) arrives at a selected time delay ($\delta\tau$) after excitation with a photon pulse (pump). The diffraction pattern recorded by the camera corresponds to a reciprocal-space snapshot of a very precise instance after optical excitation. In this type of experiments, both the electrons and the photons arrive at nearly normal incidence.

2.1.1 Ultrashort laser pulses

Oscillator. The ability to produce ultrashort laser pulses is based on the so-called Ti:Sa oscillator [88]. This device produces laser pulses with a central wavelength of 800 nm and pulse durations in the order of tens of femtoseconds. The working principle is based on the so-called Kerr-lens mode-locking. The gain medium of Ti:Sa lasers has a refractive index that increases as the intensity of the electromagnetic wave increases. Some spontaneous process, for instance knocking a mirror of the cavity, can alter the phases of the various modes of the electromagnetic field such that they combine and form a pulse. The pulse is characterized by higher peak intensities than individual continuous waves. Due to Kerr-lens mode-locking, the pulses are self-focused and favorably enhanced by

the active medium. In this way, all the continuous-wave radiation is depleted, and the produced pulses can be used for pump-probe experiments. The previously used oscillator was mode-locked by manual, mechanical motions of one cavity mirror and needed regular alignment. The oscillator in the current form of the setup (Vitara from Coherent) is completely automatized and mode-locking is achieved in a short period of time.

Amplifier. The pulse energy of oscillators (in the order of nano-Joules) is insufficient for triggering energetically demanding phenomena in condensed-matter systems. For this reason, the pulses are additionally enhanced in devices called amplifiers. Amplifiers, are repeatedly passing the pulses of Ti:Sa oscillators from a second gain medium to enhance their energy. To avoid destroying the gain medium the oscillator pulses are stretched in time, before amplification, and recompressed before exciting the device. In addition, the oscillator is delivering pulses with a repetition rate of 80 MHz, but the amplifier (in the current experiments) has a repetition rate of 1-4 kHz. These repetition rates allow the investigated sample to lose the excess heat to the environment before the arrival of the next pulse (reversibility and absence of static heating). The original setup used a multi-pass Ti:Sapphire amplifier with central wavelength 800 nm, energy per pulse of 1 mJ and 30 fs pulse duration and repetition rate 1 kHz. In the course of the present thesis, the experimental apparatus was upgraded in order to implement a commercial, regenerative amplifier laser system (Astrella, Ultrafast Ti:Sapphire Amplifier, from Coherent) with central wavelength 800 nm, pulse duration 42 fs, repetition rate 4 kHz and energy per pulse of 1.6 mJ.

Nonlinear frequency conversion. Although the pulses of amplifiers are sufficiently powerful for most applications, they are still limited regarding their photon energy. The central wavelength of the amplified pulses is still equal with 800 nm. In order to study a broad range of phenomena in metals, semiconductors and insulators, the frequency of the pulses is converted using crystals with nonlinear optical response. One example is second harmonic generation (SHG) inside Barium Borate (BaB_2O_4 or simply BBO). When 800 nm radiation is focused in BBO, the material absorbs two photons from the laser field and emits one photon with double energy (400 nm). The emerging 400 nm radiation has been used to excite ultrasmall, Au nanoclusters in **Chapters 3-5**. In addition, the experimental setup was upgraded in order to include commercial, automatized nonlinear optics setups. These devices are termed 'TOPAS' and 'Near-UV/Vis' (from Light Conversion) and deliver wavelengths from 250 nm to 2.5 μm. These tunable photon sources for pumping

have been used in **Chapter 6**. Owning to nonlinear optics it becomes possible to excite and study a broad range of materials like large-band-gap insulators, narrow-band gap semiconductors and metals. For an overview of nonlinear light-matter interactions that alter the frequency of light see the work of Boyd [89].

2.1.2 Photoelectron pulses

Electrons from two-photon emission. Having ultrashort laser pulses enables the production of ultrashort electron pulses using the photoelectric effect. In the current setup the used pulses contain ~10^3 electrons each. One important requirement is that each photoelectron is emitted with nearly zero, initial kinetic energy. When this holds true, all electrons are accelerated uniformly towards the sample and the pulse-duration and time-resolution are minimized. In addition, a small energy spread of the electrons is beneficial for the quality of diffraction patterns. To minimize the initial energy of electrons and their final energy spread, the energy input in every electron needs to match the work function of the metallic cathode. This is again achieved by a nonlinear optics setup called NOPA (noncollinear optical parametric amplifier) [90]. Before going into details about this setup, **figure 2.2** illustrates the central concepts behind its use.

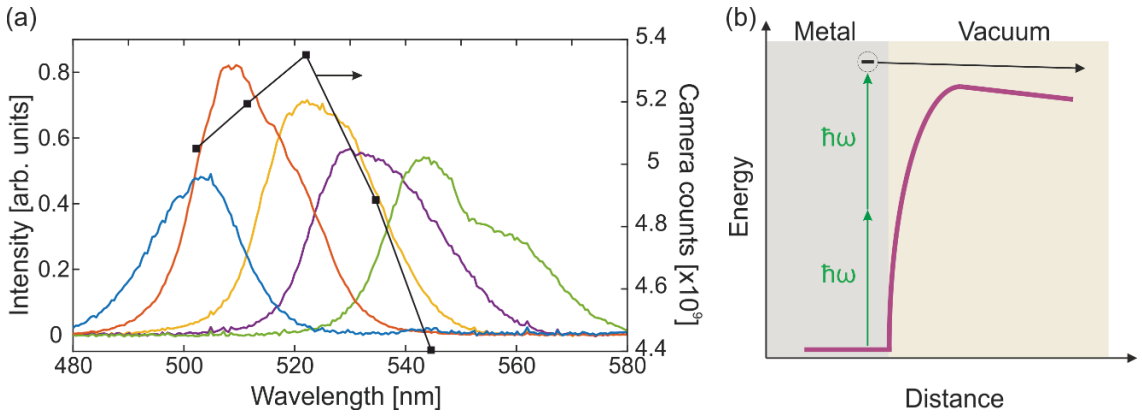

Figure 2.2: Production of ultrashort electron pulses from ultrashort pulses of photons with tunable wavelengths. (a) Various NOPA spectra (colored solid lines, left vertical axis) and the frequency-dependent counts produced by photoelectrons on the camera (black squares and line, right vertical axis). **(b)** Schematic of the two-photon photoemission process. The energy of the photons is tuned so that the two-photon energy is nearly equal with the cathode's work function. In this case, the initial momentum of electrons is close to zero, leading to a better time-resolution and better transverse coherence.

The NOPA setup converts the 800 nm radiation, emerging from the amplifier, to the 490-570 nm range. **Figure 2.2.a** shows some example spectra of the NOPA (left axis of the diagram). In the same figure, the number of camera counts (directly proportional to the number of electrons) is plotted as a function of the central wavelength with black squares and lines (right axis of diagram). Photoemission emerges around 530 nm, which corresponds to a photon energy of 2.38 eV. This critical photon energy depends on various factors but most importantly on the material of the cathode, which is Au in the used setup. **Figure 2.2.b** shows what happens inside Au when it is irradiated by the 520 nm pulses. If the intensity is sufficient, an electron of Au can absorb two photons, cross the energy barrier and move to the vacuum. The used radiation needs to have minimum photon energy (maximum wavelength) to minimize the energy spread but, simultaneously, it should produce a sufficient amount of electrons for recording diffraction patterns with low signal-to-noise ratio. The schematic in **figure 2.3** shows the NOPA setup. A total power of 170 mW (800 nm) is inserted into the NOPA setup from the amplifier (the rest of the power is used for diagnostics like stability measurements) and produces 3 mW of power for the electron gun.

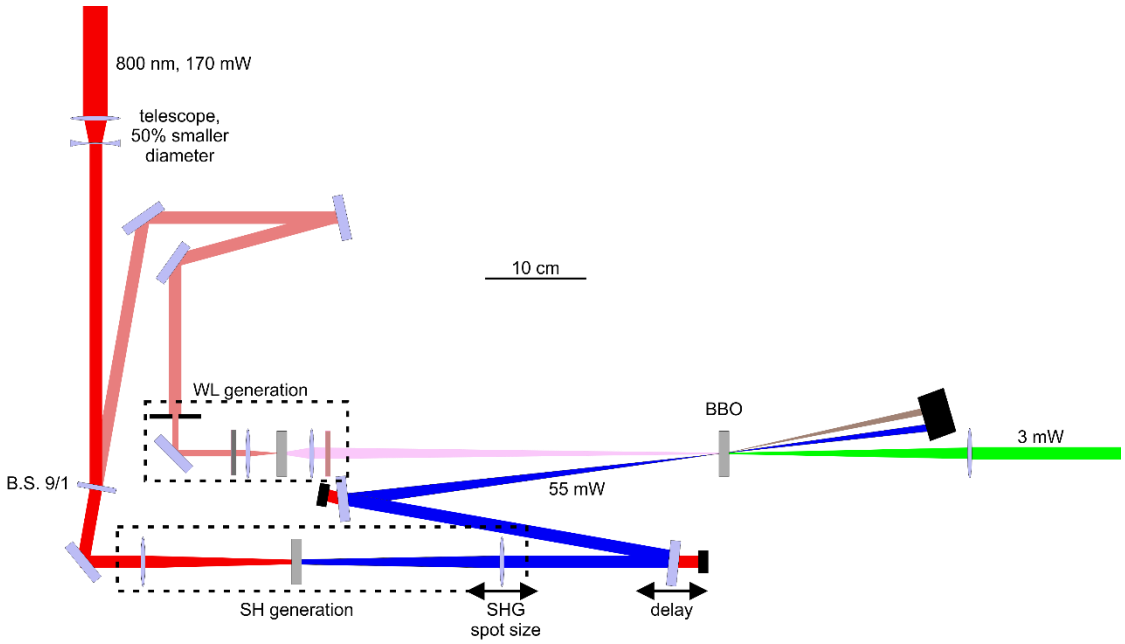

Figure 2.3: Current design of the NOPA setup. The scale bar (10 cm) is used to show the actual distances between the optical components. For more details see the main text.

A telescope is decreasing the beam diameter by 50%. The beam is split into two arms at a ratio of 9/1 for SHG and WL generation, respectively. The weak pulses transmit through an iris and a neutral density filter and get focused with a lens of 30 mm focal distance in a Sapphire crystal with a thickness of 3 mm for WL generation. Wavelengths shorter than 700 nm are filtered out and the WL is finally refocused with a second lens of 30 mm focal distance. The intense pulses are used for SHG (400 nm) in a BBO crystal (type I, Altechna), 6x6 mm wide, 0.5 mm thick, with θ=29.2^o and φ=90^o and protective coatings for 400 and 800 nm. The 800 nm radiation is focused with a lens of 200 mm focal distance and the emerged 400 nm light is collected with a lens of 150 mm focal distance. The residual 800 nm radiation is rejected with the use of two mirrors that are reflecting only the 400 nm light.

In the final BBO, energy is transferred from the intense SHG to the WL pulses and specific wavelengths are amplified. The BBO for NOPA (type I, Altechna) is 5x5 mm wide, 2 mm thick, and has angles for crystal cut of θ=29^o and φ=90^o. The protective coating is for 400-600 nm wavelengths and the surface quality is appropriately high. The resulting, amplified light has wavelengths in the order of 490-570 nm and it is used to produce electrons. The SHG light and the Idler (emission of infrared photons so that energy and momentum are conserved) are rejected with a beam dump.

Photon pulses coming out of the NOPA have increased pulse duration due to dispersion in the various transmitting optical elements and for this reason they get recompressed with a two-prism compressor. The two-prism compressor is a device that recompresses the pulse by guiding its faster frequency components into longer travel paths. Finally, a delay-stage is fine tuning the propagation time in the probe arm in order to adjust the pump-probe delay. After the NOPA and the prism compressor the pulses need to have a spherical, homogeneous mode in order to increase the coherence of the electron beam. Spatial coherence and in particular the transverse coherence length (normal to the direction of the beam), are factors that determine the quality of the diffraction patterns and resolution in reciprocal space [91].

2.1.3 Electron diffractometer

Photocathode. The photoelectrons are produced and accelerated in an electron gun, which delivers them in the field-free area, where the sample is located. The photocathode

is shown in **figure 2.4**. The focused NOPA pulses travel in the cathode's interior and arrive on its central, upper surface, which supports a transparent, circular Sapphire crystal. The surface of Sapphire is covered with 2 nm of Cr (for adhesion) and 20 nm of Au (for photoemission). The cathode's surface is polished to optical quality in order to maintain strong electric fields without arcing. The cathode is placed 6-10 mm from a grounded Si wafer that acts as the anode (with a 100 μm hole on its center for the electrons to exit).

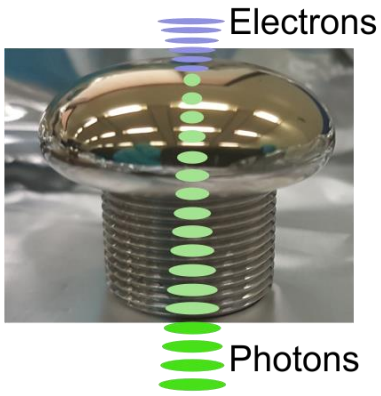

Figure 2.4: Photocathode. The NOPA pulses are focused on the cathode were they produce electrons for the FED experiment. The NOPA focus is in the order of 70-90 μm in the current apparatus.

On the one hand, shorter cathode-anode distances (close to 6 mm) result in higher electric fields, shorter propagation times for the electrons and, subsequently, better time-resolution. On the other hand, the longer cathode-anode distances (close to 10 mm) maximize the lifetime of the cathodes (typically in the order of months). The lifetime of the electron gun is limited by spontaneous arc discharges that damage the Au surface and create permanent electric currents.

Ultrahigh voltage. The electron gun and the entire electron diffractometer are placed in an ultrahigh vacuum chamber (minimum pressure in the order of 10^{-9}-10^{-10} mbar). The diffractometer's design allows high temporal resolution (100-300 fs) with multi-electron pulses (10^3 to 10^4). For pulses containing more than one electron, the pulse duration is constantly rising due to Coulomb repulsion (space charge forces) [92]. The pulse duration is kept short by accelerating the electrons to velocities of ~0.5 c so that space charge forces do not act for long time. Accelerating voltages of 60-100 kV are supplied by a DC high voltage power supply (Heinzinger). At these voltages the electron velocities are in the order of 0.45-0.55 c and the propagation time is 12-15 ps until reaching the sample.

Pulse broadening due to Coulomb repulsion can also be minimized by making the diffractometer as compact as possible [38], [91]. This is achieved by placing the magnetic lens after the sample and limiting the gun-sample distance to few millimeters. In view of all the above factors, the instrumental time-resolution can be as short as 100 fs [38]. The time-resolution of the employed setup is based on the maximum compactness of its design. The alternative is to compress the electron pulses before their arrival on the sample using oscillating electric fields. The author of this work has constructed a replica of the electron gun for a scientific collaboration with the group of Dr. Peter Baum (Ultrafast Electron Imaging Research Group, MPQ-LMU). In these experiments terahertz radiation was used for compression of the electron pulses (~3 e^- per pulse, 75 kV) and gave pulse durations of 28 fs (FWHM), more details can be found in the work of D. Ehberger *et al*. [93].

In the diffractometer, the magnetic lens (**figure 2.5**) was redesigned in order to increase its stability. The manipulator was exchanged and the new rod is thicker and longer resulting in better mechanical stability (**figure 2.5.i**). The magnetic lens is surrounded by Cu that is used to subtract heat and improve thermal stability (**figure 2.5.ii**). The lower part of the whole construction is connected with a cable made of Al foil that is damping mechanical vibrations (**figure 2.5.iii**).

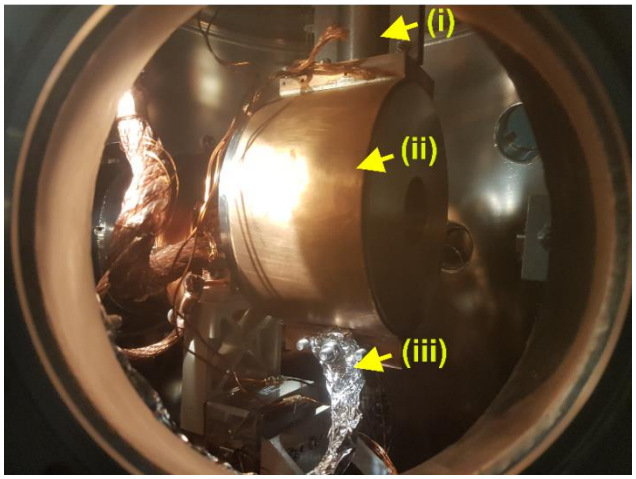

Figure 2.5: The magnetic lens used for recording the electron diffraction patterns. The magnetic lens in the upgraded apparatus is supported by a more stable rod (i), enclosed inside Cu for better thermal stability (ii) and connected to a cable made from Al foil for damping of vibrations (iii).

2.1.4 Apparatus & laboratory

The simple experimental scheme of **figure 2.1** is realized with an apparatus that combines the femtosecond laser system with the non-linear optics and the electron diffractometer that were explained in the three previous sections. The current, upgraded design is shown in **figure 2.6**. The amplifier pulses are split into the pump arm (light red area) and the probe arm (light green area) at a ratio of 9 to 1.

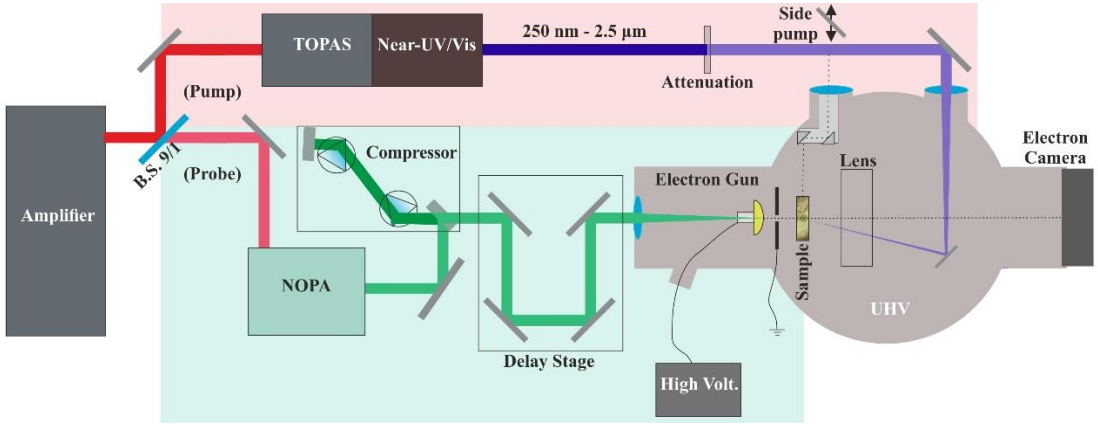

Figure 2.6: Schematic illustration of the experimental apparatus in its present form. The output of a 4 kHz amplifier laser system is splitted into two arms: the pump and the probe. The photon energy of the pump pulses is tunable. The probe pulses are transformed from 800 nm to ~540 nm radiation and finally into electron pulses at a metallic (Au) cathode. The FED experiment takes place in ultrahigh vacuum (UHV) conditions. For normal incidence, the angle between the pump and probe directions is in the order of 5^{o} to achieve velocity matching. An alternative configuration, where the pump and the probe beams form a 90^{o} angle, can be achieved with the 'side pump' optical path.

In the frame of this doctoral work, the FED setup has been reassembled in a clean room facility (see **figure 2.7**). Inside the clean room, the temperature and the humidity of the environment is kept constant offering a more stable operation of the femtosecond laser system. The humidity is kept at (40±4)% and the temperature at (22±0.1) ^{o}C (measurement carried out during the first two weeks of 2019). The experimental layout was redesigned to minimize the heat generated close to the optical table as this improves the long-term stability. All the electrical devices that produce heat but need to be accessible for every day operation are located inside water-cooled racks (**fig. 2.7.i**). The optical table and the electron diffractometer are shown in **fig. 2.7.ii**. All other electrical devices are placed inside a neighboring, isolated room, called the hot-room (**fig. 2.7.iii**).

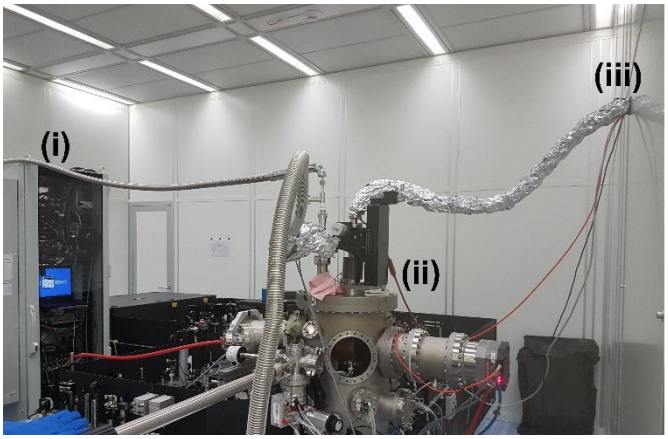

Figure 2.7: The femtosecond electron diffraction setup and the clean-room laboratory. The diffractometer (i), is connected to a water-cooled rack (ii) and to a neighboring room (iii) where all the heat-generating electrical devices are kept. This ensures stable laboratory conditions.

The fluctuations of the amplifier and the NOPA outputs (see **figure 2.8**) are in the order of 0.15% and 0.18%, respectively.

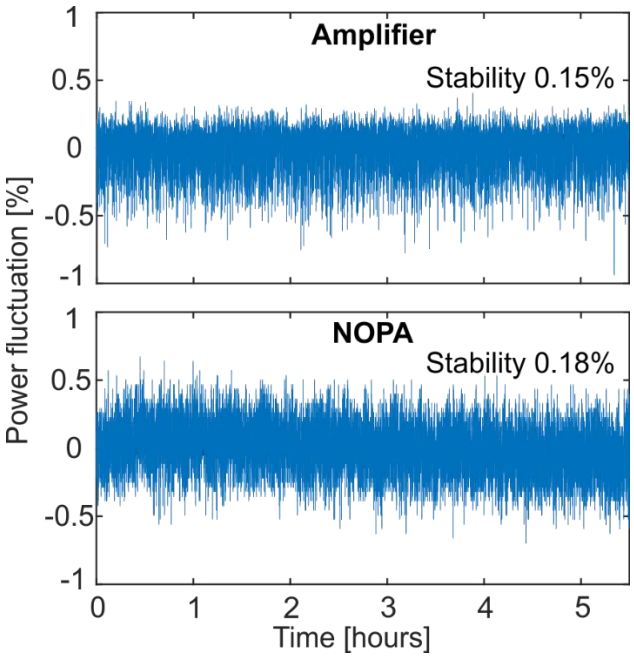

Figure 2.8: Power fluctuations of the amplifier and NOPA outputs. (a) The fluctuations of the amplifier output are 0.15%, relatively to the average power. **(a)** The fluctuations of the NOPA output are in the order of 0.18%.

For all the experiments reported in this work, diffraction and pumping have been carried out at near normal incidence. However, it is also interesting to perform pump-probe experiments with a tilted crystalline sample. Tilting the sample allows the observation of lattice motions that occur perpendicular to the crystal surface. The author of this thesis have implemented such a functionality in the FED setup, which has been used by Waldecker *et al*. [75] for studying the lattice dynamics of laser-excited antimony. Sample tilting and velocity-matching are achieved with the use of an appropriate sample holder. **Figure 2.9.a** shows the geometry of the experiment. For the tilted geometry, velocity-matching is achieved when $v_e/c = \tan\theta$, where v_e is the velocity of electrons that depends on the acceleration voltage, c is the speed of light and θ the angle between electrons and photons. For an acceleration voltage of 93 kV, the sample's tilt is 28°. The laser pulses enter the UHV chamber from a side window (see **fig. 2.6**). Subsequently, the laser pulses get translated by two prism-shaped mirrors (**figure 2.9.b**) so that they reach the sample. The sample holder has the desired angle (**figure 2.9.c**) for four out of twelve of the samples. **Figure 2.9.d** shows the entrance-holes for electrons and photons.

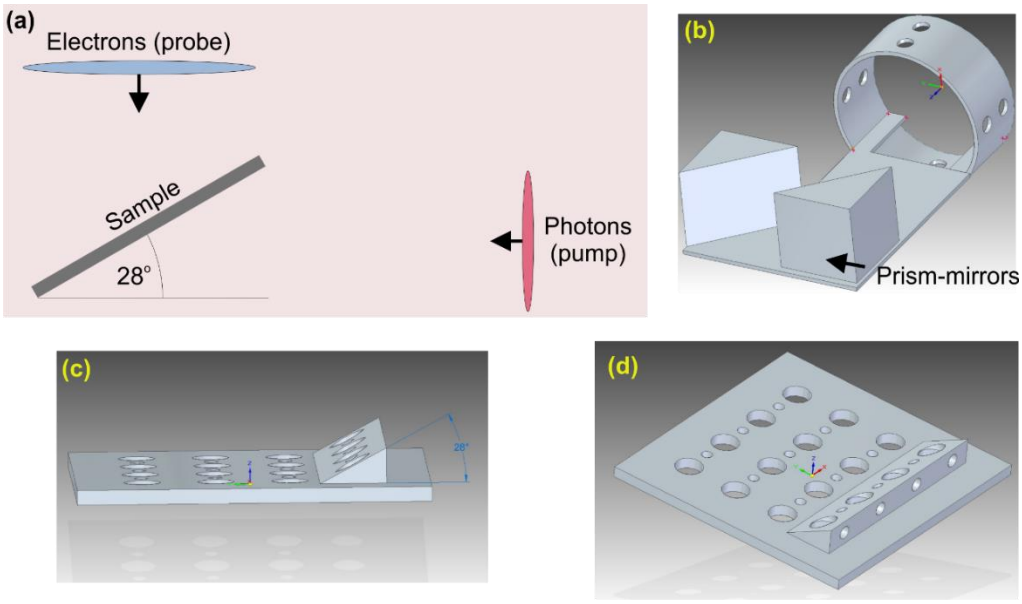

Figure 2.9: Pump-probe experiments with titled crystals. (a) Geometry of the experiment. **(b)** Optics for guiding the pump pulses inside the UHV chamber. **(c)** Sample holder where four of the samples are tilted with 23o degrees for experiments that are carried out with 93 kV electrons. **(d)** Another view of the sample holder where the entrance-holes for the laser beam are visible. For more details see the main text.

2.2 Analysis of diffraction patterns

This section illustrates the diffraction patterns acquired with FED, how the diffraction patterns are analyzed and the physical meaning of the various, extracted quantities.

2.2.1 Typical forms of diffraction patterns

Some examples of diffraction patterns acquired with FED are shown in **figure 2.10**. The diffraction pattern of **figure 2.10.a** corresponds to free-standing, thin-films of polycrystalline Au. Due to the random orientation of crystalline domains the diffraction pattern contains Debye-Scherrer rings. **Figure 2.10.b** shows the diffraction pattern of single-crystalline, multilayer flakes of WSe_2. In this case the diffracted electrons form spots.

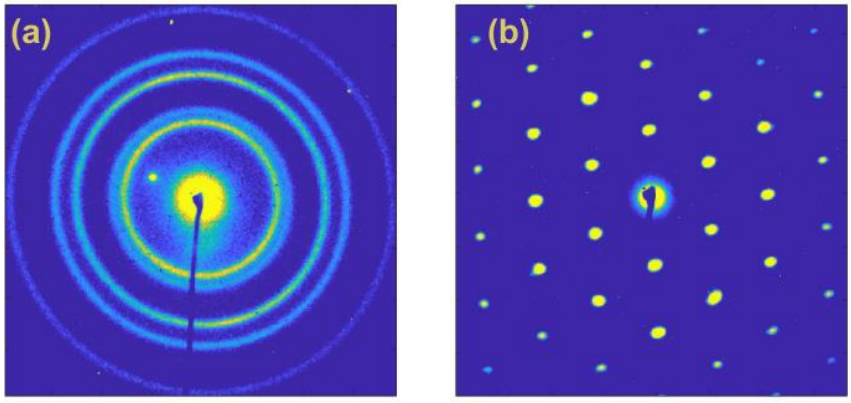

Figure 2.10: Electron diffraction patterns of polycrystalline and single crystalline materials for normal incidence of electrons. (a) Debye-Scherrer rings of free-standing, polycrystalline films of Au. **(b)** Diffraction spots of free-standing, single-crystalline flakes of WSe_2.

Generally, in homogeneous, free-standing, membrane-like samples, one needs to extract the intensity of the Bragg spots [94] or the Debye-Scherrer rings [78] and the intensity distribution of the inhomogeneous background [94].

2.2.2 Subtraction of background and fitting of diffraction peaks

This section explains the analysis of diffraction patterns for ultrasmall, zero-dimensional nanostructures on membrane-like, amorphous substrates. All measured diffraction patterns are processed by subtracting the dark counts of the electron camera and applying a flat-field that corrects the inhomogeneous efficiency of the pixels.

The processed diffraction patterns in **Figures 2.11.a** and **2.11.b** belong to Au nanoclusters with 923 atoms (Au_{923}) on a-C membranes of 20 nm thickness and bulk-like, free-standing, thin-films of Au with a thickness of 30 nm, respectively. Upon initial inspection the diffraction patterns of Au nanoclusters and bulk Au are similar. Further, quantitative analysis requires accurate determination of the radii, widths and intensities of the Debye-Scherrer rings, which is explained in the following.

Because the diffraction patterns are isotropic, their diffraction intensity is radially averaged and plotted as a function of distance (S) from the zero-order peak (**figure 2.11.c**, blue solid line). The most intense peak of the diffraction pattern (zero-order) is located at its center (see **fig. 2.11.a**). This contribution to the signal is approximated by the dashed-dot green line (**fig. 2.11.c**) and it is subtracted by the radial-average of Au_{923} / a-C. In addition, a diffraction pattern of the bare a-C substrate is measured at the same conditions and the signal is also radially averaged (brown dash-dot line, **fig. 2.11.c**). The radial-average of the bare a-C substrate is also subtracted from the Au_{923} / a-C.

The remaining, diffraction intensity (solid black line, **fig. 2.11.c**) is solely due to electrons that scatter in the Au_{923} nanoclusters. The distance from the zero-order (S), which can be directly measured in pixels, is transformed into the scattering vector that is measured in $Å^{-1}$. This transformation is based on literature values for the crystallographic planes of FCC Au. **Figure 2.11.d** shows the final diffraction pattern of Au_{923} nanoclusters (blue data-points) and the fitting (red line). The fitting contains a number of peaks and a finite background between them. The peaks are due to the electrons that get elastically scattered by the crystal-planes of the Au_{923} nanocrystals. The finite signal between the peaks constitutes the background of inelastically scattered electrons.

The background of inelastically scattered electrons has been fitted globally (the same function for all scattering angles and all peaks) and, for testing purposes, locally (for individual peaks or groups of peaks). For the global fitting, the functions that were used were either third order polynomials or a linear combination of a Lorentzian peak (at S=0)

and a function that decays as $1/S^2$. For the local fitting, simple linear functions were used. Both procedures (local and global fitting of background) were followed to check that the extracted dynamics of the peak profiles do not originate from the choice of the background and to estimate the uncertainty of the fitting.

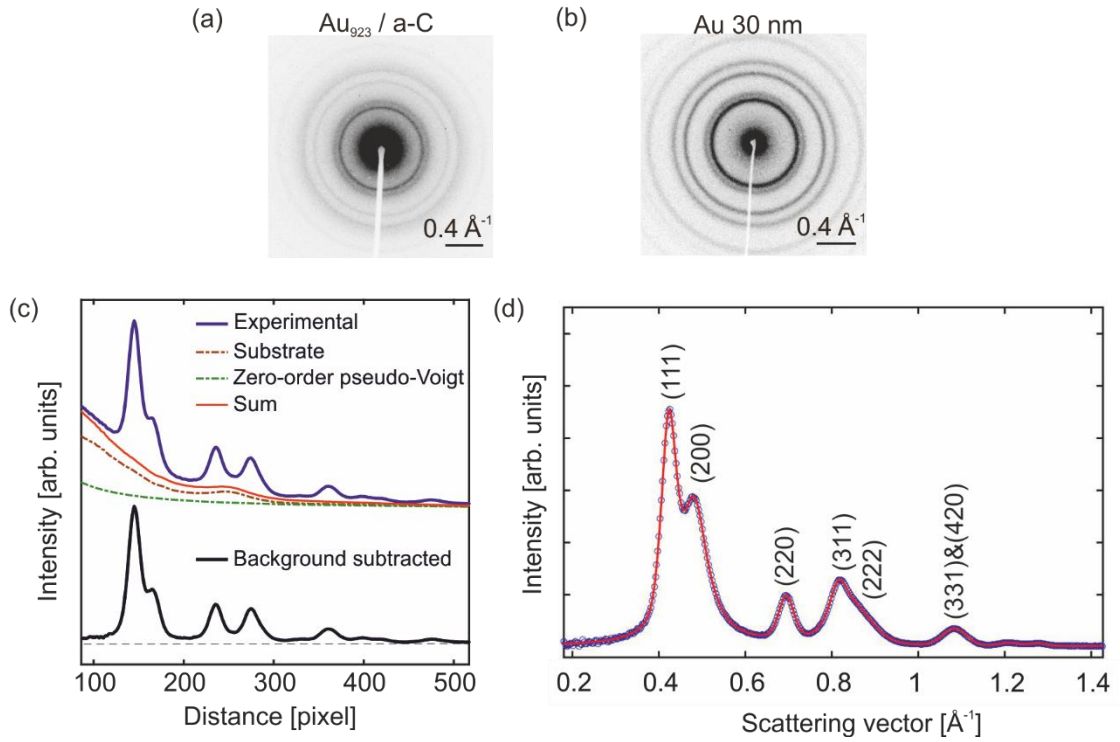

Figure 2.11: Analysis of diffraction patterns for Au_{923} nanoclusters supported on amorphous substrates. (a) The diffraction pattern of supported Au_{923} NCs. **(b)** The diffraction pattern of free-standing, bulk-like, thin-films of Au (30 nm thickness) shown for comparison. The diffraction patterns are radially averaged in order to extract the intensity as a function of the scattering angle. **(c)** The radially averaged intensity for Au_{923} NCs on Si-N (blue), the substrate contribution (brown) and the zero order estimated contribution (green). The background-free radial average is shown with black. **(d)** The background-free, radial average of Au_{923} NCs on a-C (blue datapoints) and a fit using pseudo-Voigt peak-profiles (red line).

The peaks of elastically scattered electrons are fitted with pseudo-Voigt profiles, meaning a linear combination of one Lorentzian and one Gaussian function. An initial estimation of the height (h), width (w), position (p) and Gaussian-Lorentzian mixing factor (n) of each peak is used as the starting point of the fitting. The typical upper and lower constraints for the fitted parameters are [10·h, 10·w, 1.2·p, 1] and [0.01·h, 0.1·w, 0.8·p, 0], respectively. The extracted quantities for the diffraction peaks are their intensities

(arbitrary units), their positions ($Å^{-1}$) and their widths ($Å^{-1}$). The width is defined to be equal for the Lorentzian and the Gaussian contributions of the pseudo-Voigt function. This procedure is followed for the diffraction patterns of all pump-probe delays.

2.2.3 The observables of diffraction

The previous section have demonstrated the procedure for extracting the intensity, the position and the width of diffraction peaks. In FED, as in conventional electron diffraction, the electrons scatter on the various crystal planes of the sample (real-space), interfere, and form diffraction peaks (reciprocal-space) on the detector. This section explains the real-space atomic motions in solids and their experimental signatures in reciprocal-space. The main assumption is that diffraction is kinematic, meaning that there is no multiple scattering. This assumption is based on the nanoscale dimensions of all investigated samples. The equations that follow are based on the work of Peng *et al*. [95].

The radiation used in diffraction experiments can be electrons, X-rays and neutrons. After passing from a solid the radiation forms certain patterns on the detector. With appropriate analysis, these patterns can reveal the crystal structure of the investigated sample in great detail. Depending on the type of radiation, diffraction is more sensitive to the nuclear positions or the electron orbitals. For instance, X-rays are electromagnetic waves and they interact more strongly with the electron orbitals by polarizing them, while electrons interact with the electron orbitals and the atomic nuclei with Coulomb interactions.

The scattering amplitude of the radiation from the crystal is called structure factor *F* and it is given by:

$$F(\vec{g}) = \sum_j f_j^e \exp\left[i\vec{g}\cdot\vec{r}_j\right]. \qquad \text{R 2.1}$$

The summation is carried out over all the atoms in the unit cell. The f_j^e is the atomic scattering factor (or atom form factor) for the j-*th* atom and when the scattered radiation is electrons, $\vec{g}$ is the scattering vector that is a linear combination of the axis vectors of the reciprocal lattice and $\vec{r}_j$ is the position vector of the j-*th* atom with respect to the origin of the unit cell. The value of the structure factor depends on the Miller indices of the crystallographic planes that scatter the radiation. For Au and generally FCC metals: $F = 4f_j^e$ when h, k, l have the same parity and $F = 0$ otherwise.

The atomic scattering factors depend on the angle of scattering, the wavelength and the type of radiation ($f_j^e = f_j^e(\sin\theta/\lambda)$). The electron diffraction simulations presented in **Chapter 5** used the method of Coleman *et al.* [96]. The atomic scattering factors were parametrized with 5 Gaussian distributions according to the work of Peng *et al*. [97].

The observable of diffraction is the scattered intensity. The intensity is calculated from the structure factor according to:

$$I = |F|^2 . \qquad \text{R 2.2}$$

The equations so far did not take into account that the atoms are moving around the lattice points and this can affect the intensity. The thermal motion of the atoms can be approximated by modifying the expression for the structure factor. The new form of the structure factor:

$$F(\vec{g}) = \sum_j T_j \, f_j^e \exp\left[i\vec{g}\cdot\vec{r}_j\right], \qquad \text{R 2.3}$$

includes one additional quantity, the T_j, which is the so-called temperature factor. The temperature factor creates a Gaussian uncertainty of atomic positions due to thermal motions and it is given by:

$$T_j = \exp\left[-\frac{1}{2} < \left(\vec{g}\cdot\vec{u}_j\right)^2 >\right], \qquad \text{R 2.4}$$

where $\vec{u}_j$ is the instantaneous displacement of the j-*th* atom in the unit cell and the averaging is over all possible configurations in thermal equilibrium. Assuming that the thermal vibrations are harmonic and isotropic, it is possible to derive a relationship of the form:

$$T_j = \exp[-Bs^2], \qquad \text{R 2.5}$$

where s is a slightly different definition for the scattering vector ($s = g/2\pi$) and $B = 8\pi^2 < u_j^2 >/3$ is the Debye-Waller factor. The Debye-Waller factor is proportional to the atomic mean-square-displacement $< u_j^2 >$ and thus diffraction can be used to quantify atomic motions. For materials with one atom per unit cell (*e.g.* Au) the index j is dropped. In the FED experiments the time-dependent atomic mean-square-displacement ($< u^2 >_{(t)}$) can be calculated from the time-dependent intensity ($I_{hkl}(t)$) with the relationship:

$$I_{hkl}(t) = I_{hkl}(t<0)\cdot \exp\left[-\frac{4\pi^2}{3D_{hkl}^2}\left(< u^2 >_{(t)} - < u^2 >_{(t<0)}\right)\right]. \quad \text{R 2.6}$$

This relationship reveals the first observable of diffraction, namely, the intensity of diffraction peaks that is used to quantify the vibrational excitation (see **figure 2.12.a**). The next observable of diffraction is the position of diffraction peaks. Additive interference can happen when the scattering vector is a linear combination of the axes vectors of the reciprocal lattice and due to this:

$$|\vec{s}| = \frac{1}{D_{hkl}}. \quad \text{R 2.7}$$

Hence, the position of diffraction peaks can be used to observe changes of the volume of the unit cell. Crystal (contraction/) expansion leads to (expansion/) contraction of its diffraction pattern (see **figure 2.12.b**).

Finally, the width of diffraction patterns depend on the number of scattering centers (lattice points) of the crystal. If a crystal loses atoms, or if a crystal becomes partially melted or amorphous, the width of diffraction peaks is increasing (see **figure 2.12.c**). In order to understand this phenomenon [7] one can calculate the structure factor of a linear chain in real space with atomic positions $r_j = ma$, where $m = 1,2,3,\dots,M$. The intensity is given by:

$$I(k) = F^*F = \frac{\sin^2\frac{1}{2}Mak}{\sin^2\frac{1}{2}ak}. \quad \text{R 2.8}$$

The peaks appear when k is an integer multiple of $2\pi/a$ and their width is increasing when the number of scattering centers M is decreasing. For illustration in more dimensions see **figure 2.13**. This figure shows the image in real- and reciprocal-space of two small lattices with M=4 and M=13 atoms; the broadening of diffraction peaks at smaller sizes is obvious and it follows a 1/M dependence. A more complete description for the correlation between the size of nanocrystals and the width of diffraction peaks, can be found in **Chapter 4** and it is based on the Williamson-Hall method [98]. This model takes into account the effect of inhomogeneous strain in the crystallites.

The correspondence between real-space atomic motions and reciprocal-space peak dynamics, as summarized in **figure 2.12**, is applicable to 0D nanostructures. For instance,

lattice expansion is not an appropriate observable for bulk-like, thin-films. The reason is that thin-films are constrained in the two spatial dimensions perpendicular to the electron beam and hence lattice expansion remains unobserved for prolonged time delays. Similarly, deterioration of crystallinity can be recorded and analyzed quantitatively once the crystallite is smaller than the transverse coherence length of the diffracted electrons, which is larger than 4 nm [38]. Conclusively, when the crystallite has nanometer scale dimensions, the FED experiments provide a rich variety of phenomena that can be observed.

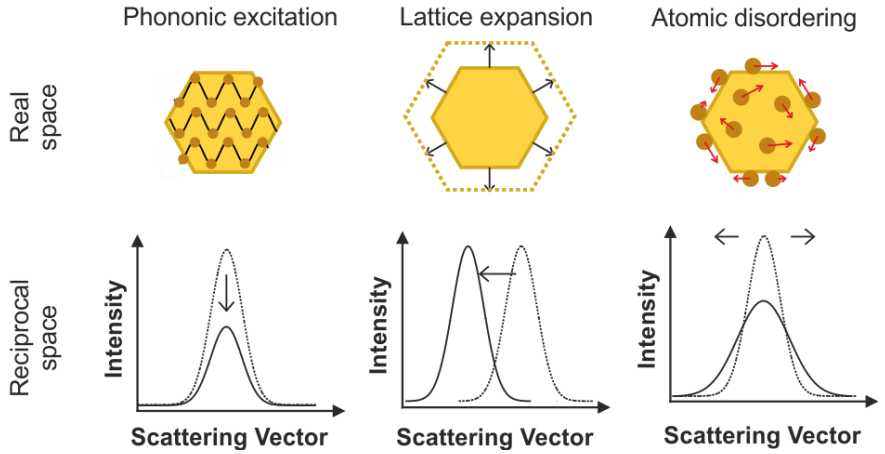

Figure 2.12: Various structural changes in real space and the corresponding observables of FED in reciprocal space for 0D nanostructures. Vibrational excitation, lattice expansion and disorder affect the intensity, position and width of diffraction peaks, respectively.

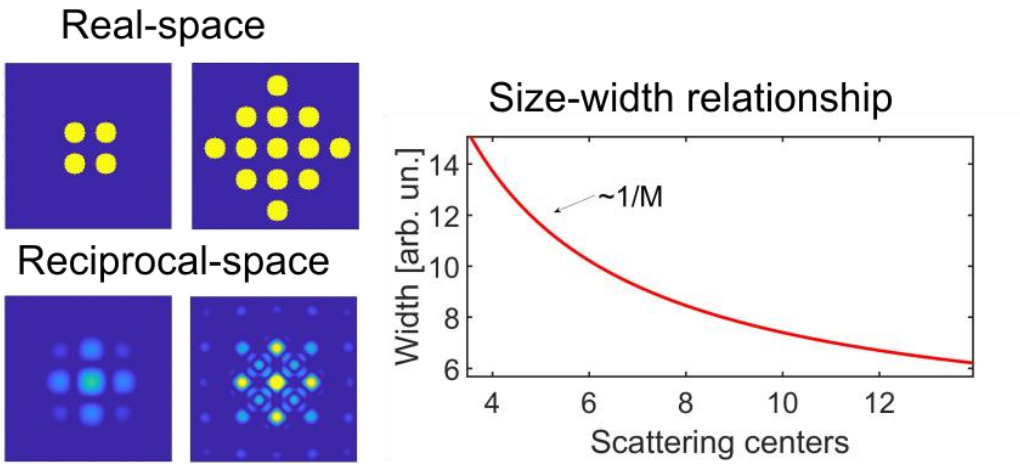

Figure 2.13: Illustration of the correlation between the size of the crystallite and the width of diffraction spots.

2.2.4 Extraction of the lattice energy content

The next step is to establish a theoretical connection between the atomic mean-square-displacement $< u^2 >$ and the vibrational energy or the lattice temperature of the material. This will allow measuring microscopic energy transfer rates. The following equations are based on the work of Peng *et al.* [95] and it is assumed that the material is isotropic, harmonic and thermalized. The atomic mean-square-displacement is given by the squares of the amplitudes of all phonons (a_q^2) in the material according to the relationship:

$$< u^2 > = \frac{1}{2} \sum_q a_q^2 \,, \qquad \text{R 2.9}$$

where a_q^2 is the square of the amplitude of the *q-th* mode and the factor of 1/2 is for time-averaging a sinusoidal function. The summation is over all the normal modes of the crystal. The mean, total energy of each phonon (E_q) is given by:

$$E_q = \frac{1}{2} k_q a_q^2 \,, \qquad \text{R 2.10}$$

where $k_q = M\omega_q^2$ is the force constant for this phonon. The total mass of the crystal *M* enters the equation and can be rewritten as $M = mN$, where *N* is the total amount of atoms. The average amplitude of each phonon is given by:

$$a_q^2 = \frac{2\, E_q}{m\, N\, \omega_q^2} \,, \qquad \text{R 2.11}$$

The energy of the *q-th* phonon is:

$$E_q = \left(n_q + \frac{1}{2} \right) \hbar \omega_q \,. \qquad \text{R 2.12}$$

The number of phonons n_q obeys Bose-Einstein statistics:

$$n_q = \frac{1}{\exp\left(\frac{\hbar \omega}{k_B T} \right) - 1} \,. \qquad \text{R 2.13}$$

The total mean-square-displacement of atoms can now be written:

$$< u^2 > = \frac{1}{2} \sum_q a_q^2 = \sum_q \frac{\hbar}{m\, N\, \omega_q} \left(n_q + \frac{1}{2} \right) \,. \qquad \text{R 2.14}$$

The summation over all normal modes can be replaced by an integral of the phonon density of states $g(\omega)$ with respect to the angular frequency ω. After some calculations the exponential of the Bose-Einstein distribution results in the appearance of a hyperbolic function. The final result is:

$$< u^2 > = \frac{3\hbar}{2m} \int_0^{\omega_{max}} \coth\left(\frac{\hbar\omega}{2k_B T}\right) \frac{g(\omega)}{\omega}\, d\omega \ . \qquad \text{R 2.15}$$

The temperature dependence of $< u^2 >$ is usually parametrized with a fourth order polynomial function of temperature and it is experimentally measured with diffraction [95]. In reverse, diffraction can also be used to measure the temperature. Most of the diffraction signal is due to scattering on the atoms (nuclei plus core-electrons) and the contribution of bonding electron orbitals is generally small [95]. Hence, the probed temperature is the lattice temperature T_L. At ultrafast timescales the lattice temperature T_L can increase due to microscopic couplings with other subsystems such as the electrons. The most important microscopic couplings for the current work are discussed in the next section.

2.3 Microscopic couplings

The previous section has discussed that FED can probe the time-evolving energy content of the lattice. This section reviews the most usual physical phenomena that trigger variations of the lattice energy content.

2.3.1 Electron-phonon coupling

The first important coupling for experiments that are based on laser-induced phenomena is electron-phonon coupling. The equations bellow are from the work of Allen [8]. The work of Allen is based on the transport equations for electrons and phonons (Bloch-Boltzmann-Peierls equations) [99]. Initially, the electrons and the lattice are in the same temperature. An incident laser pulse excites the electrons and establish a hot electron gas of temperature T_E. The electronic temperature will gradually decrease, in order to re-establish thermodynamic equilibrium with the phonons, according to the rate equation:

$$\frac{dT_E}{dt} = \gamma(T_L - T_E) \ . \qquad \text{R 2.16}$$

The coupling constant γ is given by:

$$\gamma = \frac{3\hbar\lambda < \omega^2 >}{\pi k_B T_E} \ . \qquad \text{R 2.17}$$

This expression for the electron-phonon coupling constant can be found, for instance, in the work of Brorson *et al*. [100]. The next step is to derive equations for the electron distribution f_k and phonon distribution n_Q. These equations can be found in the work of Allen. The rate equations for electrons and phonons ($\partial f_k/\partial t$ & $\partial n_Q/\partial t$) ensure that the total energy of the system is conserved. To ensure momentum conservation, the phonon wavenumber Q is always: $Q = \pm(k - k')$. The modelled interaction is that of electron-phonon coupling and it is assumed that electron-electron and phonon-phonon interactions are efficient enough so that the electrons and the phonons are always obeying Fermi-Dirac and Bose-Einstein statistics, respectively. The energy transfer from the electrons to the phonons is given by:

$$\frac{\partial E_{el}}{\partial t} = \frac{4\pi}{\hbar} \sum_{kk'} \hbar\omega_Q \, |M_{kk'}|^2 \, S(k,k') \, \delta\left(\varepsilon_k - \varepsilon_{k'} + \hbar\omega_Q\right) \ . \qquad \text{R 2.18}$$

The summation is performed over all possible transitions from an initial electronic state with momentum k to a final electronic state with momentum k'. Each scattering event changes the electron's energy by $\hbar\omega_Q$. It is possible that due to symmetry reasons, some of the transitions are completely prohibited or that others are strongly favored. The scattering cross-section is quantified by the so-called matrix element $|M_{kk'}|^2$. The δ function ensures that scattering will happen only if the energy difference between the initial and the final electronic state ($\varepsilon_k - \varepsilon_{k'}$) is matching the energy of a phonon ($\hbar\omega_Q$). The last term to be explained is $S(k,k')$ that is given by:

$$S(k,k') = (f_k - f_{k'})n_Q - f_{k'}(1 - f_k) \qquad \text{R 2.19}$$

The $S(k,k')$ is called the thermal factor. The thermal factor originates, partially, on the requirement of having an occupied, initial, electronic state with momentum k and at the same time an unoccupied, final, electronic state with momentum k'. The probability that

this requirement (Pauli blocking) is fulfilled is $f_k(1-f_{k'})$. The thermal factor is also taking into account the temperature-dependent occupation of phononic states n_Q.

The next step followed by Allen was to calculate the vibrational density of states, modulated by the spectrally resolved electron-phonon coupling. This quantity is called the electron-phonon spectral function or the Eliashberg function and it is given by:

$$a^2F(\varepsilon,\varepsilon',\omega)=\frac{2}{\hbar N_C^2 g(\varepsilon_F)}\sum_{kk'}|M_{kk'}|^2\delta\big(\omega-\omega_Q\big)\delta(\varepsilon_k-\varepsilon)\delta(\varepsilon_{k'}-\varepsilon')\,, \qquad \text{R 2.20}$$

where $\varepsilon,\varepsilon',\omega$ are the initial and final electronic energy and the phonon frequency respectively, while $g(\varepsilon_F)$ is the electronic density of states at the Fermi level. The N_C is a normalization factor (inverse of the unit cell volume).

The Eliashberg function is an important quantity for: (i) the relaxation of electrons in laser-excited metals, (ii) the theory of superconductivity and (iii) the inelastic scattering events observed in scanning tunneling spectroscopy measurements. In fact, scanning tunneling spectroscopy can record directly the Eliashberg function (second derivative of the current with respect to the voltage at low temperatures) as shown by Schackert *et al.* [101] and Minamitani *et al.* [102].

The energy transfer rate between electrons and phonons ($\partial E_{el}/\partial t$) can be written as an integral [78] that contains the Eliashberg function:

$$\frac{\partial E_{el}}{\partial t}=-\frac{2\pi N_C}{g(\varepsilon_F)}\int_0^{\infty}d\omega\,(\hbar\omega)^2a^2F(\omega)\,[n(\omega,T_E)-n(\omega,T_L)]\,\times \qquad \text{R 2.21}$$

$$\times\int_{-\infty}^{+\infty}d\varepsilon\,g^2(\varepsilon)\,\frac{\partial f(\varepsilon,T_E)}{\partial\varepsilon}\,.$$

The factors n and f are the Bose-Einstein and Fermi-Dirac distributions, respectively. The energy transfer rate (Wm^{-3}) is connected with the coupling constant ($Wm^{-3}K^{-1}$) through the relationship:

$$G_{E-PH}=\frac{1}{T_E+T_{PH}}\,\frac{\partial E_{el}}{\partial t}\,. \qquad \text{R 2.22}$$

Ab-initio calculations of G_{E-PH}, which were based on the formalism of Allen and the Eliashberg function, have been used to study nonthermal structural dynamics in Al [78] and Sb [75].

2.3.2 Measurement of electron-phonon coupling with FED

The first requirement of an FED experiment is to selectively excite the electrons in order to create a hot Fermi Dirac distribution. Subsequently, energy flows from the electrons to the phonons according to the picture of interacting heat baths in **figure 1.1** and the gradual lattice excitation is detected with electron diffraction. The electronic excitation is achieved by irradiating the sample with femtosecond laser pulses at optical or near-infrared frequencies.

Figure 2.14 shows a simple schematic illustration of the underlying physical processes. Photons are primarily absorbed by the electrons, leaving the lattice unaffected. A detailed description of light-matter and electron-electron interactions, during this initial step, is not necessary for our scope as explained immediately. Independently of the exact laser-induced electronic transitions, electron-electron interactions lead to rapid thermalization of the electrons. The time for electronic thermalization depends on the excitation density and it can be measured by time-resolved photoemission [103]. In order to achieve a measurable amount of lattice heating, the typical excitation fluence (0.5-3 mJ/cm^2) is sufficient for electron thermalization within ~100 fs (upper limit), a timescale that is comparable with the instrumental time-resolution. It is worth noting that plasmonic oscillations [45], a well-known feature of metallic nanostructures, are part of the short-living electronic processes and are not explicitly included in the analysis of energy flow. Plasmonic excitations in metal NCs are decaying into hot carriers within ~10 fs [104].

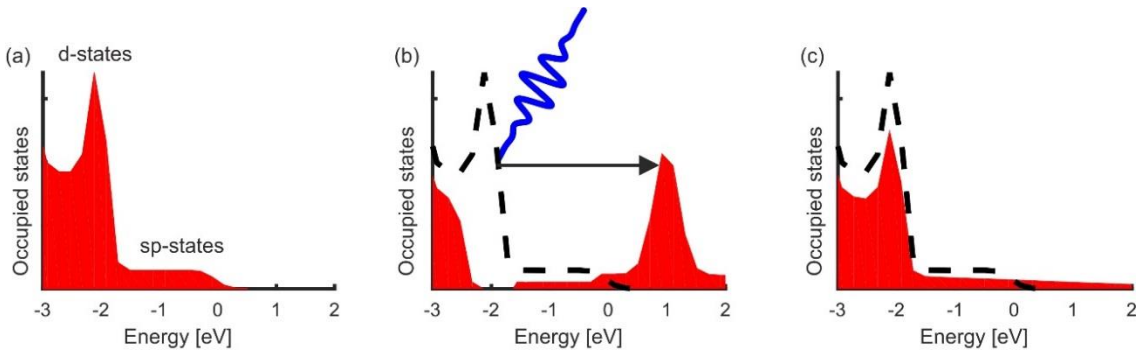

Figure 2.14: Schematic illustration of laser induced hot electron generation. (a) The occupied states in Au have sp-character at the Fermi level and d-character at deeper

energy levels [105]. **(b)** Absorption of a 400 nm light leads to (de-) population of states (below) above the Fermi level including the d-states. **(c)** Electrons thermalize and acquire a Fermi-Dirac distribution of high electronic temperature within 100 fs. (The degree of excitation is exaggerated for visualization purposes.)

The thermalized, hot electron gas is cooling by generation of phonons (electron-phonon coupling). The next requirement is accomplishing quantitative measurements of ultrafast lattice heating using FED. FED has access to all the observables of conventional diffraction, which is sensitive to temperature changes [95] (see also **section 2.2.4**).

The time-evolving lattice temperature T_L and knowledge of the electronic and lattice heat capacities, allows measuring the electron-phonon coupling strength (**figure 2.15**). Electronic and vibrational heat capacities are obtained by the electronic and vibrational densities of states according to Fermi-Dirac and Bose-Einstein statistics respectively.

For bulk-like, free-standing, thin-films of simple metals a widely used approach is the so-called two-temperature model (TTM) [8], [105], [106]. In TTM, the electrons and the phonons are treated as two heat baths with distinct temperatures and heat capacities (**figure 2.15.a**). The two heat baths have different temperatures and can exchange heat at a rate G_{e-ph}. The energy input (from the laser) is expressed as a source term in the equation that gives the electronic temperature. For non-magnetic materials (present work) the electrons' spins are not taken into account. All these assumptions transform the scheme of **figure 2.15.a** into a system of two coupled differential equations:

$$\frac{dT_E\,(t)}{dt} = -\frac{G_{e-ph}}{C_E}(T_E - T_L) + S(t) \quad , \qquad \text{R 2.23}$$

$$\frac{dT_L\,(t)}{dt} = \frac{G_{e-ph}}{C_L}(T_E - T_L) \quad . \qquad \text{R 2.24}$$

Equations R 2.23 and R 2.24 are used for a non-linear fit of the experimental lattice temperature evolution acquired with equations R 2.6 and R 2.15. A typical time-evolution for the two temperatures is shown in **figure 2.15.b**. These calculations correspond to bulk Au. The electronic temperature is reaching a maximum value of around 3000 K. Subsequently, the electrons cool down and the lattice is heating up until the two temperatures meet at approximately 500 K. The larger temperature change observed for electrons is due to the small, electronic heat capacity.

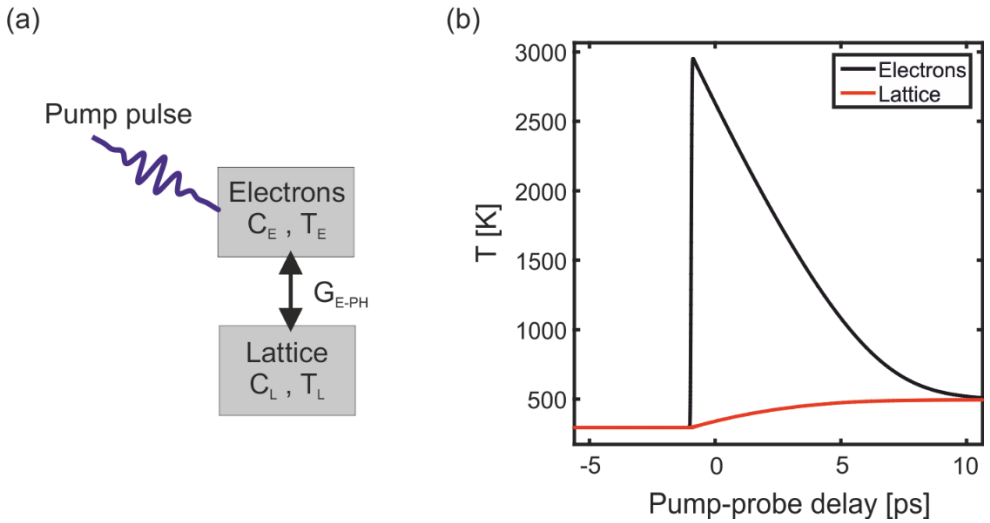

Figure 2.15: The two-temperature model (TTM) for a simple metal (Au). (a) In the TTM, a non-magnetic metal (here Au) is considered as two heat baths in contact. These are the electrons and the lattice (phonons) of the solid. The excess energy, to initiate electron-lattice nonequilibrium, is offered by a laser pulse. **(b)** The evolution of the electronic (black solid line) and lattice (red solid line) temperatures in the TTM.

Limitations of the TTM. The TTM is a versatile tool for measuring G_{e-ph} and it is more meaningful than simple phenomenological arguments based on the extraction of simple time-constants. Yet, its predictions have been proven to deviate from the exact electron-lattice equilibration dynamics. The reason is that phonons of different branches can have different coupling strength to electrons leading to non-thermal lattice conditions [78]. The theoretical work of Allen [8] indicates that the electron-phonon coupling strength can vary across the various phonon frequencies.

The electron-phonon coupling is better described by a spectral function (the Eliashberg function) rather than a single constant. In a slightly different notation, involving the electronic band structure, Bernardi *et al.* [107] have shown that individual electronic states of Si can show very different electron-lattice interaction strengths in response to (solar) light and during the first picosecond. All these considerations point towards the need to develop models that are not strictly applicable to well-thermalized lattice degrees of freedom.

The TTM equations represent the energy content of the lattice with a single temperature and the electron phonon coupling with a single factor. To take into account non-thermal

phonon distributions, it is essential to have support from *ab-initio* molecular dynamics [75], [78] or to carry out a momentum-resolved analysis of the diffraction patterns [94], [108], [109]. These objectives are currently unfeasible for nanoscale heterostructures. Heterogeneity and absence of long-range translational symmetry make momentum-resolved FED studies and ab-initio simulations currently unfeasible. As a result of these complications, the presently reported analysis is using a single lattice temperature for each component of the heterostructure, which represents an effective measure of the average, lattice energy content.

However, the author of this thesis has developed a fitting algorithm – according to the work of Waldecker *et al*. [78]. – to study incoherent, phonon-phonon interactions in the Peierls-distorted, semimetal, Sb [75]. **Figure 2.16.a** shows the vibrational density of states of Sb. Interestingly, the acoustic (red) and optical (blue) phonon spectra are well-separated in the energy (/frequency) axis. This allows to consider the acoustic and optical phonons as two distinct subsystems. The total Eliashberg function results in the temperature-dependent electron-phonon coupling shown in **figure 2.16.b** with a black line. The Eliashberg function is based on *ab initio* simulations of T. Zier, F. H. Valencia, M. E. Garcia, and E. S. Zijlstra. The integral of the Eliashberg function has been used to separate the contributions of the optical phonons (blue curve in **fig. 2.16.b**) and the acoustic phonons (red curve in **fig. 2.16.b**). Based on this procedure, optical phonons have stronger coupling to the electrons than the acoustic ones.

Next, the TTM was replaced by the non-thermal lattice model (NLM) [78]. The interacting subsystems are three: the electrons, the optical phonons and the acoustic phonons. The author has used the vibrational density of states to calculate the heat capacity and the atomic mean-square-displacement for each type of phonon. The solution of the NLM is shown in **figure 2.16.c**. Optical phonons become hotter during the first 5 ps and al lattice temperatures are eventually equilibrated at ~5-6 ps. Yet, the atomic mean-square-displacements shown in **figure 2.16.d**, are very different. In the NLM the fitted quantity is the mean-square-displacement and not the lattice temperature.

The lower-frequency phonons are considerably more efficient in producing a decay of the intensity of diffraction peaks. For this reason, a simple fit with the TTM (with linear temperature-dependence of the coupling constant) seems to coincide with the ab-initio electron-phonon coupling of acoustic phonons (see dashed line in **figure 2.16.b**).

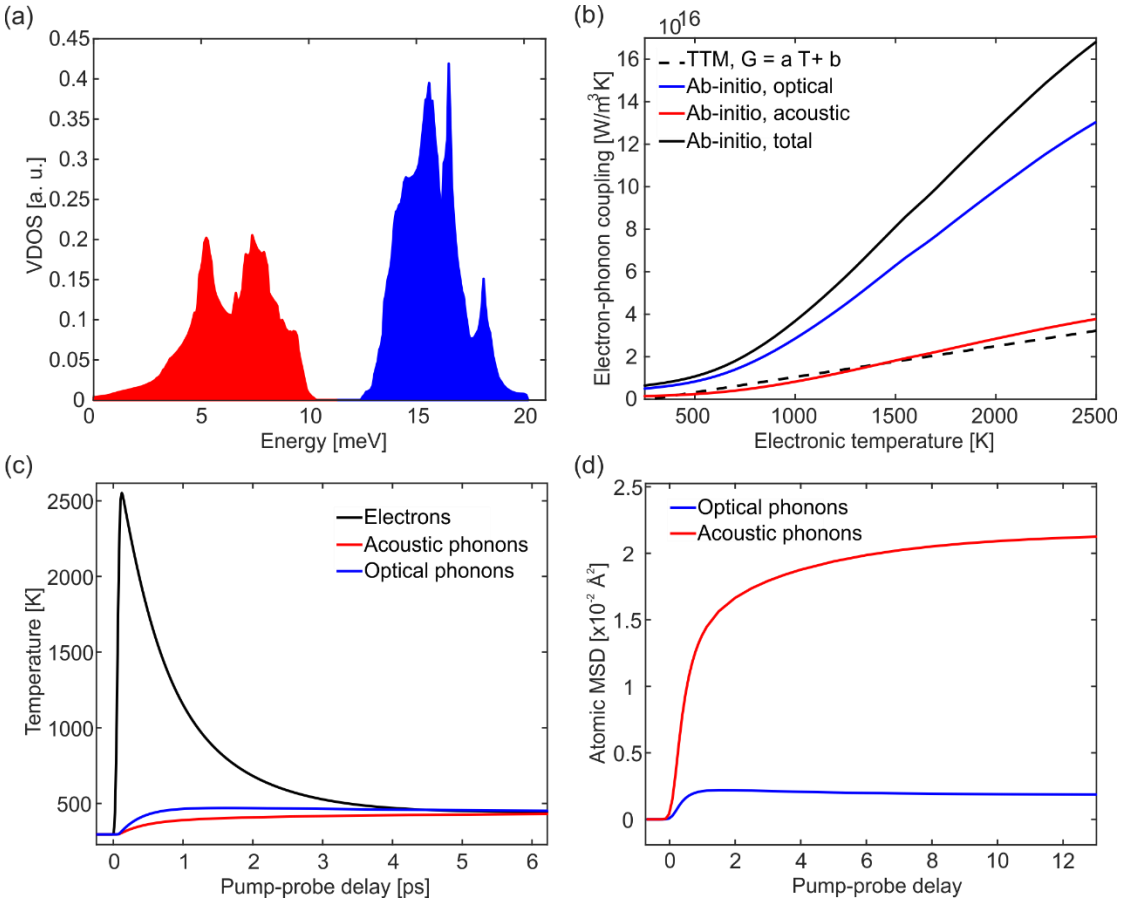

Figure 2.16: The nonthermal-lattice-model (NLM) for a Peierls-distorted semimetal (Sb). (a) The VDOS of acoustic phonons (red) and optical phonons (blue) exhibits a clear separation in the energy. **(b)** The total electron-phonon coupling from ab initio simulations (black solid line) can be separated into the electron-phonon coupling of optical (blue line) and acoustic (red line) phonons. The optical phonons have the strongest coupling with the electrons. **(c)** The simulated temperature evolutions of the electrons (black line), optical phonons (blue line) and acoustic phonons (red line according to the NLM. During electron-lattice nonequilibrium, the optical phonons are transiently getting hotter. **(d)** The quantity that is finally fitted is the atomic MSD. The total MSD (measured by FED) is the sum of the MSD due to optical phonons (blue) and the MSD due to acoustic phonons (red). Evidently, the strongly coupled optical phonons have a limited effect on the FED measurement. For more information see the main text.

2.3.3 Interfacial transmission of phonons & electrons

Intrinsic interactions, such as electron-electron, electron-phonon and phonon-phonon interactions, are sufficient for studying energy flow in homogeneous elements and chemical compounds. Of course most devices are inhomogeneous since it is necessary to bring together different materials to perform some complicated function (see also **Chapter 1**). This is a particularly important aspect for nanoscale devices. In nanoscale devices a significant amount of atoms is located at surfaces and interfaces and hence the chemical environment plays an important role in energy flow. If the nanostructure is, for instance, 3 nm thick and made of Au, it takes only 1 ps for phonons to travel from its top to the bottom layer and reach the substrate surface. In this case the extrinsic energy flow to the support needs to be taken into account in order to investigate energy flow at ultrafast timescales. This work is about energy flow in nanoscale heterostructures and hence the transmission of electrons and phonons at the interface needs to be considered. The importance of such investigations for present-day applications in electronics is discussed in the work of Eric Pop *et al.* [41].

Vibrational coupling. One of the pioneers in the understanding of interfacial energy transfer was Pyotr Kapitza who worked in the field of low-temperature physics. Owning to his contributions, the interfacial conductance of phonons is also termed Kapitza conductance. The following theoretical considerations are based on the works of Challis [110] and Stoner *et al.* [111]. First the interfacial phonon transmission, or vibrational coupling W_{PP} is defined with the relationship:

$$\dot{q} = W_{PP}\,\Delta\mathrm{T} \quad , \qquad \text{R 2.25}$$

where $\dot{q}$ is the heat flux and ΔT the temperature difference across the interface. If the vector normal to the interface is $\hat{z}$, the interfacial phonon transmission W_{PP} is given by:

$$W_{PP} = \frac{1}{V}\frac{\partial}{\partial T}\sum_{k}\hbar\omega_k\; n(\omega_k, T)\,|\vec{v}_k \cdot \hat{z}|\; t_k \quad , \qquad \text{R 2.26}$$

where the summation is over all the phonon modes, $\hbar\omega_k$ is the energy of one phonon, $n(\omega_k, T)$ is the Bose-Einstein distribution, $\vec{v}_k$ is the phonon group velocity and t_k is a transmission coefficient.

According to Challis [110] and Stoner *et al.* [111], the transmission coefficient expresses various processes of interfacial phonon reflection without transmission of energy. Reflection at the interface can occur for three main reasons. First, the phonons obey the law of Snell, meaning that they get refracted at the interface. If the phonon is transmitted from a soft material A to a stiff material B ($v_A < v_B$, where v the speed of sound), then it can experience total internal reflection. For total internal reflection the angle of incidence (θ) needs to be:

$$\theta > \sin^{-1}\left(\frac{v_A}{v_B}\right) \quad . \qquad \text{R 2.27}$$

Second, the transmission coefficient is never unity, even at normal incidence, and this is due to the so-called acoustic mismatch. For electromagnetic waves, reflection at normal incidence is due to the discontinuity of the refractive index or the dielectric constant. For phonons, reflection at normal incidence is due to the discontinuity of the acoustic impedance (Z), which is defined as the product of the mass density and the sound velocity. The transmission coefficient based on this mechanism is:

$$t_k = \frac{4Z_A Z_B}{(Z_A + Z_B)^2} \quad . \qquad \text{R 2.28}$$

Third, a transmission coefficient smaller than unity can also result from the vibrational densities of states of the two materials. A phonon in material A with frequency ω_A will couple more efficiently with a phonon in material B that has the same frequency. This means that for efficient vibrational coupling, the vibrational densities of states of the two materials must have significant overlap in the frequency the domain.

Electronic coupling. Similar relationships and considerations can be made for the transmission of electrons across the interface and in this case the phenomenon is described as electronic coupling or electronic Kapitza conductance [112]. Another possible mechanism of interfacial energy transfer is when an electron of material A is inelastically scattered at the interface and produces a phonon in material B. The detection of interfacial polarons in nanoscale heterostructures [113] proves that, in principle, interfacial electron-phonon interactions can indeed take place. The contribution of interfacial electron-phonon interactions to the interfacial energy flow is discussed in the theoretical work of Sergeev [114].

2.4 Molecular dynamics simulations

For a better understanding of the experimental results it is often desirable to make comparisons with molecular dynamics simulations from first-principles. Quantum mechanical simulations in nonequilibrium conditions are not feasible for the investigated, nanoscale systems due to the lack of translational symmetry and the number of atoms (~10^3). However, because the investigated nanostructures are mesoscopic objects and because some of the investigated phenomena are slower than the electron-lattice relaxation, the author and his colleagues employed classical molecular dynamics (MD) simulations (**Chapter 5**). Classical MD simulations solve the Newton's equations and use statistical ensembles from classical thermodynamics.

Finite differences. The atomic trajectories have been solved with the Velocity-Verlet algorithm. The time-evolving positions and the velocities are given by:

$$\vec{x}(t+\delta\tau) = \vec{x}(t) + \vec{v}(t)\,\delta\tau + \frac{1}{2}\,\vec{a}(t)\,\delta\tau^2 \quad , \qquad \text{R 2.29}$$

$$\vec{v}(t+\delta\tau) = \vec{v}(t) + \frac{\vec{a}(t)+\vec{a}(t+\delta\tau)}{2}\,\delta\tau \quad . \qquad \text{R 2.30}$$

Interatomic potentials. The interatomic interactions are described by 12-6 Lennard-Jones potentials (unless stated otherwise). These interatomic potentials have the general form:

$$V_{LJ}(r) = 4\varepsilon\left[\left(\frac{\sigma}{r}\right)^{12} - \left(\frac{\sigma}{r}\right)^{6}\right] \quad , \qquad \text{R 2.31}$$

where r is the interatomic distance, ε is the maximum depth of the potential energy surface and σ the distance at which the interatomic potential becomes positive and repulsive. The parameters of the empirical potentials are based on DFT simulations of selected atomic arrangements. For more information see **Chapter 5**.

Statistics. All MD simulations have been performed in the NVT ensemble, meaning constant number of particles (N), constant volume (V) and constant temperature (T). The temperature has been kept constant using the Nosé-Hoover thermostat [115], [116]. Conceptually, all thermostats are resembling the two-temperature-model. The first heat bath is the simulated system, the temperature of which needs to be fixed. The second heat bath is fictitious, it represents the environment and it interacts with all the simulated atoms, keeping their average kinetic energy in the order of k_BT.

Electron diffraction simulations. The real-space trajectories of the MD simulations were used to calculate theoretical diffraction patterns. The electron diffraction simulations have been carried out using the method of Coleman *et al*. [96]. The atomic scattering factors were parametrized with 5 Gaussian distributions according to the work of Peng *et al*. [97]. Two important parameters for the simulations of the electron diffraction patterns are the thickness of the Ewald sphere, which was set to 0.06 $Å^{-1}$, and the spacing of the computational grid for the reciprocal spacing, which was set to 0.007 $Å^{-1}$. The radius of the Ewald sphere was calculated for the energy of the electrons used in the experiment. For an energy E=90 keV, the relativistic De Broglie wavelength is λ=3.9 pm and the Ewald sphere radius is 26 $Å^{-1}$.

Chapter 3. Ultrafast energy flow in 0D/2D heterostructures

This chapter is devoted to the study of ultrafast energy flow in heterostructures of Au nanoclusters (0D) on thin-film substrates (2D) and it is based on the publication: '*Ultrafast Heat Flow in Heterostructures of Au Nanoclusters on Thin-Films: Atomic Disorder Induced by Hot Electrons*', ACS Nano, 2018, 12 (8), pp 7710-7720, by Th. Vasileiadis *et al*. [117]. The structure of this chapter follows a 'top-down' approach, starting from the dynamics of bulk Au, after the dynamics of Au nanoislands and finally ultrasmall Au nanoclusters.

The first section (**section 3.1**) shows the dynamics of electron-lattice equilibration in bulk, free-standing, thin-films of Au, as measured by FED. The measurements of homogeneous, bulk Au serve as a reference before proceeding with spatially confined and heterogeneous samples that contain Au nanostructures. The next section (**section 3.2**) presents FED measurements of Au islands on graphene. The study of these samples reveals the effect of heterogeneity in the absence of drastic, spatial confinement. The next sections deal with heterostructures that contain ultrasmall Au_{923} nanoclusters (NCs) on various thin-film substrates (0D/2D heterostructures). **Section 3.3** describe the morphology (**3.3.1**) and the Debye-Waller dynamics (**3.3.2**) of the spatially confined 0D/2D heterostructures. **Section 3.4** is devoted in the development of a model for ultrafast energy flow in 0D/2D heterostructures (**3.4.1**) and the various inputs that are required (**3.4.2**). Finally, the model of ultrafast energy flow is used in **section 3.5** in order to extract the various microscopic coupling constants. Based on the model, it is possible to acquire a realistic estimation for the time-evolution of the electronic temperature of the NCs, which cannot be observed directly with FED.

3.1 Debye-Waller dynamics of bulk Au

Using FED to record the ultrafast, structural dynamics of bulk, homogeneous Au is an important task before proceeding with heterostructures that contain spatially confined Au. The acquired information ensures the validity of the employed experimental and computational methods and serves as a reference in order to indicate confinement-

induced phenomena. Bulk Au has well-known structural dynamics and, hence, the results are discussed briefly (a more detailed presentation is carried out for spatially confined systems). The samples are free-standing, homogeneous, thin-films of Au suspended on Cu TEM grids. The thickness is in the order of 10 nm, meaning that strong spatial confinement is not expected. For simple metals, quantum confinement phenomena are expected to emerge when the characteristic dimension is equal or smaller than the Fermi wavelength (see time-resolved optical measurements in reference [118]), which for Au is λ_F=0.5 nm, or for larger structures (5-15 nm) at ultralow temperatures (T≤90 mK) (see transport measurements in reference [119]).

The time-resolved diffraction patterns of bulk Au (see **fig. 2.10.a** for the diffraction pattern of bulk Au) are recorded with FED at room temperature. **Figure 3.1.a** shows the ultrafast experimental decay of the intensity of various diffraction peaks (circles). All data sets can be reproduced by exponential decays (solid lines) with time-constants of 4.5 ps.

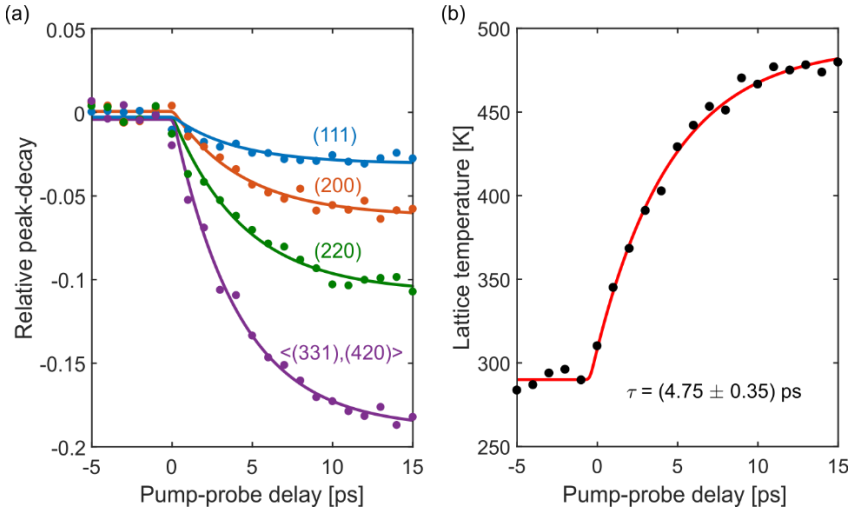

Figure 3.1: Ultrafast lattice temperature evolution and TTM fitting of bulk, free-standing, thin-films of Au. (a) Experimental peak-decay of photo-excited Au lattice (circles) and exponential decays (solid lines, same color). The indices denote the diffraction peak. **(b)** The predicted electron temperature evolution (black circles) together with the fitted lattice temperature evolution (red line).

The decay of the intensity of diffraction peaks is transformed, using the Debye-Waller formalism (**section 2.2.3**), into an effective lattice temperature. The temperature-dependence of the Debye-Waller factor is found from the work of Peng *et al*. [95]. The resulting lattice temperature evolution can be finally modelled with the TTM (**section**

2.3.4) in order to extract the electron-phonon coupling constant and/or fitted with an exponential decay in order to quantify the rapidity of electron-lattice equilibration. **Figure 3.1.b** shows the ultrafast lattice temperature evolution of the photo-excited Au film (black circles) and the exponential fitting (red line), which gives a time-constant of (4.75±0.35) ps. The corresponding width and the scattering angle of the various diffraction peaks in this measurement remain unchanged. The dynamics are single-exponential, meaning that after ~10 ps the electrons and the lattice are in equilibrium. Thermal relaxation of the sample with its environment proceeds in the nanosecond to millisecond timescale.

Electron-phonon coupling- & time-constants of bulk Au. The extracted electron-phonon coupling constant from various measurements is $G_{e-ph} = 2.7 \cdot 10^{16}\ W/m^3K$. This value is in excellent agreement with optical pump-probe experiments and TTM modelling by Brorson *et al*. [100] that gave $G_{e-ph} = 2.61 \cdot 10^{16}\ W/m^3K$. Time-resolved diffraction studies give a characteristic timescale for electron-lattice equilibration in the order of ~4-6 ps [120], [121]. However, the time-constant for electron-lattice equilibration depends on the absorbed fluence and the heat capacity in addition to the coupling constant (**fig. 3.2**).

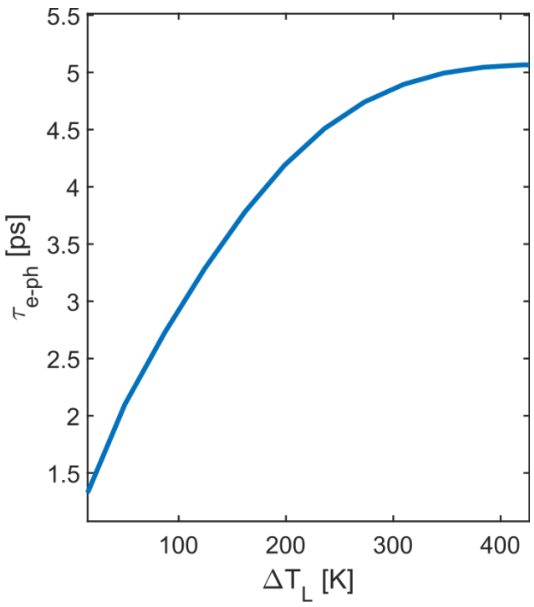

Figure 3.2: Time-constant of electron-lattice equilibration from exponential fitting of the TTM solutions. The TTM has been solved for various fluences and the resulting lattice temperature evolution has been fitted with an exponential decay in order to simulate the apparent time-constant. The time-constant ($\tau_{e\text{-}ph}$) is plotted as a function of the maximum, lattice temperature increase (ΔT_L). The maximum time-constant is around 5 ps. For small, absorbed fluences (small ΔT_L) the time-constant approaches the 1 ps timescale.

Figure 3.2 shows the dependence of the electron-phonon equilibration time on the lattice temperature rise, as predicted by the TTM. Generally, processes that take place within 1-6 ps can be safely associated with electron-lattice equilibration. This information will be useful for the FED measurements of spatially confined Au on surfaces.

3.2 Debye-Waller dynamics of Au islands on graphene

The next sample under investigation is Au (nominal thickness ≥ 3 nm) deposited on few-layer graphene with evaporation. These samples are heterogeneous but without strong spatial confinement. Strong quantum confinement phenomena are not expected, however, the large surface-to-volume ratio of these structures facilitates exchange of energy with their chemical environment (graphene substrate) at ultrafast timescales. **Figure 3.3** shows FED measurements of polycrystalline thin-films of Au grown on few-layer graphene.

Thick Au on C. For a nominal thickness of ~10 nm, Au forms discontinuous films on graphene (**figure 3.3.a**). After excitation, lattice heating cause the diffraction peaks to decay (**figure 3.3.b**), due to the Debye-Waller effect, with a time-constant $\tau = (3.4 \pm 0.3)\ ps$, which can be attributed to electron-lattice equilibration.

Thin Au on C. For a nominal thickness of 3 nm, Au forms ramified objects resembling nanoislands (**figure 3.3.c**). In this sample the decay of intensity follows bi-exponential dynamics with time-constants $\tau_1 = (3.1 \pm 0.8)\ ps$ and $\tau_2 = (40 \pm 5)\ ps$ respectively (**figure 3.3.d**). The fast process can be attributed to electron-lattice equilibration in Au, based on its time-constant. The slow process (τ_2) is significantly slower than electron-phonon interactions and it can result from interfacial energy flow from the graphene substrate through transmission of phonons.

Previous knowledge on Au / C heterostructures. Previous works with time-resolved electron diffraction of Au nanoislands on graphene have observed the same retardation of lattice equilibration. The slow process has vanished once the Au/C interface was intercalated with organic ligands [122]. The offered, qualitative explanation was as in the present work that the slower lattice equilibration is due to phonon transmission from the hotter substrate. The present experiments and the comparison of the 10 and 3 nm thick

samples shows that interfacial energy transfer to the substrate becomes increasingly important as the dimensions of the adsorbed nanostructure become smaller.

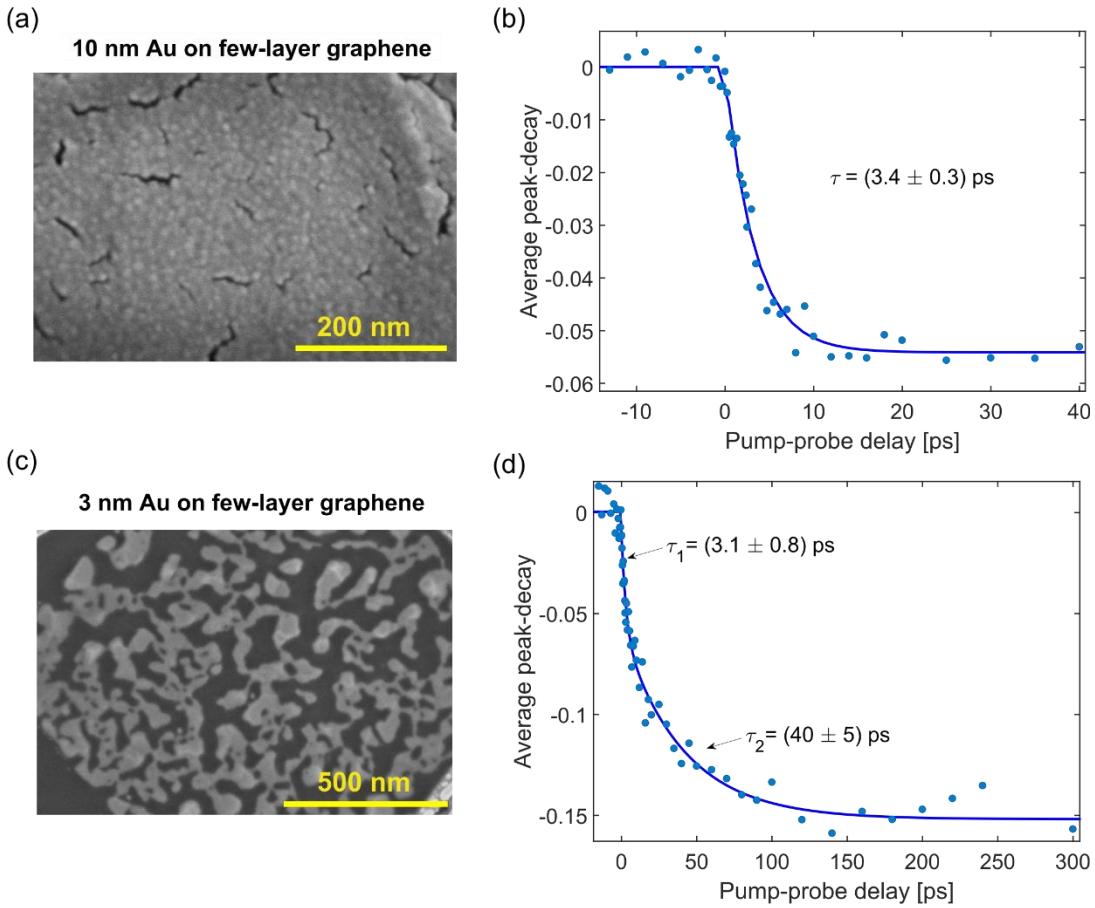

Figure 3.3: Thickness-dependent lattice dynamics of Au deposited on graphene. **(a) & (b)** Scanning electron microscopy (SEM) image of 10 nm Au deposited on graphene and average decay of intensity of diffraction peaks measured by FED, respectively. **(c) & (b)** SEM image of 3 nm Au deposited on graphene and average decay of intensity of diffraction peaks measured by FED, respectively. Lattice equilibration is achieved within ~10 ps for 10 Au film and within ~100 ps for 3 nm Au.

Ensemble-uncertainty. The samples investigated here are highly polycrystalline and polydisperse. Thus, an accurate examination based on the Debye-Waller effect is not feasible. The Debye-Waller factor, the lattice heat capacity and other lattice properties might vary greatly among the probed islands. Instead, the next sections are devoted to supported, Au NCs with very narrow distribution of size and very limited structural allotropes. In the case of size-selected NCs, all lattice parameters can be accurately identified.

3.3 Debye-Waller dynamics of Au_{923} nanoclusters on thin-films

Section **3.3.1** reports the morphology of size-selected Au NCs on thin-film substrates and section **3.3.2** the FED measurements of their Debye-Waller dynamics on various thin-film substrates.

3.3.1 Synthesis and characterization of Au_{923} nanoclusters

The samples contain Au NCs with a precise number of atoms and well-defined geometric shapes. This section examines how the NCs distribute on the thin-film, their size and their shape. The NCs under investigation have been provided by the scientific group of Professor Richard Palmer (Swansea University). Metallic NCs (~10 to 10^3 atoms) have increased stability for certain amount of atoms [123]. In this work, the selected NCs were $Au_{923\pm23}$ supported on various thin-films. For completeness the next two paragraphs refer to the preparation and characterization that they followed. These items of information are essential for the FED experiments, because the relative masses of the NCs and of the substrate and the overall sample morphology, determine the heat capacities and how energy flows.

The procedure starts with sublimation of Au in a radio frequency magnetron plasma sputtering source [124]. Gaseous atoms condensate and form NCs. All NCs enter a mass-selector (time-of-flight mass filter) in order to select a specific magic number [125]. For the presently reported experiments the NCs contained 923±23 Au atoms. The uncertainty of the NC size (23 atoms) corresponds to the standard deviation of their size and it depends on the diameters of the entrance and exit slits of the mass-selector. Finally, the NCs get deposited on selected substrates. Before deposition the NCs are decelerated to avoid destruction during impact (soft-landing regime, kinetic energy <2 eV/atom) [126].

To avoid surface-diffusion, aggregation and coalescence, the substrates are pre-treated by ion-bombardment. The created defects act as binding sites for the adsorbed NCs [126], [127]. Defect creation by ion bombardment ensures homogeneous dispersion on the surface of the substrate. Characterization of the NCs size, surface density and morphology is carried out by electron microscopy. The distribution of NCs is visualized with aberration-corrected scanning transmission electron microscopy (STEM) in high-angle annular dark-field mode (HAADF) and it is shown in **figure 3.4.a**.

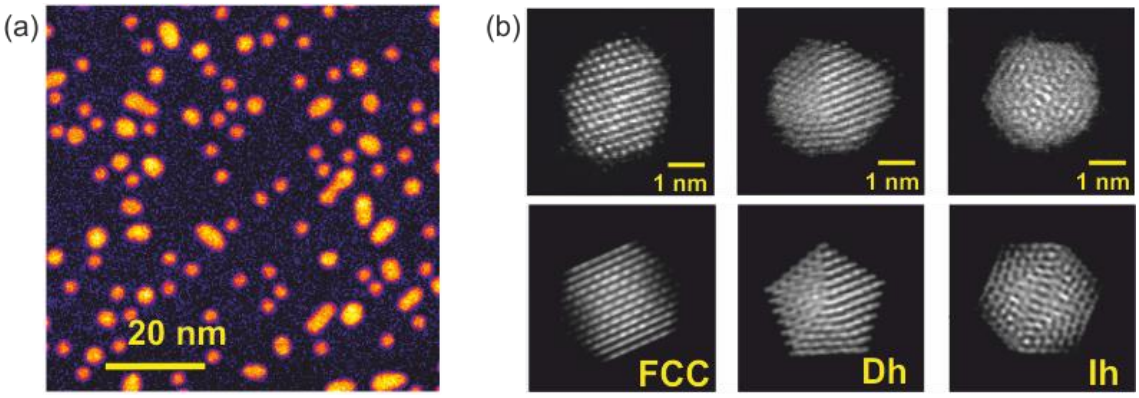

Figure 3.4: Electron microscopy of size-selected Au_{923} NCs. (a) The distribution of Au_{923} NCs on the surface of thin-films of a-C visualized with STEM-HAADF imaging. **(b)** Upper images: high-resolution electron microscopy of individual NCs, Lower images: Electron diffraction simulations of ideal single-crystalline (FCC), decahedral (Dh) and icosahedral (Ih) geometries that were used to categorize the NCs and perform statistics.

For all types of substrate, studied in the present chapter, the surface density was 8 NCs per 100 nm^2. Most NCs were isolated (75%) and the rest formed dimers and trimers. High-resolution electron microscopy and comparison with simulated structures (**figure 3.4.b**) were used to identify individual NCs. The single NCs had mostly Decahedral (37%) or FCC structure (35%) and the amorphous-like Icosahedral were nearly eliminated (3%). The NCs, examined here, have been deposited on two different types of substrates. The first type of substrate is light-absorbing, thin-films of amorphous, sp^2 C (a-C) of 20 nm thickness. The second type of substrate is light-transparent, thin-films of Silicon-Nitride (Si-N) with 20 nm thickness. The next section examines and compares the ultrafast lattice dynamics of Au NCs on these two types of substrate.

3.3.2 Dynamics of Au_{923} nanoclusters on absorbing and transparent thin-films

After optical excitation the lattice is perturbed and the intensity, position and width of diffraction peaks are changing as explained in **figure 2.12**. This chapter is focused on the time-variations of the intensity only (Debye-Waller effect), which are associated with atomic vibrations. The intensity of the peaks is determined as their total area and not the height, in order to avoid misconceiving peak-profile changes (structural changes) as

Debye-Waller dynamics. Lattice motions such as expansion or surface melting are separately examined in the next chapter. The measurements presented here have been carried out with sub 100 fs pulses of 400 nm radiation. The experiment with Au_{923} NCs on Si-N has been carried out with an incident fluence of ~2.7 mJ/cm^2 and the experiment with Au_{923} NCs on a-C has been carried out with an incident fluence of ~5.1 mJ/cm^2.

Figure 3.5 shows the relative changes of intensity, as a function of pump-probe delay, for various diffraction peaks of Au_{923} NCs on Si-N (**fig. 3.5.a**) and of Au_{923} NCs on a-C (**fig. 3.5.b**). As expected from the Debye-Waller effect, after photoexcitation all diffraction peaks (circles) decay while the inelastic background (black squares and lines) is rising. The colored solid lines in **figure 3.5.a & b** stem from calculations based on the Debye-Waller effect. Each peak-decay is translated into an effective atomic MSD. The MSD, averaged over all peaks, is then translated back into a peak-decay. The aim of this procedure is to show that the observed peak-decay obeys the $\Delta I \sim e^{-\Delta\langle u^2\rangle s^2}$ dependence predicted by the Debye-Waller theory (the importance of this check will be clarified further in **Chapter 5**).

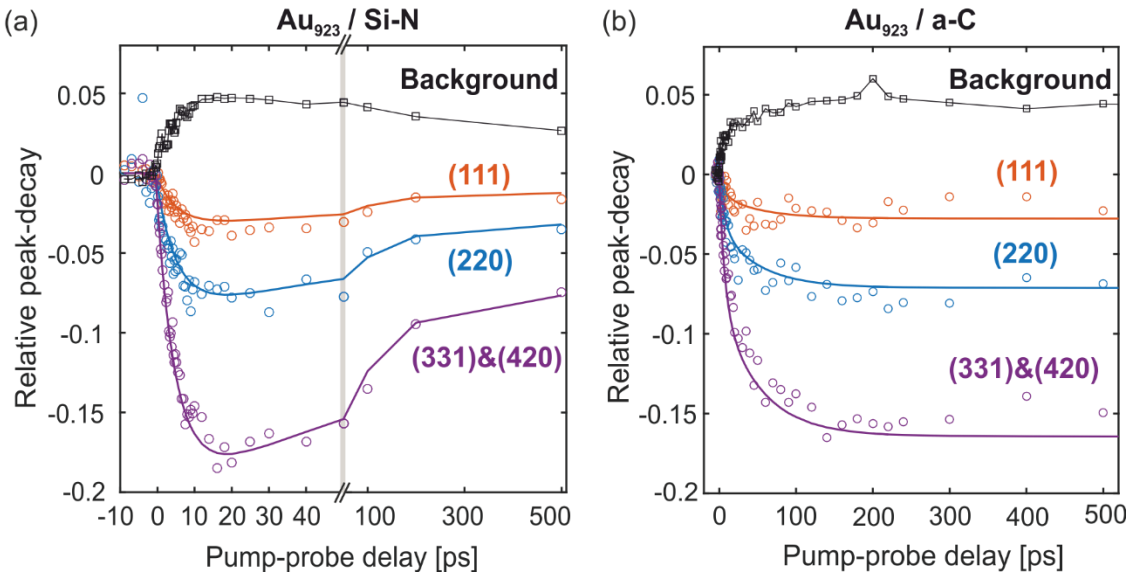

Figure 3.5: Laser-induced decay of diffraction peaks for Au_{923} NCs on different substrates. (a) Peak-decay of size-selected Au_{923} on 10 nm Si-N. **(b)** Peak-decay of size-selected Au_{923} on 20 nm a-C. Black squares and lines shown the rise of the inelastic scattering background. The open circles give the experimental relative decay of various diffraction peaks of Au_{923} NCs and the solid lines the predicted evolution based on the Debye-Waller effect.

For Au_{923} on Si-N the peaks shown initially a decay (lattice heating) with a time-constant τ_1=5.0 ± 0.7 ps. Subsequently, the peak intensity is increasing without fully recovering (lattice cooling) with a time-constant of τ_1=120 ± 50 ps. For Au_{923} on a-C the initial decay of intensity is suppressed and has a time-constant τ_1=6 ± 2 ps, while ~60% of the peak decay is due to a slower process that has a time-constant τ_2=80 ± 40 ps.

The observed dynamics differ markedly on the two substrates despite the fact that the NCs are the same. A qualitative, for now, explanation is as follows. During the first ~10 ps, the energy content of the lattice is increasing, mainly due to intrinsic electron-phonon coupling in Au NCs. The processes occurring at a timescale of ~100 ps can be explained as interfacial energy transfer to the substrates (see also the dynamics of bulk-like Au islands on graphene in **section 3.2**).

On the one hand, the Si-N substrate is transparent and hence it remains unexcited at room temperature immediately after photo-excitation. The NCs lattices equilibrate with the hot electrons and simultaneously their excess heat is transmitted at a slower pace to Si-N to restore thermodynamic equilibrium at the interface. On the other hand, the a-C substrate can absorb the incident radiation and deplete the laser pulse. In that case, a-C is at a higher temperature after electron-lattice equilibration and heat is transmitted towards the NCs. For this reason, the slow process has the reverse effect on a-C and on Si-N. The interpretation offered so far is solely based on qualitative arguments. For a quantitative description, the observed peak-decay should be translated into an effective lattice temperature and a model of ultrafast energy flow needs to be applied.

3.4 Model of energy flow in 0D/2D heterostructures

Section **3.4.1** introduces a model of ultrafast energy flow that aims for a quantitative description of the substrate-dependent Debye-Waller dynamics of Au NCs (shown in **3.3.2**). Section **3.4.2** allocates the various inputs of the model, namely the electronic and lattice heat capacities and Debye-Waller factor for Au NCs. The heat capacities of the a-C [128] and Si-N [129] substrates are found from literature.

3.4.1 Intrinsic and extrinsic interactions in nanoscale heterostructures

Quantitative analysis of lattice equilibration in 0D/2D heterostructures can be achieved with a model of energy flow for nanoscale heterostructures, developed by the author of this work [117]. A schematic diagram of the model is shown in **figure 3.6**. In analogy with the TTM, each material contains two heat baths, the electrons and the lattice (phonons). The electrons and the lattice, of each material, can exchange energy with electron-phonon coupling. This type of interaction can be termed intrinsic. Both the nanostructure and the substrate can absorb energy from the incident laser pulse, depending on their optical properties. Laser-irradiation brings the two materials in non-equilibrium conditions. Restoration of thermodynamic equilibrium between the two components is carried out by transmission of excited carriers and phonons, across the interface and towards the less-excited part. This additional type of interactions can be termed extrinsic.

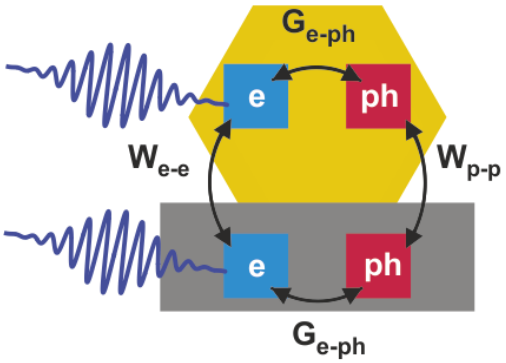

Figure 3.6: Model of ultrafast energy flow in 0D/2D heterostructures. Both the NCs and the substrate can be excited by the laser pulse. Each material has intrinsic electron-lattice interactions (G_{e-ph}) and extrinsic interactions across the interface. Interfacial energy flow is carried out by electronic (W_{e-e}) and vibrational (W_{p-p}) coupling.

In analogy with the TTM, the diagram of **figure 3.6** is translated into a system of four coupled differential equations:

$$\frac{dT_E^{Au}}{dt} = -\frac{G_{E-PH}^{Au}}{C_E^{Au}}(T_E^{Au} - T_L^{Au}) + \frac{W_{e-e}}{L^{Au}C_E^{Au}}(T_E^S - T_E^{Au}) + S^{Au}(t), \qquad \text{R 3.1}$$

$$\frac{dT_L^{Au}}{dt} = \frac{G_{E-PH}^{Au}}{C_L^{Au}}(T_E^{Au} - T_L^{Au}) + \frac{W_{p-p}}{L^{Au}C_E^{Au}}(T_L^S - T_L^{Au}), \quad \text{R 3.2}$$

$$\frac{dT_E^S}{dt} = -\frac{G_{E-PH}^S}{C_E^S}(T_E^S - T_L^S) - \frac{W_{e-e}}{L^S C_E^C}(T_E^S - T_E^{Au}) + S^S(t), \quad \text{R 3.3}$$

$$\frac{dT_L^S}{dt} = \frac{G_{E-PH}^S}{C_L^S}(T_E^S - T_L^S) - \frac{W_{p-p}}{L^S C_E^S}(T_L^S - T_L^{Au}). \quad \text{R 3.4}$$

Each of these equations describe the time-evolving temperature (T) of one of the subsystems. Heat diffusion is not taken into account because of the nanoscale dimensions of all the involved materials. The temperatures of the electrons and the lattice are denoted by the lower index (E or L respectively). The material is given by the upper index (Au for the Au_{923} NCs and S for the substrate). The same nomenclature applies for the indices of the heat capacities (C) and the electron-phonon coupling constants (G). The interfacial energy transfer rates with electronic and vibrational coupling are given by W_{e-e} and W_{p-p}, respectively. Finally, the absorbed laser fluence in each material is given by source terms (S) with a Gaussian temporal shape:

$$S(t) = \frac{F}{LC_E}\frac{\exp[-4\,ln(2)\,(t-t_o)^2/w^2]}{w/2\sqrt{\pi/\ln(2)}}\,, \quad \text{R 3.5}$$

where F is the absorbed fluence, L and C_E the nominal thickness and electronic heat capacity of each material. Finally, w and t_o are the FWHM and the arrival time of the laser pulse.

Electron-phonon interactions at the interface (scattering events in which a charge carrier in material 1 is exciting a phonon in material 2) are not taken into account. Recent work has shown that such phenomena can indeed take place in different low-dimensional heterostructures [113]. However, in the present work it was possible to reproduce the experimental observations without taking into account interfacial electron-phonon interactions and for this reason it is not considered an important channel of energy flow for the investigated systems (lower scattering probability).

3.4.2 Inputs of the model: heat capacities and Debye-Waller factor of Au_{923} nanoclusters

The previous section (**3.4.1**) introduced the model of energy flow in 0D/2D heterostructures and the concepts of intrinsic and extrinsic interactions. The present section examines the inputs of the model and allocates the required information based on the existing literature and on various theoretical considerations. The physical properties of solids can be modified due to spatial confinement and, hence, it is necessary to take into account the size of Au_{923} NCs.

Electrons' confinement. As the nanostructure gets smaller, the surface-to-volume ratio is increasing. Atoms on the surface are under-coordinated and have the ability to move. Hence, their bonding and dynamics are expected to be different than in the bulk. Spatial confinement, can lead to the formation of new electronic and vibrational states. The discontinuity of the potential close to the surface can lead to the formation of electronic bound states, known as surface states [130]. Modification of electronic states can also occur throughout the volume when the nanoscale solid is strongly confined in some or all spatial dimensions [131]. This second mechanism starts to be important when one of the spatial dimensions approaches the Fermi wavelength of electrons (for Au $\lambda_F \sim 0.5$ nm).

Electronic heat capacity of Au_{923} NCs. For all the analysis, the electronic heat capacity of the studied Au nanostructures was assumed to be identical with their bulk counterpart. This assumption can be justified in two ways. First, the Thomas-Fermi screening length for Au is $r_{TF} \cong \frac{1}{2}(a_o^3/n)^{1/6} \sim 1.6$ Å [2]. The Thomas-Fermi screening length is much smaller than the characteristic dimensions of the investigated nanostructures. For comparison, Au_{923} NCs have an average diameter of ~3 nm. As a result, the fraction of electrons affected by the surface will be small and the surface-induced modifications of the electronic heat capacity can be neglected.

The second justification, for using the electronic heat capacity of bulk Au, is based on thermal broadening. As the size of a metallic nanocluster decreases, the electronic bands transform into molecular- or atomic-like states [131] and the density of states acquires energy gaps. Such phenomena, if present, affect the electronic heat capacity. Major confinement effects are expected to arise if thermal broadening is smaller than the energy gaps. A simple assumption is that close to the Fermi level, the gaps are equally spaced. Then, the critical size for electronic quantum confinement is $E_F/k_BT \sim 200$ atoms. Despite

the simplicity of these arguments the result is realistic. Recent studies have shown a deviation from the metallic behavior, in terms of optical properties, for NCs smaller than Au_{333} [132].

Phonons' confinement. Regarding phonons, in a zero-dimensional metallic solid, long wavelength acoustic phonons transform into collective vibrational modes [133], similar to the normal modes of an elastic sphere (breathing and toroidal modes). This occurs when the wavelength of the phonon becomes comparable with the dimension of the nanocrystal itself. Moreover, the vibrational density of states is significantly modified for all frequencies compared to the bulk counterpart in very small clusters (see for instance fig. 6 in the work of Cuenya *et al*. [134]).

Lattice heat capacity of Au_{923} NCs. Regarding the lattice degrees of freedom of Au NCs, metallic surfaces and nanostructures are characterized by enhanced mobility of atoms for temperatures well below the melting point [135]. The melting temperature of bulk Au is 1400 K. Buffat *et al.*[136] have shown, using electron diffraction, that the melting point of Au nanostructures shows a size-dependent decrease. Modern experiments using electron microscopy, have visualized the nanocluster surface becoming rough or completely melted, while atoms in the interior remain crystalline [35]. Below the melting point all the lattice degrees of freedom for bulk Au have vibrational character. Yet, on the surface of a nanocrystal, atoms have multiple, possible configurations and, stochastically, some of these vibrations can decompose into translational modes and *vice versa* (surface diffusion) [135]. Coexistence of liquid and solid regions is associated with peaks in the lattice heat capacity, as shown by calorimetry measurements [137] and molecular dynamics simulations [138].

All these phenomena are naturally included in atomistic simulations. For size-selected Au_{923} NCs, the heat capacity has been obtained by the works of Sauceda *et al*. [133], [139]. The low temperature values of the heat capacity [139] have been extrapolated using the vibrational density of states [133] and the standard relationship for the heat capacity of Bosonic systems:

$$C_L = \int \frac{\partial n_B(\hbar\omega, T_L)}{\partial T_L} F(\omega)\hbar\omega \, d\omega \qquad \text{R 3.6}$$

where n_B is the Bose-Einstein distribution, T_L the lattice temperature and ω the phonon angular frequency. All properties have been averaged over the various structural allotropes of NCs with similar size and weighted by the relative abundancies given by HR-TEM. The resulting temperature dependent heat capacity for the Au_{923} NCs is shown in **figure 3.7**.

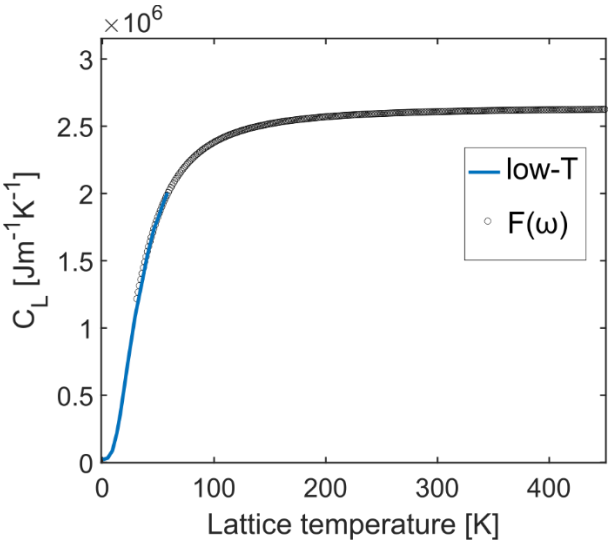

Figure 3.7: Lattice heat capacity of Au_{923} NCs, calculated based on the works of Sauceda *et al.*[133], [139]. More details can be found in the main text.

For comparison, the lattice heat capacity of bulk Au is in the order of $2.49 \cdot 10^6$ J/m^{3}K at room temperature.

Debye-Waller factor of Au_{923} NCs. An additional property of materials that is modified upon spatial confinement is the Debye-Waller factor or atomic MSD. In general the atomic MSD or the Debye-Waller factor B [95], are given as a polynomial function of the lattice temperature (T_L) [95]. However, for most materials the polynomial function above 80 K is close to linear and hence one can write: $< u^2 > \cong a \cdot T_L$, where a is a material specific constant. The slope a has been shown to be size-dependent by Buffat *et al.* [140]. The relationship of a with the diameter (D) of the nanocluster is given by: $a = a_b + a_n/D$, where a_b is the bulk value and the second term due to surface effects. Based on the works of Buffat *et al.* [140] and Solliard [141] and for Au_{923} NCs ($D \sim 3\,nm$) the $a = 9.88 \cdot 10^{-5}$ Å$^2/K$. Regarding the B-factor ($B=8\pi^2<u^2>/3$), the same coefficient is $2.5 \cdot 10^{-3}$ Å$^2/K$. Compared to bulk Au, the slope of the atomic MSD (versus temperature) is

increased by ~20%. In an intuitive way, this indicates that Au_{923} NCs have softer lattice compared to bulk Au.

3.5 Measurement of electron-phonon coupling and interfacial phonon transmittance in 0D/2D heterostructures

With all the above considerations it is now possible: (1) to use the Debye-Waller temperature-dependence and transform the peak-decay into an effective lattice temperature and (2) to use the electronic and lattice heat capacities in order to simulate the time evolution of the lattice temperature. The nominal thickness of Au_{923} NCs is 1.4 nm. The thickness of Si-N and a-C thin-films are 10 and 20 nm, respectively. Hence, the heat capacities of the investigated samples are known.

Figure 3.8.a shows the lattice temperature evolution of Au_{923} NCs on Si-N (blue circles) as a function of the pump-probe delay time. The system of coupled differential equations of the model of ultrafast energy flow are used for a nonlinear fitting of the data that is shown with a solid blue line. The predicted lattice temperature evolution of the Si-N substrate is shown with a dashed blue line. In the case of Au_{923} / Si-N heterostructures, the source term of the substrate is set to zero, since Si-N is transparent at this wavelengths (the optical band gap of SiN_x films is ~5 eV [142]). Moreover, the response of the electrons in the substrate have been deactivated, in the final fitting, because the large band gap forbids electronic excitations in Si-N. Hence, the electronic coupling (W_{e-e}) was set to zero to improve the fitting convergence.

Figure 3.8.a gives emphasis in two different timescales (horizontal axis). From -10 to 0 ps all systems are in room temperature. From 0 to 15 ps the lattice temperature of Au_{923} NCs is rising to a maximum value of 440 K but the Si-N lattice temperature is almost stable. Finally, from 15-500 ps the lattice temperature of Au_{923} NCs (/Si-N) is clearly dropping (/increasing). The predicted temperature of the Si-N substrate (dashed blue line) is slowly rising and eventually gets equal with that of Au_{923} NCs (solid blue line) at approximately 500 ps.

The underlying physical processes that dominate these time evolutions are schematically shown in **figure 3.8.b**. Lattice heating of Au_{923} NCs in the 0 to 15 ps time-interval stems from generation of hot electrons, directly from the laser beam, and subsequent relaxation

by electron-phonon coupling ($G_{E\text{-}PH}$ in **fig. 3.8.b**). Lattice cooling of Au_{923} NCs in the 15-500 ps time-interval is due to phonon transmission (W_{PP} in **fig. 3.8.b**).

Extracted coupling constants for Au_{923} / Si-N. The measured electron-phonon coupling constant of Au_{923} NCs is $G_{e-ph} = (2.0 \pm 0.2) \cdot 10^{16}\, W/m^3$. The electron-phonon coupling constant of Au_{923} NCs is ~70% compared to bulk Au. The vibrational coupling of Au_{923} NCs with Si-N is $W_{p-p} = (16 \pm 8) MW/m^2K$.

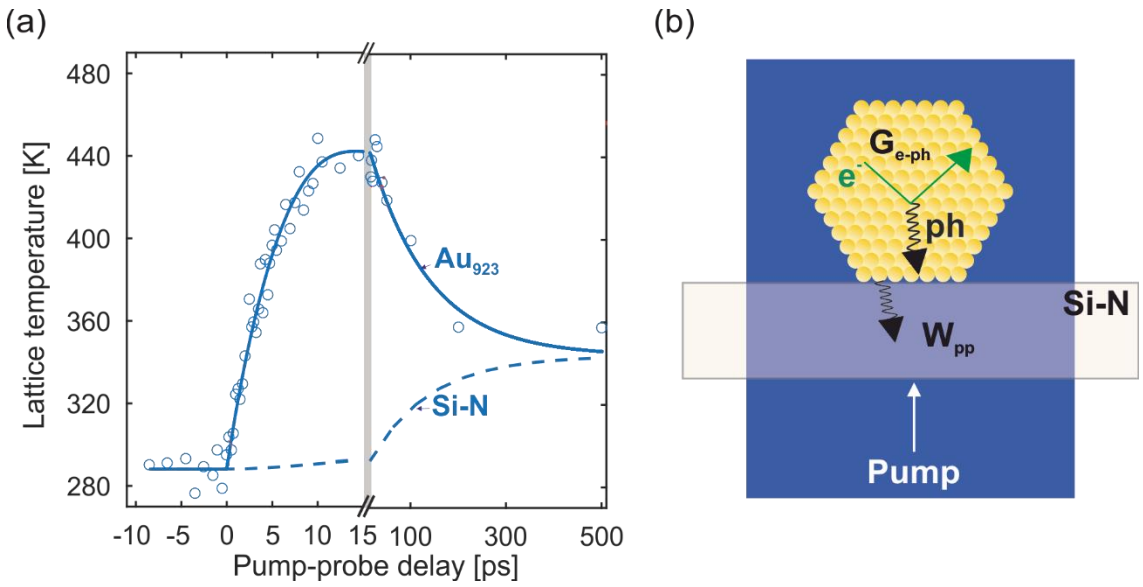

Figure 3.8: Ultrafast evolution of lattice temperature for Au_{923} NCs on Si-N and mechanism of energy flow. (a) The effective lattice temperature of photoexcited Au_{923} NCs on Si-N (blue data points) calculated by means of the Debye-Waller effect. The results of non-linear fitting with the 0D/2D energy flow model, for the Au NCs and the Si-N substate are shown with blue solid and dashed line respectively. **(b)** Schematic illustration of the ultrafast energy flow pathway. Electron-phonon coupling within the NCs is initiated by the laser pulse, while vibrational coupling brings the NCs and the substrate in thermodynamic equilibrium.

The same modelling concept is now applied for Au_{923} NCs on a-C. The experimental evolution of the effective lattice temperature is shown in **figure 3.9.a** (red data points) together with the fitted lattice temperature (red solid line) and the fitted substrate temperature (dashed solid line). The predicted temperature of Au_{923} NCs shows first a small rise (of ~50 K) due to electron-phonon coupling within 5 ps. Thus, the laser-induced generation of hot electrons in the Au_{923} NCs is depleted in the presence of absorbing C. Next, from 15 to 100 ps the lattice temperature of Au_{923} NCs keeps rising at

a slower pace to a maximum value of ~470 K. After 100 ps, the lattice temperatures of Au_{923} NCs (solid line) and a-C (dashed line) are equal and the heterostructure is locally equilibrated.

The most dominant, underlying physical processes are schematically shown in **figure 3.9.b**. Electron-phonon coupling inside the Au_{923} NC is greatly suppressed and hence excluded from the diagram. The most intense lattice heating, due to hot electrons, occurs in the a-C substrate. The excessive phonons that are generated by this process can be partially transmitted to the Au_{923} NC, giving rise to the slow dynamics shown in **figure 3.9.a**.

Extracted coupling constants for Au_{923} / a-C. The measured electron-phonon coupling constant (G_{e-ph}) of Au_{923} NCs on a-C is again lower than in bulk Au and equal with $(1.6 \pm 0.9) \cdot 10^{16}\ W/m^3K$. The uncertainty in this case is larger because intrinsic and extrinsic interactions have the same effect (lattice heating). Regarding extrinsic energy flow, the vibrational coupling is $W_{p-p} = (90 \pm 10)\ MW/m^2K$, while the electronic coupling is smaller by a factor of 10 and again it does not appear to be an important channel for equilibration. In agreement with the findings presented here, recent studies using two-photon photoemission, have shown suppressed generation of hot electrons in Ag when it is in contact with graphite [143].

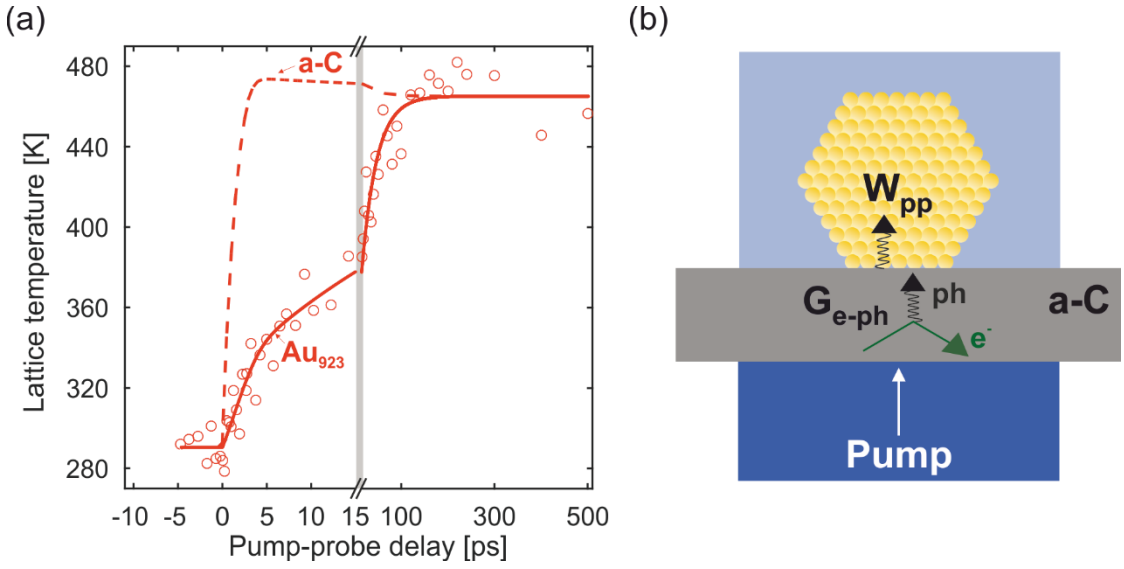

Figure 3.9: Ultrafast evolution of lattice temperature for Au_{923} NCs on a-C and mechanism of energy flow. (a) The effective lattice temperature of photoexcited Au_{923} NCs on a-C (red data points) calculated by means of the Debye-Waller effect. The results of non-linear fitting with the 0D/2D energy flow model, for the Au_{923} NCs and the a-C substate are shown with red solid and dashed line respectively. **(b)** Schematic

illustration of the ultrafast energy flow pathway. Generation of hot electrons within the NCs is inhibited by the laser-absorbing substrate. The absorbed fluence in a-C leads to heating of its lattice by electron-phonon coupling. Finally, vibrational coupling transfers heat to the NCs and brings the two materials in thermodynamic equilibrium.

An interesting finding is that the vibrational coupling on a-C is larger than on Si-N by a factor of 5.6. Vibrational coupling is governed by selection rules for phonon-phonon interactions at the interface. In addition, vibrational coupling can be affected by the morphology of the surface. Based on the sp^2 bonding character of the used C substrates, the surface is expected to contain distorted graphene flakes and nanotubes. The existence of such structures results in nanometer-scale roughness. This can increase the effective contact area and potentially lead to higher energy transfer rate.

The present chapter demonstrated how FED can be used for quantitative measurements of interfacial energy transfer. Up to now, interfacial energy transfer has been widely studied with time-resolved thermoreflectance [111], [144]–[148]. The observables of optical spectroscopies are based on the refractive index of materials, which by its turn has a complicated dependence on the underlying electronic and structural changes. To overcome these difficulties, the current work, and recent publications by other teams, employ time-resolved diffraction that is directly sensitive to the lattice response [70], [79]–[81], [149], [150].

Evolution of electronic temperature. The experiment with Au_{923} NCs on Si-N has been carried out with an incident fluence of ~2.7 mJ/cm^2 resulting in a lattice temperature increase of ~150 K. The experiment with Au_{923} NCs on a-C has been carried out with nearly double incident fluence (~5.1 mJ/cm^2), yet the resulting lattice temperature increase was similar (~180 K). The applied model of energy flow proves that this is indeed the expected behavior based on the optical absorption and the heat capacities of the various materials that are involved. The presented model has one additional advantage: it provides a reliable estimation of the electronic temperature evolution that is not accessible experimentally by FED. The predicted electronic temperatures for Au_{923} NCs on Si-N and a-C are shown in **figure 3.10**. Although the maximum lattice temperature is similar in both types of substrate, the maximum electronic temperature is drastically different. The maximum electronic temperature is ~3300 K and ~1300 K for Au_{923} NCs on Si-N and a-C, respectively. Hence, selection of the substrate and

adjustment of the laser fluence can result in a specific lattice temperature increase, in the presence, or in the near absence, of hot electrons. The following chapter takes advantage of this phenomenon, in order to indicate structural changes that are driven by hot electrons.

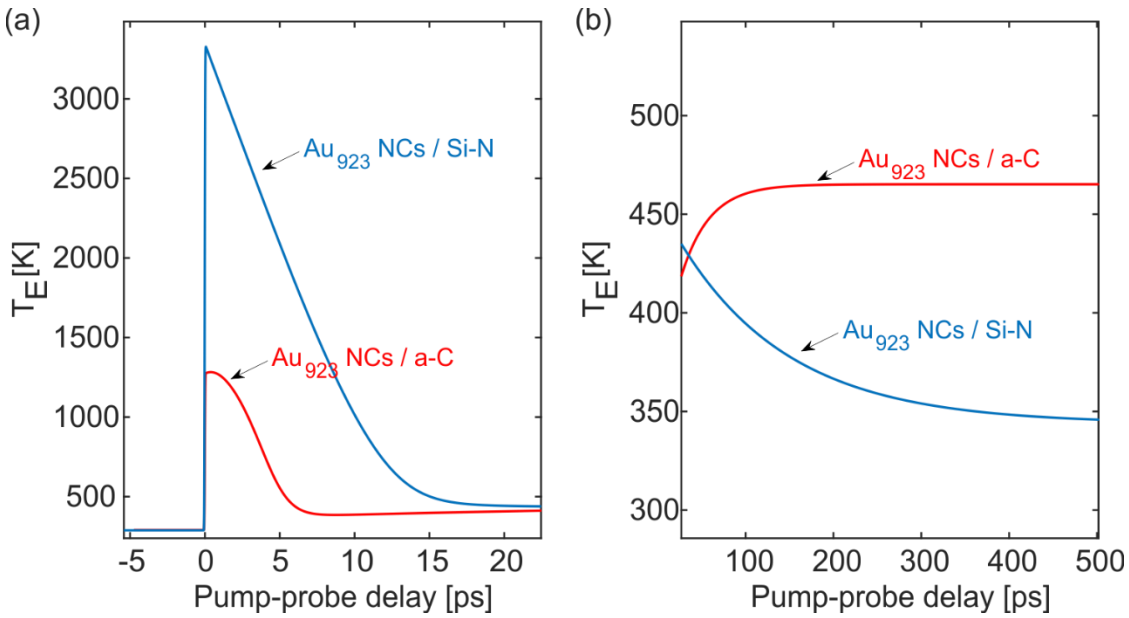

Figure 3.10: Predicted electronic temperature evolution of Au_{923} NCs on absorbing a-C and transparent Si-N. (a) Electronic temperatures during electron-lattice non-equilibrium. The maximum electronic temperature of Au_{923} NCs is ~3300 K on Si-N and ~1300 K on a-C although the maximum lattice temperatures are similar. **(b)** Electronic temperatures after electron-lattice equilibration. After electron-lattice equilibration, the electronic temperature is closely following the lattice temperature of the NCs.

Chapter 4. Ultrafast structural changes in 0D/2D heterostructures

The previous chapter investigated ultrafast energy flow in 0D/2D heterostructures. The present chapter examines the ultrafast structural changes of the 0D nanostructures in response to this ultrafast energy flow. The FED measurements extract the intensity (Debye-Waller dynamics), scattering angles (unit cell volume) and width (degree of crystallinity) of the various diffraction peaks (see **figure 2.12**). The results presented here originate from the same data sets used for the analysis of the ultrafast energy flow (unless if it is stated otherwise), but the employed observables are the time-dependent scattering angle (**section 4.1**) and the dynamics of the width of diffraction peaks (**section 4.2**). The observed, ultrafast atomic motions have some implications for surface chemical reactions, which are discussed in **section 4.3**.

4.1 Anharmonic structural properties of Au_{923} nanoclusters

The standard description of phonons is strongly based on having a harmonic, interatomic potential of the form $V(r) \propto r^2$, where r is the interatomic distance or some other spatial coordinate. This harmonic approximation is almost perfectly valid at low temperatures, when the solids' atoms are constrained very close to their mechanical-equilibrium positions. The harmonic approximation is an extremely successful concept, with the Debye-Waller effect being one of its many outcomes. An interesting (but well-known) fact is that the harmonic approximation fails to predict two phenomena that are readily accessible even by human senses. The first is lattice expansion and the second is the phononic thermal conductivity. More information can be found in chapter 25 of Ashcroft & Mermin [2].

Generally, processes that do not conserve the number of phonons are non-harmonic (anharmonic). Phonon-phonon interactions are solely based on anharmonicity but anharmonic phenomena play a role even for electron-phonon interactions [151]. On the one hand, anharmonic phenomena are extremely important for an in-depth understanding of ultrafast energy flow in solids. On the other hand, anharmonic lattice expansion plays a

crucial role in devices with nanoscale features, such as nanotips for atomic visualization and manipulation [152], especially when laser-illumination is involved. In the investigated nanosystems, namely Au_{923} NCs on Si-N and on a-C, anharmonicity manifests as lattice expansion at ultrafast timescales. Based on all the above, it is certainly interesting and within the scope of the present work to study these phenomena.

The previous chapter has shown the laser-induced Debye-Waller dynamics. The effect of anharmonicity and thermal expansion in the Debye-Waller factor has been examined by Maradudin *et al*. [153] (see section IV, pages 2539-2540). Generally, the anharmonic contributions to the Debye-Waller factor are considered to be small (compare relationships 4.1, 4.4 & 4.9 in ref. [153]). Nevertheless, anharmonic phenomena are naturally included in the previous Debye-Waller analysis, since the temperature-dependence of the atomic MSD has been found from experiments [140], [141]. The Debye-Waller analysis of **Chapter 3** have not offered any striking signature of anharmonicity. In contrast, lattice expansion can only occur in the presence of anharmonicity and thus it is the most ideal, sensitive probe for such phenomena.

Section 4.1.1 examines the dynamics of expansion. **Section 4.1.2** combines the lattice expansion dynamics with the Debye-Waller dynamics to measure the thermal expansion coefficient. Since thermal expansion, as a term, is closely connected to thermal states, **section 4.1.3** presents an alternative root for quantifying expansibility. **Section 4.1.4** employs static electron diffraction to show that even in equilibrium the Au_{923} NCs have modified volume of the unit cell compared to bulk Au. Finally, **section 4.1.5** discusses the implications of the measured anharmonic properties on the previously measured values of microscopic coupling constants.

4.1.1 Ultrafast lattice expansion

Figure 4.1 shows the relative expansion of Au_{923} NCs on Si-N (blue circles) and Au_{923} NCs on a-C (red circles) as a function of the pump-probe delay time. Both time traces can be fitted with bi-exponential decay (solid lines). The extracted dynamics are similar with that of the peak-decay (**figure 3.5**). For Au_{923} NCs on Si-N, the lattice expands during electron-lattice nonequilibrium with a time constant of $\tau_1 = (3.8 \pm 0.7)\, ps$. Thermal equilibration with the Si-N substrate is accompanied by lattice shrinking with a time-constant of $\tau_2 \sim 140\, ps$. For Au_{923} on a-C, the NCs expansion is again bi-exponential but

the slow process has the reverse effect (expansion) and the time constant is $\tau_2 = (52 \pm 6)\, ps$.

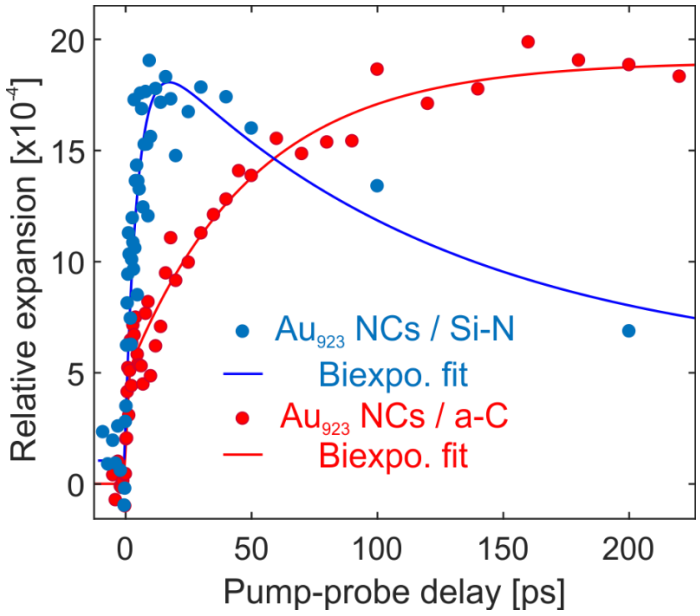

Figure 4.1: Relative expansion of Au$_{923}$ NCs on absorbing a-C and transparent Si-N. The relative expansion probed by the scattering angle of diffraction peaks by FED. The optical and thermal substrate properties lead to very different dynamics while the maximum expansion is similar for both experiments.

Lattice expansion at the picosecond timescale. The short time-constant of lattice expansion ($\tau_1 = 3.8\, ps$ for Au$_{923}$ / Si-N) is clearly faster than the short time-constant of the Debye-Waller dynamics ($\tau_1 = 5.0\, ps$, same measurement). **Figure 4.2** shows the lattice expansion as a function of the pump-probe delay time for an additional measurement of Au$_{923}$ NCs on Si-N.

This measurement has been carried out at a higher fluence of 3 mJ/cm^2. The black line is a fit with the sum of an exponential growth (gray line) and a step-function (green line). This ultrafast behavior of the Au$_{923}$ volume has been observed for all substrates and it causes an apparent shortening of the time-constant τ_1 for bi-exponential fittings. The slow process (gray line) can be safely interpreted as the lattice expansion that accompanies lattice heating by electron-phonon coupling. The ultrafast process (green line) can be attributed to the large internal pressure exerted by hot conduction electrons [154]. After photoexcitation, the electrons become transiently hotter than 3000 K. At these temperatures and for a similar noble metal (Ag), the pressure of the electron gas is ~800 times larger than close to room temperature according to the results of Perner *et al.* [154].

According to the radius of Au_{923} (1.5 nm) and the speed of sound in bulk Au ($3.2 \cdot 10^3$ m/s) the laser-induced expansion of NCs can be as fast as 0.5 ps.

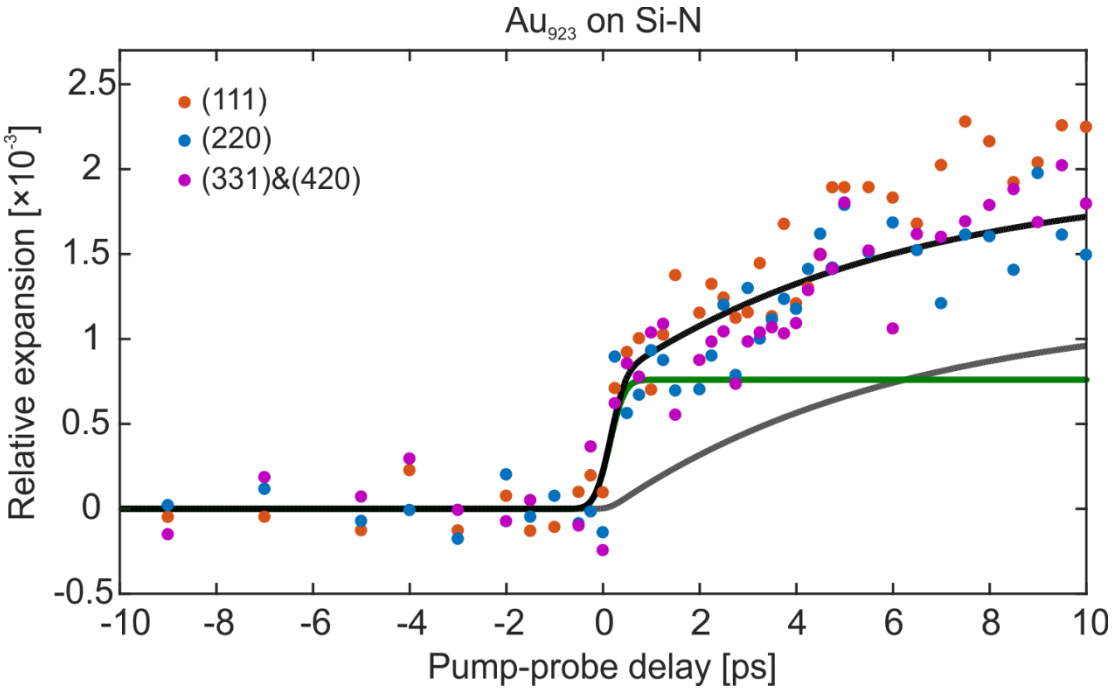

Figure 4.2: Relative expansion of Au_{923} NCs on Si-N for a fluence of 3 mJ/cm^2. Relative expansion probed by three different peaks: (111), (220) and the weighted average of (331) & (420) (orange, blue and magenta data-points respectively). The black line is a fitting with an exponential growth (grey line) plus a process that is limited by the time-resolution (green line).

4.1.2 Thermal expansion coefficient of Au_{923} nanoclusters

Apart from the short time-delays (0-10 ps), the lattice can be considered well-thermalized for the first 0.5 ns after photoexcitation. Hence, it is reasonable to measure the thermal expansion coefficient of the Au_{923} NCs. FED provides access to both the energy content of the lattice and its volume. The effective lattice temperature and the relative, lattice expansion are used to extract the thermal expansion coefficient, or linear expansibility.

This procedure is shown in **figure 4.3**. The horizontal axis is the lattice temperature extracted from the Debye-Waller effect. The vertical axis is the relative expansion probed by the scattering angle of diffraction peaks. The data points represent different samples (circles for Au_{923}/a-C and stars for Au_{923}/Si-N) and different diffraction peaks (orange for (111), blue for (220), magenta for the weighted average of (331)&(420)). Each data point

corresponds to an ultrafast, reciprocal-space snapshot, were the lattice temperature is transiently at an elevated temperature.

The black line is a linear fit to the data that is used to extract the average thermal expansion coefficient, while the gray area represents the 95% confidence intervals. The thermal expansion coefficient is $a_L = (9.9 \pm 0.6) \cdot 10^{-6}\, K^{-1}$ for Au_{923}/Si-N and $a_L = (9.1 \pm 0.3) \cdot 10^{-6}\, K^{-1}$ for Au_{923}/a-C. The thermal expansion coefficient for bulk Au is $14 \cdot 10^{-6}\, K^{-1}$ [155]. For comparison, **figure 4.3** also shows a linear increase (green solid line) that represents the thermal expansion of bulk Au close to room temperature. In conclusion, the thermal expansion coefficient of Au_{923} NCs appears to be lower than that of bulk Au.

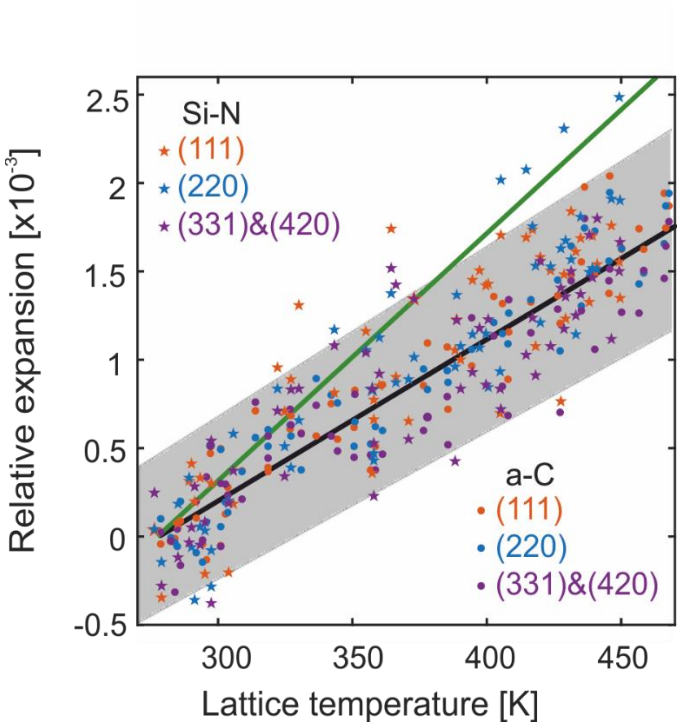

Figure 4.3: Measurement of thermal expansion coefficient for Au_{923} NCs on a-C and on Si-N. The relative expansion is plotted as a function of the effective lattice temperature for each pump probe delay. The data points are FED experiments of Au_{923}/Si-N (stars) and Au_{923}/a-C (circles). Different colors correspond to different diffraction peaks. The black solid line is a linear fit and the gray area its 95% confidence intervals. The green solid line is the expected behavior for bulk Au.

4.1.3 Anharmonicity of Au_{923} nanoclusters

In order to be fully compatible with non-thermal lattice phenomena, it is desirable to find ways for quantifying lattice expansibility without the need of estimating a lattice temperature. In a recent work (supplemental material [117]), the author has proposed using the ratio of the mean-displacement to the atomic MSD for quantifying lattice expansion in nonequilibrium measurements. The advantage is that both observables are directly probed by FED.

The experimental relative expansion as a function of the atomic MSD for multiple measurements of Au_{923}/Si-N and Au_{923}/a-C is shown in **figure 4.4**. The data points are fitted with a linear function. For thermal conditions and for bulk Au the slope is expected to be $A = 0.175\ \text{Å}^{-2}$. The experimental slope is decreased compared to bulk Au by $(8.7 \pm 1.6)\%$ for Au_{923}/Si-N and $(21.6 \pm 1.9)\%$ for Au_{923}/a-C.

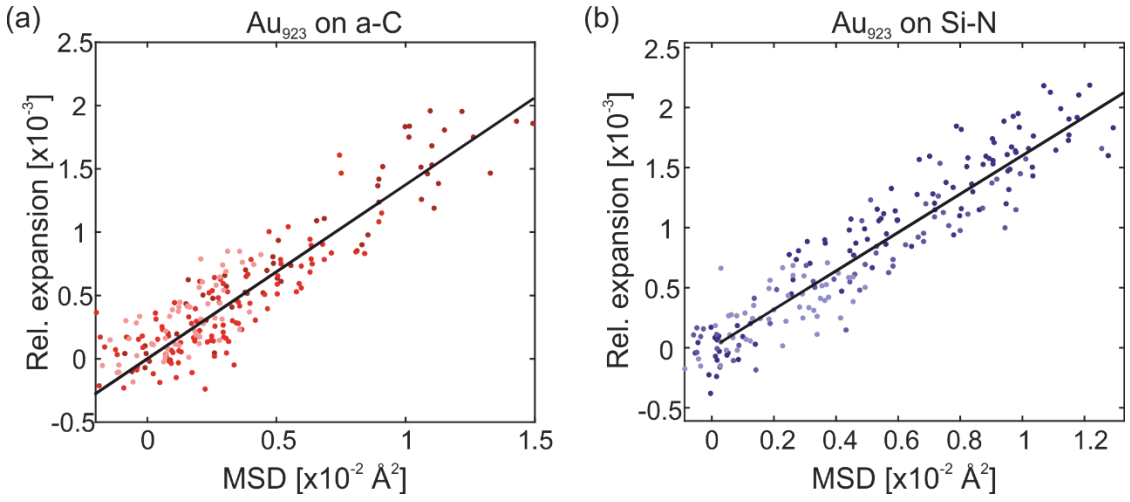

Figure 4.4: Relative expansion as a function of atomic MSD. (a) The relative expansion as a function of atomic MSD for Au_{923} on a-C. Both quantities are averaged over the (111), (220), (331) and (420) peaks. **(b)** The same plot for Au_{923} on Si-N. Datapoints of different colors represent measurements with different fluences and the black solid line is a linear fit that is used to extract the slope (anharmonicity constant).

Physical meaning of the mean-displacement to MSD ratio. Consider, for simplicity, a one-dimensional system with atomic position $u(t)$ and potential $V(u)$. The system is close to mechanical equilibrium where $u = u_o$ and $V'(u_o) = 0$. The equation of motion is:

$$\ddot{u} = -\frac{V'(u)}{m} \ . \qquad \text{R 4.1}$$

Using Taylor expansion the equation of motion can be rewritten as:

$$\ddot{u} = -(u-u_o)\frac{V''(u_o)}{m} - \frac{1}{2}(u-u_o)^2\frac{V'''(u_o)}{m} + \cdots \ . \qquad \text{R 4.2}$$

The higher order terms are ignored from now. If on average the particle does not experience a net force or acceleration ($\langle \ddot{u} \rangle_t = 0$) then the last equation becomes:

$$\langle (u-u_o) \rangle_t \approx -\frac{1}{2}\frac{V'''(u_o)}{V''(u_o)}\langle (u-u_o)^2 \rangle_t \ \ . \qquad \text{R 4.3}$$

The bracket on the left is the mean-displacement and the bracket on the right is the atomic MSD. Instead of the mean-displacement it is possible to use the relative-expansion and in this case the anharmonicity constant (A) is defined as:

$$A = \frac{rel.-exp.}{MSD} \approx -\frac{1}{2u_o}\frac{V'''(u_o)}{V''(u_o)} \ \ . \qquad \text{R 4.4}$$

The anharmonicity constant A has some similarities with the thermal expansion coefficient a_L, which is given by:

$$a_L = \frac{rel.-exp.}{\Delta T} \approx -\frac{k_B}{4u_o}\frac{V'''(u_o)}{\left(V''(u_o)\right)^2} \ , \qquad \text{R 4.5}$$

according to equation 4.8 of Maradudin *et al*. [153].

In view of all the above it is noted that:

(a) The analysis of the previous section (**4.1.2**) have shown that the Au_{923} NCs have smaller thermal expansion coefficient than bulk Au.

(b) The analysis of the present section (**4.1.3**) have shown that the Au_{923} NCs have smaller anharmonicity constant than bulk Au.

The Au_{923} NCs on a-C experience the slowest dynamics, with a time-constant of 80 ps and full equilibration at 100 ps. These timescales are significantly longer than the intrinsic electron-lattice interactions (5 ps), meaning that the NC lattice degrees of freedom can be considered well-thermalized. For Au_{923} NCs on a-C and for Au_{923} NCs on Si-N, the expansion coefficient and the anharmonicity constant are smaller than in bulk suggesting that the interatomic potential is permanently modified due to the large surface-to-volume ratio of the nanostructure. The thermal expansion coefficient and the anharmonicity

constant of Au_{923} NCs on Si-N and on a-C can be slightly different due to the different pathways for ultrafast energy flow.

4.1.4 Static compression of Au_{923} nanoclusters

From the comparison of Au_{923} NCs and literature values for bulk Au it becomes clear that spatial confinement in all directions of space results in decreased thermal expansion and anharmonicity. Thermal expansion depends on the third derivative of the interatomic potential and it is expected to be affected by slight modifications of the interatomic potential close to the surface. Beyond dynamic thermal expansion, which requires changing the temperature, surface tension leads to permanent compression of Au NCs by 0.6% relatively to bulk Au at equilibrium. This effect has been measured by recording electron diffraction patterns of Au_{923} NCs on graphene in thermal equilibrium at room temperature (**figure 4.5**).

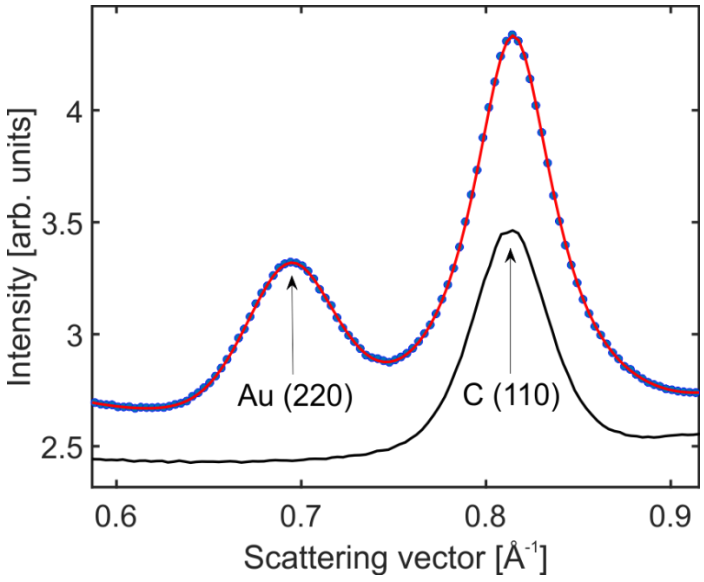

Figure 4.5: Electron diffraction of Au_{923} NCs on graphene showing static lattice compression at room temperature. Static electron diffraction of Au_{923} NCs on graphene (blue data points), fitting with pseudo-Voigt profiles (red line) and static electron diffraction of bare graphene (black solid line) shown for comparison. Using the (110) peak of graphene as a reference, the radius of the (220) peak of Au_{923} is found to be at a larger scattering angle compared to bulk Au by ~0.6% (compression in real-space).

Graphene is used a reference in order to relate the measured scattering angles with real distances between crystal planes. Graphene is not expected to be affected by the

deposition of Au NCs, due to their low coverage and the absence of strong Au-C chemical bonds. The (110) peak of graphene, corresponding to an interplane spacing of $D_{110} = 1.2280$ Å, is used as a reference for the scattering angle. Fitting with pseudo-Voigt peak profiles shows that the neighboring (220) peak of Au_{923} NCs ($D_{220} = 1.4391$ Å, for bulk Au) is located at higher scattering angle than what is expected for bulk Au. This means that in real space the Au_{923} nanolattices are permanently compressed. By fitting 11 diffraction patterns, with 5 s exposure each (55,000 electron pulses) the average contraction is $(0.63 \pm 0.05)\%$. For similar sizes of NCs the bond-length contraction found with EXAFS was $\sim 0.5 - 2\%$ [156], [157].

Decreased thermal expansion in metallic NCs has been observed previously with extended x-ray absorption fine structure (EXAFS) for Au [158] and Pt [159] NCs and it was attributed to surface tension [37], [158], [160], [161]. Surface tension itself was found to increase in Au NCs compared to surfaces of bulk Au by 40% [158].

4.1.5 The role of anharmonicity in lattice equilibration

In the previous sections, static and time-resolved electron diffraction experiments, and various methods for analyzing the data, have shown that lattice expansion is suppressed in Au_{923} NCs. The importance of lattice anharmonicity extends beyond macroscopic motions such as thermal expansion. Regarding microscopic phenomena, the interaction between phonons is allowed due to the anharmonicity of the interatomic potential [99]. Phonon-phonon interactions are an integral part for the restoration of thermodynamic equilibrium among the various lattice degrees of freedom [75], [78], [94], [108], [109]. In FED experiments, having finite phonon-phonon interaction strengths can lead to an apparent retardation of lattice dynamics [75], [78].

In view of the observed suppression of anharmonicity in Au_{923}, the simplest explanation for the apparent decrease of electron-phonon energy transfer rate G_{e-ph} (**Chapter 3**) is due to weaker anharmonicity and weaker phonon-phonon interactions. This explanation is preferred over a genuine reduction of G_{e-ph} due to spatial confinement, which has not been observed by other experimental techniques at this size regime [162].

In more detail, electron-phonon coupling in simple metals is stronger for the high frequency, longitudinal acoustic phonons (LA) compared to the low frequency, transverse

acoustic phonons (TA) [78]. Thus, after electron-lattice equilibration the LA modes will get transiently hotter than all other modes. However, the contribution of LA modes to the observed Debye-Waller decay is the lowest because the phonon amplitude is inversely proportional to the frequency, see **section 2.2.4** and equation R 2.11. In this way, FED is sensitive to phonon-phonon interactions in addition to electron-lattice equilibration. The observed reduction of lattice anharmonicity, compared to bulk Au, can lead to a slower equilibration of TA and LA modes and an apparent decrease of G_{e-ph} when the measurement is carried out by FED and the TTM model. As an example, the sensitivity of FED to phonon-phonon interactions can lead to a reduction of the G_{e-ph} measured by TTM, by a factor of ~2 for Aluminum (see fig. 3.c of [78]).

4.2 Surface premelting of Au_{923} nanoclusters

An additional observable provided by FED is the time-evolving width of diffraction peaks, which is associated with atomic motions that deteriorate crystallinity. For Au_{923} NCs on Si-N, upon photoexcitation and electron-lattice equilibration the widths of the (111), (220), (331) and (420) diffraction peaks increase (peak broadening) as shown in **figure 4.6.a**.

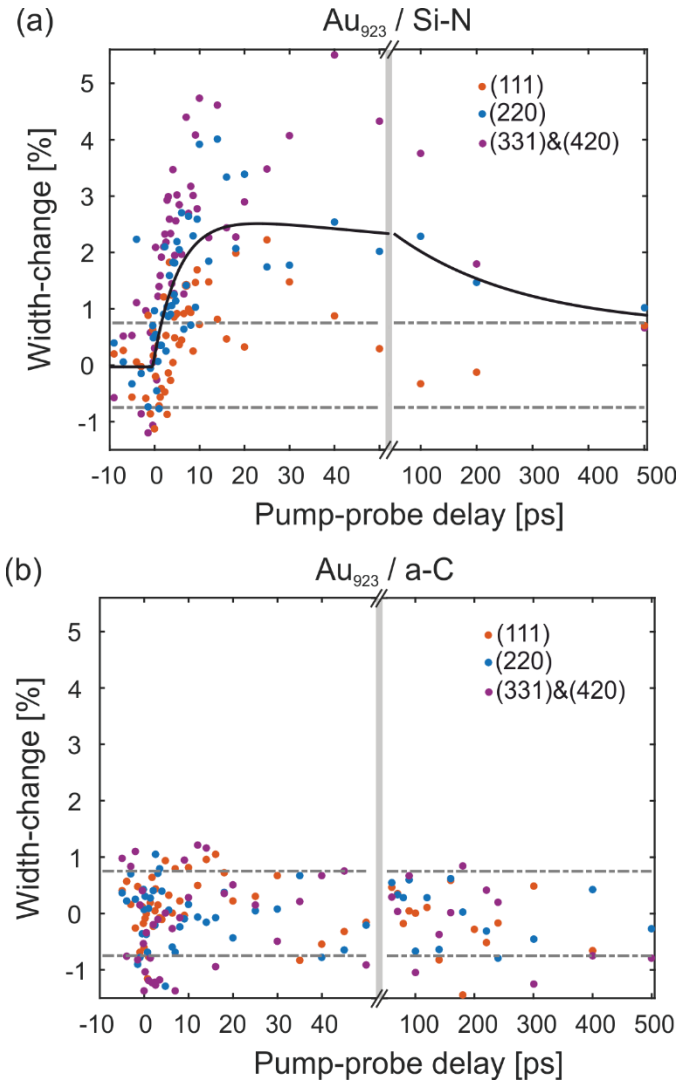

Figure 4.6: Ultrafast evolution of the width of diffraction peaks for Au923 NCs on transparent and absorbing substrates. (a) The change of width (%) for various peaks of Au_{923} NCs on Si-N (datapoints), a bi-exponential fit of the average width change (black solid line) and the 95% confidence intervals before excitation (dashed grey lines). **(b)** The same plot for Au_{923} on a-C. This time the width does not follow bi-exponential dynamics and remains stable within the uncertainty of the measurement and the fitting procedure.

Peak broadening is larger for diffraction peaks located at high scattering angles. The average width can be fitted with a bi-exponential function (solid black line). Initially, the average width increases by $(2.8 \pm 0.4)\%$ with a time-constant $\tau_1 = (5.8 \pm 1.5)\, ps$. Subsequently, the width decreases again with a time-constant $\tau_2 \sim 200\, ps$, suggesting a restoration of the initial crystalline arrangement. The same analysis has been performed for Au_{923} NCs on a-C and it shown in **figure 4.6.b**. In this case the widths of all diffraction peaks stay constant within the uncertainties of the measurement and the fitting

procedure. Multiple measurements at lower fluences have yield the same result (see Sup. Inf. of [117]).

For a better understanding of the physical process causing peak broadening, the measurements of Au_{923} NCs on Si-N have been repeated with various incident pump fluences (**figure 4.7)**. **Figure 4.7.a** shows the average width increase of (111), (220) and (331)&(420) as a function of pump-probe delay for various incident fluences. For the highest incident fluence (3 mJ/cm^2), peak broadening persists up to 0.5 ns. **Figure 4.7.b** shows the average width increase over the 14-30 ps time interval plotted as a function of the incident pump fluence (data points with error bars). The observed fluence dependence can be fitted with a non-linear function (red line) of the form aF^n where F is the fluence and $n = 2.4$.

The width of diffraction peaks can be limited by the transverse coherence of the probing electrons [91]. The transverse coherence length of the used FED apparatus is $\geq 4\,nm$ [38], meaning larger than the Au_{923} NC's diameter ($D \sim 3\,nm$), and hence it is sufficient for investigating genuine physical processes related with the crystalline order. In general, the width of diffraction peaks depends on two factors: the domain size of the crystallites and inhomogeneous strain [98]. For bulk crystals and large particles, ultrafast increase of the width of diffraction peaks can be the result of inhomogeneous laser excitation.

Short pulse durations (in comparison with the timescale for heat diffusion) can lead to inhomogeneous strain of the lattice across the penetration depth of radiation [163]. It has also been reported that a transient gradient in the electronic temperature can cause strain and melting, affecting in this way the width of diffraction peaks [164]–[166]. The mechanisms mentioned so far are not applicable for Au_{923} NCs. The diameter of the Au_{923} (~3 nm) is clearly smaller than the penetration depth of 400 nm radiation for Au (16 nm based on Johnson *et al.* [167]). The characteristic time for sound propagation from the surface to the center of Au_{923} is ~1 ps. Hence, inhomogeneous strain and temperature gradients persisting significantly beyond this timescale can be excluded.

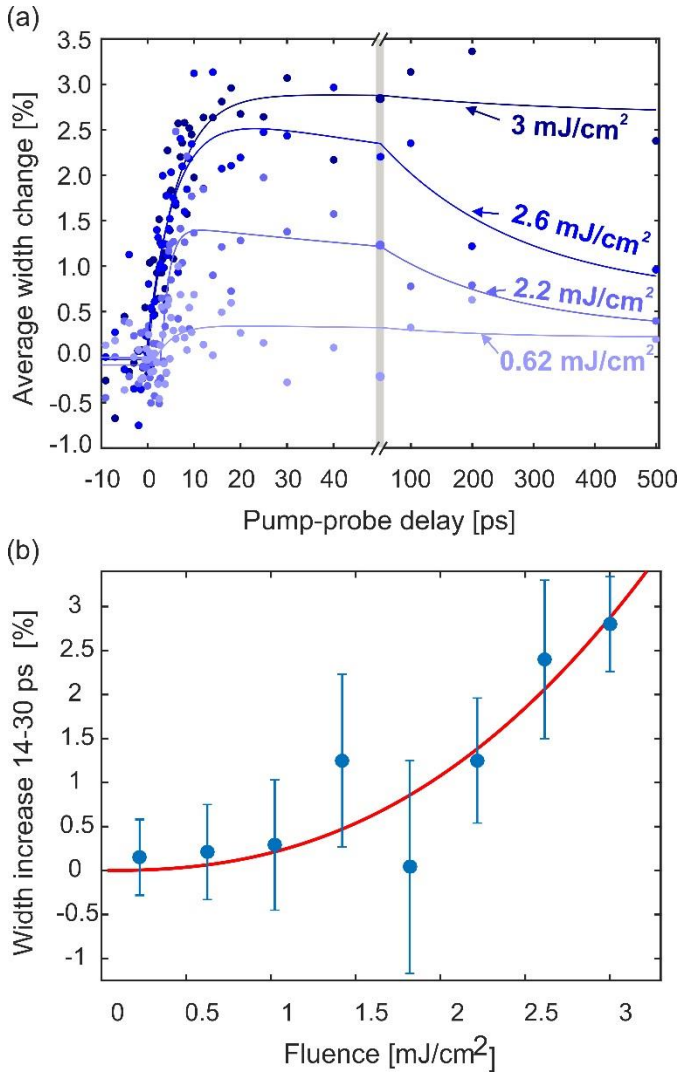

Figure 4.7: Fluence dependence of peak broadening for Au_{923} NCs on Si-N. (a) Average width change of all diffraction peaks as a function of pump-probe delay. For the highest fluence the peaks are clearly broadened even after 0.5 ns. **(b)** Maximum width increase (14-30 ps) as a function of the incident fluence.

For small NCs, the most appropriate explanations are: (1) surface premelting that reduces the effective size of the crystallites and (2) collective vibrations that cause fluctuations of the NC shape. Collective vibrations, such as breathing and toroidal sphere-modes, lead to inhomogeneous atomic displacements and hence inhomogeneous strain across the NC volume [168]. These vibrations can be coherent for individual NCs without producing a coherent signal in the FED observables due to polydispersity [169]. Although the existence of collective NC vibrations should not be excluded, collective vibrations cannot account for the entire peak-broadening signal that persists for 0.5 ns. The observed peak-

broadening dynamics are interpreted as NC premelting based on the following considerations.

Vibrations of Au_{923} NCs should have a period of 1 ps or lower [170]. Given the fact that the NCs are small and adhered on a larger substrate, collective vibrations are expected to have limited lifetimes, certainly smaller than 0.5 ns. However, long timescales for recovery are expected in the case of surface premelting because the atoms have to diffuse on the NC surface until finding the binding sites that minimize the energy of the system.

Second, collective vibrations are incompatible with the observed fluence dependence. The energy injected into collective vibrations (ΔE) is expected to have a linear dependence on the incident fluence. The vibrational amplitude (A) and the inhomogeneous strain are also expected to depend linearly on each other. Based on the harmonic oscillator model ($\Delta E \sim A^2$) the inhomogeneous strain should have a sublinear dependence on the incident fluence. Instead, the nonlinear, exponential-like increase (**fig. 4.7.b**), suggests that atoms have to overcome an energy barrier, as in the case of surface premelting. All these qualitative considerations point towards surface premelting as the main cause of the observed peak broadening.

Beyond qualitative arguments, it is possible to disentangle contributions from surface premelting and inhomogeneous strain through the so-called size-strain analysis [98], [171]. This type of analysis is based on the Williamson-Hall model [98] in which the width of diffraction peaks (β) is connected with the diameter of the crystallite (D) and the inhomogeneous strain (ε) through the relationship:

$$\beta = \frac{K\lambda}{D\cos\Theta} + 4\varepsilon\tan\Theta \qquad \text{R 4.6}$$

where K is a constant close to unity that depends on the shape of the crystallite, λ is the De Broglie wavelength of the probe electrons and Θ the scattering angle of each diffraction peak. In order to use relationship R 4.6, the experimental values of $\beta\cos\Theta$ are plotted as a function of $\sin\Theta$. These quantities, averaged over negative delays and the 12-30 ps interval, are shown, together with a linear fit in **figure 4.8**.

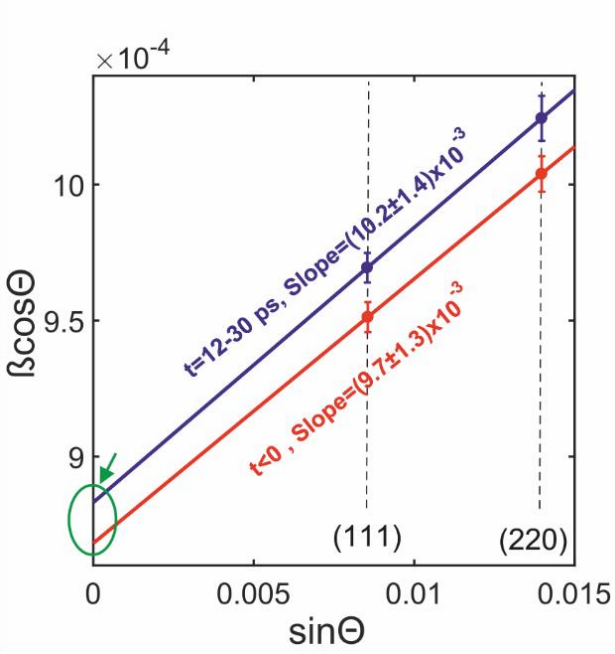

Figure 4.8: Williamson-Hall plot before and after photoexcitation. The values on the horizontal axis are acquired experimentally from the position of diffraction peaks. The values on the vertical axis are acquired experimentally from the position and the width of diffraction peaks. The width and the angle are in radians. The offset (marked by a green circle) can only result from a reduction of the size of the crystalline core at positive time delays.

The slope (A) is proportional to inhomogeneous strain ($A = 4\varepsilon$) while the intercept with the vertical axis (B) is inversely proportional to the NCs diameter ($B = K\lambda/D$). After photoexcitation the slope is similar but the y-intercept is larger meaning that the diameter of NCs has decreased. The reduction of the NC size accounts for 90% of the observed peak broadening. Since the number of atoms per NC is expected to remain constant, the apparent decrease on the crystallite size can be explained by the formation of a liquid-like layer on the NC surface, which removes atoms from the crystalline core.

The observed change in size corresponds to 50 ± 20 atoms in a liquid-like state, meaning ~14% of the surface gets melted. In the present experiments, the maximum temperature (440 K) is significantly lower than the melting point of bulk Au (~1400 K). The critical temperature for surface premelting at this size regime has been estimated with *in-situ* electron microscopy to be ~ 800 K [35]. Thus the observed laser-induced lattice heating is insufficient for thermally activated surface premelting. Another indication for the non-thermal nature of atomic disordering is that the process starts upon photoexcitation and proceeds at ultrafast timescales, comparable with the characteristic timescale for electron-

lattice interactions. The findings of the present work agree well with several previous studies on laser-excited Au NCs. Plech *et al.* [172] have reported a surface phase transition for supported Au nanostructures at atypically low temperatures for surface premelting. Clark *et al.* [171] have visualized the formation of a liquid outer shell of atoms on a laser-excited Au nanoparticle using coherent X-ray diffraction imaging. Taylor *et al.* [50] have shown that laser-irradiated Au nanorods transform into spheres through the formation of a surface layer of mobile Au atoms at lower temperatures than the melting point of Au.

Dependence of peak-broadening on the electronic temperature. An interesting question is why peak broadening is absent for Au_{923} NCs on a-C (**figure 4.6.b**). If the nature of the process is non-thermal, differences between Au_{923}/Si-N and Au_{923}/a-C are expected because the two samples have very different pathways for energy flow. As shown in **figures 3.8** and **3.9**, both samples reach a maximum lattice temperature of 440-460 K. However, the maximum electronic temperatures are drastically different (**figure 3.10**). The Au_{923}/Si-N sample has a maximum electronic temperature of ~3300 K (surface premelting occurs) while the Au_{923}/a-C sample has a maximum electronic temperature of ~1300 K (surface premelting does not occur). All measurements that were carried out are plotted in **figure 4.9** in terms of maximum increase of average width versus maximum electronic temperature.

The observed trend suggests that surface premelting takes place only under pronounced electron-lattice nonequilibrium. As mentioned already, for $T_E^{max} \geq 3000\,K$ the hot electrons have high enough pressure to set the atoms of metallic nanostructures in motion [154] and, potentially, to destabilize the lattice and induce atomic disordering.

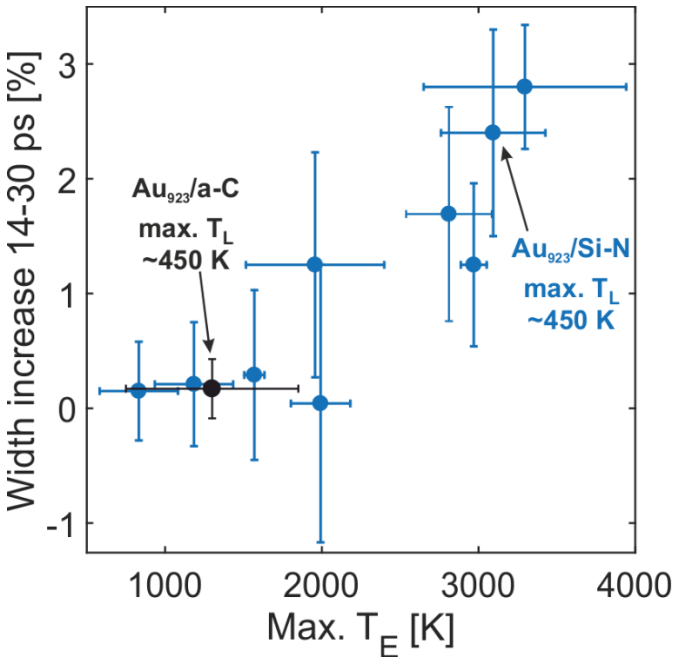

Figure 4.9: Maximum width increase as a function of the maximum electronic temperature predicted by the 0D/2D model of energy flow. Blue datapoints represent fluence dependent measurements of Au_{923} NCs on Si-N. The singla black datapoint is the measurement of Au_{923} NCs on a-C. Although the maximum lattice temperature is similar, the electronic temperature and the width change are drastically different for the two types of substrate.

4.3 Implications of hot electron induced premelting for surface chemical reactions

A very important feature of metallic NCs is mobile imperfections on their surface, such as mobile adatoms and vacancies. **Figure 4.10** shows snapshots of a molecular dynamics simulation (more information in **chapter 5**) of Au_{923} at 600 K. On the one hand, surface atoms tend to form closely packed facets (**figure 4.10.a**) to minimize their energy. On the other hand, surface diffusion generates mobile adatoms and vacancies (**figure 4.10.b**).

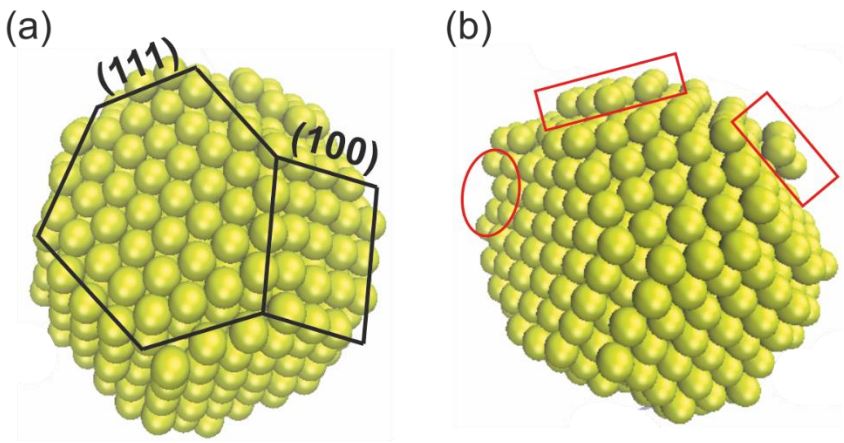

Figure 4.10: Coexistence of atomic order and disorder in the surface of Au_{923} NCs. The depicted structures are snapshots from classical molecular dynamics simulations carried out at 600 K (**Chapter 5**). Small aggregates of atoms acquire crystalline arrangements with closely packed facets of surface atoms as shown in **(a)**. The ability of atoms to move gives rise to mobile surface adatoms and vacancies as shown in **(b)**. Based on these simulations, the atoms on the surface of the Au_{923} cluster are in a constant, dynamic balance between ordered and disordered arrangements.

The molecular dynamics simulations shown in **figure 4.10** suggest that the shape of spatially confined, noble metals is a very dynamic property. Atoms close to the surface are continuously balancing between ordered and disordered atomic arrangements. The microscopic mechanism through which hot electrons induce disordering of surface atoms and surface premelting in Au NCs remains an open question.

Population of antibonding states. Non-thermal destabilization of crystals due to electronic excitations is most commonly found in semiconductors [173]–[175]. In semiconductors, moving a significant fraction of electrons from the valence (bonding) to the conduction (anti-bonding) states (using an intense, femtosecond laser pulse) can alter the potential energy surface and set the atoms in motion. Laser-induced modifications of the potential energy surface can initiate coherent phonons [75] in the perturbative regime, or completely destabilize the crystal and induce melting [173].

Charging. The mechanism for semiconductors is not applicable for simple metals (like Au) where close to the Fermi level the occupied and unoccupied states are of the same character. However, the potential energy surface of bulk Au is known to change at high electronic temperatures [176], resulting in modified structural dynamics [13]. Interestingly, Rapacioli *et al*. [177] have recently shown that charging (+1 or -1 electron) drops the melting temperature of Au_{20} clusters from 1102 K (neutral) to 826-866 K

(charged), indicating that microscopic electric fields have a pronounce effect on the lattice stability of spatially confined metals (see also the study of Cuny *et al*. [178]).

Population of surface states. The potential energy surface of surface atoms is expected to be very different than for bulk atoms. Based on several surface science studies, the potential energy surface of adatoms on metals (and thus their mobility) is greatly affected by electronic surface states [179]–[183]. Moreover, theoretical calculations have shown that adatom-adatom interactions are mediated by surface states [183], [184]. In reverse, surface states are strongly interacting with surface imperfections [185]–[187]. On Au_{923}, surface states can be confined within NC facets (marked by black lines in **figure 4.10.a**) and acquire spatially inhomogeneous shapes [188]. Localization of surface states also takes place on edges [189].

Changing the distribution of electrons in surface states has been shown to mobilize surface atoms. The external stimuli used to modify surface states and subsequently mobilize surface atoms were (i) heating [190] (see figure 5 of referenced work) (ii) manipulation of atoms on surfaces [191] (iii) electron transfer from metallic tips [192] and (iv) laser pulses [193]. In line with all these studies, the proposed scenario is that surface premelting is due to atomic disordering triggered by (de)population of surface states (below) above the Fermi level at high electronic temperatures [117].

Status of theory modelling. Ultrafast electron excitation of metallic surfaces is known to induce desorption [194], diffusion and dimer formation [195], as well as dissociation [51] of small, molecular adsorbates. The underlying mechanisms involve efficient coupling of electronic degrees of freedom, of the metal substrate, to the degrees of freedom of the adsorbed molecule (see for instance Misewich *et al*. [194] and Brandbyge *et al*. [196] and the review article of Frischorn *et al*. [52]). Generally, the metal's surface atoms are considered 'frozen' and the phonons play a minor role. However, the present findings (see also Vasileiadis *et al*. [117]) suggest that the surface atoms of laser-excited metals are highly mobile.

In this case, theoretical calculations of laser-induced reactions on metal surfaces might need to take into account the mobility of surface atoms of the metal itself. The recent theoretical work of Scholz et al. [197] have studied the dynamics of CO molecules on Ru. In this work it is stated (page 165447-13): *'diffusion is somewhat affected by phonons, in addition to hot-electron mediated dynamics… phonons affect the hot-electron mediated*

desorption dynamics considerably, leading to desorption yields easily an order of magnitude larger… phonons act on similar time scales as the electron-hole pairs, at least in the sense that they enhance the energy transfer to the molecule from the surface on a few-ps time scale… substrate phonon motion should be consulted in the future to make a more definitive statement'.

Picturing all atomic motions on a metallic nanostructure, or surface, as phonons might not be sufficient. Diffusive motions might also play a role in ultrafast, chemical reactions. Small, metallic clusters, with surface imperfections are known to have drastically enhanced catalytic activity compared with clusters of well-defined morphology [62]. Thus, it is possible that ultrafast, diffusive motions of surface atoms, imperfections *etc* (similar with surface melting) offer chemically- or catalytically-active sites at ultrafast timescales.

Comparison with *in situ* surface science studies. Interestingly, surface science studies using *in situ* scanning tunneling microscopy (STM) have reached a similar conclusion. Hot electrons can be generated not only by femtosecond laser pulses but also during catalytic and surface chemical reactions [59]. The investigated Au_{923} NC is in the size regime where the efficiency of catalytic CO oxidation becomes maximum [55]. Catalytic oxidation of CO is halted by sintering of Au NCs (diffusion is causing small NCs to merge and form larger, catalytically inactive particles). In the work of Yang *et al.* [56] it is stated: *''It is certainly plausible that hot electrons generated by CO oxidation could induce the detachment of Au monomers from supported Au particles, initiating the sintering process''*. The present FED study is supportive of this hypothesis. Energetic electrons, originating from breakage of chemical bonds, can migrate on localized surface states of NCs and change the mobility of surface atoms.

This last comparison, between a time-resolved FED study and an *in situ* STM study, highlights the potential significance of surface atom - hot electron interactions for lattice-dynamics, catalysis and chemical reactions in confined metallic systems. Further measurements with time-resolved diffraction or the recently developed time-resolved microscopies [198] can be used to shed extra light on these very interesting phenomena.

Chapter 5. Ultrafast rotational motions of 0D nanostructures on 2D crystals

The previous chapters were focused on atomic vibrations, lattice expansion and atomic disordering in 0D nanostructures supported on amorphous thin-films. Most of the FED observables stem from phonons and structural changes driven by phonons, like anharmonic lattice expansion and crystal melting. In principle, it is also possible that motions of the phonons' frame of reference, meaning motions of the entire nanocrystal, can produce some additional observables in reciprocal space. When the nanocrystal is composed of only few hundred atoms, the nanocrystal rotational and translational motions occur in the picosecond timescale.

The results presented in this chapter show that in addition to atomic vibrations, 0D nanostructures supported on surfaces exhibit restricted rotations at ultrafast timescales. These rotational motions are termed librations in analogy with molecular systems. The model system under consideration is size-selected Au_{923} NCs on ultrathin graphite. The real-time observation of librations is possible due to the sensitivity of diffraction to the crystal orientation and the femtosecond time duration of the electron pulses. Unlike the previous chapter, where the substrates were amorphous, the substrate examined here is crystalline (few-layer graphene). Surface crystallinity is imposing an initial, preferred orientation for the deposited NCs that is perturbed after laser excitation. The experimental results are complemented by molecular dynamics and electron diffraction simulations. Theoretical simulations and experimental results are in quantitative agreement. The chapter concludes with a detailed analysis of energy flow that involves both atomic vibrations and librations of nanoclusters.

5.1 Au_{923} / few-layer graphite heterostructures

The investigated heterostructure contains size-selected Au_{923} NCs and few-layer graphite. This section explains the synthesis and characterization procedures.

5.1.1 Electron microscopy

The ultrathin graphitic substrate (denoted by Gr) contains areas with single-layer thickness (graphene), bilayer and few-layer (up to 8) based on HR-TEM images. The lateral diameter of crystalline domains is ~100 μm based on the diffraction pattern. To improve the mechanical stability and avoid folding, the Gr substrate is supported on a lacey-carbon network on its one side. For this reason the average thickness of C is raised to approximately 10 nm. The unsupported side of Gr is decorated with size-selected $Au_{923\pm23}$ NCs. These clusters are prepared in the gaseous phase, as described in previous chapters, and deposited on Gr in the soft-landing regime (kinetic energy less than 2 eV per Au atom). Prior to this step the surface of Gr is bombarded with high energy ions in order to create surface defects. Surface defects act as binding sites for the Au_{923} NCs and suppress translational diffusion, which can result in aggregation and coalescence. The distribution of Au_{923} NCs on Gr has been examined by HAADF imaging (Dawn Foster, University of Birmingham and Richard E. Palmer, University of Swansea). A typical HAADF image is shown in **figure 5.1**.

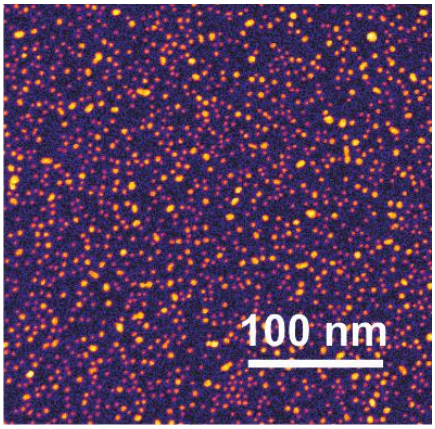

Figure 5.1: HAADF imaging of Au_{923} NC / Gr heterostructures. The surface density corresponds to 2.6 NCs per 100 nm^2 or a nominal thickness of 0.45 nm. The contrast of each NC is proportional to the number of atoms and in this way it is possible to quantify the amount of monomers, dimers, trimers and tetramers that unavoidably form after deposition on Gr. Furthermore, it is possible to quantify the relative abundancies of the various structural allotropes, like FCC, Dh, Ih or amorphous NCs.

In HAADF imaging the contrast of each cluster is proportional to the total amount of atoms. In this way it is possible to record the size-distribution of the NCs. Unavoidably,

some clusters aggregate after deposition and form larger structures. The NCs are 59.5% monomers, 22.8% dimers, 12.0% trimers and 5.7% tetramers. The preparation conditions can be used to control the various structural allotropes of monomers. In this work the preparation conditions result in 37% Dh (polycrystalline Decahedral), 35% FCC (single crystalline FCC) and 3% Ih (nearly amorphous Icosahedral) with the rest having irregular shapes.

5.1.2 Static electron diffraction

The equilibrium structure of Au_{923} NCs / Gr heterostructures is now examined by static electron diffraction. The probe electrons are accelerated by a voltage of 90 kV corresponding to a De Broglie wavelength λ=3.9 pm. The electrons arrive on the sample perpendicular to the substrate surface and illuminate an area of ~100 μm. The resulting diffraction patterns are integrated for 50 s. Each electron pulse has ~10^3 electrons and the repetition rate is 1 kHz meaning that there are ~$5 \cdot 10^7$ electrons per diffractogram. The diffraction pattern of the Au_{923}/Gr heterostructure is shown in **figure 5.2.a** (left). For comparison, the same image shows the diffraction pattern of Au_{923}/a-C heterostructures (**fig. 5.2.a** right). Because of the limited domain size of Gr and the quasi-random orientation of Au_{923} NCs, the electron diffraction patterns consist of Debye-Scherrer rings. The most discernible difference between Au_{923}/Gr and Au_{923}/a-C is the intense diffraction rings of Gr located at ~0.5 $Å^{-1}$ and ~0.8 $Å^{-1}$.

To achieve a more accurate comparison the diffraction intensity has been radially averaged and plotted (after background subtraction) in **figure 5.2.b** (blue data points). The radial averages are then fitted with pseudo-Voigt peak profiles (red solid lines). The most intense peaks of Au_{923}/Gr belong to the Gr substrate, the experimental diffraction pattern of which is shown for comparison in the same plot with a black solid line. Fitting with pseudo-Voigt peak profiles reveals one additional difference between the two substrates. The intensity ratio of (220)/(111) is 0.58 for Au_{923}/Gr and 0.23 for Au_{923}/a-C. These ratios indicate that Au_{923} NCs on a-C have fully random orientation of nanocrystalline domains, while Au_{923} NCs on Gr have a partial orientation of their (111) crystallographic direction vertical to the substrate and parallel to the incident electron beam. The information given here, regarding the preferred orientation of Au_{923} NCs on graphene, applies also for the time-resolved FED experiment shown in the next section.

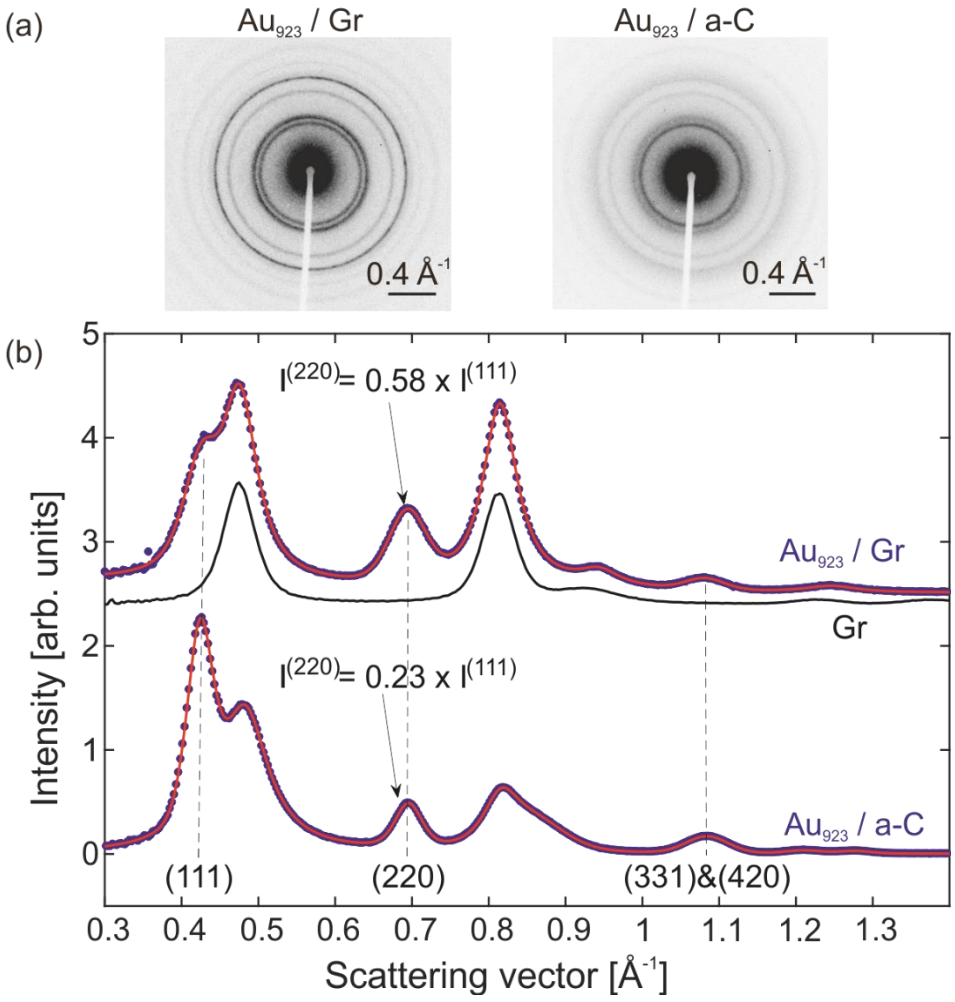

Figure 5.2: Diffraction patterns and radially averaged intensity of the Au_{923} NCs / graphene heterostructure and comparison with Au_{923} NCs / a-C. (a) Electron diffraction patterns of Au_{923} NCs on Gr (left) and Au_{923} NCs on a-C (right). **(b)** Radially averaged intensity of the experimental diffraction patterns after background subtraction for Au_{923} NCs on Gr and Au_{923} NCs on a-C (blue data points) and bare Gr substrates (black solid line). The most obvious difference between the two samples is the intense diffraction peaks of Gr. Fitting with pseudo-Voigt peak-profiles (red solid lines) shows that the (220) peak of Au_{923} NCs on Gr is enhanced compared to the (111). This indicates that the Au nanocrystalline domains on Gr have a preferred (111) orientation. For Au_{923} NCs on a-C the (220)/(111) ratio suggests that the crystallites are randomly oriented.

The Au_{923} NCs on graphene, examined by FED, have also been studied with molecular dynamics (MD) simulations, in order to get a better understanding of (i) their tendency to acquire a (111) crystal orientation and (ii) their ultrafast atomic and NC motions. A representative MD simulation of a Au_{923} NC on graphene is shown in **figure 5.3**. This NC

has a FCC structure, meaning that it is single-crystalline. Many interesting phenomena can become evident from this image, for instance ripples in graphene and Au adatoms on the NC's facets. Most importantly, the (111) crystal orientation is clearly evident, in agreement with the analysis of the experimental electron diffraction patterns of **figure 5.2**. The MD simulations have been performed over several NCs of different crystal structures and for several temperatures. More information are given in later sections.

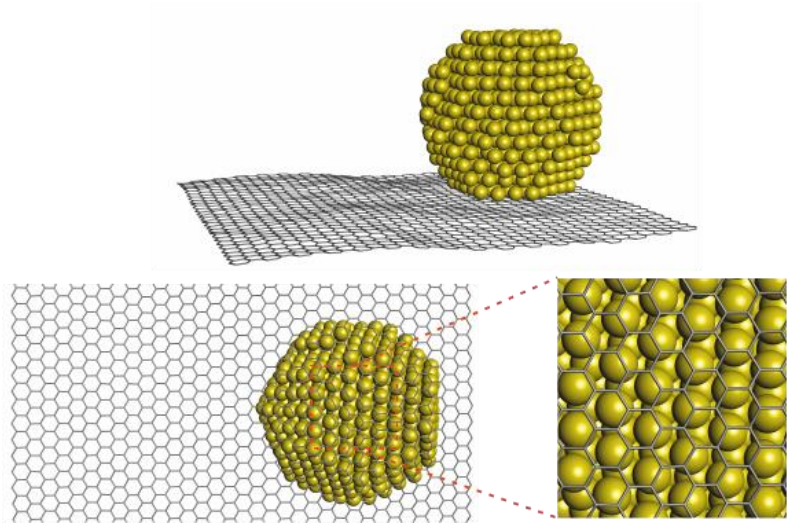

Figure 5.3: Side and top view of a FCC Au_{923} NC on a single layer of graphene simulated with MD. Upper image: a FCC NC on a single layer graphene after relaxation. Lower image: The FCC NC tends to adhere on graphene with its (111) surface facet. The zoom-in (right) shows the crystalline interface of graphene and Au.

5.2 Femtosecond electron diffraction on Au_{923} on graphene

The electron diffraction patterns presented in the previous section correspond to the equilibrium morphology of Au_{923} NCs on Gr. For the results presented in the current section, the electron diffraction patterns of Au_{923} NCs / Gr heterostructures are recorded in a time-resolved, pump-probe manner. The main experiment shown here used 400 nm radiation and an incident fluence of (3.8 ± 0.6) mJ/cm^2.

5.2.1 Ultrafast peak-decay and expansion

After the arrival of the laser pulse (t=0) the lattice exhibits various nonequilibrium motions that deteriorate crystallinity and lead to a decay of diffraction intensity within picoseconds (**figure 5.4.a**). Simultaneously, due to the anharmonicity of the interatomic potential and the enhanced atomic motion, the lattice expands. The observed lattice expansion (**figure 5.4.b**) is detected as a shift of diffraction peaks to lower scattering angles. An important observation is that both the (111) and (220) peaks show similar relative expansion in accordance with isotropic atomic vibrations and lattice expansion (**fig. 5.4.b**). The next step is to check if the observed peak-decay (**fig. 5.4.a**) can also be fully explained in terms of isotropic, atomic vibrations and the Debye-Waller effect.

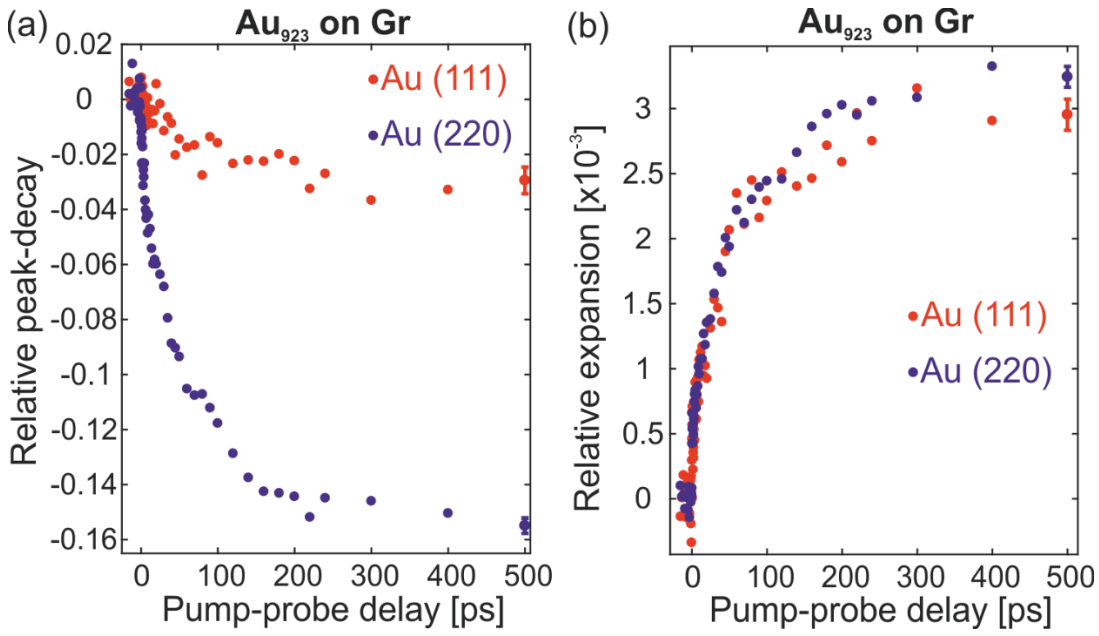

Figure 5.4: Ultrafast peak-decay and expansion of Au_{923} NCs on Gr recorded with FED. (a) Ultrafast relative decay of the (111) and (220) peaks for Au_{923} NCs on Gr. **(b)** Ultrafast relative expansion of Au_{923} NCs on Gr probed from the (111) and (220) peaks. Lattice expansion manifests as a shift of diffraction peaks to lower scattering angles. Expansion is isotropic, meaning that different crystallographic directions experience a similar amount of relative change, while the agreement of the observed peak-decay with the Debye-Waller behavior needs additional examinations.

The experiments on Au_{923} / Gr heterostructures are now compared with Au_{923} / a-C heterostructures, which are known to obey the Debye-Waller dynamics from the analysis of **Chapter 3**. The comparison of lattice dynamics in Au_{923} / Gr and Au_{923} / a-C is shown

in **figure 5.5**. **Figure 5.5.a** shows the measured peak-decay of Au_{923} / a-C for the (111) and (220) peaks (red and blue squares respectively). The same plot shows the (111) and (220) peak-decays of Au_{923} / Gr for comparison (same color dashed lines). For this measurement the (111) peak-decay happens to coincide on both substrates. Yet, the (220) peak-decay for a-C substrate is significantly suppressed compared with the (220) peak-decay for Gr substrate. **Figure 5.5.b** shows the relative expansion of Au_{923} NCs on a-C for the (111) and (220) peaks (red and blue squares respectively). Both peaks show similar relative expansion (isotropic thermal expansion) as in the case of Gr substrates (**fig. 5.4.b**).

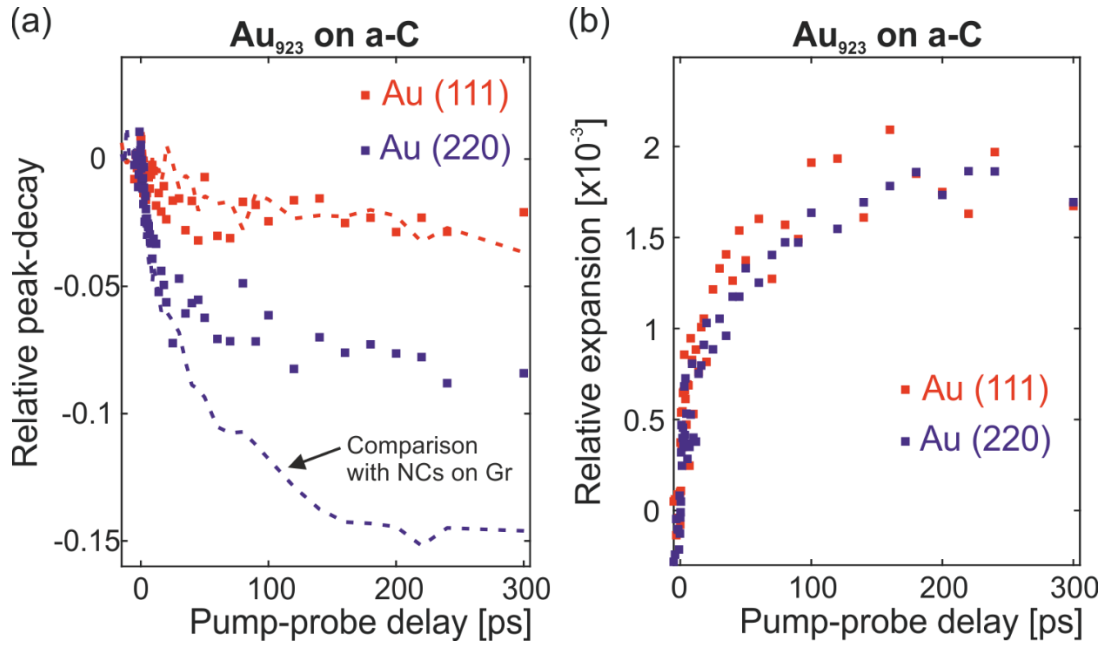

Figure 5.5: Ultrafast peak-decay and peak-shift of Au_{923} NCs on a-C and comparison with Au_{923} NCs on Gr. (a) Ultrafast relative decay of the (111) and (220) peaks for Au_{923} NCs on a-C (red and blue squares respectively). The data shown in **figure 5.4** are plotted again here for comparison (dashed lines). **(b)** Relative expansion of Au_{923} NCs on a-C probed from the (111) and (220) peaks. The lattice expansion of Au_{923} on a-C is isotropic (same for all diffraction peaks) as in the case of Au_{923} on Gr. The comparison of the two heterostructures reveals the existence of some process that affects the intensity but not the scattering angle of diffraction peaks, acts on top of the Debye-Waller effect and appears for Gr but not for a-C substrates.

The comparison reveals that for Au_{923} NCs on Gr, some lattice motion affects the diffraction dynamics in a way that cannot be described by the Debye-Waller behavior.

5.2.2 Deviation from Debye-Waller behavior

The previous section presented the dynamics of peak-decay and expansion for Au_{923} NCs on Gr. The comparison of Au_{923} / Gr and Au_{923} / a-C heterostructures revealed that in the first case the peak-decay dynamics deviate from the Debye-Waller behavior. The most profound deviation is the unusually strong peak-decay of the (220) peak. This sections presents a method for quantifying the deviation of the observed peak-decays from those predicted by the Debye-Waller relationship.

The Debye-Waller method works well for Au_{923} NCs on a-C and on Si-N. For these samples the temperature, extracted from the MSD, and the observed lattice expansion have been used to measure the thermal expansion coefficient. For Au_{923} NCs the thermal expansion coefficient is $a_L = (9.5 \pm 0.7) \cdot 10^{-6}\,\mathrm{K}^{-1}$ (averaged over all experiments). For Au_{923} / Gr the peak-decay dynamics are more complicated and the lattice temperature can be alternatively found from the observed thermal expansion and the known thermal expansion coefficient. Using this simple procedure the final temperature corresponding to the data shown in **figure 5.4** is ~600 K ($\Delta T \sim 300\,K$). Although the extracted MSD of each peak does not reflect the lattice energy content, the average MSD is close to the expected value for lattice heating. The average MSD is used to calculate back the expected decay of each peak based on the Debye-Waller effect. **Figure 5.6.a** compares the expected peak-decay (dashed lines) and the experimental peak-decay (data points) of the (111) and (220) diffraction peaks (red and blue respectively) of Au_{923} NCs on Gr.

The deviations between the experimental and the actual peak-decays are plotted in **figure 5.6.b** for the (111) and (220) peaks with red and blue circles, respectively. This new quantity rises only in the presence of lattice dynamics that do not obey the Debye-Waller relationship. The deviation from the Debye-Waller behavior emerges with biexponential dynamics (solid lines). The fast process has time-constant τ_1=(4±2) ps and accounts for 40% of the overall effect. The slow process has time-constant τ_2=(110±40) ps. The (111) peak shows a positive deviation from the Debye-Waller decay by ~1% (decreases less than expected) and the (220) peak a negative deviation by ~4% (decreases more than expected).

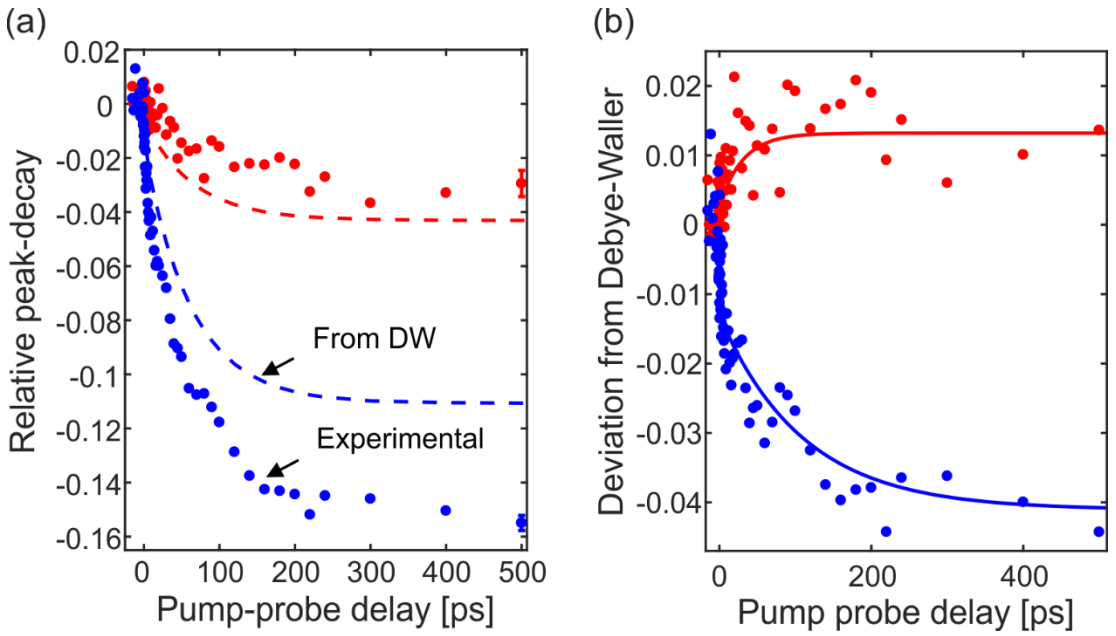

Figure 5.6: Deviation of peak-decay from Debye-Waller dynamics for Au_{923} NCs on Gr. (a) Observed (circles) and predicted by Debye-Waller (dashed lines) peak decays of (111) and (220) (red and blue respectively). **(b)** The deviation between observed and expected peak decays (circles) and biexponential fittings (solid lines).

5.2.3 Fluence dependence of deviation

The time-evolving deviation of diffraction peaks (**fig. 5.6.b**) can be alternatively plotted as a function of the lattice temperature instead of the pump-probe time-delay. Multiple measurements with different fluences can reveal the fluence dependence of the underlying NC dynamics. **Figure 5.7.a** shows the deviation of the (220) peak as a function of the temperature extracted from lattice expansion for 4 measurements with different fluences.

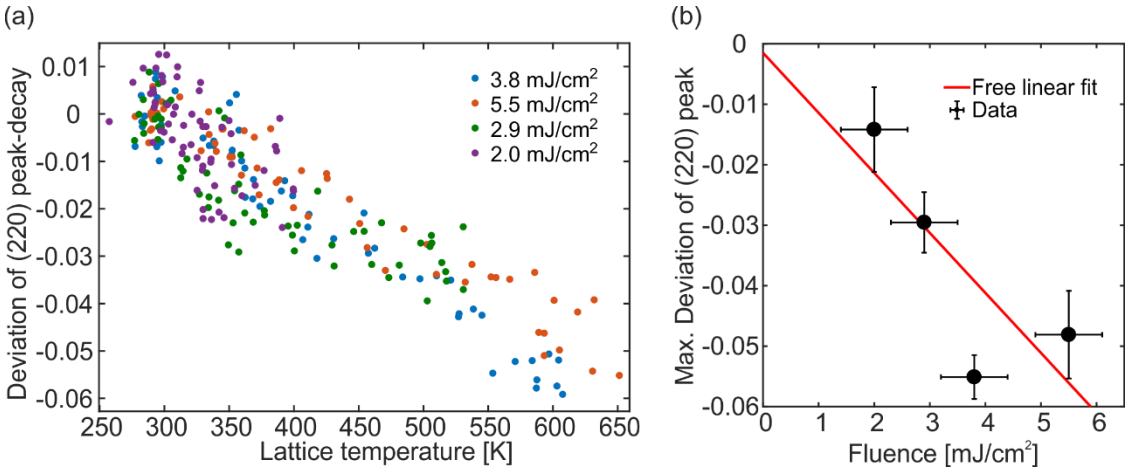

Figure 5.7: Fluence dependence measurements with FED. (a) Deviation of the (220) peak versus lattice temperature from expansion. Different colors correspond to different measurements with varying incident fluence (see figure legend). **(b)** Maximum deviation versus incident fluence (data-points with error-bars) and an unconstrained linear fit (red solid line). Each data-point in (b) is the average deviation of the (220) peak in the 220-500 ps time-interval.

Figure 5.7.b shows the maximum deviation of the (220) peak as a function of the incident fluence. The projection of each data point on the vertical axis corresponds to the average deviation over the 220-500 ps time-interval (last four data-points in each data-set of **figure 5.7.a**). The vertical error bars are the standard deviation of the same data points. For all measurements the deviation seems to follow a linear trend with the lattice temperature. The red line is an unconstrained linear fit. The linear fitting tends to zero for zero laser fluence. The same linear trend is visible in **figure 5.7.a** when the deviation is given as a function of temperature. The linear dependence on the incident laser fluence and on the lattice temperature suggests that the underlying physical process is thermally excited.

5.3 Molecular dynamics simulations of Au_{923} on graphene

The present section presents molecular dynamics simulations (MD) of Au_{923} on graphene that aim in understanding NC motions beyond atomic vibrations. The simulations have been carried out by Emmanuel Skountzos (University of Patras), Vlasis Mavrantzas (ETH Zurich & University of Patras) and the author of this thesis. The goal of the MD

simulations is (i) to gain a microscopic understanding on the various lattice motions of Au_{923} NCs on Gr, (i) to perform electron diffraction simulations on the MD trajectories and (iii) to compare the theoretical diffraction dynamics with the FED experiments.

5.3.1 Preparation and deposition of Au_{923} on graphene

The MD simulations are classical, they are based on Newtonian mechanics and semi-empirical interatomic potentials. A simplified but efficient method to simulate the homogeneous distribution of NCs is to use periodic boundary conditions. The simulation box has a volume of (7 x 7.1 x 15) nm^3. Periodic boundary conditions are applied in the dimensions parallel to graphene (X-Y plane). The surface density of Au on graphene for the MD simulations is 2 NCs per 100 nm^2 of graphene. In this way, the MD simulation mimics the surface distribution shown in **figure 5.1** and includes substrate phonons with considerably longer wavelength than the NC.

The MD simulations have been carried out with the LAMMPS software [199]. In this type of simulations, the trajectories of all atoms are solved using the Velocity-Verlet algorithm [199]. The selected time step is 1 fs. The range of all interactions is 15 Å and above this range tail corrections were employed. The temperature was kept constant with the Nosé-Hoover thermostat [115], [116]. The chosen interatomic potentials for the MD simulation were of 12-6 Lennard-Jones type. The interactions between Au atoms were modelled according to the interatomic potential given by Heinz *et al.* [200]. Interatomic interactions in graphene were modelled according to the all-atom DREIDING force-field [201]. The Au-C interactions were modelled according to the interatomic potential of Lewis *et al.* [64].

The simulations start by preparing separately the Au_{923} NCs and the graphene layer. The graphene layer was designed and let to equilibrate for 1 ns with an NPT simulation (constant number of particles N, constant pressure P and constant temperature T). The NCs were constructed in two ways. The first way was to cut a sphere of Au with 923 atoms from a bulk Au crystal, heat it to 800 K (the experimental, surface premelting temperature of Au_{923} NCs) and gradually cooled down to room temperature with 70 K/ns. The final product was a realistic nanocluster with FCC morphology. The second way to construct the NCs was to make the initial design purely with geometrical considerations. The NC in this case was designed to be Dh. The Dh NC was also heated to an elevated

temperature and gradually cooled down to allow the surface to reconstruct and acquire its most favored atomic configuration.

The two materials were brought together in a NVT simulation (constant number of particles N, constant volume V and constant temperature T) with a starting temperature of 600 K. Au NCs with either FCC or Dh morphology were left with a completely random orientation at a distance of 1 nm above graphene. Long range, van der Waals interactions adsorbed the NCs on graphene in sub-ns timescales. Within the first ns the structure became fully relaxed based on the time-evolution of the total energy of the system and the Au/graphene interaction energy. After this initial step the simulation time was extended by 1 ns. All quantities under consideration are measured in this last phase, when the system is relaxed. The computational experiment carried out at 600 K is repeated 10 times for Dh and 10 times for FCC NCs. Then the temperature is gradually lowered to 300 K with steps of 50 K and at each step all measurements are repeated (the measured quantities are various angular motions of the NCs and their diffraction patterns). All measured quantities are averaged over 20 trajectories and given as a function of temperature.

An equilibrated Au_{923} NC / graphene system has been shown in **figure 5.3**. For FCC NCs the most favored binding facet with graphene is the (111). The FCC NCs are single-crystalline and hence the orientation of the entire crystallite is (111). For Dh NCs the most favored binding site is the (100). This is mainly due to the large area of (100) surface facets for Dh NCs. However, the crystallographic texture is again (111). The reason is that the Dh NC has a complicated internal crystal structure (it contains 5 tetrahedral crystallites). Hence, although the binding facet of Dh NCs is (100) their internal structure has a partial (111) crystallographic texture.

5.3.2 Atomic trajectories from molecular dynamics simulations

The next step is to examine the various NC motions. Changing the temperature between 600 K and 300 K does not result in any major structural change. The only visible atomic reconfiguration is a limited amount of surface atoms that begin to diffuse on the surface close to 600 K. **Figure 5.8** shows four snapshots of the MD simulation taken between 300 K and 600 K. The Au_{923} NC in **figure 5.8** has a Dh morphology. The NC is constantly translating in the X-Y plane (parallel to graphene), vibrating in the Z axis (perpendicular

to graphene) and rotating. Rotations occur in three different directions of space. In two of the three dimensions of space the NC rotations are constrained to only few degrees because of the underlying graphene structure.

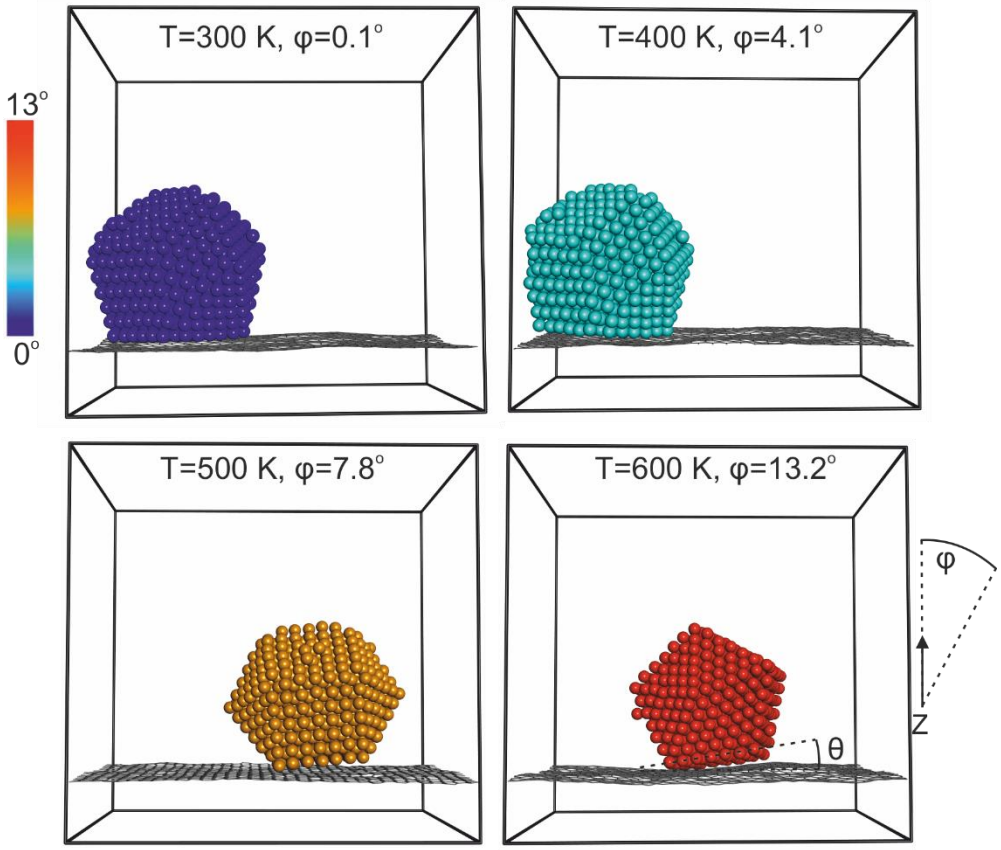

Figure 5.8: Snapshots from the MD simulations showing a Dh Au_{923} NC moving on graphene. Each simulation box corresponds to a certain temperature (given on the top). The NC translates and rotates in various ways. The interesting rotations are the ones corresponding to the angles φ and θ. The angle φ is formed between the normal vector of the NC binding facet and the z-axis. The angle θ is formed between the normal vector of the NC binding facet and the normal vector of the underlying graphene layer. In every snapshot the Au atoms are colored according to the angle φ. In a diffraction experiment where the electrons arrive perpendicular to the z-axis, the angle φ the temperature-dependent angle φ will modify the intensities of the various diffraction peaks. The angle θ is important because it modulates the Au/C interface.

The angular momentum vector can be vertical to graphene. In this case it is possible to observe even full rotations after a certain amount of time. The interesting motions, in view of the FED experiments, are the two remaining rotations that have an angular momentum vector parallel to graphene. These rotations cause the NCs to tilt with respect

to the Z axis or the normal vector on the graphene surface. This angle is denoted as φ and it is shown schematically in **figure 5.8** (down right corner). To assist the reader, the Au atoms in its snapshot are colored according to the value of this angle (see color bar in **fig. 5.8**, upper left corner).

The measurement of the φ angle is described here. The binding facet of the Au NC contains several atoms. The position vectors of these atoms can be used to calculate an average normal vector $\hat{n}$. The tilting angle is then calculated according to $\varphi = \cos^{-1}(\hat{n} \cdot \hat{z})$ where $\hat{z} = (0,0,1)$. The angle φ is temperature dependent. Its statistical distribution is shown in **figure 5.9.a**. As the temperature rises from 300 K to 600 K the NCs the tilting angles φ are increasing. The average angle is φ=2.2° and φ=3.2° at 300 K and 600 K, respectively.

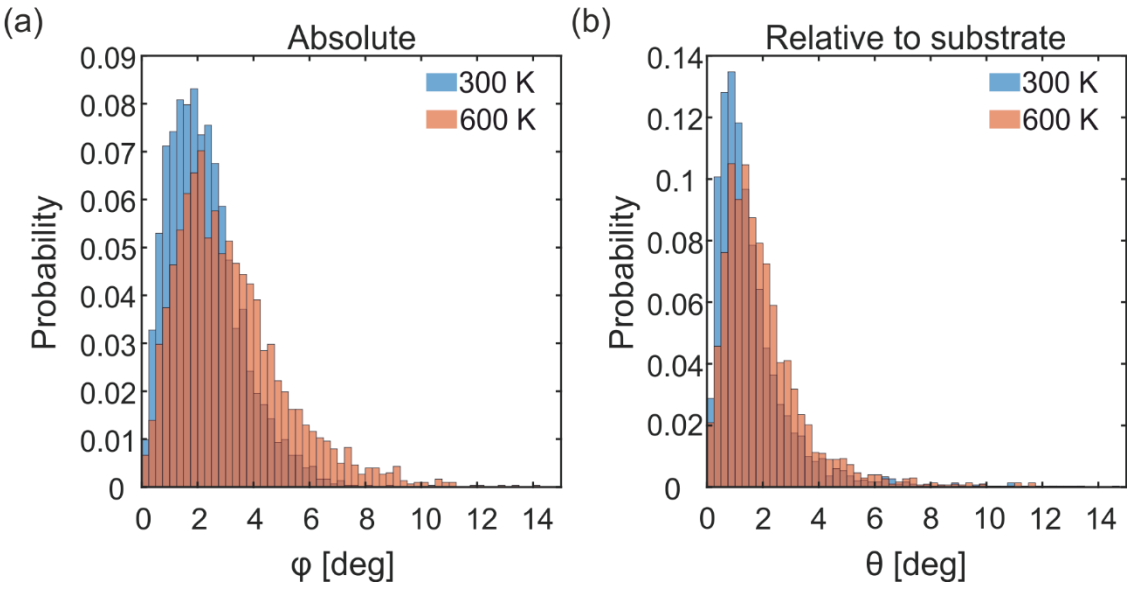

Figure 5.9: Statistical distributions of the θ and φ angles of Au_{923} NCs on graphene (10 Dh and 10 FCC NCs weighted by their relative proportions). (a) Probability distribution over the various angles at 300 K (blue) and 600 K (orange). **(b)** Same for the angle θ. As the temperature rises the average value of the φ and θ angles is rising.

The question examined now is if the NCs are simply tilting due to surface phonons and ripples in graphene, while remaining strongly attached on it, or if they are transiently unsticking and rotate in a distinct way. This can be examined by the angle θ between the Au binding facet and the underlying graphene plane. The angle θ is shown schematically in **figure 5.8** (last snapshot). The measurement of the angle θ starts by finding the C atoms that are in the closest distance from the Au binding facet. The positions vectors of

these C atoms are used to calculate an average vector $\hat{g}$ normal to the underlying graphene atoms. Then the angle between graphene and the Au binding facet is $\theta = \cos^{-1}(\hat{n} \cdot \hat{g})$. The θ angle is also temperature dependent. Its statistical distribution for 300 K and 600 K is given in **figure 5.9.b**. On average θ is 1.6° at 300 K and 2.0° at 600 K.

Although the observable (modified diffraction intensity) is produced by the angle φ, the angle θ is important from a physics perspective. In the ground state the angle θ=0. As the temperature rises, or in nonequilibrium conditions, the angle θ>0. This is expected to modify the adhesion of the Au NC on graphene. As a result, the NC can become transiently mobile in other directions of space. This means that the angular motions along θ can modify the potential energy surface of other, independent degrees of freedom. The work of Guerra *et al.* [65] has shown this for the unconstrained rotations (angular momentum vertical to graphene), using MD simulations and investigations of the correlation between translational and rotational motions. In addition to NC transfer, angular motions along θ might be important for understanding the exact mechanism of energy flow between the two materials, since they modify the Au/C interface. Summarizing all the above, constrained rotations of NCs along the θ angle might play an important role for energy- and mass-transport phenomena.

The rotational motions that cause the φ and θ angles are restricted, meaning that the maximum angles are always few degrees, insufficient for complete rolling of the NCs. In addition, their frequency is in the GHz range (see next section). These motions can be described as librations. The term libration stems from the latin verb *librare*, which means ‘‘trying to balance’’, and describes an oscillatory, angular motion. The term libration is most often used in vibrational spectroscopy of molecules.

5.3.3 Timescale and frequency of rotational motions

The next interesting question is what are the timescales of the NC rotations, which cause the φ and θ angles. As described before, each NC is let from a 1 nm distance to get adsorbed on graphene. Some of the NCs fall with a large angle, causing them to bounce and tilt. The time-dependence of φ after landing is shown in **figure 5.10**. The large rotational motions caused by landing are damped within ~300 ps. After 1 ns the NC is tilting due to thermal motions and the flexibility of the NC/graphene heterostructure.

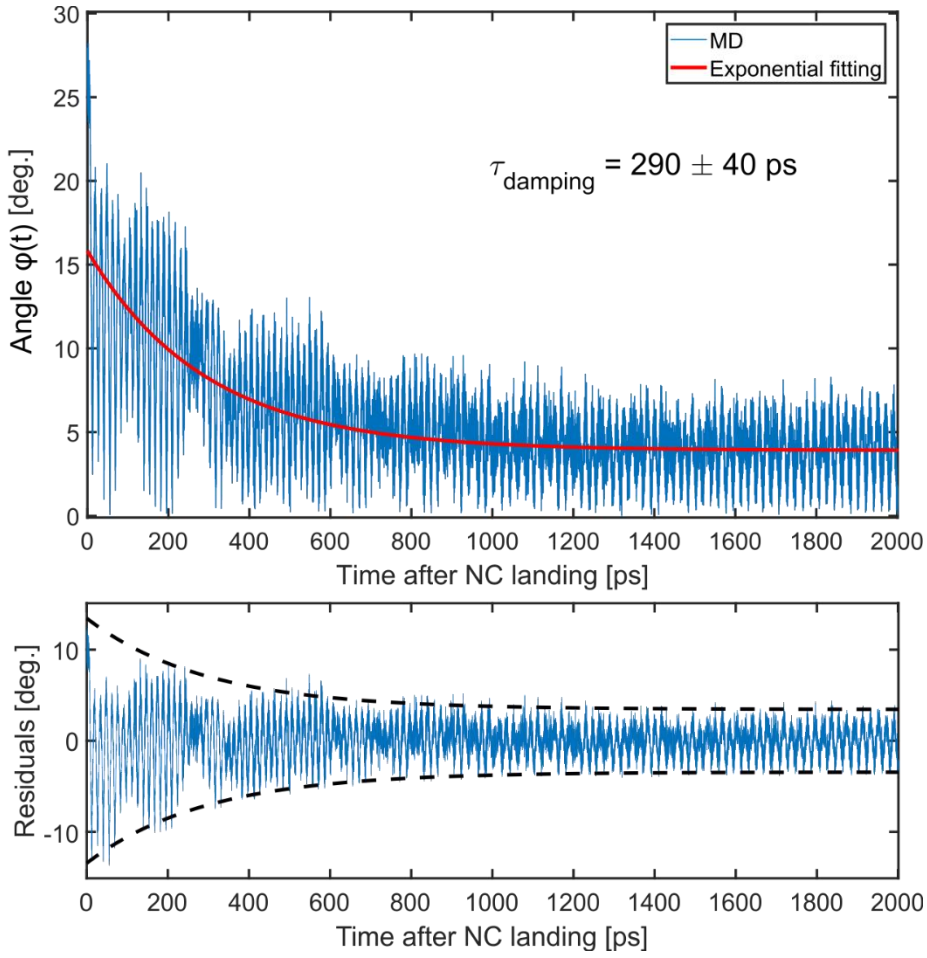

Figure 5.10: NC librations launched by landing on graphene. A Au_{923} NCs adsorbs on graphene and starts to librate. The libration angle φ as a function of the simulation time is shown in the upper diagram (blue). The red line is an exponential decay fitting. The characteristic time for damping is 290±40 ps. The lower diagram shows the residuals. The back dashed lines correspond to the same exponential decay with 290 ps time-constant.

The Fourier transform of the φ angle in the time interval 1-2 ns after landing is shown in **figure 5.11** for a Dh NC (**fig. 5.11.a**) and for a FCC NC (**fig. 5.11.b**). The dominant frequency of the oscillations of the φ angle is 57 GHz on average. Since these rotational motions are in the picosecond timescale they can be directly observed by FED. In fact, the fastest possible response predicted by the MD simulations T/4~4 ps, is matching the fast time-constant found by FED τ_1=(4±2) ps (see also **figure 5.6.b** and relevant discussion).

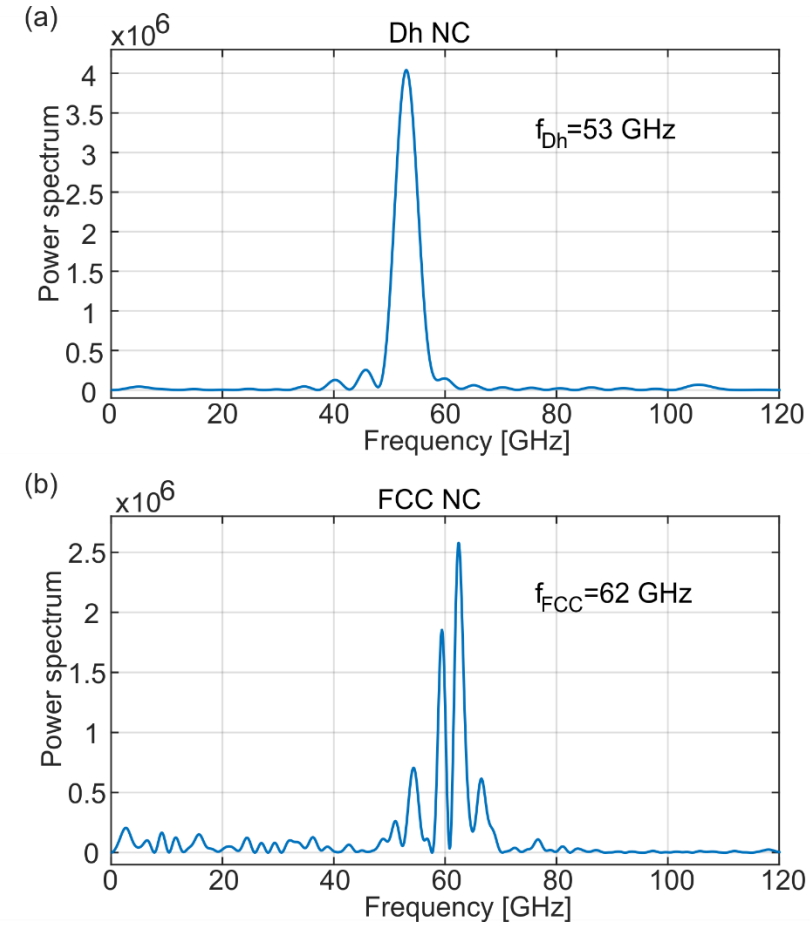

Figure 5.11: Dominant frequency of NC librations on graphene. (a) For a Dh NC the libration frequency is 53 GHz. **(b)** For a Dh NC the libration frequency is 62 GHz. The spectra are calculated by a Fourier-Transform of the data shown in **figure 5.10**. More details can be found in the main text.

5.4 Electron diffraction simulations

Librations are a potential cause of the deviation from the Debye-Waller behavior. For a quantitative confirmation of this scenario the MD-derived atomic trajectories are used to simulate the temperature-dependent, electron diffraction patterns. Then, the theoretical diffraction patterns are compared with the FED experiments.

5.4.1 Diffraction patterns of FCC and Dh nanoclusters

MD trajectories have been transformed into diffraction patterns using the method of Coleman *et al.* [96] that is implemented in LAMMPS. A central quantity in diffraction is the so-called Ewald sphere and its thickness. The radius of the Ewald sphere in the simulation was $1/\lambda$ where λ is the De Broglie wavelength of the electrons used in the FED experiment. The thickness of the Ewald sphere is connected with the energy dispersion of the electrons and it was selected to be equal with 0.06 $Å^{-1}$ in order to fit various diffractograms measured by the FED apparatus in use. The computational grid of the reciprocal space had a spacing of 0.007 $Å^{-1}$. The electron diffraction patterns were radially averaged and the results are shown in **figure 5.12**.

The average diffraction patterns of FCC and Dh NCs are shown in **figure 5.12.a** and **5.12.b**, respectively. The electrons arrive perpendicular to the graphene layer as in the FED experiment. Because the FCC NCs bind on graphene with their (111) facets, the (220) diffraction peak is the strongest while the intensity of (111) is almost zero. Dh NCs bind with the (100) facet but they still have an intense (220) peak, of comparable intensity with the (111) peak, because they contain tetrahedral crystalline domains. At this point it becomes clear why the FED diffraction pattern of Au_{923} NCs / Gr heterostructures, shown in **figure 5.2**, has intense (220) peak. The Au_{923} NCs tend to form FCC and Dh structures which then have a preferred orientation on graphene as shown with MD.

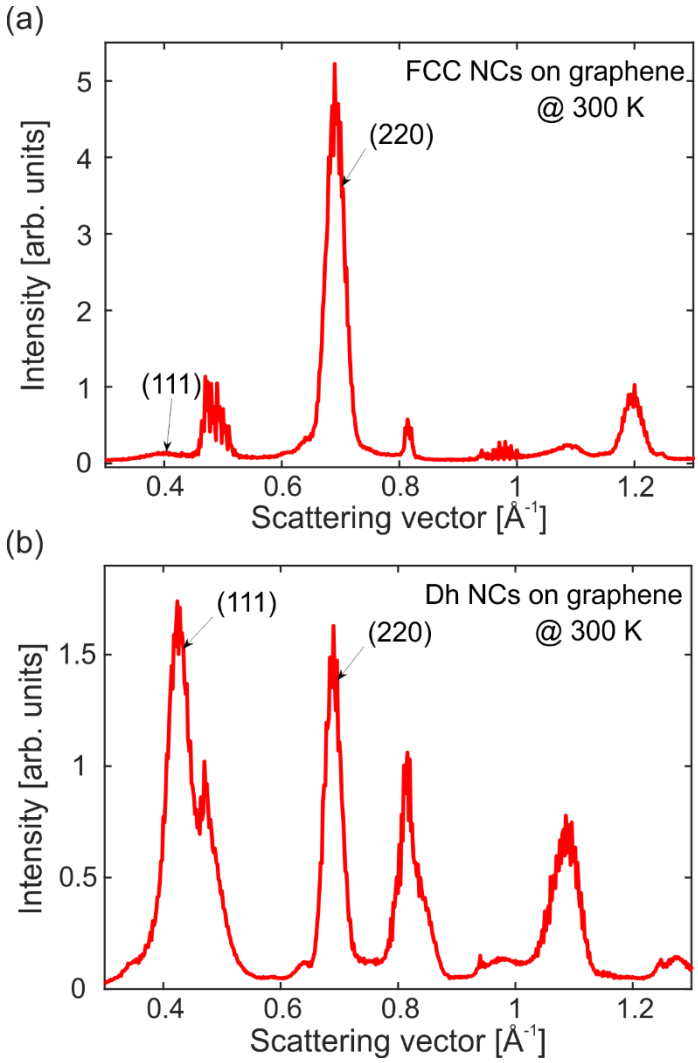

Figure 5.12: Theoretical electron diffraction patterns of MD-simulated Au_{923} NCs on graphene. (a) The average electron diffraction pattern of 10 FCC Au_{923} NCs on graphene. **(b)** The average electron diffraction pattern of 10 Dh Au_{923} NCs on graphene. The electrons arrive perpendicular to graphene as in the FED experiment. It becomes immediately apparent that the existence of FCC and Dh NCs leads to a significant enhancement of the intensity of the (220) peak compared to the (111).

5.4.2 Theoretical modelling of the experimental diffraction patterns

The comparison of the MD-derived diffraction patterns (**fig. 5.12**) with the experimental diffraction patterns acquired with FED (**fig. 5.2**) is not straightforward. The examined samples have a variety of structures apart from FCC and Dh. This paragraph examines the mechanism of NC binding on graphene in more detail. The aim is to understand which structures can become oriented.

Figure 5.13 shows the diffraction pattern of one Au_{923} NC that was adsorbed on graphene at 300 K and annealed up to 600 K. The initial diffraction pattern of the as-adsorbed NC is shown in red and after annealing with blue. The change in the diffraction pattern is dramatic but this is not due to rotations as described above. In this case the system is insufficiently annealed. When the NC is adsorbed on graphene, few surface adatoms are trapped at the Au/C interface. As a result the NC is tilting and the (111) and (200) peaks at ~0.4 $Å^{-1}$ become intense. As the system is heated up to 600 K, surface diffusion is activated and the few adatoms at the interface are irreversibly removed from that region. In this way surface diffusion lets the NC to acquire its most preferred orientation. In the FED experiment the required annealing is carried out during the preparation of the experiment. Indeed, during this phase the (220) peak was observed to become permanently more intense in less than one second. In the MD simulation the annealing is carried out at 600 K for 1 ns, as mentioned earlier, and every measurement is carried out only after this step.

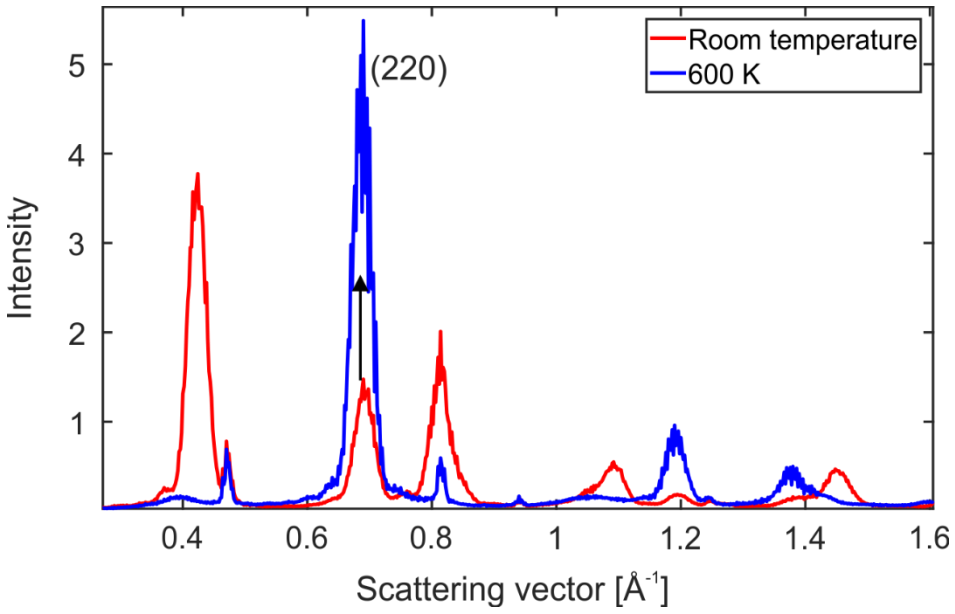

Figure 5.13: A detailed view on NCs orientation on graphene. Au_{923} NCs contain surface imperfections and adatoms that can modify the diffraction pattern. The red curve shows the diffraction pattern of an as-adsorbed Au_{923} FCC NC on graphene at room temperature (MD simulations). Few adatoms prevent the NC from acquiring its (111) orientation and thus the (111) peak is enhanced and the (220) peak is suppressed (the electrons arrive perpendicular to graphene). Thermal annealing up to 600 K causes the diffraction pattern to change (blue curve) by removing trapped Au adatoms from the Au/C interface. More details can be found in the main text.

Surface diffusion is sufficient to restructure well-defined FCC and Dh structures and make them oriented. However, the sample contains in addition very irregular NCs. In this case the required restructuring would be so intense that the maximum temperature should be close to the surface premelting (800 K) or melting (1400 K) point. In the experiment, these irregular structures remain with a nearly random orientation. In order to compare the electron diffraction simulations and the FED experiment we make the assumption that only the well-defined FCC and Dh structures can become oriented and the orientation of all other structures is completely random. The model diffraction pattern is then given by:

$$I_{Model} = a \cdot I_{oriented} + b \cdot I_{Random} + c \cdot I_{Substrate} \ , \qquad \text{R 5.1}$$

where $I_{oriented}$ is the normalized diffraction pattern of FCC and Dh NCs as given be MD and electron diffraction simulations, I_{Random} is the measured diffraction pattern of randomly oriented Au_{923} NCs on a-C and $I_{Substrate}$ is the measured diffraction pattern of the Gr substrate. The mixing coefficients are $(a, b, c) = (0.16, 0.45, 0.39)$. The result is shown in **figure 5.14** (red solid line), together with the experimental diffraction pattern (blue circles). Both diffraction pattern correspond to the equilibrium structure at ~300 K.

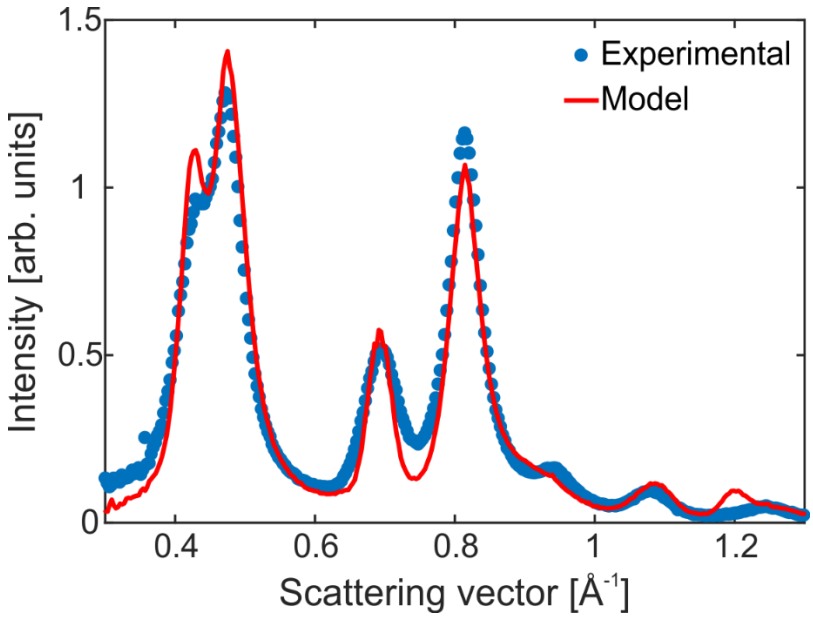

Figure 5.14: Experimental and theoretical electron diffraction pattern of Au_{923} NCs on Gr. The experimental radial average shown with blue circles (see also **figure 5.2** and relevant discussion). The model curve (solid line) corresponds to the MD-simulated FCC and Dh NCs while the rest of the structural allotropes are hypothesized to have completely random orientation as in a-C.

5.4.3 Temperature dependent diffraction patterns

The next step is to examine the temperature-induced changes in the diffraction peaks of the MD structures. **Figure 5.15** shows the relative intensity change ΔI defined as:

$$\Delta I(S) = \frac{I^{600\,K}(S) - I^{300\,K}(S)}{\int I^{300\,K}(S)dS} \quad \text{R 5.2}$$

In **figure 5.15** the electrons arrive either perpendicular to graphene (orange) as in the FED experiment and all preceding simulations, or in powder diffraction mode (blue). The simulated peak dynamics are reproducing all the observables of FED. Lattice heating is causing the peaks to decay and the inelastic background to increase (Debye-Waller effect). In addition, thermal expansion is causing the peaks to shift to lower scattering angles. The most important observation is that the (220) peak shows the strongest decay when the electrons arrive perpendicular to graphene. Thus, the NC librations have definitely an effect on the diffraction pattern when the electron beam is parallel to the initial NC orientation.

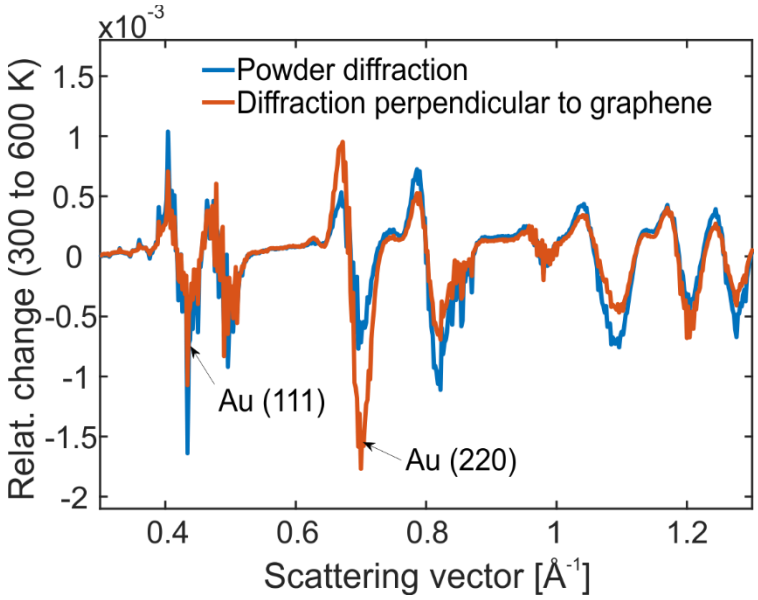

Figure 5.15: Relative changes of electron diffraction patterns caused by heating from 300 K to 600 K. Blue is for powder diffraction and orange for electrons arriving perpendicular to graphene. The decay of the (220) peak becomes more intense in the latter case.

5.4.4 Comparison of experiments and simulations

This section compares the predictions of the MD and electron diffraction simulations with the FED experiment. The relative peak-decay in the theoretical diffraction patterns has been measured for electrons arriving perpendicular to graphene and for powder diffraction. The first type of diffraction is sensitive to the Debye-Waller effect (atomic vibrations) and the NC librations. The second type of diffraction is only sensitive to the Debye-Waller effect (atomic vibrations). The difference between the two peak-decays is plotted as a function of temperature in **figure 5.16.a** for the (220) peak and **figure 5.16.b** for the (111) peak (black squares & lines). For comparison, the two figures also show the deviation from Debye-Waller as measured by FED versus the lattice temperature measured from expansion [circles, blue for (220) and red for (111)]. The simulations predict an additional decay of the (220) peak by ~4% and a smaller decay of the (111) peak by ~1% at 600 K. These theoretical values are in quantitative agreement with the FED experiments (**fig. 5.16**), see also the dynamics in **fig. 5.6**.

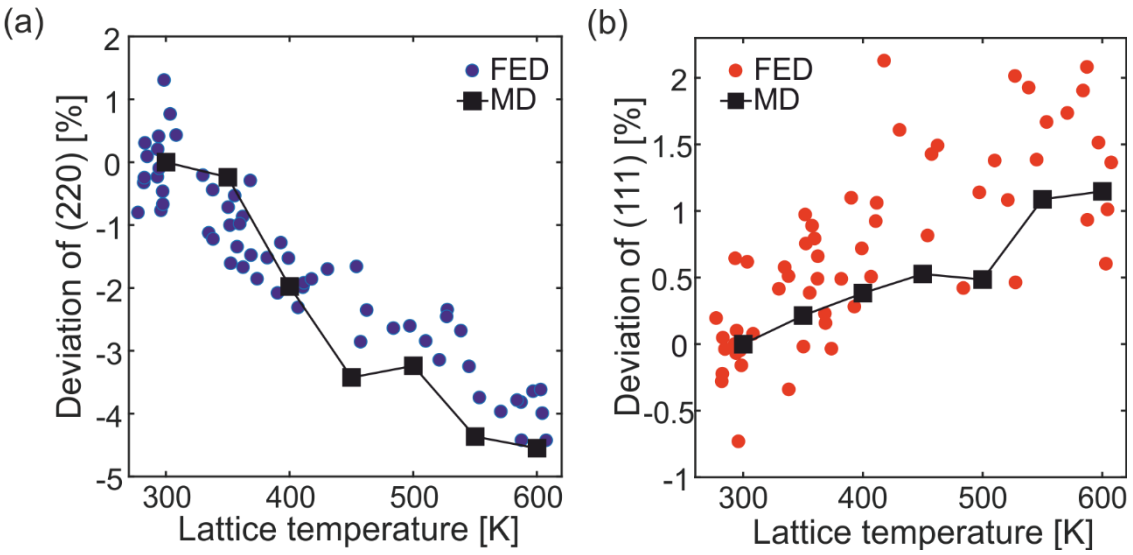

Figure 5.16: Deviation of peak-decay from Debye-Waller dynamics for Au_{923} NCs on Gr. Deviation of the peak decay from the expected Debye-Waller behavior for the (220) and (111) peaks, **(a)&(b)** respectively. The MD simulations are shown with squares connected by lines and the FED data are shown with circles.

In all the above it was shown that librations of NCs and atomic vibrations coevolve and both of them affect the time-dependent diffraction patterns. When the NCs start from an oriented state, as in the case of Au FCC and Dh NCs on graphene, the energy content of

atomic vibrations needs to be found from the observed expansion and not from the Debye-Waller effect. The following two sections examine and compare the energy flow into librations and vibrations. For the energy of atomic vibrations the author retrieves the methods developed in **chapter 3**. The energy content of librations can be found with the aid of MD simulations and basic principles of classical mechanics and statistical physics.

5.5 The role of librations in the ultrafast energy flow

Each NC contains a large number of vibrational degrees of freedom (3×923), 3 translations, 1 rotational degree of freedom with angular momentum vertical to graphene and 2 librations. The NC libration is a type of motion that has been directly observed with FED for the first time in the current work (to the best of the author's knowledge). Atomic vibrations in nanostructures have been examined before with FED (see **Chapter 3** and references therein). The study of ultrafast energy flow in this chapter has some new aspects compared with **Chapter 3**. These new aspects are:

- The equations have been extended to include the strongly coupled optical phonons of graphene (SCOPs).
- The excitation mechanism of the NC librations is now identified.

Due to the equipartition theorem most of the energy is stored in atomic vibrations. For this reason, it is possible to examine first the energy flow to atomic vibrations and ignore temporarily the participation of librations and other NC motions. Section **5.5.1** deals with atomic vibrations and **5.5.2** with librations.

5.5.1 Ultrafast energy flow to atomic vibrations

The energy content of atomic vibrations (effective lattice temperature) is extracted from the observed lattice expansion and the previously measured thermal expansion coefficient of Au_{923} NCs (**Chapter 4**). The lattice temperature evolution is fitted with a model of energy flow similar to that presented in **Chapter 3**. This procedure allows measuring the energy transfer rate from phonons of the Gr substrate to atomic vibrations in the Au_{923} NC. The energy transfer rate from phonons of Gr to NC librations is examined in the

following section. In this way it becomes possible to compare the energetic contributions and dynamics of atomic vibrations and librations of NCs.

The used model of energy flow is shown in **figure 5.17**. Each material (Au_{923} NCs and Gr substrate) is represented by electronic and phononic subsystems. Au is splitted into subsystems as in the simple TTM. Au is a metal with one atom per unit cell so the vibrational lattice excitations correspond solely to acoustic phonons. Because Au is spatially confined it possess, in addition, translational and rotational motions like librations. These motions are noted in the schematic but not included in the equations due to their small overall energetic contribution, as discussed before.

Because graphene is crystalline it is now possible to have a more detailed description for its vibrational degrees of freedom compared to a-C (**chapter 3**) that is lacking long-range order. Graphene has two atoms per unit cell and hence it has optical and acoustic phonons. Optical phonons in graphene are known to be strongly coupled to the electronic degrees of freedom. Electronic excitations can relax by optical phonon emission in sub-picosecond timescales [74], [109], [202]. The excited phonons thermalize with the acoustic phonons in 1-100 ps [109].

Hence, the Gr substrate contains three subsystems: the electrons, the strongly-coupled optical phonons (SCOPs) and the acoustic phonons. The latter constitute the majority of lattice excitations. Acoustic phonons have the highest contribution to the overall heat capacity and for that reason they are denoted as the Gr total lattice. In the schematic of figure **5.17** every arrow represents an energy transfer rate that needs to be specified if it is known, otherwise it is extracted by fitting the experimental lattice temperature evolution.

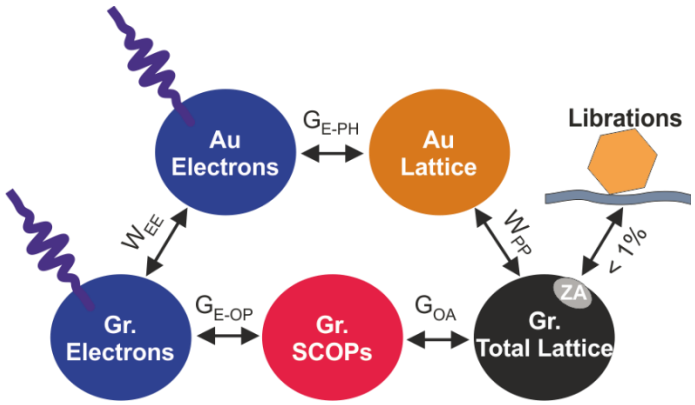

Figure 5.17: Microscopic subsystems and interactions in the Au_{923} NC / Gr heterostructure. Au is splitted into electrons and lattice excitations. In addition Au NCs can librate but the overall energetic contribution is small (see next section). Graphene is represented by electrons, strongly coupled optical phonons and all other lattice degrees of freedom (mostly acoustic phonons in terms of heat capacity). Each material has distinct light-mater interactions and hence the optical absorption can differ in the two layers. The contribution of the NC librations to the overall energy flow is small and hence librations are not included in the corresponding set of differential equations. The NC librations couple to a small fraction of the graphene phonons, the flexural ZA phonons of certain wavelengths (discussed in the next section).

The simple schematic of **figure 5.17** is translated into a system of coupled differential equations of the form:

$$C_E^{Au}\frac{dT_E^{Au}}{dt} = -G_{E-PH}(T_E^{Au} - T_L^{Au}) + W_{EE}(T_E^{Gr} - T_E^{Au}) + S^{Au}(t), \quad \text{R 5.3}$$

$$C_L^{Au}\frac{dT_L^{Au}}{dt} = G_{E-PH}(T_E^{Au} - T_L^{Au}) + W_{PP}(T_L^{Gr} - T_L^{Au}), \quad \text{R 5.4}$$

$$C_E^{Gr}\frac{dT_E^{Gr}}{dt} = -G_{E-Op}\left(T_E^{Gr} - T_{Op}^{Gr}\right) - W_{EE}(T_E^{Gr} - T_E^{Au}) + S^{Gr}(t), \quad \text{R 5.5}$$

$$C_{Op}^{Gr}\frac{dT_{Op}^{Gr}}{dt} = G_{E-Op}\left(T_E^{Gr} - T_{Op}^{Gr}\right) - G_{OA}\left(T_{Op}^{Gr} - T_L^{Gr}\right), \quad \text{R 5.6}$$

$$C_L^{Gr}\frac{dT_L^{Gr}}{dt} = G_{OA}\left(T_{Op}^{Gr} - T_L^{Gr}\right) - W_{PP}(T_L^{Gr} - T_L^{Au}), \quad \text{R 5.7}$$

where T is for temperature, G for intrinsic couplings (within the same material), W for extrinsic couplings (between different materials), C for heat capacities and S for temporal profiles of absorbed laser fluences. The upper indices denote the material and the lower indices denote the subsystems. These equations are used to fit the lattice temperature

evolution. This set of equations depends on many parameters that cannot be fitted simultaneously. However, the intrinsic couplings are known from the investigation of **Chapter 3** and the works of others. The remaining, fitting parameters for this heterostructure are the electronic and vibrational couplings between the two materials W_{EE} and W_{PP}, respectively, and the absorbed fluence in each of the two materials.

For studying energy flow it is essential to know the heat capacity of every subsystem. For the Au_{923} NCs the electronic and vibrational heat capacities are known from the analysis presented in **Chapter 3**. For the simulation of Gr, the author used information from the article of Liu *et al.* [203]. The heat capacity of SCOPs is given by a 3rd order polynomial function of temperature that is based on time-resolved Raman spectroscopy of graphite [204]. The used polynomial dependence applies for temperatures between 500 K and 2500 K. The theoretical temperature range of SCOPs in the current work lies mostly within these limits. Regarding the various coupling constants, the electron-phonon and phonon-phonon coupling of Gr used here can reproduce the temperature evolutions shown in the supplementary information of Liu *et al.* [203].

Figure 5.18 shows the time-dependent temperatures of the electrons, SCOPs and acoustic phonons in graphene (**fig. 5.18.a**), the electrons and the phonons of Au (**fig. 5.18.b**) and the final equilibration between Au NC and Gr substrate after ~200 ps (**fig. 5.18.c**). The orange curve in **figure 5.18.c** needs to match the experimental evolution of the NCs lattice temperature and this is achieved during the nonlinear fitting by tuning the values for the absorbed fluences of each material and the electronic and vibrational coupling constants across the interface.

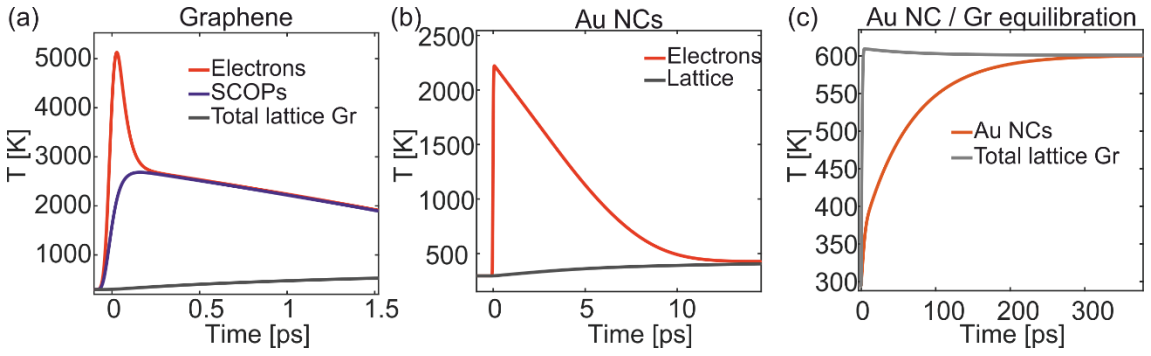

Figure 5.18: Ultrafast evolutions of temperature in the subsystems of the Au_{923}/Gr heterostructure. (a) Electrons, SCOPs and total lattice excitations in the Gr substrate. **(b)** Electron-phonon coupling in Au NCs at short time-delays. **(c)** Equilibration

(vibrational coupling) of the Au NC and Gr substrate lattices at longer time-delays. The orange curve corresponds to the lattice temperature Au NCs and reproduces accurately the experimental evolution of the lattice temperature.

From the evolutions of lattice temperatures for the Au NCs and the graphitic substrate (**figure 5.18.c**) it is clear that the temperature change due to interfacial phonon transmission is much larger for the Au NCs than for the graphitic substrate. This means that the lattice heat capacity of the NCs' layer is smaller than the heat capacity of the substrate by a factor of ~28. The reason for this is that the model takes into account the extra mass of sp^2 C in the substrate, due to the lacey Carbon support of graphene. The lacey Carbon structure is shown in the SEM image of **figure 5.19.a**. The morphology of the entire heterostructure is schematically shown in **figure 5.19.b**. The relative amounts of Au and C in the model are schematically shown in **figure 5.19.c**.

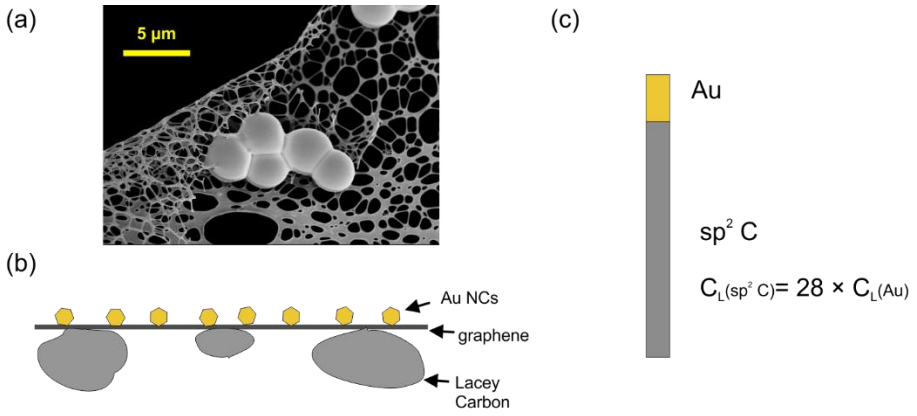

Figure 5.19: Morphology and mass distribution in the Au_{923}/Gr heterostructure. **(a)** The lacey Carbon structure that is used to stabilize graphene. **(b)** Schematic illustration of the morphology of the entire Au_{923}/Gr heterostructure. **(c)** Schematic depiction of the relative amounts of Au and C in the model of ultrafast energy flow.

Figure 5.20 shows the final result of the procedure, the experimental lattice temperature evolution (blue circles), the fitted curve (red solid line) and the residuals of the fitting which are in the order of ±20 K. The fitting suggests that electronic coupling is an order a magnitude smaller than the vibrational coupling and hence it does not seem to play an important role in the equilibration of the two lattices and the dynamics in the 10-500 ps time interval. The vibrational coupling from three measurements and several fittings with different assumptions gives an average value W_{PP}=(14 ± 4) MW/m^{2}K. Moreover, **figure**

5.20 shows the fitting of the effective lattice temperature with a biexponential decay function. The fast time-constant (1-5 ps) is attributed to intrinsic electron-lattice interactions and the slow time-constant is attributed to slow, vibrational coupling. The characteristic time-constant for vibrational coupling 62 ± 4 ps.

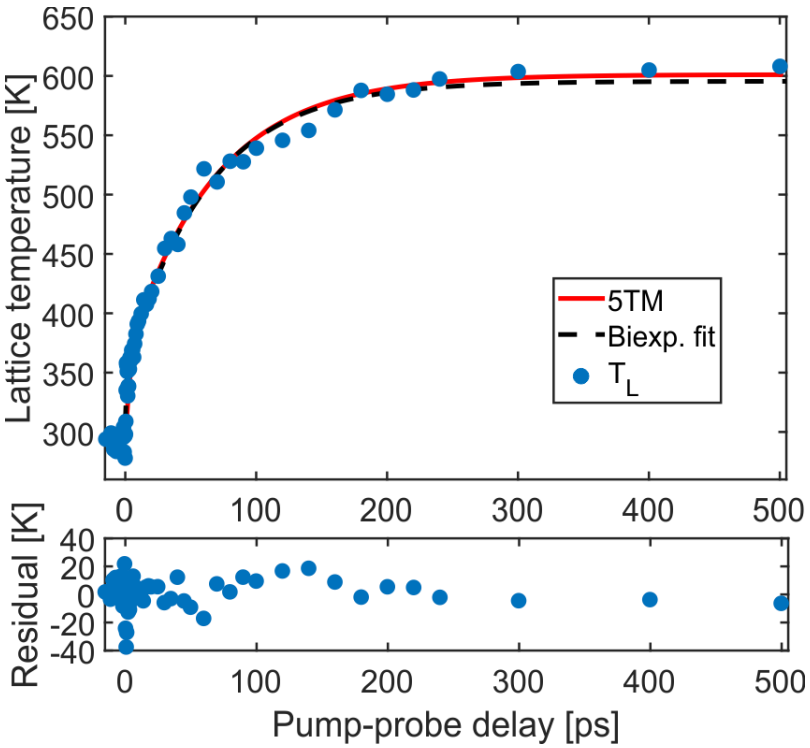

Figure 5.20: Lattice temperature evolution of Au_{923} NCs on Gr and fitting with the model of ultrafast energy flow. The experimental lattice temperature evolution (blue circles) is found from the observed thermal expansion. The lattice temperature of Au NCs predicted by the model of energy flow is shown here with a red curve. The residuals of the fitting are within ± 20 K. The data can also be fitted with a biexponential decay (dashed black line). Based on the biexponential fitting, the characteristic time-constants are τ_1=(4.5 ± 3.4) ps for electron-lattice equilibration, and τ_2=(62 ± 4) ps for vibrational coupling.

The measured energy transfer rate (14 ± 4 MW/m^{2}K) is in good agreement with the theoretical work of Duda *et al.* [205], who found the vibrational coupling at the interface of Au and graphite (// to the c-axis) to be equal with 15 MW/m^{2}K. The work of Schmidt *et al.* [146] measured a vibrational coupling of 25 MW/m^{2}K at the interface of bulk Au and c-oriented graphite using time-resolved thermoreflectance. The interfacial coupling of Au NCs is expected to be reduced compared with closed, Au thin-films because the

contact area is smaller. In addition, the vibrational coupling of Au_{923} NCs and graphene is comparable with the Au_{923} NCs / Si-N heterostructures (16 MW/m^{2}K) and significantly smaller than the Au_{923} NCs / a-C heterostructures (90 MW/m^{2}K). It is possible that a-C substrates have enhanced surface roughness, since they contain flexible strands of C atoms, like wires, nanotubes and graphene segments, and therefore the contact area is higher. Moreover, the amorphous structure might provide a larger phase-space for interfacial phonon transmission compared with the Au (111) / c-axis interface.

A final remark is that the energy transfer rate per NC (ΔE) can be written as $\Delta E = W_{PP} \cdot S \cdot \Delta T$, where S is the graphene area per NC (~38 nm^2) and ΔT is the initial temperature difference before lattice-lattice equilibration (~300 K). The energy transfer rate from phonons of graphene to atomic vibrations of one NC can be re-expressed as $\Delta E \sim 1$ eV/ps. This number is used in the next section to compare the energy flow to atomic vibrations with the energy flow to NC librations.

5.5.2 Ultrafast energy flow to nanocluster librations

This section compares the energetics of atomic vibrations in NCs and NC librations. This is accomplished with the use of: (i) the parabolic approximation, (ii) the angular amplitude from MD, (iii) the angular frequency from MD and (iv) the time-constants from FED. The activation of NC librations requires energy and angular momentum. The energy and the angular momentum come from the acoustic phonons of graphene. The three bands of acoustic phonons of graphene are the flexural ZA phonons, where the atomic vibrations are out-of-plane, and the in-plane longitudinal (LA) and transverse (TA) acoustic phonons. Based on the work of Panizon *et al.* [206], who explored ballistic thermophoresis of NCs on graphene, the graphene phonons that can transfer momentum, and hence angular momentum, to adsorbed NCs are flexural ZA phonons or TA and LA phonons anharmonically coupled to ZA. The energy transfer rate from graphene waves to NC librations is estimated using simple classical mechanics. The analysis begins with a brief description of all NC motions with respect to graphene.

Each NC has a number of translational and rotational degrees of freedom that are depicted in **figure 5.21**. The motion of NCs on graphite or graphene follows a stick-slip pattern that is also known as Lévy flights [63], [207]. The translations in the X-Y plane (parallel to graphene, **fig. 5.21.a**) can have oscillatory character or they can result in a net motion

of the entire NC. The stick-slip motion originates on the dynamic equilibrium between translations and oscillations. Rotations with angular momentum vector normal to graphene (**fig. 5.21.b**) exhibit similar stick-slip behavior (see figure 2.a of Guerra *et al.* [65]).

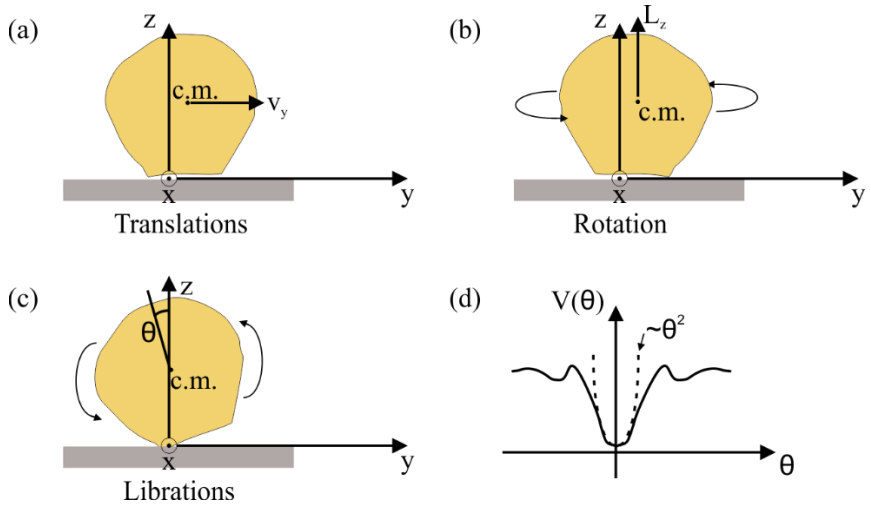

Figure 5.21: The degrees of freedom of supported, rigid NCs. (a) Three translations, here parallel to the Y-axis. (b) Rotation about the Z-axis. (c) Librations, here about the X-axis. (d) Schematic illustration of the parabolic approximation for the unknown, angular potential of librations.

The other NC motions are always oscillatory if the temperature is not sufficient for desorption. These are translations in the Z-axis (normal to graphene) and librations (**fig. 5.21.c**). Librations involve small angular displacements and hence their unknown energy landscape can be approximated with a parabolic function (**fig. 5.21.d**).

Using the parabolic approximation the angular potential of librations is given by:

$$V(\theta) = \frac{1}{2} V_o \theta^2. \qquad \text{R 5.8}$$

The Lagrangian for librations is:

$$L = \frac{1}{2} I \dot{\theta}^2 - \frac{1}{2} V_o \theta^2, \qquad \text{R 5.9}$$

where I is the moment of inertia of the NC. The solution to the corresponding Euler-Lagrange equation is simply:

$$\theta(t) = \theta_o \cos \omega t. \qquad \text{R 5.10}$$

The moment of inertia of the NC (I) and the frequency of librations (ω) are connected with the relationship:

$$\omega = \sqrt{\frac{V_o}{I}} \ . \qquad \text{R 5.11}$$

For Au_{923} we have on average $I = 2.7 \cdot 10^{-40} kg \cdot m^2$. The dominant frequency given by the MD simulations ($f = 57\ GHz$) gives $\omega = 2\pi f = 3.6 \cdot 10^{11}\ s^{-1}$. With this frequency the torque per rad (≡ energy) acting on each NC is:

$$V_o = I\omega^2 \cong 35\ \frac{nN \cdot nm}{rad} \ . \qquad \text{R 5.12}$$

The average tilt angle with respect to graphene is $\langle\theta\rangle = 1.6^o$ at 300 K and $\langle\theta\rangle = 2.0^o$ at 600 K. With these numbers we can calculate the average, rotational kinetic energy from:

$$\langle E_K \rangle = \frac{1}{2}\ I\ \langle\dot{\theta}^2(t)\rangle = \frac{1}{4}\ I\ \langle\theta\rangle^2\omega^2 \ , \qquad \text{R 5.13}$$

where an additional factor $1/2$ comes from the time-average of $\sin^2 \omega t$. The average (kinetic or potential) energy is 40 meV at 300 K and 70 meV at 600 K per NC.

The excess energy of librations (30 meV/NC) is transferred to the NCs by a biexponential process as measured by FED. The time-constants measured from the (220) peak are approximately τ_1~4 ps (40% amplitude) and τ_2~110 ps (60% amplitude). The corresponding energy transfer rates are in the order of 3 meV/ps and 0.2 meV/ps. Dynamics that involve more than one energy transfer rate might arise from the timescales of generation and thermalization of acoustic phonons in graphene that occurs in the 100 ps timescale [109]. The energy transfer rate to atomic vibrations is ~1 eV/ps, meaning three orders of magnitude higher than for librations. This is to be expected since only a small fraction of graphene phonons can exert torque and transfer angular momentum to the NCs.

For the ultrafast energy flow it is also important to examine the absorption cross section of the NCs. The lattice heat capacity for Au is $C_L = 2.5 \cdot 10^6\ Jm^{-3}K^{-1}$ (only atomic vibrations). A temperature difference $\Delta T = 300\ K$ corresponds to an energy input:

$$\Delta E = \Delta T \cdot C_L \cdot \frac{4}{3}\pi R^3 = 66\ eV \ . \qquad \text{R 5.14}$$

This energy, stored in atomic vibrations, is much larger than the energy of librations. The excess energy of atomic vibrations corresponds to absorption of ~20 photons (400 nm)

per NC. The incident laser fluence is 3.8 mJ/cm^2, meaning $3 \cdot 10^3$ photons per NC. The absorbed energy that ends in the NCs' lattices is in the order of 0.7% (with respect to the incident laser pulse) and the absorption of the entire heterostructure (including the lacey Carbon support, see **fig. 5.19**) is ~20%.

Excitation mechanism of NC librations. The scattering cross section is more efficient when the phonon wavelength is similar with the characteristic length of the NC binding facet. The average binding facet of Au_{923} (for FCC and Dh NCs) is 2.6 nm. Another important criterion can be frequency matching. For flexural ZA phonons the dispersion relationship has the form $\omega(k) \sim ak^2$ where $a = 6.2 \cdot 10^{-7}\, m^2/s$ [208], [209]. The frequency of librations from the simulations is 57 GHz which for graphene translates into a wavelength of 8.3 nm. In summary, the graphene phonons that couple with NC librations have wavelengths in the range of 2-8 nm and flexural ZA character.

Future prospects. Librations and other rotational and translational motions are important for energy and mass transport involving nanoscale building blocks on surfaces. For instance, Guerra *et al*. [65] has shown the translations and rotations of NCs are coupled. Rotations can transiently decrease the adherence to the substrate and at this moment the NC can translate giving rise to the stick-slip pattern of motion.

In principle all rotational degrees of freedom of supported nanocrystals should be visible by FED providing that the system starts from an oriented state. For instance, rotational motions with angular momentum normal to the substrate could be observed if the equilibrium state of the system would be characterized by epitaxial order. In addition, FED can probe nonequilibrium phonon populations in the substrate. Some examples are the works of [109] and [94]. From all the above, an interesting, future prospect is the combined study of nanoscale adsorbate motions and phonon dynamics in the substrate.

Having access simultaneously to atomic vibrations and rotational motions of nanostructures at ultrafast timescales is important for a detail understanding of morphological changes in functional, nanoscale heterostructures. On the one hand, atomic vibrations of nanostructures with large surface-to-volume ratio, are precursor states to diffusing surface adatoms. On the other hand, collective lattice motions, like librations, are precursor states to diffusion, aggregation or desorption of entire nanoclusters. The well-known phenomenon of sintering is a deleterious effect of nano-catalysts and

proceeds with diffusion of adatoms (relevant with **Chapter 4**) but also with migration of small clusters [60] (relevant with **Chapter 5**).

Chapter 6. Energy flow in 2D metal / 2D semiconductor heterostructures

The previous chapters have examined the ultrafast dynamics of 0D metals (Au_{923} NCs) on 2D materials of zero band gap (graphene) as well as 0D metals on insulators (ultrathin films of Si-N). The present chapter is devoted to the study of quasi two-dimensional Au islands (2D metal) on single-crystalline, layered WSe_2 (2D semiconductor). The heterostructure is synthesized by exfoliation of multilayer flakes of WSe_2 and subsequent deposition of Au in an electron beam evaporator. Static electron diffraction shows that Au is growing epitaxially on WSe_2, opening up the way for many interesting experiments that probe the nonequilibrium structure of the lattice and the electrons in reciprocal space. The nanoscale morphology, optical properties and electronic structure of Au on WSe_2 are characterized by transmission electron microscopy, optical spectroscopy and static angle-resolved photoelectron spectroscopy (ARPES), respectively. Next, the samples are used for time-resolved FED experiments with various photon energies for excitation. When the photon energy is lower than the optical gap, the electronic excitation of WSe_2 is mediated by the Au nanostructures. The FED investigations of the ultrafast lattice dynamics of Au / WSe_2 heterostructures are complemented by time- and angle-resolved photoelectron spectroscopy (tr-ARPES), which probes the ultrafast electronic dynamics. The experimental findings of both techniques demonstrate an acceleration of electron-lattice equilibration in WSe_2 when its surface is decorated by Au nanostructures.

6.1 Static properties and ultrafast dynamics of pure WSe_2

6.1.1 Transition metal dichalcogenides

The semiconducting compound WSe_2 belongs to the family of the so-called transition metal dichalcogenides (TMDCs). TMDCs are indirect band-gap semiconductors with covalently-bonded, two-dimensional atomic layers stacked together by weaker van der Waals interactions. Some examples of TMDCs are WSe_2 (present work), MoS_2, $MoSe_2$ and WS_2. The atoms in each layer of TMDCs have a hexagonal arrangement and for this

reason they are termed graphene-like semiconductors. Contrary to graphene, which is a zero band-gap material, the TMDCs are semiconducting and, thus, more appropriate for the construction of nanoscale, electronic devices [210]. Due to their weak, interlayer bonding, thin flakes of TMDCs can be exfoliated down to single unit cell thickness. As the thickness of TMDCs is decreasing, their electronic properties change and their indirect band-gap can turn to direct in single layers [210]. Layers of different TMDCs and other two-dimensional materials like metallic graphene and insulating hBN (hexagonal Boron-Nitride), can be stacked vertically with Van der Waals interactions [211], [212] in order to construct ultrathin transistors and other nanoelectronic devices. This work is devoted to multilayer WSe_2 that preserves the well-known electronic structure of the bulk material. The next section discusses the electronic and lattice dynamics of pure WSe_2 based on recent works.

6.1.2 Nonequilibrium properties of pure WSe_2

The electronic and lattice dynamics of pure WSe_2 have been the subject of many recent experimental and theoretical works. The various scattering processes in the electronic subsystem of WSe_2 have been studied with time- and angle-resolved photoemission (tr-ARPES) by Bertoni *et al*. [213] and Puppin *et al*. [27], [214]. These measurements were mostly sensitive to the first, surface trilayer due to the limited escape depth of photoelectrons. Owning to this surface sensitivity, the researchers managed to demonstrate spin-, valley- and layer-polarization of laser-induced electronic excitations. The photon energies of the pump pulses were in resonance with the lowest excitonic transition, called the A-exciton [215], located at an energy of 1.63 eV.

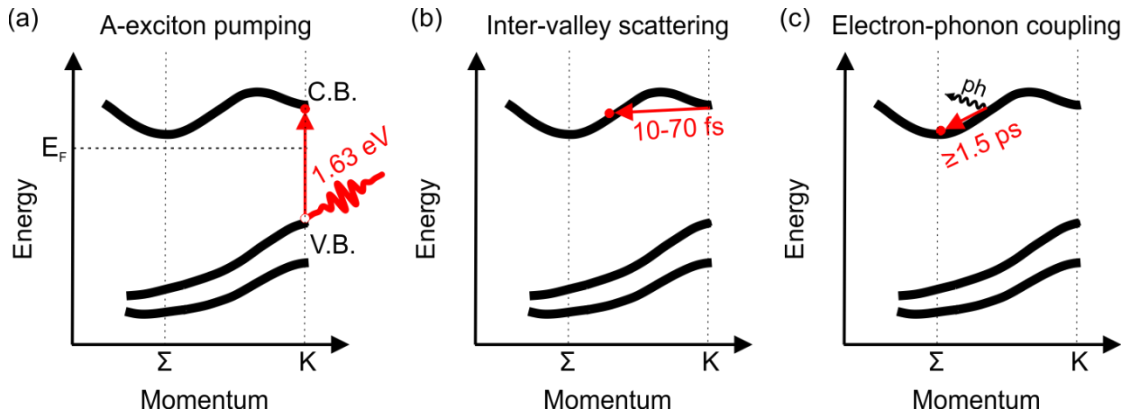

Figure 6.1: Electron-lattice nonequilibrium states for bare WSe_2 pumped at the A-exciton resonance. (a) Irradiation with photons of 1.63 eV energy (760 nm wavelength) result in the formation of the so-called A excitons that involve a hole at the top of the valence band and an excited electron at the local minimum of the conduction band at the K point of the Brillouin zone. **(b)** The bright A exciton scatters from the K towards the Σ valley within 10s of fs. **(c)** The relaxation of excited electrons at the global minimum of the valence band occurs with electron-phonon coupling in 1.5 ps or more. This picture is based on the works of Bertoni *et al.* [213], Puppin *et al.* [27], [214] and Waldecker *et al.* [94].

The resulting electronic transitions occur at the K-point of the Brillouin zone, and elevate electrons from the top of the valence band to the local minimum of the conduction band (**fig. 6.1.a**). The global minimum of the conduction band is in the Σ-point of the Brillouin zone. The excited electrons scatter away from K and towards Σ within 10s of fs (**fig. 6.1.b**). Finally, the electrons relax in the conduction band minimum at Σ through electron-phonon coupling (**fig. 6.1.c**). More details on the electronic band structure of WSe_2 and Au/ WSe_2 are given in the section that follows.

The final electron-lattice relaxation due to hot electrons at the Σ-valley has been investigated with FED by Waldecker *et al.* [94]. In this experiment the excitation was carried out with photons of 1.55 eV energy (800 nm wavelength). The pump spectrum had a significant overlap with the A-exciton resonance. The incident laser fluence was 7 mJ/cm^2. Under these conditions, the effective atomic MSD is first increasing, with a time-constant of 1.83±0.13 ps, reaching a maximum value of ~$4 \cdot 10^{-3}$ Å^2 at about 5-10 ps, and then relaxes at ~$3.5 \cdot 10^{-3}$ Å^2 with a time-constant of 19±5 ps. The initial increase is due to electron-lattice equilibration and the subsequent, smaller decrease is due to thermalization of the lattice degrees of freedom by phonon-phonon interactions. The ultrafast evolution

of nonequilibrium phonons have been probed by a momentum-resolved analysis of the inelastic background of the diffraction patterns.

The author of the present work has conducted additional FED experiments on pure WSe_2. The experimental results are shown in **figure 6.2** and they are in agreement with the work of Waldecker *et al.* [94]. The sample is irradiated with photons of 1.62 eV energy (765 nm wavelength) in order to pump the A-exciton resonance. The incident fluence is 8 mJ/cm^2.

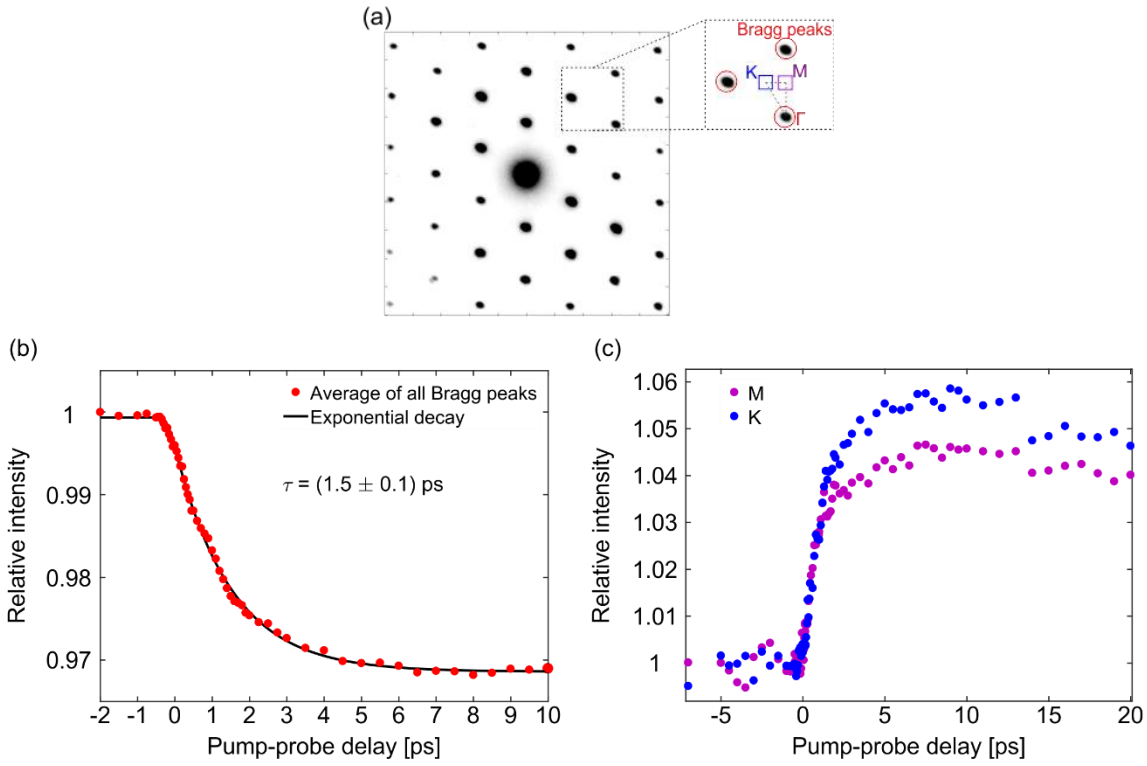

Figure 6.2: FED measurements of pure WSe_2 pumped at the A-exciton resonance. **(a)** The hexagonal electron diffraction pattern of pure WSe_2. The inset shows the first Brillouin zone, which is used for a momentum-resolved analysis of the phonon dynamics. **(b)** The Debye-Waller dynamics of the Bragg peaks after photoexcitation (red circles). The black line is a fit with an exponential decay. The extracted time-constant is 1.5 ps. **(c)** The population of the K-point phonons overshoots at about 5-10 ps, while the difference with the M-point phonons is gradually restored at later pump-probe delays. The rise times of the phonon populations are (1.2 ± 0.2) ps and (1.0 ± 0.1) ps for the K and M phonons, respectively.

The hexagonal electron diffraction of pure WSe_2 is shown in **figure 6.2.a**. The inset shows the various points of the Brillouin zone relatively to the Bragg peaks. **Figure 6.2.b**

shows the pump-probe dynamics of the intensity of the Bragg peaks. The excited charge carriers generate phonons that cause a decay of the intensity of Bragg peaks according to the Debye-Waller effect. Simultaneously, the inelastic scattering background is increasing, as shown in **figure 6.2.c**. The diffracted electrons can scatter from phonons in the sample and exchange momentum, thus, a momentum-resolved analysis of the inelastic scattering background can resolve the momentum-resolved, nonthermal phonon dynamics. As shown in **figure 6.2.c** (and in the work of Waldecker *et al*. [94]) the phonon population in the K-point is clearly higher than in the M-point at ~10 ps. Fitting with single exponentials the initial rise gives characteristic time-constants for the enhancement of the phonon populations of (1.2 ± 0.2) ps and (1.0 ± 0.1) ps for the K and M points of the Brillouin zone, respectively. At later pump-probe delays the differences between the two phonon populations are gradually removed.

6.1.3 Interaction of WSe_2 with Au

The interaction of chalcogens and chalcogenides with Au nanostructures is a very interesting and open subject regarding the ground-state [216] as well as the nonequilibrium [217] properties of such systems. Heterostructures of nanostructured Au and TMDCs are very promising materials regarding their light-matter interactions. Wang *et al*. [44] have shown a 20,000-fold enhancement of photoluminescence from WSe_2 flakes suspended on 20-nm gaps of a Au substrate. Kleemann *et al*. have demonstrated highly-nonlinear excitonic transitions in WSe_2 flakes embedded in Au plasmonic nanocavities [218]. Wang *et al*. have investigated similar phenomena in heterostructures of monolayer WS_2 and Au nanotriangles [219]. Heterostructures of WSe_2 and Au nanoparticles can also be used for surface-enhanced Raman scattering [220], [221] with potential applications in chemical sensors. Moreover, the use of ultrathin semiconductors in nanoscale transistors and optoelectronic devices will most probably involve the attachment of some metallic electrodes, for instance ultrathin films of Au, on the TMDC surface [222]. For that purpose, the interface between Au and TMDCs has been extensively studied by various techniques in close-to-equilibrium conditions [223], [224].

In the present work, the addressed question is how electrons and phonons interact within each component and across the interface in nano-metal / TMDC heterostructures. Previous works have shown that Au and Ag can grow epitaxially on WSe_2 without the

need of strict requirements regarding temperature or deposition rates [225]. Epitaxy of metals at room temperature have also been shown for MoS_2 [226]. In reverse, Au can also serve as a substrate for the epitaxial growth of MoS_2 nanoislands [227]. The adhesion of Au on MoS_2 might be enhanced by the formation of strong Au-S bonds [228]. In line with this possibility, a surface layer of Au can facilitate the exfoliation of single layers of MoS_2 [229]. The chalcogen elements (S, Se and Te) are some of the few materials that can form chemical bonds with Au and the nature of the chalcogen / Au interfacial bonding is a very interesting and open subject [216].

6.2 Synthesis and characterization of Au / WSe_2 heterostructures

6.2.1 Static electron diffraction

For the present experiments, single crystals of WSe_2 have been mechanically exfoliated into flakes with thicknesses of 10-30 nm based on their optical absorption. Exfoliation is carried out with the viscoelastic stamping technique [230]. The followed procedures are described in detail in the Master thesis of D. Zahn [231]. The exfoliated flakes have been transferred on TEM grids (Cu) and covered with Au on their one side using an electron beam evaporator. The nominal thickness of Au was 2 nm and the deposition rate was 2.2 Å/min. Finally, these samples have been examined by FED. Typical static diffraction patterns are shown in **figure 6.3**.

Single-crystalline WSe_2 flakes has hexagonal diffraction pattern. A second family of hexagonal spots, of weaker intensity and identical orientation, belongs to epitaxially grown Au. The most intense peak of Au is shown in the zoom-in insets and it corresponds to the (220) peak. The neighboring peak of WSe_2 is the (110). The (220) peak of Au is more intense than the (111) of Au in accordance with the (111)-orientation of Au crystallites on WSe_2. A weak hexagonal pattern appears close to the Bragg peaks of Au and WSe_2 due to secondary scattering. These superlattice-peaks are also termed the Moiré pattern. The time-resolved experiments have been carried out in the thinnest areas of the flakes and where the epitaxial order appeared to be complete.

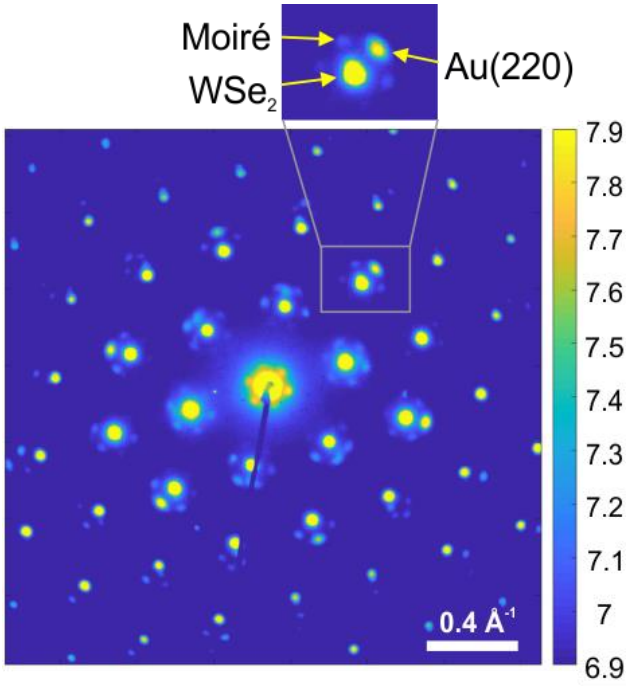

Figure 6.3: Static diffraction patterns of Au / WSe_2 heterostructures measured by the FED setup and plotted in logarithmic scale. The brightest hexagonal pattern is the diffraction pattern of single-crystalline WSe_2. The weaker hexagonal pattern is the diffraction pattern of epitaxial Au. The zoon-in inset shows the (220) peak of Au, which is the most intense, and the neighboring peak of WSe_2. A third family of hexagonal spots appears close to the Bragg peaks the so-called Moiré pattern, which is associated with secondary scattering involving both crystal structures. The diffraction pattern proves that the growth of Au on WSe_2 is epitaxial and with (111) orientation.

6.2.2 Characterization with transmission electron microscopy

For a more detailed knowledge of the morphology of Au / WSe_2 heterostructures, the same samples have been examined by TEM. Some of the recorded images are shown in **figure 6.4**. The Au overlayer is always observed to form islands, which can be seen as regions of higher contrast in **figure 6.4.a**. At this coverage Au grows islands instead of extended, closed films due to surface tension. The characteristic, lateral dimension of the Au islands is 10±3 nm based on the image in **figure 6.4.b**. The estimated average thickness of these islands (different than the nominal thickness, which is 2 nm) is in the order of 4-4.5 nm, meaning that 40-50% of the surface is covered by Au. The islands have dark, strip-like patterns with a periodicity of 1.09 ± 0.05 nm (**fig. 6.4.c)**.

Based on their long, spatial periodicity, the dark stripes are interpreted as the so-called Moiré fringes [232]. In general, the Moiré pattern of two hexagonal crystals has hexagonal symmetry [233] but linear structures can also arise if the sample is slightly tilted [232]. Interestingly, the Moiré fringes are also visible in the vicinity of the islands, although their contrast is weaker (**fig. 6.4.d)**. A potential explanation is that the crystal order of the last few layers of WSe_2 is altered in the presence of Au.

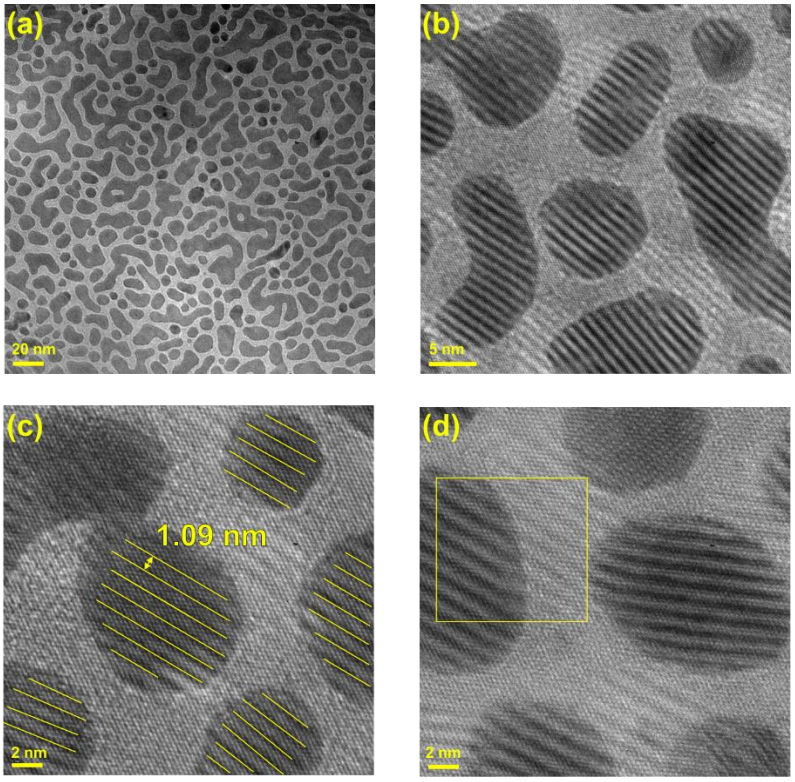

Figure 6.4: Transmission electron microscopy of Au nano-islands on WSe_2. (a) Low magnification TEM image showing Au islands on the surface of WSe_2. **(b)** High magnification image that was used to estimate the coverage of Au and the average dimension of the islands. **(c)** TEM image showing the dark stripes (Moiré fringes) and the lines that were used to measure their spatial periodicity. **(d)** An image showing the Moiré fringes on the islands and on the neighboring, uncovered areas of WSe_2. *TEM measurements carried out by Dr. Emerson Coy (NBMC Poznan).*

To ensure that the sample remains unaffected by the laser fluences used in the FED experiment (≤ 3 mJ/cm^2), the irradiated and non-irradiated areas of the sample have been examined by TEM and electron diffraction. The results are shown in **figure 6.5**. The irradiated areas have been indicated with optical microscopy images and real-space, electron images acquired during the FED experiments. A close inspection of the TEM

images (**fig. 6.5.a** and **6.5.c**) and the electron diffraction patterns (**fig. 6.5.b** and **6.5.d**) did not reveal any discernible changes.

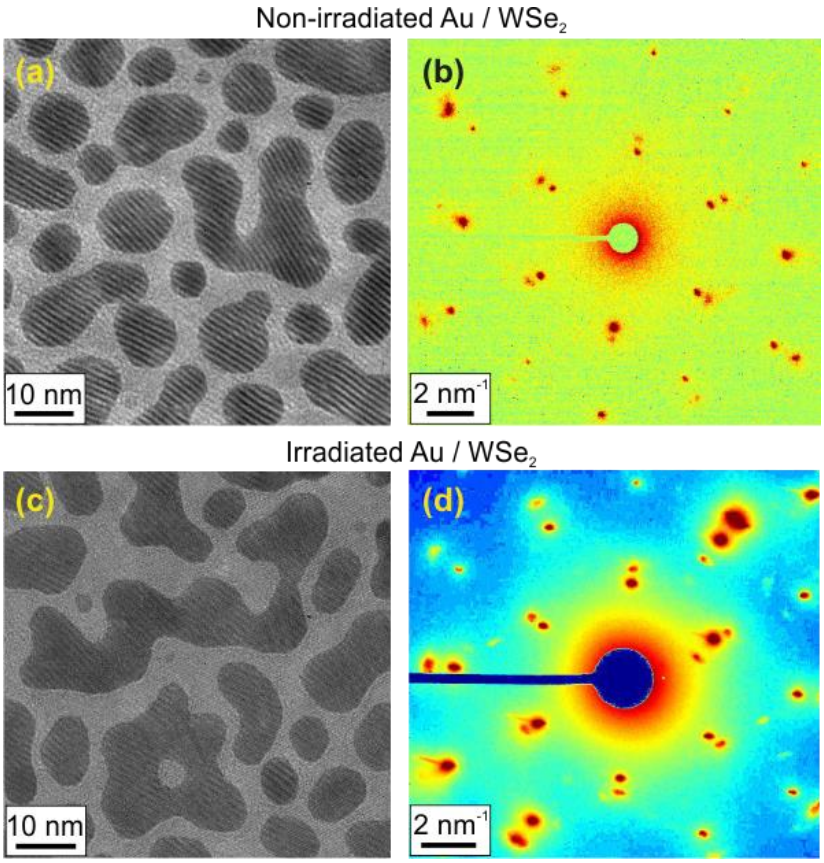

Figure 6.5: Transmission electron microscopy and diffraction of irradiated and non-irradiated areas. (a) & **(b)** Electron microscopy and diffraction of non-irradiated areas. **(c)** & **(d)** Electron microscopy and diffraction of irradiated areas with fluences up to ~3 mJ/cm^2 using 840 nm radiation.

6.2.3 Momentum-resolved mapping of the electronic structure

In order to design and carry out a meaningful, laser-based experiment, like FED, it is useful to know the electronic structure and optical absorption of the investigated sample at near-equilibrium conditions. The electronic structure has been examined using ARPES. The measurements were carried out by Maciej Dendzik, Sang Eun Lee and Laurenz Rettig (Dynamics of Correlated Materials, PC department, Fritz Haber Institute).

Briefly, in the ARPES experiment the smooth surface of a single crystal of WSe_2 is decorated with Au. A hemispherical analyzer is measuring the kinetic energy (E_K) and the angle (θ) of the photoemitted electrons. The crystal momentum of the electrons parallel to the surface ($k_{//}$) is then given by:

$$k_{//} = \sqrt{2mE_K}\sin\theta\,, \qquad \text{R 6.1}$$

and their binding energy (E_B) by:

$$E_B = \hbar\omega - E_K - W \qquad \text{R 6.2}$$

where W is the work function that depends on the material and some experimental conditions.

The measured quantities E_B and $k_{//}$ give the band structure of the material. The results for Au / WSe_2 are shown in **figure 6.6**. The inset shows the area of the band structure that determines the electrical properties of the sample. On the one hand, the intense band, which is nearly 1 eV below the Fermi level, is the highest point of the conduction band of WSe_2. Most of the excitation of WSe_2 begins at this point when the sample is illuminated with near-band gap photons. On the other hand, the weak band that is crossing the Fermi level is the 6sp band of Au. DFT calculations performed by Dr. Maciej Dendzik were used to identify more spectral features of the sample's valence band. For instance, the signal between -2.5 and -3 eV and at high momenta ($k_{//} > 1$ Å^{-1}) is due to the 5d states of Au. A weak feature at the Γ point ($k_{//} \approx 0$) and down to -0.5 eV is a surface state of Au. Finally, the upper band of WSe_2 has a replica of lower energy by 0.5 eV due to spin-obit coupling [234].

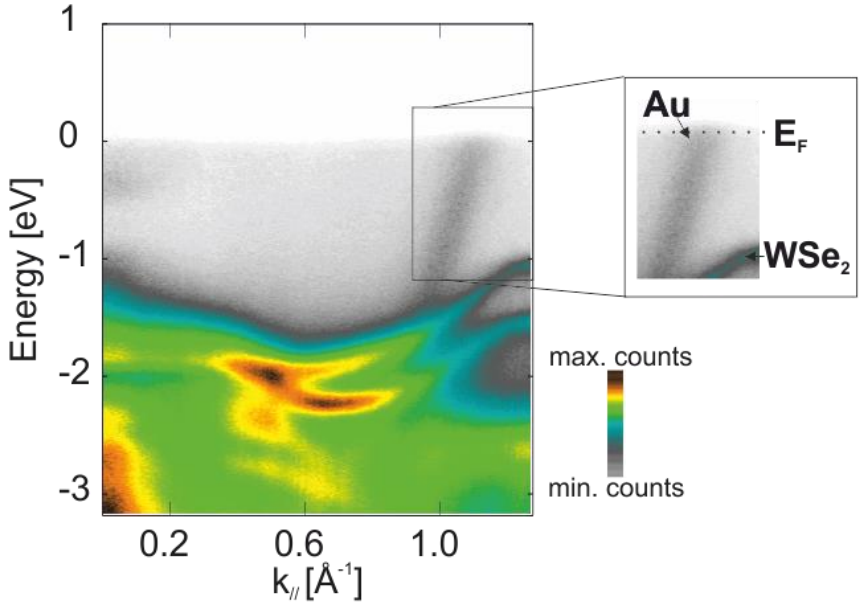

Figure 6.6: Electronic band structure of Au / WSe_2 heterostructures (second derivative plot) measured with static ARPES. The inset shows the valence band maximum of WSe_2 and the sp states of Au that cross the Fermi level. *In collaboration with Dr. Maciej Dendzik, Sang Eun Lee and Dr. Laurenz Rettig (PC dep. FHI, Berlin).*

6.2.4 Optical properties of pure and Au-decorated WSe_2

Due to the pronounced existence of Au states in the band structure, it is expected that the optical absorption of the Au / WSe_2 sample is modified compared to bare WSe_2. For this reason the author of this study has collaborated with the group of Prof. Dr. Stephanie Reich (Freie Universität, Berlin) to measure optical absorption in an appropriate optical setup. The measurements have been carried out together with Niclas Müller and Yu Okamura.

The setup uses the radiation emerging from a white-light laser source and two 100x objectives for focusing light on the sample and collecting the reflected and the transmitted part of the radiation. Reference spectra are taken either on a silver mirror for the reflection geometry, or on neighboring empty windows of the TEM grid for the transmission geometry. Knowing the spectrum of the white-light source allows for an accurate determination of the percentages of transmission (T in %), reflection (R in %) and absorption (A=100-T-R) at each wavelength.

The investigated Au / WSe_2 samples are prepared in the same way as in the FED experiments. An ultrathin flake of WSe_2 is supported on a TEM grid and a certain spot on its surface (selected with an optical camera) is used to measure the absorption spectrum (or absorbance) of pure WSe_2. Subsequently, the surface of WSe_2 is covered with 2 nm of Au and the measurements are repeated on the same spot of the sample. The absorption spectra of pure WSe_2 and Au / WSe_2 are shown in the upper diagram of **figure 6.7** with blue and orange solid lines, respectively. The lower diagram of **figure 6.7** shows the modification of the absorption spectrum induced by Au. The absorption of WSe_2 is enhanced by 2-5% apart from the A-exciton resonance peak that is decreased by 4%.

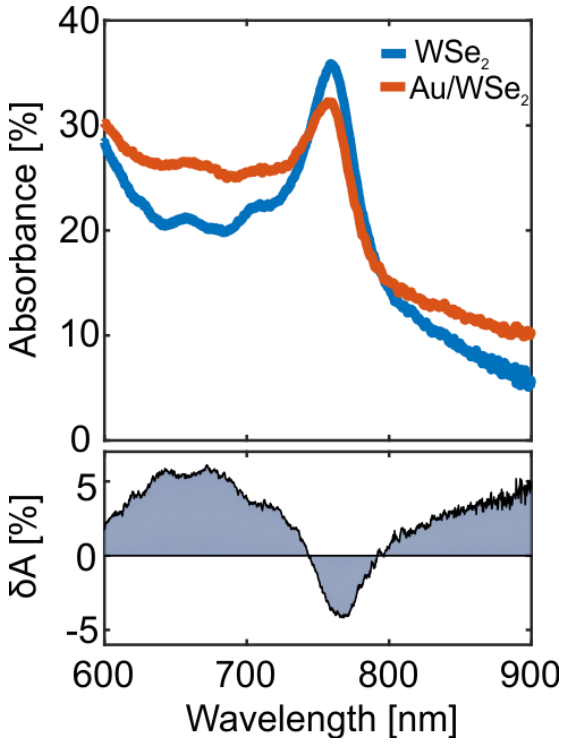

Figure 6.7: Linear absorbance of bare WSe_2 and Au / WSe_2 heterostructures. Upper diagram: Absorbance of bare WSe_2 (red solid line) and Au / WSe_2 (blue solid line) heterostructures. Both measurements correspond to the same flake and approximately the same spot. **Lower diagram:** The difference in the absorption spectrum induced by the deposition of Au. The absorption of WSe_2 is enhanced by 2-5% apart from the A-exciton resonance peak that is decreased by 4%. *In collaboration with the group of Prof. Stephanie Reich, Niclas Müller and Yu Okamura (FU Berlin).*

6.3 Lattice response of Au-decorated WSe_2 to various photon energies

The following sections present FED experiments with Au / WSe_2 heterostructures. The photon energy of the pump pulse has been tuned to match the A-exciton resonance and the enhanced absorption region within the optical gap (see **figure 6.7**). The spectra for pumping are shown in **figure 6.8** together with the absorption spectrum of Au / WSe_2 heterostructures for comparison. The central wavelengths are 760 nm (red line) and 840 nm (dark magenta line). The conversion of the 800 nm radiation of the amplifier laser system to these photon energies is carried out with nonlinear optics that are discussed in **section 2.1.1**. The 760 nm radiation pumps the A-exciton, while the 840 nm excites the electrons into the optical gap of pure WSe_2.

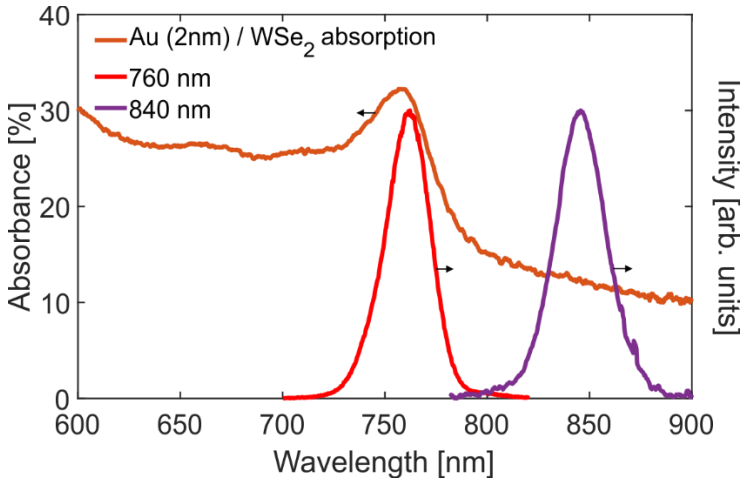

Figure 6.8: Absorption spectrum Au / WSe_2 and pump spectra for FED experiments. Absorbance Au / WSe_2 heterostructures (orange solid line), pump spectrum with 760 nm central wavelength (red solid line) and pump spectrum with 840 nm central wavelength (dark magenta solid line).

6.3.1 Structural dynamics in response to the A exciton

The surface of WSe_2 has been decorated with Au nano-islands of 2 nm nominal thickness. The pump photon energies have been tuned with a TOPAS in order to much the A-exciton resonance as determined by optical measurements on pure WSe_2. The spectrum is shown in **figure 6.8** (red curve). The central wavelength corresponds to a photon energy of 1.62 eV. The incident laser fluence – for this measurement and for all measurements presented at later sections – have been accurately determined by opening the UHV chamber and measuring the spot profile and the incident laser power at the exact, sample position. For the A-exciton pumping, the incident laser fluence was 2.4 mJ/cm^2. In all experiments the photons used for pumping arrive from the side of Au.

The ultrafast lattice heating of the heterostructure is studied by means of the Debye-Waller effect. The atomic MSD of Au has been derived from the peak decay as described in **Chapter 3**. However, for WSe_2 the situation is more complicated. Oppositely to elemental materials, which have a single Debye-Waller factor, compounds have one Debye-Waller factor per type of atom [95]. In addition, the Debye-Waller factor is considered an isotropic quantity for Au, but for WSe_2 it is expected to depend on the crystallographic direction due to the highly anisotropic bonding network (strong in-plane bonding and weak out-of-plane bonding). For simplicity, the peak decays of WSe_2 are

translated into an effective MSD based on the Debye-Waller relationship as in the work of Waldecker *et al*. [94]. This effective MSD represents the uncertainty in the position of the crystal's basis but not the MSDs of the individual W and Se atoms.

The effective MSD is shown in **figure 6.9.a** for Au and **figure 6.9.b** for WSe_2. The MSD of Au is initially rising, reaching a maximum value of about $2\text{-}3\times10^{-2}$ Å at approximately 20 ps, and finally dropping with a time constant of ~50 ps to ~1×10^{-2} Å. The signal-to-noise ratio of Au is low because all its diffraction peaks are significantly weaker in intensity than the peaks of WSe_2. The blue solid curve in **figure 6.9.a** is a biexponential fit that gives a time-constant for the initial rise of (9.8 ± 1.5) ps. Fitting only the (220) peak of Au (its most intense peak) gives a time-constant for the initial rise of (7 ± 1) ps for the Debye-Waller decay and for the lattice expansion of Au nanoislands. An important observation is that the initial rise of the MSD of Au nanoislands on WSe_2 is slower than other Au nanostructures as well as bulk Au films, where the electron-phonon equilibration has a characteristic time-constant of 4-6 ps (**Chapter 3**).

The effective MSD of WSe_2 (orange circles in **figure 6.9.b**) is fitted with a biexponential decay function (red solid line). The MSD is initially rising by $(4.5 \pm 0.2) \cdot 10^{-3}$ Å^2 with a time-constant $\tau_1 = (1.0 \pm 0.2)\, ps$. This time-constant for electron-lattice equilibration is shorter than for pure WSe_2 pumped at the A exciton resonance ($\geq 1.5\, ps$). At longer timescales the effective MSD exhibits an additional rise by $(2.8 \pm 0.2) \cdot 10^{-3}$ Å^2 with a time-constant $\tau_2 = (50 \pm 12)\, ps$. This additional rise at longer pump-probe delays suggests that in Au / WSe_2 heterostructures there is additional energy transfer from Au towards WSe_2, in order to achieve complete thermodynamic equilibrium. The time-constant τ_2 is in the typical range for interfacial energy transfer by phonon transmission, as shown now.

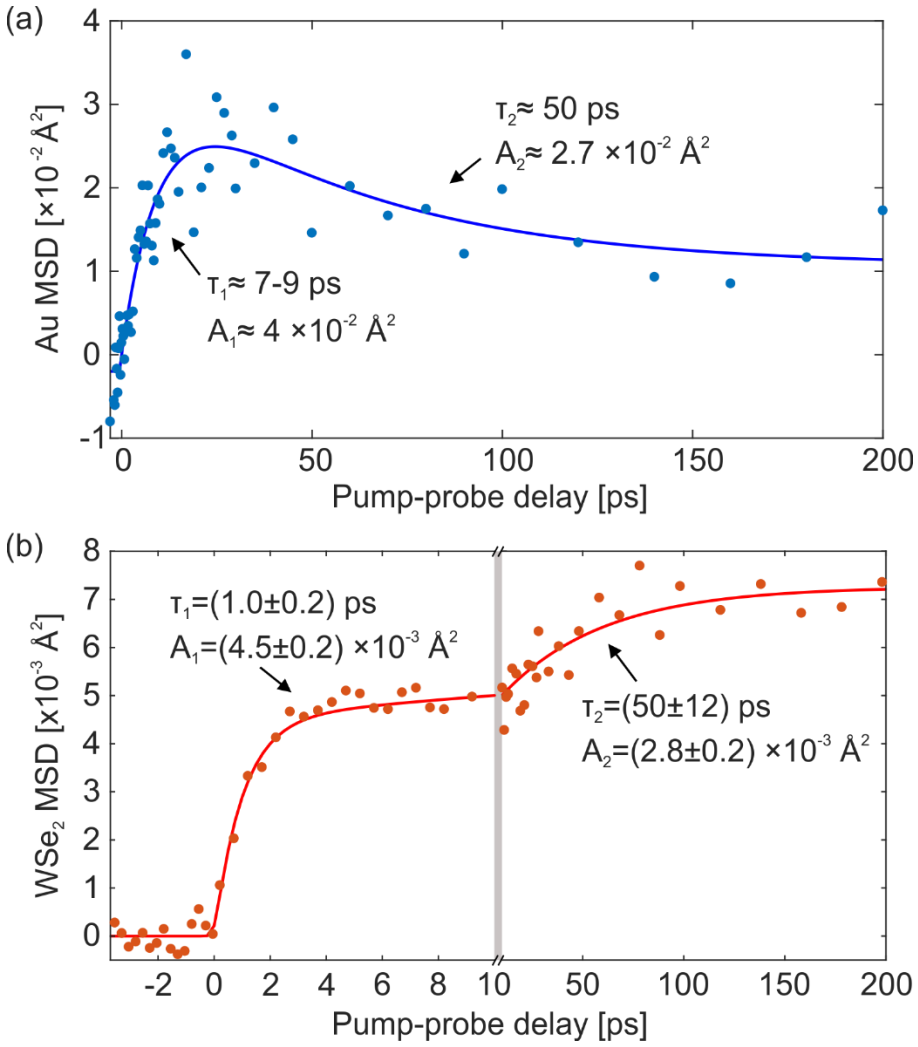

Figure 6.9: Ultrafast evolution of the MSD of Au and WSe_2. (a) The experimental MSD for Au (blue circles) and a biexponential fitting (blue solid line). **(b)** The effective MSD for WSe_2 (orange circles) and a biexponential fitting (red solid line). The signal-to-noise ratio for Au is lower because the diffraction peaks are weaker in intensity.

In order to examine if interfacial phonon transmission is a plausible mechanism for the long dynamics of the Au/WSe_2 heterostructure, the MSD of Au has been transformed into an effective lattice temperature, as described in **Chapter 3**, and the result is shown in **figure 6.10** with blue circles. As discussed already for the MSD, the signal-to-noise ratio for the lattice temperature of Au is poor due to the limited amount of diffraction peaks, their small intensity and their proximity to intense peaks of WSe_2. Initially, the temperature of Au is rising to about 550 K and then it decays to 400 K in 40 ps.

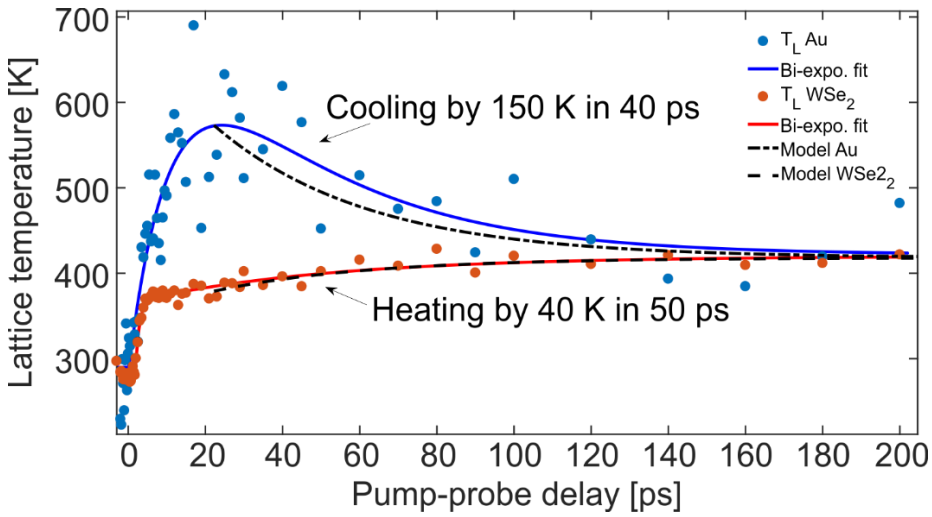

Figure 6.10: Ultrafast evolution of the effective lattice temperatures of Au and WSe_2. The experimental lattice temperature of Au and its biexponential fitting are shown with blue circles and a blue solid line, respectively. The estimated lattice temperature of WSe_2 (see text for details) and its biexponential fitting are shown with orange circles and an orange solid line. The black dashed lines are the results of a simple model of interfacial energy flow with transmission of phonons.

Given the fact that Au and WSe_2 reach thermodynamic equilibrium at t=200 ps (equal lattice temperatures), the temperature dependence of the Debye-Waller factor of WSe_2 can be approximated by a linear function $\Delta B = a \cdot \Delta T$, where $a = 5.3 \cdot 10^{-5}$ Å$^2/K$ (or $1.4 \cdot 10^{-3}$ Å$^2/K$ for the $\Delta\langle u^2 \rangle$). The time-constants and amplitudes of the Au and WSe_2 temperature evolutions are probed by bi-exponential fittings shown in **figure 6.10** with blue and orange solid lines, respectively.

The procedure of **Chapter 3** for measuring interfacial phonon transmission from the evolution of the effective lattice temperatures is now repeated for the Au / WSe_2 heterostructure. The model is a simple TTM where the interacting heat baths are the lattices of the Au nanoislands and the WSe_2 flake. This model is used to measure the interfacial phonon transmission from the relaxation dynamics between 20 and 200 ps.

While Au is cooling down by 150 K, the temperature of WSe_2 appears to increase by 40 K. This can be explained by the heat capacities and masses of the two materials. The inputs of the model are the thicknesses of the two materials ($L_{Au} = 2\ nm$ and $L_{WSe2} = 10\ nm$) and the lattice heat capacities. The lattice heat capacities are $Cl_{Au} = 2.49 \cdot 10^6$ J/m^{3}K and $Cl_{WSe2} = 1.98 \cdot 10^6$ J/m^{3}K. The lattice heat capacity of WSe_2 has been found from the work of Bolgar *et al.* [235]. The interfacial phonon transmission for the

Au / WSe_2 interface is $100\ MW/m^2K$. The theoretical evolution of the Au and WSe_2 temperatures are given by the dashed, black lines of **figure 6.12**. The equations of the TTM are:

$$\frac{dT_L^{Au}}{dt} = -\frac{W_{PP}}{L_{Au}Cl_{Au}} \cdot (T_L^{Au} - T_L^{WSe2}) \quad , \qquad \text{R 6.3}$$

$$\frac{dT_L^{WSe2}}{dt} = \frac{W_{PP}}{L_{WSe2}Cl_{WSe2}} \cdot (T_L^{Au} - T_L^{WSe2}) \quad , \qquad \text{R 6.4}$$

where W_{PP} is the interfacial phonon transmission or vibrational coupling and T_L^{Au} and T_L^{WSe2} the temperatures of the two lattices. The interfacial phonon transmission of Au nanoislands on WSe_2 ($100\ MW/m^2K$) is slightly higher than that of Au_{923} NCs on a-C ($90\ MW/m^2K$) and significantly higher than for Au_{923} NCs on Si-N ($16\ MW/m^2K$) and Au_{923} NCs on graphene ($14\ W/m^2K$). This can be explained by the large contact area of the nanoislands with the substrate and the epitaxial stacking of Au atoms on WSe_2.

The extracted lattice temperature have also been used to extract the thermal expansion coefficient. The Au nanoislands exhibit lattice expansion (shift of the Bragg peaks to lower scattering angles) with the same dynamics like the Debye-Waller decay. The thermal expansion coefficient of Au nano-islands is $a_L = (8.0 \pm 0.7) \cdot 10^{-6}\ K^{-1}$, which is similar with the value that was found for Au NCs in **Chapter 4**. The peaks of WSe_2 do not show lattice expansion. Based on the work of El-Mahalawy *et al*. [236] the thermal expansion coefficient of WSe_2 is $(2.7 \pm 0.2) \cdot 10^{-5}\ K^{-1}$and, thus, it can be detected by the FED apparatus. However, the motion of two-dimensional materials is constrained normal to the electron beam and, hence, their lattice expansion is suppresed at ultrafast timescales.

6.3.2 Electronic dynamics in response to the A exciton

Since Au grows epitaxially on the surface of WSe_2 single crystals, it is feasible to perform time- and angle-resolved photoelectron spectroscopy (tr-ARPES) in order to probe the ultrafast electronic dynamics and complement the results of FED, which probes solely the lattice response. These considerations have initiated a collaboration with the group of Dr. Laurenz Rettig (Physical Chemistry department, Fritz Haber Institute) and Dr. Tommaso

Pincelli, Dr. Shuo Dong and Dr. Samuel Beaulieu who have performed tr-ARPES experiments.

Figure 6.11 shows experimental results from tr-ARPES experiments. Photoexcitation is carried out by photons of 800 nm wavelengths, leading to the formation of A-excitons. The image in **figure 6.11.a** is the experimental band structure of Au / WSe_2 in equilibrium. The Fermi level is located at E=0. The states that cross the Fermi level belong to the sp band of Au. The states at $k_{//}$ = -1.3 $Å^{-1}$ and E ~ -1 eV is the top of the valence band of WSe_2. The signal in the region E > 0 is almost absent apart from some signal close to the Fermi edge (rescaled to be visible). After excitation with 800 nm pulses, photons get absorbed from the electrons and populate states above the Fermi level (E > 0). The band structure plotted in **figure 6.11.b** corresponds to a pump-probe delay of 50 fs. Three square shapes mark the positions of the most prominent, excited electronic states. The A-excitons form by transferring electrons to the K-point of the Brillouin zone, marked by a cyan square. In order to establish electron-lattice equilibrium, the electrons need to reside and relax at the bottom of the valence band, in the Σ valley, marked by dark red square. In addition, the Au islands are also electronically excited. The excited electronic states of the sp band are marked by a dark yellow square.

The intensities (electron counts per s) of these three regions are integrated and plotted as a function of the pump-probe delay time in **figure 6.11.c**. The time-trace with the shortest lifetime (cyan curve) belongs to the K states. The situation is similar with pure WSe_2, where the signal at the K-point decays within 70 fs. The hot electrons of the Au sp band are shown with the yellow curve, and their population decreases as the electron-lattice relaxation proceeds. Finally, the dark red curve shows the relaxation of the electrons at the Σ valley.

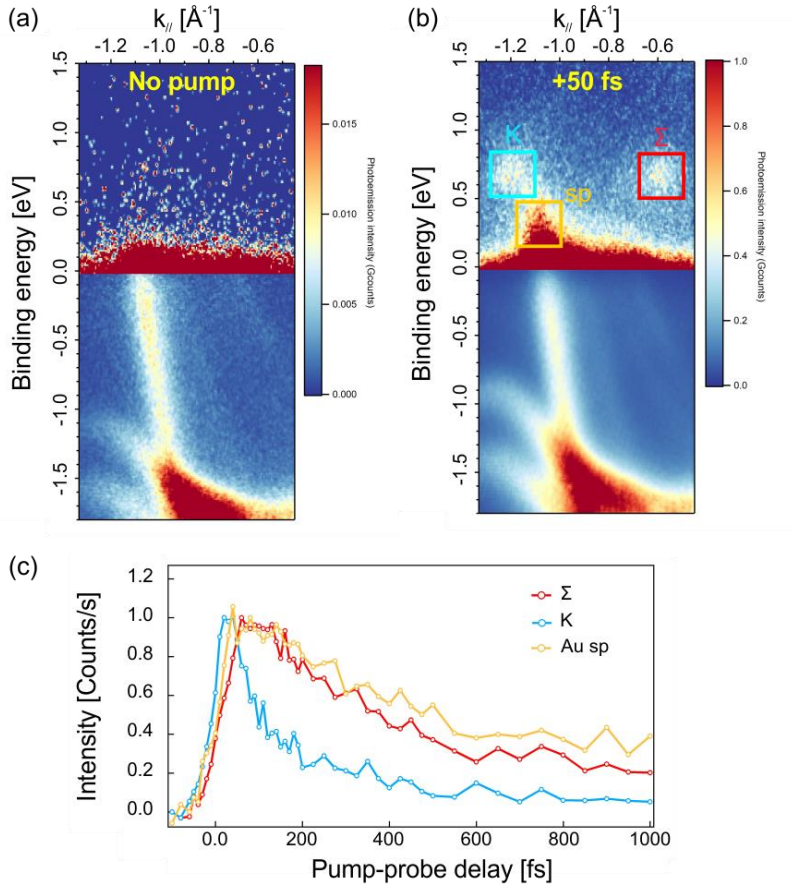

Figure 6.11: Time-resolved ARPES of Au / WSe_2 heterostructure. (a) Experimental band structure of Au / WSe_2 at equilibrium conditions (no pump). **(b)** Experimental band structure of Au / WSe_2 heterostructure at a pump probe delay of 50 fs. The K and Σ valleys of WSe_2 are marked with cyan and dark red squares, respectively. The excited sp states of Au are marked with the yellow square. **(c)** Population dynamics of the excited states at the K and Σ valleys of WSe_2 and at the sp band of Au. For additional information on the technique of tr-ARPES the reader is referred to the work of Puppin *et al.* [27] and Bertoni *et al.* [213]. *The plots of this figure have been provided by Dr. Tommaso Pincelli (PC department, FHI, Berlin).*

The most interesting finding of tr-ARPES is that the electrons at the Σ valley, in the presence of Au nanostructures, relax much faster than in pure WSe_2. This Au-induced change in the ultrafast dynamics of the Σ is illustrated in **figure 6.12**. In this figure, both time-traces correspond to an incident laser fluence of 1 mJ/cm^2. The measurement of pure WSe_2 has been performed at the same crystal with that of **figure 6.11** but before deposition of Au. Obviously, the dynamics of the hot electron relaxation in the Σ valley are significantly accelerated. The characteristic time-constant of the population at the Σ valley drops from 3-4 ps to ~400 fs.

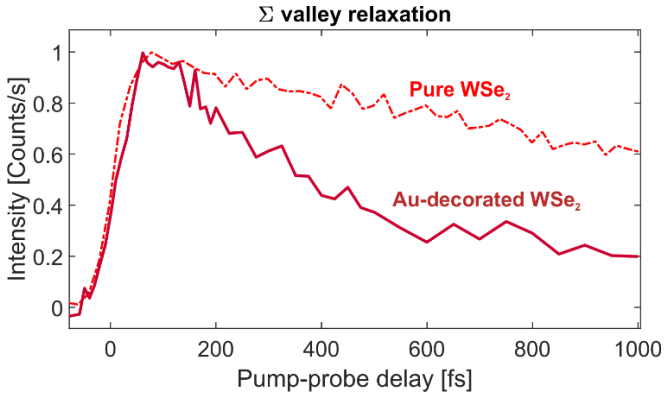

Figure 6.12: Electronic relaxation at the Σ valley of WSe_2 with and without Au nanoislands on its surface. The characteristic lifetime of hot electrons at the Σ valley drops from 3-4 ps to ~400 fs when the surface of WSe_2 is decorated by Au nanoislands. Both measurements have used 800 nm radiation and 1 mJ/cm^2 fluence.

In view of the results of tr-ARPES, an important observation of the FED experiments is that the lattice response to the A exciton is shorter for Au-decorated WSe_2 (1 ps, see **figure 6.9**) compared to pure WSe_2 ($\geq$ 1.5 ps, see **figure 6.2**). In parallel, the electron-phonon equilibration in the Au nanoislands is 7-9 ps (see **figure 6.9.a**), distinctively slower than other Au structures. The same time-constant is: (i) 4.5 ps for Au NCs on graphene, (ii) 6 ps for Au NCs on a-C, (iii) 5 ps for Au NCs on Si-N and (iv) 4-6 ps for bulk Au.

The proposed explanation is that electron-hole pairs of WSe_2 transmit into Au and relax there by electron-phonon coupling leading to an effectively shorter time-constant for WSe_2 and an effectively longer time-constant for Au. This process is illustrated in **figure 6.13**. In accordance with this scenario, the optical spectroscopy of **figure 6.7** provides evidence that the formation of excitons is suppressed in the presence of Au. Moreover, the work of A. G. Čabo *et al.* [237] have shown that electrons and holes can be transmitted from a thin TMDC to Au and relax there by electron-phonon and hole-phonon coupling.

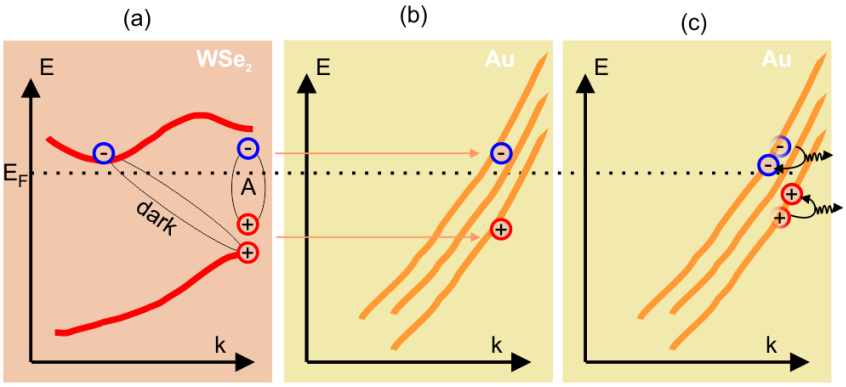

Figure 6.13: Transmission of electron-hole pairs from WSe_2 to Au. (a) A-excitons form at the direct band-gap of WSe_2 and transform into dark excitons within 10s of fs (Puppin *et al*. [27], Bertoni *et al*. [213]). **(b)** Electrons from the Σ valley and holes from the K valley are transferred to the sp states of Au. **(c)** Inside Au, electrons and holes relax towards the Fermi level by electron-phonon and hole-phonon coupling, respectively. *Adapted with modifications from A. G. Čabo et al.* [237].

6.3.2 Off-resonant pumping of Au/WSe_2 heterostructures

As seen from the results of the previous section, pumping the Au/WSe_2 heterostructure at the A-exciton resonance initiates a rich variety of electron-electron, electron-lattice and lattice-lattice interactions. This section presents FED experiments where the photon energy is smaller than the A-exciton resonance. The central wavelength is 840 nm, corresponding to a photon energy of 1.48 eV. The pump spectrum, shown in **figure 6.8** (dark magenta solid curve), has a central wavelength of 840 nm. The incident laser fluence is 2.8 mJ/cm^2. The used laser pulses are within the optical gap of pure WSe_2 and have minimum overlap with the A-exciton resonance. However, the Au nano-islands can still be excited and the scope of the present experiment is to determine the rapidity of transferring energy to the WSe_2 substrate.

The results of the FED experiment with 840 nm excitation are shown in **figure 6.14**. This experiment recorded the material's response at short timescales (-4 to 10 ps). The relative decay of the (220) peak of Au (**fig. 6.14.a**) can be reproduced by an exponential decay with a time-constant of 7 ps, in agreement with previous measurements. Despite the fact that the photon energies are within the optical gap of the semiconductor, the response of WSe_2 is initiated upon the arrival of the laser pulse and the triggered dynamics are in the sub-picosecond timescale. The relative decay of the (110) peak of WSe_2 (**fig. 6.14.b**) is fitted with an exponential decay and the time-constant is τ=(860 ± 30) fs. The effective

MSD and the effective lattice temperature of WSe_2 are shown in **figure 6.14.c**. The energy content of WSe_2 maximizes at about 3 ps. The increase in the effective MSD is $(2.70 \pm 0.02) \cdot 10^{-3}$ Å^2 and the increase of the effective lattice temperature is (52 ± 1) K.

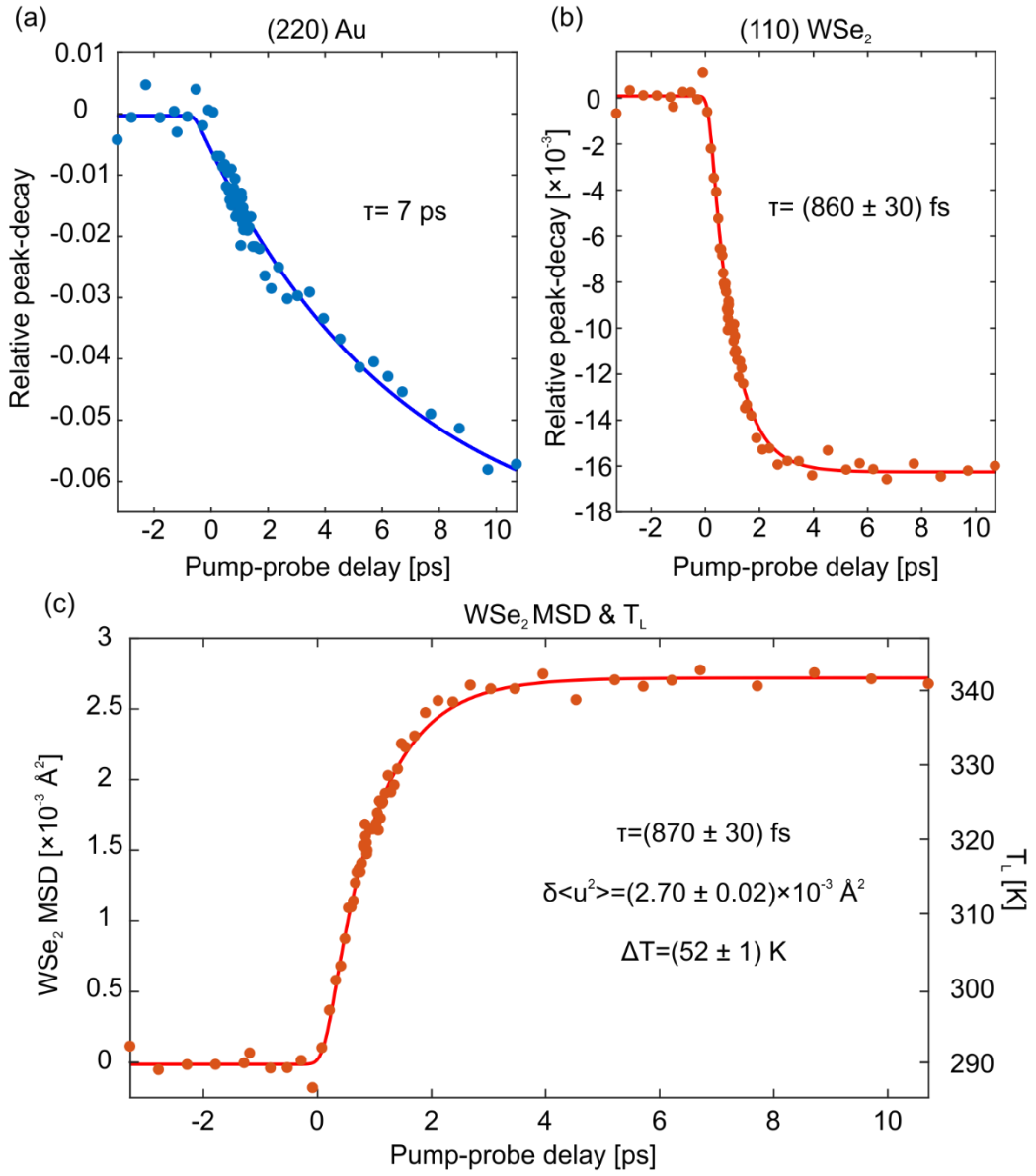

Figure 6.14: Ultrafast lattice dynamics of the Au / WSe_2 heterostructure pumped with 840 nm radiation. (a) Relative decay of the (220) peak of Au (blue circles) and exponential decay with 7 ps time-constant (blue solid line). (b) Relative decay of the (110) peak of WSe_2 (orange circles) and fitting with an exponential decay (red solid line).(c) The effective MSD (left axis) and the effective lattice temperature (right axis) of WSe_2. The experimental data-points are given by the orange circles and the red solid line is an exponential decay.

The observed, sub-picosecond lattice dynamics suggest the quasi-instantaneous (in comparison with the instrumental time-resolution) generation of excited electrons in WSe_2, despite the fact that the incident photons have lower energy than the first excitonic resonance by 144 meV.

To reassure that sub-band-gap photons are exciting charge carriers in WSe_2 (when it is decorated by Au) the experiment has been repeated with pump photons of 1300 nm wavelength. In this case the photon energy is 58% smaller than the first excitonic resonance. The fluence for this measurement is 1.16 mJ/cm^2, which is considered small for the investigated system and the wavelength used. The relative decay of the (110) peak of WSe_2 is shown in **figure 6.15**. Again, WSe_2 has an ultrafast response at timescales that are typical for intrinsic electron-lattice equilibration. From 1 ps to 20 ps the (110) peak of WSe_2 is decreased on average by (0.17±0.05)% and then it keeps decreasing in the 100-200 ps timescale. The kink at 20-60 ps has been repeatedly observed and it might be related with phonon-phonon interactions and lattice relaxation based on the work of Waldecker *et al.* [94] (see figure 2 of cited work). The next section is devoted to the dynamics of the ultrafast lattice response of WSe_2 during the first 10 picoseconds.

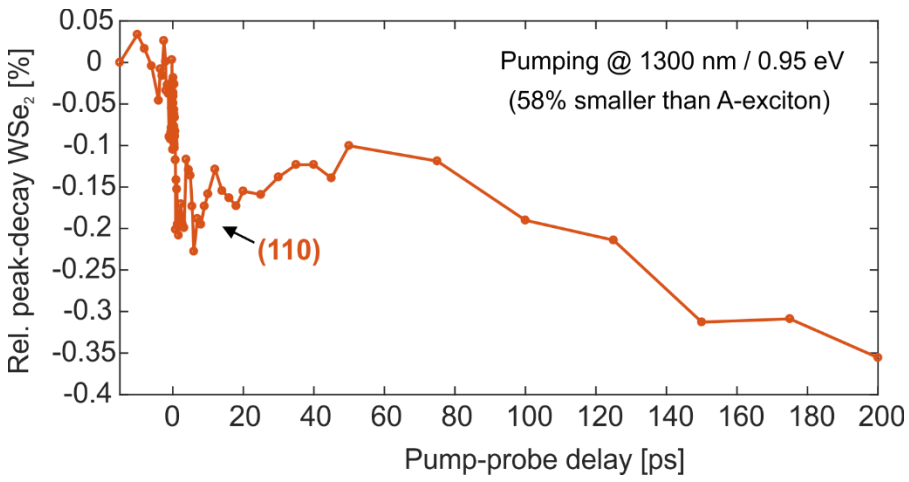

Figure 6.15: Ultrafast lattice dynamics of the Au / WSe_2 heterostructure pumped with 1300 nm radiation. The incident laser fluence is only 1.16 mJ/cm^2. From 1 ps and up to 20 ps the (110) peak of WSe_2 is decreased by (0.17±0.05)%.

The FED experiments with 840 nm and 1300 nm radiation show that in the presence of Au, sub-band-gap light can excited charge carriers in WSe_2, which then relax by electron-phonon coupling. Excitation of semiconductors' charge carriers, assisted by plasmonic

nanostructures, is a very interesting phenomenon for viable applications like photocatalysis and solar cells (see introduction). This section is focused on the relaxation of excited charge carriers with the lattice. For the experiment with 840 nm photons, the observed lattice dynamics are distinctively faster (870 fs) than pure WSe_2 pumped at the A-exciton (1.8 ps). The experiments with 840 nm photons are repeated with various fluences to investigate if the process that generates excited electrons in the semiconductor is linear (/nonlinear) and what is the effect on the time-constant.

Figure 6.16.a shows the effective MSD of WSe_2 for various fluences. Relatively to the total available laser power, the experiments have been carried out with 4 to 12% power in steps of 2%. The corresponding fluences range from 2.8 to 0.9 mJ/cm^2. The first measurement employs 12% of the available laser power. This measurement is used to determine the temporal overlap of the pump and probe pulses and for this reason it has different delay points than the others and it is shifted in time to match the time-zero of the other datasets. All measurements were carried out with the same heterostructure and on the same spot. Already from the experimental data of **figure 6.16.a**, it appears that the effective MSD has a nonlinear dependence. In addition, the dynamics are slower at high fluences. The MSD is maximized at approximately 3 ps for 12%, 2 ps for 10%, 1-2 ps for 6-8% and <1 ps for 4% (see inset for the lowest fluence).

A total of nine measurements with different fluences were carried out back-to-back on the same sample. **Figure 6.16.b** shows the average MSD at 2-5 ps (red circles) and the standard deviation for the same data set (error bars) plotted as a function of the incident laser fluence. The error bars of the incident laser fluence were measured using a continuous tracking of the laser spot intensity on a reference camera. The fluence dependence is certainly following a nonlinear relationship with the energy input.

The blue solid line in **figure 6.16.b** shows a fitting with a function of the form aF^2, where F is the fluence. Such a quadratic fluence dependence is expected if the plasmonic near-fields of Au nanoislands enhance two-photon absorption in WSe_2. Another possibility is that hot electrons, generated in Au, are transmitted to WSe_2 and deposit energy to its lattice by electron-phonon coupling. The red curve in **figure 6.16.b** is the result of a model of hot electron transfer. Hot electrons of Au have a Fermi-Dirac distribution and their temperature evolves according to the TTM. Au electrons can pass to WSe_2 and deposit their energy to its lattice. The energy dependent probability for hot electron

transmission is proportional to the product of the electronic densities of states of the two materials.

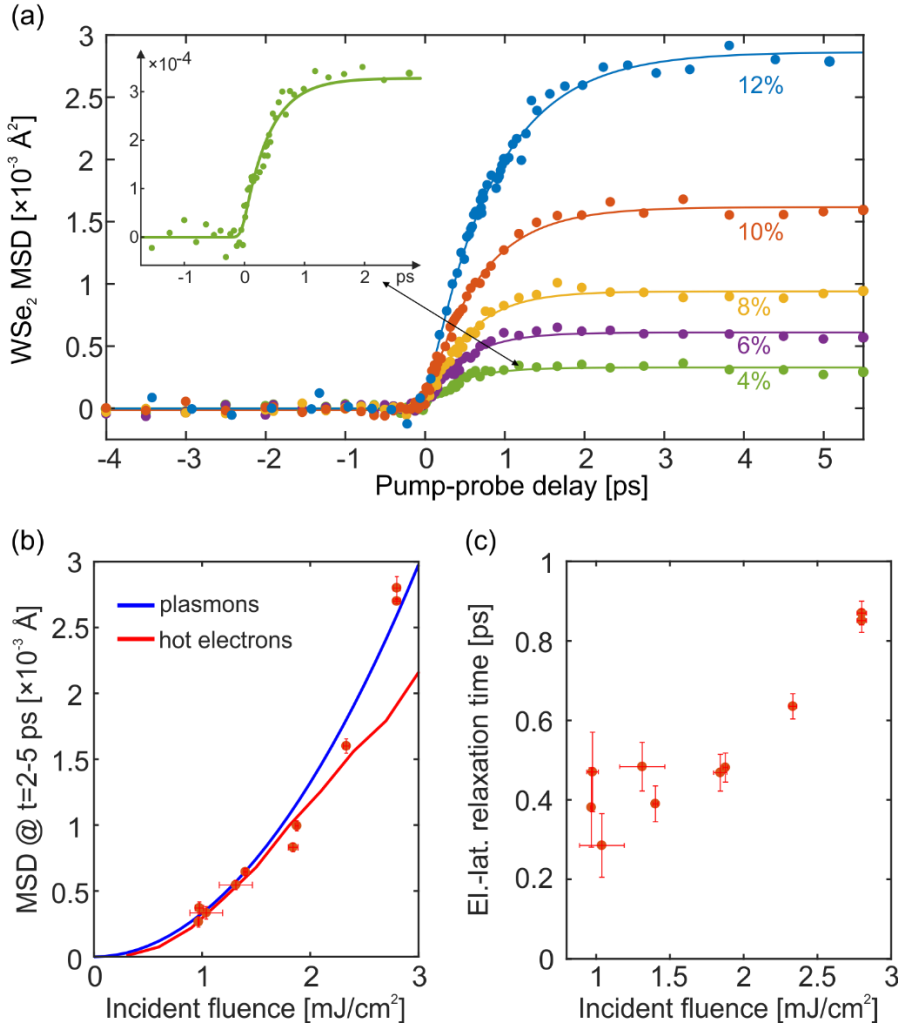

Figure 6.16: Fluence dependence measurements of Au / WSe_2 heterostructures pumped with sub-band-gap radiation of 840 nm wavelength. (a) The effective MSD of WSe_2 as a function of pump-probe delay for 4-12% pumping (relatively to the total available power) in steps of 2%. The inset shows the measurements with the lowest fluence. **(b)** The fluence dependence of the average MSD at 2-5 ps after excitation. The solid black and red lines line are models of energy flow based on plasmons (blue) and hot electrons (red), which are explained in more detail in the main text. **(c)** The fluence dependence of the time-constant of electron-lattice relaxation. The measurements follow a clear trend. The maximum time-constant is ~850 fs (for the highest fluence) and the minimum time-constant is 300-400 ps (for the lowest fluence).

The time-constant of the MSD is also fluence-dependent as shown in **figure 6.16.c**. The time-constants are extracted from fittings of exponential functions and the error bars represent the fitting uncertainties (standard deviation). At the highest fluence (2.8

mJ/cm^2) the time-constant is in the order of 850 fs. As the fluence decreases, the time-constant decreases even further, following a clear trend. The lowest fluence (1 mJ/cm^2) approaches the instrumental time-resolution (300 fs for the used experimental conditions). These relaxation dynamics are significantly faster than the relaxation of pure WSe_2 in response to the A-exciton.

The next paragraphs discuss how Au can induce optical absorption and lattice heating of WSe_2 for photon energies below its direct optical gap. **Figure 6.17** shows the static ARPES measurement of Au / WSe_2 and on top the theoretical band structure from DFT measurements (performed by M. Dendzik, Dynamics of Correlated Materials, with the GLLB-SC exchange-correlation potential). In **figure 6.17**, the blue lines are the bands of WSe_2 and the red lines are the bands of Au. All the vertical arrows represent optical transitions (without taking into account their scattering cross section). All these transitions have a photon energy that is equal with the optical gap of WSe_2. The magenta-colored arrow is the only optical transition that has both the initial and the final states within WSe_2. All other transitions (black arrows) have an initial state in Au and a final state in WSe_2. Such optical transitions can take place at the metal / semiconductor interface.

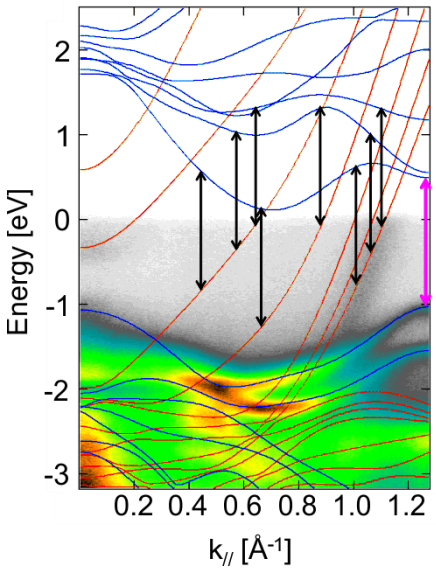

Figure 6.17: Direct optical transitions at the Au / WSe_2 interface. All arrows correspond to optical excitations with energy that matches the direct optical gap. For pure WSe_2 the only allowed optical transition is the one shown with a magenta arrow. Decoration of WSe_2 enables multiple optical transitions shown with black arrows (the transfer matrix elements for the optical transitions are not taken into account).

Based on **figure 6.17**, photons with energies close and below the optical gap, can transfer electrons to highly excited states of WSe_2 above the Fermi level due to the additional sp states of Au. For λ=840 nm the maximum energy of final states in WSe_2 is 1.48 eV above the Fermi level. These highly excited electronic states have large phase-space for electron scattering and stronger electron-phonon coupling, compared to the ones that are located close to the conduction band minimum. Thus, direct optical transitions can explain the short time-constants (~400 fs) at the low fluence regime in **figure 6.16.c**. However, direct optical transitions are expected to have a linear dependence on the incident laser fluence and thus the pronounced nonlinearity at high fluences in **figure 6.16.b** is due to some different mechanism. Another mechanism for enhanced absorption is due to the formation of new, interfacial electronic states, see for instance Krane *et al*. [227]. The corresponding optical transitions are also expected to have a linear dependence on the incident laser fluence.

Lattice heating of WSe_2 in response to sub-band-gap photons can also be activated by hot electron transfer from Au. This mechanism is illustrated in **figure 6.18**. After absorption of the photons with 840 nm wavelength at $t = 0$, electrons of Au are excited 1.48 eV above the conduction band minimum of WSe_2. In the 100 fs timescale highly-energetic, nonthermal electrons can be transferred to highly energetic states of WSe_2 and excite phonons. Even after electrons thermalize, a significant portion of the Fermi-Dirac distribution has sufficient energy for hot electron injection into WSe_2. The energy barrier for hot electron injection from Au to WSe_2 is in the order of 110 meV, which is the energy difference between the conduction band minimum and the Fermi level (see **figure 6.17** and relevant discussion). The electron-phonon coupling in Au is relatively weak and hence hot electron injection can occur even after 5 ps or more (based on the TTM). The expected fluence dependence of hot electron transfer is shown in **figure 6.16.b** (red curve). The time constants are expected to be in the order of 5 ps and hence hot electron transfer cannot account for the time-constants of electron-lattice relaxation, shown in **figure 6.16.c**.

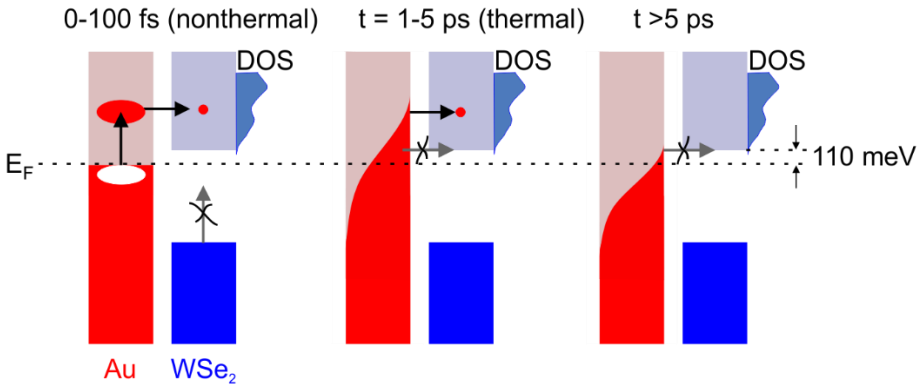

Figure 6.18: Hot electron transfer from Au to WSe_2. After absorption of the laser pulse $(t = 0)$ electrons of Au are excited above the conduction band minimum of WSe_2. In sub-picosecond timescales, highly-energetic, nonthermal electrons can be transferred to highly energetic states of WSe_2 and excite phonons. Even after thermalization and for time-delays as high as 5 ps, hot electrons can be transferred to WSe_2, since the energy barrier is only 110 meV (conduction band minimum minus the Fermi level). Energy transfer by hot electrons is suppressed for time-delays larger than 5 ps or more.

Another important phenomenon that must be taken into account is the plasmonic properties of metallic nanostructures on semiconducting surfaces. The Au nanoislands can get polarized by the external electric field of the laser and introduce local distortions to the total electric field. The strength of the electric field in the vicinity of the metallic islands is enhanced. Charge oscillations in the metal are also inducing image charges in the semiconductor. All these phenomena are shown schematically in **figure 6.19.a** (adapted with modifications from Tan *et al.* [71] see fig. 1.a in the reference). Generally, the frequency of the plasmon resonance and the field enhancement depend on the size and shape of the metallic nanostructure and on the dielectric environment. Sun *et al.* [238] have studied Au nanoislands of very similar morphology on SiO_2 (compare figures 2.a-c in the reference and **figure 6.4** of the present work). The maximum of the plasmonic peak is located at 750 nm. The plasmonic peaks of irregular Au nanoislands are broad. The intensity of the plasmon resonance drops by 50% at 600 nm and by 30% at 1000 nm. This is due to the large variety of sizes and shapes of the nanoislands. Based on this, it is expected that the 840 nm laser pulses excite plasmonic oscillations of the Au nanoislands on WSe_2.

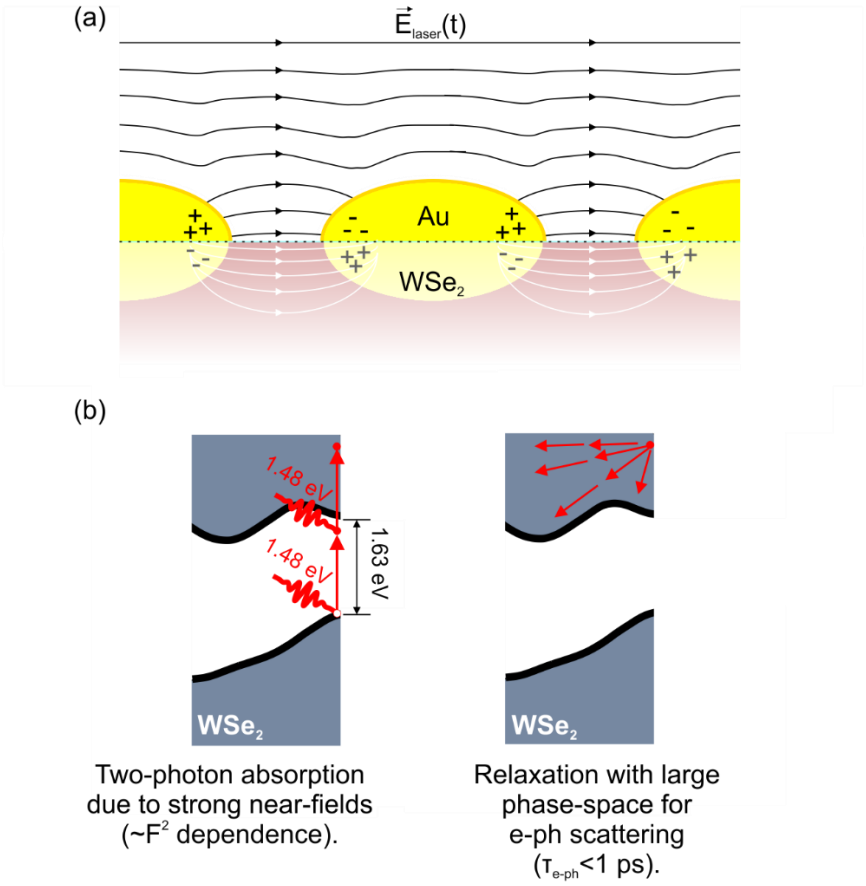

Figure 6.19: Plasmons and multiphoton absorption in Au / WSe_2 heterostructures. **(a)** The Au nanoislands get polarized by the external electric field of the laser and cause local distortions of the total electric field. **(b)** The field enhancement in the vicinity of the Au nanoislands can lead to two-photon absorption in WSe_2. **(c)** Two-photon absorption populates highly energetic levels of WSe_2 with large phase-space for electron-phonon scattering and shorter timescales for relaxation.

The plasmonic field enhancement can facilitate the interfacial optical transitions of **figure 6.17** and direct optical transitions within each component. Moreover, it can enhance nonlinear, two-photon absorption in WSe_2. The probability of two-photon absorption has a quadratic dependence on the intensity of the incident laser field. The fluence dependence measurements of **figure 6.16.b** show that the MSD (or the lattice temperature) has an approximate F^2 dependence on the incident laser fluence, which can partially originate from two-photon absorption. Similarly with interfacial optical transitions, two-photon absorption will result in highly excited electrons. For 840 nm radiation and two-photon absorption the excited electronic state can be 1.33 eV above the conduction band minimum at the K point (**figure 6.19.b**). As a result of this process, the excited charge carriers have a large phase-space for scattering and shorter lifetimes

(**figure 6.19.b**). Multiphoton absorption in WSe_2 due to the plasmonic near fields of Au nanoislands can account for the strong nonlinear lattice heating of **figure 6.16.b** and the short time-constants of **figure 6.16.c**. Based on this, plasmonic coupling of WSe_2 and Au is considered an important mechanism, especially for higher fluences.

Summary. The author of this work suggests that the nonlinear and accelerated lattice dynamics of Au-decorated WSe_2, in response to sub-band-gap photons (λ=840 nm), stem from multiple, coexisting processes. Hot electron transfer is expected to occur but it cannot be the dominant mechanism, since it contradicts the sub-picosecond lattice dynamics of WSe_2. Linear processes, such as interfacial optical transitions, are expected to prevail at low laser fluences and to give accelerated electron-lattice relaxation because the maximum energy of excited charge carriers in WSe_2 is 1.48 eV above the Fermi level. At high laser fluences, nonlinear, multiphoton absorption prevails. This process is driven by the plasmonic near-fields of Au nanoislands. In this case, the maximum energy of excited charge carriers is 1.33 eV above the conduction band minimum at the K point and the electron-lattice relaxation is again accelerated.

Chapter 7. Summary and conclusions

Ultrasmall nanostructures have large surface-to-volume ratio and hence their nonequilibrium states are strongly affected by ultrafast energy flow to and from their chemical environment. In photoexcited, supported, 0D nanoclusters, thermal equilibration proceeds through intrinsic heat flow between their electrons and their lattice and extrinsic heat flow between the nanoclusters and their substrate. In **Chapter 3**, FED experiments and a newly developed model of ultrafast energy flow in 0D / 2D heterostructures have been used to measure the various microscopic coupling constants. The model has been extended to crystalline substrates in **Chapter 5**. It is expected that the modelling described in this thesis can be adapted for a wide range of heterostructures with low-dimensional materials.

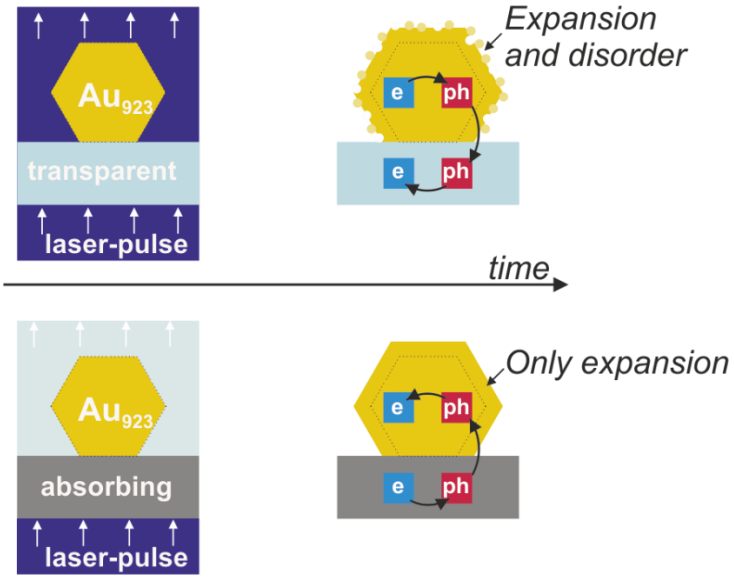

Figure 7.1: Lattice heating and structural changes of nanoclusters, induced by hot electrons or by hot substrate phonons.

The study of ultrafast energy flow gave the following results:

- The measured electron-phonon coupling constant of Au_{923} NCs is $G_{e\text{-}ph} = (1.9 \pm 0.5) \cdot 10^{16}$ W/m^{3}K, which is ~70% of the value of bulk Au

- The interfacial phonon transmission is the dominant source of lattice dynamics in the 10-100 ps timescale.
- The measured interfacial phonon transmission is: $16\ \mathrm{MW/m^2K}$ for Au_{923} NCs on Si-N, $14\ \mathrm{MW/m^2K}$ for Au_{923} NCs on graphene, $90\ \mathrm{MW/m^2K}$ for Au_{923} NCs on a-C and $100\ \mathrm{MW/m^2K}$ for Au nanoislands on WSe_2.
- The interfacial phonon transmission is higher for 0D nanostructures on surfaces with nanoscale roughness like a-C and for 2D / 2D heterostructures with large contact area, like Au nanoislands on WSe_2 single crystals.

Quantitative knowledge of the energy transfer rates between the microscopic subsystems of nanostructures is expected to be very important for the accurate design and control of the corresponding nanodevices.

Furthermore, ultrafast energy flow triggers atomic motions, such as anharmonic expansion, and lattice disordering, which manifest as distinct and quantifiable reciprocal-space observables. These motions have been examined in detail in **Chapter 4**. The anharmonicity of the interatomic potential results always in lattice expansion on ultrafast timescales. Moreover, the Au_{923} NCs exhibit ultrafast, surface premelting in conditions of pronounced electron-lattice nonequilibrium. The study of ultrafast structural changes of Au_{923} NCs gave the following results:

- The Au_{923} NCs exhibit ultrafast lattice expansion, in parallel with the Debye-Waller effect.
- The thermal expansion coefficient of Au_{923} NCs is $a_L = (9.5 \pm 0.7) \cdot 10^{-6}\ \mathrm{K^{-1}}$ and it is reduced by ~30% compared to bulk Au.
- Hot electrons can distort the lattice of Au_{923} NCs, even if the lattice temperature is below the equilibrium threshold for surface pre-melting.
- When the electronic temperature is ~3300 K, an approximate 14% of the surface is melting in 10 ps.

The motion of surface atoms and surface premelting in nonequilibrium conditions is a key-feature in catalysis. During operation, nanoscale catalysts interact with chemically generated hot electrons, their surface atoms are highly mobile and this atomic mobility is eventually leading to sintering. In view of the present results, an in-depth understanding of deleterious effects in catalysis might require ultrafast investigations of structural changes.

Structural stability of nanoscale building blocks is prone to atomic vibrations and atomic diffusion but also to translations and rotations of entire nanostructures. In **Chapter 5**, FED has been used to probe rotational motions of 0D nanostructures on crystalline surfaces. In equilibrium, the Au_{923} NCs have a preferred, crystallographic orientation on graphene due to their well-defined facets and internal crystal structure, as well as the crystallinity and flatness of the substrate. Ultrashort laser pulses are used to induce vibrational and rotational excitation of the nanoclusters and the resulting, time-dependent diffraction patterns are probed with FED. The diffraction dynamics are affected by the Debye-Waller effect, lattice expansion and NC rotations. In order to analyze these data, the experiments were supported by molecular dynamics simulations, electron diffraction simulations and simulations of ultrafast energy flow. At the end of this process it was found that the NCs exhibit constrained, angular oscillations, termed librations.

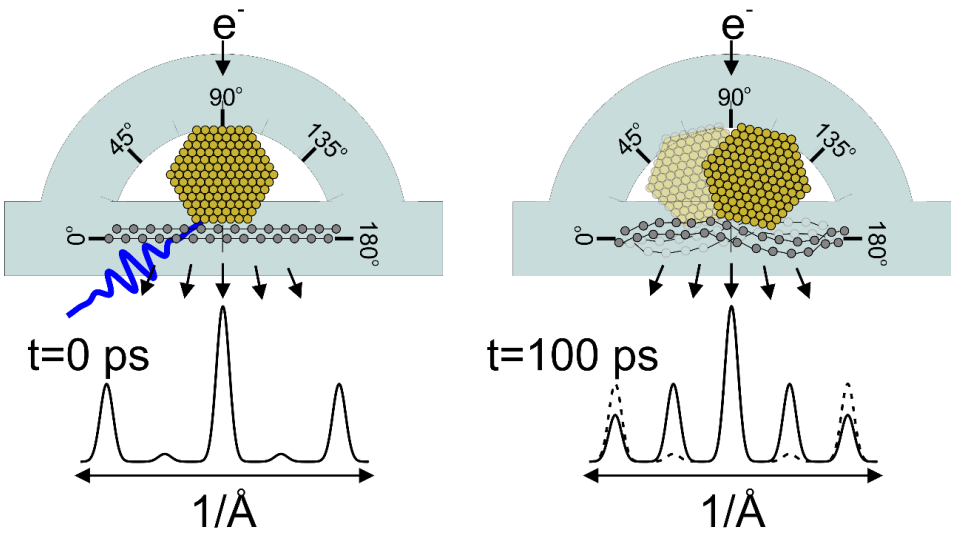

Figure 7.2: Femtosecond electron diffraction used as an ultrafast goniometer for nanocrystals.

The findings regarding ultrafast motions of entire Au_{923} NCs are summarized as follows:

- The Au_{923} NCs librate on graphene with a period of ~20 picoseconds. The torque per rad acting on each NC is estimated to be $35\, nN \cdot nm/rad$. The angular distribution of NCs with respect the graphene is 1.6° at 300 K and 2.0° at 600 K.

- The activation of NC librations follows biexponential dynamics. The time-constants measured from the (220) peak are approximately τ_1~4 ps (40% amplitude) and τ_2~110 ps (60% amplitude).
- The short time-constant suggests quasi-impulsive excitation and the long time-constant corresponds to the complete thermalization time of acoustic phonons in graphene.
- The corresponding energy transfer rates are in the order of 3 meV/ps and 0.2 meV/ps. The angular momentum transfer to the NCs is assigned to scattering of flexural ZA phonons of graphene.

The present results open up the way for ultrafast measurements of nano-objects' motions using diffractive probes. Studying the coupling between the various NC motions and the phonons of the substrate can provide a detailed view of mass-transport at the nanoscale. In addition, it is shown how molecular dynamics and electron scattering simulations can be used to design and analyze demanding experiments with mobile nanostructures.

The heterosis of nanoscale metals and semiconductors culminates in light harvesting technologies. Plasmonic photovoltaics and plasmonic photocatalysts contain spatially confined metals to concentrate electromagnetic radiation and semiconductors to enable efficient charge-separation. The performance of optoelectronic devices depends on the lifetime of the excited charge carriers. On the one hand, plasmonic metals can enhance light absorption and boost performance. On the other hand, plasmonic coupling, interfacial optical transitions and hot electron transfer can modify the dynamic properties of, otherwise, well-known semiconducting materials. Such phenomena have been studied in detail in **Chapter 6**.

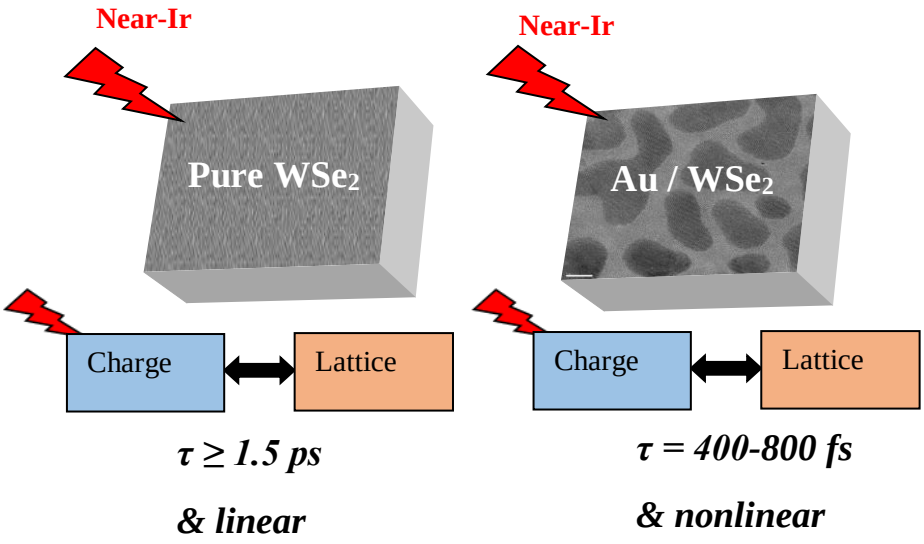

Figure 7.3: Near-infrared photons induce nonlinear lattice heating and accelerated electron-lattice relaxation in Au-decorated WSe_2.

The experiments of **Chapter 6** have shown that surface-decoration of WSe_2 with Au nanostructures can alter its electronic and lattice dynamics. The results of these studies are summarized as follows:

- Au grows epitaxially on WSe_2 without strict requirements on the growth conditions. This allows studying the structural and electronic dynamics of the heterostructure with FED and tr-ARPES, respectively, and acquire an in-depth knowledge of nonequilibrium states.
- Surface decoration with 2 nm of Au has a significant effect on the electronic and optical properties of multilayer flakes of WSe_2.
- The structural dynamics of WSe_2 in response to the formation of A-excitons are accelerated.
- In the presence of Au, WSe_2 can be excited by sub-band-gap photons. The resulting structural dynamics have a nonlinear fluence dependence. The time-constant for electron-lattice relaxation drops from ≥ 1.5 ps, for bare WSe_2, to 400-850 fs for Au-decorated WSe_2.

The enhancement of light-matter interactions in semiconductors using plasmonic nanostructures is a known phenomenon. However, the ultrafast interactions between the microscopic building blocks of the metal / semiconductor heterostructure is an open

subject. The combined use of FED and tr-ARPES can provide a direct and detailed view on the interaction of photoexcited, charge carriers and phonons.

Based on all the above, nanoscale heterostructures have a great variety of nonequilibrium phenomena and many possible pathways for ultrafast energy flow, depending on the morphology of the nanostructures, the properties of the substrate *etc*. Energy flow can drive ultrafast motions of atoms and clusters. The properties of the nanostructures' substrate can also be affected during nonequilibrium. Ultrafast diffractive probes combined with modelling and simulations can provide an in-depth understanding of such phenomena.

References

[1] F. Bloch, " Über die Quantenmechanik der Elektronen in Kristallgittern", *Zeitschrift für Phys.*, vol. 52 (7-8), pp. 555–600, 1929.

[2] N. W. Ashcroft and N. D. Mermin, "Solid State Physics", Brooks/Cole, 1976.

[3] R. O. Jones and O. Gunnarsson, "The density functional formalism, its applications and prospects", *Rev. Mod. Phys.*, vol. 61 (3), pp. 689–746, 1989.

[4] F. Reinert and S. Hüfner, "Photoemission spectroscopy - From early days to recent applications", *New J. Phys.*, vol. 7, 97, 2005.

[5] J. W. White and C. G. Windsor, "Neutron scattering-modern techniques and their scientific impact", *Rep. Prog. Phys.*, vol. 47, 707, 1984.

[6] D. A. Long, "The Raman Effect - A Unified Treatment of the Theory of Raman Scattering by Molecules", John Wiley & Sons, 2002.

[7] K. Charles, "Introduction To Solid State Physics", 8th Edition, John Wiley & Sons, 2004.

[8] P. B. Allen, "Theory of Thermal Relaxation of Electrons in Metals", *Phys. Rev. Lett.*, vol. 59 (13), pp. 1460–1463, 1987.

[9] C. W. Nicholson, A. Lücke, W.G. Schmidt, M. Puppin, L. Rettig, R. Ernstorfer and M. Wolf, "Beyond the molecular movie: Dynamics of bands and bonds during a photoinduced phase transition", *Science*, 362 (6416), pp. 821–825, 2018.

[10] T. Frigge, B. Hafke, T. Witte, B. Krenzer, C. Streubühr, A. Samad Syed, V. Mikšić Trontl, I. Avigo, P. Zhou, M. Ligges, D. Von Der Linde, *et al.*, "Optically excited structural transition in atomic wires on surfaces at the quantum limit", *Nature*, vol. 544 (7649), pp. 207–211, 2017.

[11] D. Wegkamp and J. Stähler, "Ultrafast dynamics during the photoinduced phase transition in VO_2", *Prog. Surf. Sci.*, vol. 90 (4), pp. 464–502, 2015.

[12] C. Monney, M. Puppin, C. W. Nicholson, M. Hoesch, R. T. Chapman, E. Springate, H. Berger, A. Magrez, C. Cacho, R. Ernstorfer and M. Wolf, "Revealing

the role of electrons and phonons in the ultrafast recovery of charge density wave correlations in 1*T*- $TiSe_2$", *Phys. Rev. B*, vol. 94 (16), 165165, 2016.

[13] R. Ernstorfer, M. Harb, C.T. Hebeisen, G. Sciaini, T. Dartigalongue and R.J.D. Miller, "The formation of warm dense matter: experimental evidence for electronic bond hardening in gold", *Science*, vol. 323 (5917), pp. 1033–1037, 2009.

[14] D. M. Fritz, D. A. Reis, B. Adams, R. A. Akre, J. Arthur, C. Blome, P. H. Bucksbaum, A. L. Cavalieri, S. Engemann, S. Fahy, R. W. Falcone, P. H. Fuoss *et al.*, "Ultrafast bond softening in Bismuth: Mapping a solid's interatomic potential with X-rays", *Science*, vol. 315 (5812), pp. 633–636, 2007.

[15] H. Eyring, "The activated complex in chemical reactions", *J. Chem. Phys.*, vol. 3, pp. 107–115, 1934.

[16] J. C. Polanyi and A. H. Zewail, "Direct observation of the transition state", *Acc. Chem. Res.*, vol. 28 (3), pp. 119–132, 1995.

[17] M. P. Minitti, J. M. Budarz, A. Kirrander, J. S. Robinson, D. Ratner, T. J. Lane, D. Zhu, J. M. Glownia, M. Kozina, H. T. Lemke, M. Sikorski, Y. Feng *et al.*, "Imaging Molecular Motion: Femtosecond X-Ray Scattering of an Electrocyclic Chemical Reaction", *Phys. Rev. Lett.*, vol. 114 (25), 255501, 2015.

[18] J. Yang, X. Zhu, T. J. A. Wolf, Z. Li, J. P. F. Nunes, R. Coffee, J. P. Cryan, M. Gühr, K. Hegazy, T. F. Heinz, K. Jobe, R. Li *et al.*, "Imaging CF_3I conical intersection and photodissociation dynamics with ultrafast electron diffraction", *Science*, vol. 361 (6397), pp. 64–67, 2018.

[19] A. Nilsson, J. LaRue, H. Öberg, H. Ogasawara, M. Dell'Angela, M. Beye, H. Öström, J. Gladh, J.K. Nørskov, W. Wurth, F. Abild-Pedersen and L.G.M. Pettersson, "Catalysis in real time using X-ray lasers", *Chem. Phys. Lett.*, vol. 675, pp. 145–173, 2017.

[20] E. W. Plummer, J. Shi, S. J. Tang, E. Rotenberg and S. D. Kevan, "Enhanced electron-phonon coupling at metal surfaces", *Prog. Surf. Sci.*, vol. 74, pp. 251–268, 2003.

[21] A. Jorio, R. Saito, G. Dresselhaus and M. S. Dresselhaus, "Raman Spectroscopy in Graphene Related Systems", Wiley-VCH Verlag GmbH & Co. KGaA, 2011.

[22] M. Eckert, “Max von Laue and the discovery of X-ray diffraction in 1912”, *Annalen der Physik*, vol. 524 (5), pp. A83–A85, 2012.

[23] G. Thomson, “The early history of electron diffraction”, *Contemp. Phys.*, vol. 9 (1), pp. 1–15, 1968.

[24] G. Mourou and S. Williamson, “Picosecond electron diffraction”, *Appl. Phys. Lett.*, vol. 41, 44, 1982.

[25] J. R. Dwyer, C. T. Hebeisen, R. Ernstorfer, M. Harb, V. B. Deyirmenjian, R. E. Jordan and R. J. D. Miller, “Femtosecond electron diffraction: making the molecular movie”, *Philos. Trans. A. Math. Phys. Eng. Sci.*, vol. 364 (1840), pp. 741–78, 2006.

[26] R. J. D. Miller, R. Ernstorfer, M. Harb, M. Gao, C. T. Hebeisen, H. Jean-Ruel, C. Lu, Gustavo Moriena and G. Sciaini, “Making the molecular movie: first frames”, *Acta Crystallogr. Sect. A Found. Crystallogr.*, vol. 66 (2), pp. 137–156, 2010.

[27] M. Puppin, Y. Deng, C. W. Nicholson, J. Feldl, N. B. M. Schröter, H. Vita, P. S. Kirchmann, C. Monney, L. Rettig, M. Wolf and R. Ernstorfer, “Time- and angle-resolved photoemission spectroscopy of solids in the extreme ultraviolet at 500 kHz repetition rate”, *Rev. Sci. Instrum*, vol. 90 (2), 023104, 2019.

[28] E. Beaurepaire, J. C. Merle, A. Daunois, and J. Y. Bigot, “Ultrafast spin dynamics in ferromagnetic nickel”, *Phys. Rev. Lett.*, vol. 76 (22), pp. 4250–4253, 1996.

[29] L. Waldecker, “Electron-lattice interactions and ultrafast structural dynamics of solids”, PhD Dissertation, Freien Universität Berlin, 2015.

[30] G. Lövestam, H. Rauscher, G. Roebben, B. S. Klüttgen, N. Gibson, J. P. Putaud and H. Stamm, “Considerations on a definition of nanomaterial for regulatory purposes”, *JRC Reference Reports*, 2010.

[31] W. G. Kreyling, M. Semmler-Behnke and Q. Chaudhry, “A complementary definition of nanomaterial”, *Nano Today*, vol. 5 (3), pp. 165–168, 2010.

[32] Z. W. Wang and R. E. Palmer, “Determination of the ground-state atomic structures of size-selected Au nanoclusters by electron-beam-induced transformation”, *Phys. Rev. Lett.*, vol. 108 (24), 245502, 2012.

[33] D. M. Wells, G. Rossi, R. Ferrando and R. E. Palmer, "Metastability of the atomic structures of size-selected gold nanoparticles", *Nanoscale*, vol. 7 (15), pp. 6498–6503, 2015.

[34] A. Surrey, D. Pohl, L. Schultz and B. Rellinghaus, "Quantitative measurement of the surface self-diffusion on Au nanoparticles by aberration-corrected transmission electron microscopy", *Nano Lett.*, vol. 12 (12), pp. 6071–6077, 2012.

[35] A. S. Barnard, N. P. Young, A. I. Kirkland, M. A. van Huis and H. Xu, "Nanogold: A quantitative phase map", *ACS Nano*, vol. 3 (6), pp. 1431–1436, 2009.

[36] J. B. Wagner, M. G. Willinger, J. O. Müller, D. S. Su and R. Schlögl, "Surface-charge-induced reversible phase transitions of Bi nanoparticles", *Small*, vol. 2 (2), pp. 230–234, 2006.

[37] A. Balerna and S. Mobilio, "Dynamic properties and Debye temperatures of bulk Au and Au clusters studied using extended x-ray-absorption fine-structure spectroscopy", *Phys. Rev. B*, vol. 34 (4), 2293, 1986.

[38] L. Waldecker, R. Bertoni, and R. Ernstorfer, "Compact femtosecond electron diffractometer with 100 keV electron bunches approaching the single-electron pulse duration limit", *J. Appl. Phys.*, vol. 117 (4), 044903, 2015.

[39] G. Fiori, F. Bonaccorso, G. Iannaccone, T. Palacios, D. Neumaier, A. Seabaugh, S. K. Banerjee and L. Colombo, "Electronics based on two-dimensional materials," *Nat. Nanotechnol.*, vol. 9 (10), pp. 768–779, 2014.

[40] W. J. Yu, Z. Li, H. Zhou, Y. Chen, Y. Wang, Y. Huang and X. Duan, "Vertically stacked multi-heterostructures of layered materials for logic transistors and complementary inverters", *Nat. Mater.*, vol. 12 (3), pp. 246–252, 2013.

[41] E. Pop, S. Sinha and K. E. Goodson, "Heat generation and transport in nanometer-scale transistors", *Proc. IEEE*, vol. 94 (8), pp. 1587–1601, 2006.

[42] D. Somvanshi, S. Kallatt, C. Venkatesh, S. Nair, G. Gupta, J. K. Anthony, D. Karmakar and K. Majumdar, "Nature of carrier injection in metal/2D-semiconductor interface and its implications for the limits of contact resistance", *Phys. Rev. B*, vol. 96 (20), 205423, 2017.

[43] Z. Fang, Z. Liu, Y. Wang, P. M. Ajayan, P. Nordlander, and N. J. Halas,

"Graphene-antenna sandwich photodetector", *Nano Lett.*, vol. 12 (7), pp. 3808–3813, 2012.

[44] Z. Wang, Z. Dong, Y. Gu, Y. H. Chang, L. Zhang, L. J. Li, W. Zhao, G. Eda, W. Zhang, G. Grinblat, S. A. Maier, J. K. W. Yang, C. W. Qiu and A. T. S. Wee, "Giant photoluminescence enhancement in tungsten-diselenide-gold plasmonic hybrid structures", *Nat. Commun.*, 7, 11283, 2016.

[45] S. A. Maier, "Plasmonics: Fundamentals and applications", Springer, 2007.

[46] V. Giannini, A. I. Fernández-Domínguez, S. C. Heck and S. A. Maier, "Plasmonic nanoantennas: Fundamentals and their use in controlling the radiative properties of nanoemitters", *Chem. Rev.*, vol. 111 (6), pp. 3888–3912, 2011.

[47] S. A. Maier, P. G. Kik, H. A. Atwater, S. Meltzer, E. Harel, B. E. Koel and A. A. G. Requicha, "Local detection of electromagnetic energy transport below the diffraction limit in metal nanoparticle plasmon waveguides", *Nat. Mater.*, 2(4), pp. 229-232, 2003.

[48] Y. Fang and M. Sun, "Nanoplasmonic waveguides: Towards applications in integrated nanophotonic circuits", *Light: Science & Applications*, vol. 4, e294, 2015.

[49] K. Kneipp, Y. Wang, H. Kneipp, L. T. Perelman, I. Itzkan, R. R. Dasari and M. S. Feld, "Single molecule detection using surface-enhanced raman scattering (SERS)," *Phys. Rev. Lett.*, 78, 1667, 1997.

[50] A. B. Taylor, A. M. Siddiquee, and J. W. M. Chon, "Below melting point photothermal reshaping of single gold nanorods driven by surface diffusion", *ACS Nano*, vol. 8 (12), pp. 12071–12079, 2014.

[51] S. Mukherjee, F. Libisch, N. Large, O. Neumann, L. V. Brown, J. Cheng, J. B. Lassiter, E. A. Carter, P. Nordlander and N. J. Halas, "Hot Electrons Do the Impossible: Plasmon-Induced Dissociation of H_2 on Au", *Nano Lett.*, vol. 13 (1), pp. 240–247, 2013.

[52] C. Frischkorn and M. Wolf, "Femtochemistry at metal surfaces: Nonadiabatic reaction dynamics", *Chem. Rev.*, vol. 106 (10), pp. 4207–4233, 2006.

[53] M. L. Brongersma, N. J. Halas and P. Nordlander, "Plasmon-induced hot carrier

science and technology", *Nat. Nanotechnol.*, vol. 10 (1), pp. 25–34, 2015.

[54] E. C. Tyo and S. Vajda, "Catalysis by clusters with precise numbers of atoms", *Nat. Nanotechnol.*, vol. 10 (7), pp. 577–588, 2015.

[55] I. Laou *et al.*, "Size and catalytic activity of supported gold nanoparticles : An in operando study during CO oxidation", vol. 115 (11), pp. 4673–4679, 2011.

[56] F. Yang, M. S. Chen, and D. W. Goodman, "Sintering of Au particles supported on TiO_2 (110) during CO oxidation", *J. Phys. Chem. C*, vol. 113 (1), pp 254–260, 2009.

[57] J. G. Wang and B. Hammer, "Oxidation state of oxide supported nanometric gold", *Top. Catal.*, vol. 44 (1-2), pp. 49-56, 2007.

[58] Y. Tian and T. Tatsuma, "Mechanisms and applications of plasmon-induced charge separation at TiO_2 films loaded with gold nanoparticles", *J. Am. Chem. Soc.*, vol. 127 (20), pp. 7632-7637, 2005.

[59] J. Y. Park, S. M. Kim, H. Lee, and I. I. Nedrygailov, "Hot-electron-mediated surface chemistry : Toward electronic control of catalytic activity", vol. 48 (8), pp. 2475-2483, 2015.

[60] T. W. Hansen, A. T. DeLaRiva, S. R. Challa and A. K. Datye, "Sintering of catalytic nanoparticles: Particle migration or Ostwald ripening? ", *Acc. Chem. Res.*, vol. 46 (8), pp 1720–1730, 2013.

[61] Y. G. Wang, D. Mei, V. A. Glezakou, J. Li, and R. Rousseau, "Dynamic formation of single-atom catalytic active sites on ceria-supported gold nanoparticles", *Nat. Commun.*, vol. 6, 6511, 2015.

[62] T. Imaoka, H. Kitazawa, W. J. Chun, S. Omura, K. Albrecht and K. Yamamoto, "Magic number Pt_{13} and misshapen Pt_{12} clusters : Which One is the Better Catalyst? ", *J. Am. Chem. Soc.*, vol. 135 (35), pp. 13089–13095, 2013.

[63] W. Luedtke and U. Landman, "Slip diffusion and Lévy flights of an adsorbed gold nanocluster", *Phys. Rev. Lett.*, vol. 82 (19), pp. 3835–3838, 1999.

[64] L. J. Lewis, P. Jensen, N. Combe, and J. L. Barrat, "Diffusion of gold nanoclusters on graphite", *Phys. Rev. B*, vol. 61 (23), pp. 16084–16090, 2000.

[65] R. Guerra, U. Tartaglino, A. Vanossi and E. Tosatti, “Ballistic nanofriction,” *Nat. Mater.*, vol. 9 (8), pp. 634–637, 2010.

[66] P. Pichanusakorn and P. Bandaru, “Nanostructured thermoelectrics”, *Mater. Sci. Eng. R Rep*., vol. 67 (2-4), pp. 19–63, 2010.

[67] Z. G. Chen, G. Hana, L. Yanga, L. Cheng and J. Zou, “Nanostructured thermoelectric materials: Current research and future challenge”, *Pro. Nat. Sci.-Mat*., vol. 22 (6), pp. 535–549, 2012.

[68] J. F. Li, W. S. Liu, L. D. Zhao, and M. Zhou, “High-performance nanostructured thermoelectric materials,” *NPG Asia Materials*., vol. 2 (4), pp. 152–158, 2010.

[69] M. G. Kanatzidis, “Nanostructured thermoelectrics: The new paradigm? ”, *Chem. Mat*., vol. 22 (3), pp. 648–659, 2010.

[70] B. Krenzer, A. Janzen, P. Zhou, D. Von Der Linde and M. Horn-Von Hoegen, “Thermal boundary conductance in heterostructures studied by ultrafast electron diffraction”, *New J. Phys.*, vol. 8, 190, 2006.

[71] S. Tan, A. Argondizzo, J. Ren, L. Liu, J. Zhao and H. Petek, “Plasmonic coupling at a metal/semiconductor interface”, *Nat. Photonics*, vol. 11 (12), pp. 806–812, 2017.

[72] P. A. DeSario, J. J. Pietron, D. E. DeVantier, T. H. Brintlinger, R. M. Stroud and D. R. Rolison, “Plasmonic enhancement of visible-light water splitting with Au-TiO_2 composite aerogels”, *Nanoscale*, vol. 5 (17), pp. 8073–8083, 2013.

[73] S. Pillai, K. R. Catchpole, T. Trupke and M. A. Green, “Surface plasmon enhanced silicon solar cells”, *J. Appl. Phys.*, vol. 101 (9), 093105, 2007.

[74] R. P. Chatelain, V. R. Morrison, B. L. M. Klarenaar and B. J. Siwick, “Coherent and incoherent electron-phonon coupling in graphite observed with radio-frequency compressed ultrafast electron diffraction”, *Phys. Rev. Lett.*, vol. 113 (23), 235502, 2014.

[75] L. Waldecker, T. Vasileiadis, R. Bertoni, R. Ernstorfer, T. Zier, F. H. Valencia, M. E. Garcia and E. S. Zijlstra, “Coherent and incoherent structural dynamics in laser-excited antimony”, *Phys. Rev. B*, vol. 95 (5), 054302, 2017.

[76] T. Frigge, B. Hafke, T. Witte, B. Krenzer and M. Horn-Von Hoegen, "Non-equilibrium lattice dynamics of one-dimensional In chains on Si(111) upon ultrafast optical excitation", *Struct. Dyn.*, vol. 5, 025101, 2018.

[77] L. Waldecker, T. A. Miller, M. Rudé, R. Bertoni, J. Osmond, V. Pruneri, R. E. Simpson, R. Ernstorfer and S. Wall, "Time-domain separation of optical properties from structural transitions in resonantly bonded materials", *Nat. Mater.*, vol. 14 (10), pp. 991–995, 2015.

[78] L. Waldecker, R. Bertoni, R. Ernstorfer and J. Vorberger, "Electron-Phonon Coupling and Energy Flow in a Simple Metal beyond the Two-Temperature Approximation", *Phys. Rev. X*, vol. 6 (2), 021003, 2016.

[79] K. Sokolowski-Tinten, X. Shen, Q. Zheng, T. Chase, R. Coffee, M. Jerman, R. K. Li, M. Ligges, I. Makasyuk, M. Mo, A. H. Reid, B. Rethfeld et al., "Electron-lattice energy relaxation in laser-excited thin-film Au-insulator heterostructures studied by ultrafast MeV electron diffraction", *Struct. Dyn.*, vol. 4 (5), 054501, 2017.

[80] J. Pudell, A. A. Maznev, M. Herzog, M. Kronseder, C. H. Back, G. Malinowski, A. von Reppert and M. Bargheer, "Layer specific observation of slow thermal equilibration in ultrathin metallic nanostructures by femtosecond X-ray diffraction", *Nat. Commun.*, vol. 9 (1), 3335, 2018.

[81] T. Witte, T. Frigge, B. Hafke, B. Krenzer and M. Horn-von Hoegen, "Nanoscale interfacial heat transport of ultrathin epitaxial hetero films : Few monolayer Pb(111) on Si(111)", *Appl. Phys. Lett.*, vol. 110, 243103, 2017.

[82] C. Y. Ruan, Y. Murooka, R. K. Raman and R. A. Murdick, "Dynamics of size-selected gold nanoparticles studied by ultrafast electron nanocrystallography", *Nano Lett.*, vol. 7 (5), pp. 1290–1296, 2007.

[83] A. R. Esmail, A. Bugayev and H. E. Elsayed-Ali, "Electron diffraction studies of structural dynamics of bismuth nanoparticles", *J. Phys. Chem. C*, vol. 117 (17), pp. 9035–9041, 2013.

[84] G. M. Vanacore, J. Hu, W. Liang, S. Bietti, S. Sanguinetti and A. H. Zewail, "Diffraction of quantum dots reveals nanoscale ultrafast energy localization", *Nano*

Lett., 14 (11), pp. 6148–6154, 2014.

[85] Xuan Wang, Hamidreza Rahmani, Jun Zhou, Matthew Gorfien, Joshua Mendez Plaskus, Dong Li, Ryan Voss, Cory A. Nelson, Kin Wai Lei, Abraham Wolcott, Xiaoyang Zhu, Junjie Li and Jianming Cao, "Ultrafast lattice dynamics in lead selenide quantum dot induced by laser excitation", *Appl. Phys. Lett.*, vol. 109 (15), 153105, 2016.

[86] Z. Y. Li, N. P. Young, M. Di Vece, S. Palomba, R. E. Palmer, A. L. Bleloch, B. C. Curley, R. L. Johnston, J. Jiang and J. Yuan, "Three-dimensional atomic-scale structure of size-selected gold nanoclusters", *Nature*, vol. 451 (7174), pp. 46–48, 2008.

[87] R. E. Palmer, S. Pratontep and H. G. Boyen, "Nanostructured surfaces from size-selected clusters", *Nat. Mater.*, vol. 2 (7), pp. 443–448, 2003.

[88] W. Demtroder, "Laser Spectroscopy", Vol. 2., Springer, 2008.

[89] R. W. Boyd, "Nonlinear Optics", Elsevier, 2003.

[90] T. Wilhelm, J. Piel and E. Riedle, "Sub-20-fs pulses tunable across the visible from a blue-pumped single-pass noncollinear parametric converter", *Opt. Lett.*, vol. 22 (19) , pp. 1494–1496, 1997.

[91] C. Gerbig, A. Senftleben, S. Morgenstern, C. Sarpe and T. Baumert, "Spatio-temporal resolution studies on a highly compact ultrafast electron diffractometer", *New J. Phys.*, vol. 17, 043050, 2015.

[92] B. J. Siwick, J. R. Dwyer, R. E. Jordan and R. J. D. Miller, "Ultrafast electron optics: Propagation dynamics of femtosecond electron packets", *J. Appl. Phys.*, vol. 92 (3), 1643, 2002.

[93] D. Ehberger, K. J. Mohler, T. Vasileiadis, R. Ernstorfer, L. Waldecker and P. Baum, "Terahertz compression of electron pulses at a planar mirror membrane", *Phys. Rev. Appl.*, vol. 11 (2), 024034, 2019.

[94] L. Waldecker, R. Bertoni, H. Hübener, T. Brumme, T. Vasileiadis, D. Zahn, A. Rubio and R. Ernstorfer, "A Momentum-Resolved View on Electron-Phonon Coupling in Multilayer WSe_2", *Phys. Rev. Lett.*, vol. 119 (3), 036803, 2017.

[95] L. M. Peng, S. L. Dudarev and M. J. Whelan, "High-energy electron diffraction and microscopy," Oxford Science Publications, 2004.

[96] S. P. Coleman, D. E. Spearot and L. Capolungo, "Virtual diffraction analysis of Ni [0 1 0] symmetric tilt grain boundaries", *Model. Simul. Mater. Sci. Eng.*, vol. 21 (5), 055020, 2013.

[97] L. M. Peng, G. Ren, S. L. Dudarev and M. J. Whelan, "Robust parameterization of elastic and absorptive electron atomic scattering factors", *Acta Crystallogr. Sect. A Found. Crystallogr.*, vol. 52 (2), pp. 257–276, 1996.

[98] G. K. Williamson and W. H. Hall, "X-ray line broadening from filed aluminium and wolfram", *Acta Metall.*, vol. 1 (1), pp. 22–31, 1953.

[99] J.M. Ziman, "Electrons and phonons: The theory of transport phenomena in solids", Oxford University Press, 1960.

[100] S. D. Brorson, A. Kazeroonian, J. S. Moodera, D. W. Face, T. K. Cheng, E. P. Ippen, M. S. Dresselhaus and G. Dresselhaus, "Femtosecond room-temperature measurement of the electron-phonon coupling constant λ in metallic superconductors", *Phys. Rev. Lett.*, vol. 64 (18), pp. 2172–2175, 1990.

[101] M. Schackert, T. Märkl, J. Jandke, M. Hölzer, S. Ostanin, E. K. U. Gross, A. Ernst and W. Wulfhekel, "Local measurement of the Eliashberg function of Pb islands: Enhancement of electron-phonon coupling by quantum well states" , *Phys. Rev. Lett.*, vol. 114 (4), 047002, 2015.

[102] E. Minamitani, R. Arafune, N. Tsukahara, Y. Ohda, S. Watanabe, M. Kawai, H. Ueba and N. Takagi, "Surface phonon excitation on clean metal surfaces in scanning tunneling microscopy", *Phys. Rev. B*, vol. 93 (8), 085411, 2016.

[103] W. S. Fann, R. Storz, H. W. K. Tom and J. Bokor, "Electron thermalization in gold", *Phys. Rev. B*, vol. 46 (20), 13592, 1992.

[104] J. R. M. Saavedra, A. Asenjo-Garcia and F. J. García De Abajo, "Hot-electron dynamics and thermalization in small metallic nanoparticles", *ACS Photonics*, vol. 3 (9), pp. 1637–1646, 2016.

[105] Z. Lin, L. V. Zhigilei and V. Celli, "Electron-phonon coupling and electron heat capacity of metals under conditions of strong electron-phonon nonequilibrium",

Phys. Rev. B, vol. 77 (7), 075133, 2008.

[106] S. I. Anisimov, A. M. Bonch-Bruevich and M. A. Elyashevich, "Effect of powerful light fluxes on metals", *Sov. Phys. Tech. Phys.*, vol. 11, p. S.945-952, 1967.

[107] M. Bernardi, D. Vigil-Fowler, J. Lischner, J. B. Neaton and S. G. Louie, "*Ab initio* study of hot carriers in the first picosecond after sunlight absorption in silicon", *Phys. Rev. Lett.*, vol. 112 (25), 257402, 2014.

[108] T. Chase, M. Trigo, A. H. Reid, R. Li, T. Vecchione, X. Shen, S. Weathersby, R. Coffee, N. Hartmann, D. A. Reis, X. J. Wang and H. A. Dürr, "Ultrafast electron diffraction from non-equilibrium phonons in femtosecond laser heated Au films", *Appl. Phys. Lett.*, vol. 108 (4), 041909, 2016.

[109] M. J. Stern, L. P. René de Cotret, M. R. Otto, R. P. Chatelain, J. P. Boisvert, M. Sutton and B. J. Siwick, "Mapping momentum-dependent electron-phonon coupling and nonequilibrium phonon dynamics with ultrafast electron diffuse scattering", *Phys. Rev. B*, vol. 97 (16), 165416, 2018.

[110] L. J. Challis, "Kapitza resistance and acoustic transmission across boundaries at high frequencies", *J. Phys. C Solid State Phys.*, vol. 7 (3), pp. 481–495, 1974.

[111] R. J. Stoner and H. J. Maris, "Kapitza conductance and heat flow between solids at temperatures from 50 to 300 K", *Phys. Rev. B*, vol. 48 (22), 16373, 1993.

[112] M. L. Huberman and A. W. Overhauser, "Electronic Kapitza conductance at a diamond-Pb interface", *Phys. Rev. B*, vol. 50 (5), 2865, 1994.

[113] C. Chen, J. Avila, S. Wang, Y. Wang, M. Mucha-Kruczyński, C. Shen, R. Yang, B. Nosarzewski, T. P. Devereaux, G. Zhang and M. C. Asensio, "Emergence of Interfacial Polarons from Electron-Phonon Coupling in Graphene/h-BN van der Waals Heterostructures" , *Nano Lett.*, vol. 18 (2), pp. 1082–1087, 2018.

[114] A. Sergeev, "Electronic Kapitza conductance due to inelastic electron-boundary scattering," *Phys. Rev. B*, vol. 58 (16), pp. R10199–R10202, 1998.

[115] S. Nose, "Constant-temperature molecular dynamics", *J. Phys. Condens. Matter*, vol. 2, SA115, 1990.

[116] W. G. Hoover, "Canonical dynamics: Equilibrium phase-space distributions",

Phys. Rev. A, vol. 31 (3), 1695, 1985.

[117] T. Vasileiadis, L. Waldecker, D. Foster, A. Da Silva, D. Zahn, R. Bertoni, R. E. Palmer and R. Ernstorfer, "Ultrafast heat flow in heterostructures of Au nanoclusters on thin-films: Atomic-disorder induced by hot electrons", *ACS Nano*, vol. 12 (8), pp. 7710–7720, 2018.

[118] O. Varnavski, G. Ramakrishna, J. Kim, D. Lee and T. Goodson, "Critical size for the observation of quantum confinement in optically excited gold clusters", *J. Am. Chem. Soc.*, vol. 132 (1), pp. 16–17, 2010.

[119] F. Kuemmeth, K. I. Bolotin, S. F. Shi and D. C. Ralph, "Measurement of discrete energy-level spectra in individual chemically synthesized gold nanoparticles", *Nano Lett.*, vol. 8 (12), pp. 4506–4512, 2008.

[120] M. Ligges, I. Rajković, C. Streubühr, T. Brazda, P. Zhou, O. Posth, C. Hassel, G. Dumpich and D. von der Linde, "Transient (000)-order attenuation effects in ultrafast transmission electron diffraction", *J. Appl. Phys.*, vol. 109 (6), 063519, 2011.

[121] T. G. White, P. Mabey, D. O. Gericke, N. J. Hartley, H. W. Doyle, D. McGonegle, D. S. Rackstraw, A. Higginbotham and G. Gregori, "Electron-phonon equilibration in laser-heated gold films", *Phys. Rev. B*, vol. 90 (1), 014305, 2014.

[122] W. Liang, S. Schäfer and A. H. Zewail, "Ultrafast electron crystallography of heterogeneous structures: Gold-graphene bilayer and ligand-encapsulated nanogold on graphene", *Chem. Phys. Lett.*, vol. 542, pp. 8–12, 2012.

[123] P. Pyykkö, "Structural properties: Magic nanoclusters of gold", *Nat. Nanotechnol.*, vol. 2 (5), pp. 273–274, 2007.

[124] S. Pratontep, S. J. Carroll, C. Xirouchaki, M. Streun and R. E. Palmer, "Size-selected cluster beam source based on radio frequency magnetron plasma sputtering and gas condensation", *Rev. Sci. Instrum.*, vol. 76 (4), 045103, 2005.

[125] B. Von Issendorff and R. E. Palmer, "A new high transmission infinite range mass selector for cluster and nanoparticle beams", *Rev. Sci. Instrum.*, vol. 70 (12), 4497, 1999.

[126] M. Di Vece, S. Palomba and R. E. Palmer, "Pinning of size-selected gold and

nickel nanoclusters on graphite", *Phys. Rev. B*, vol. 72 (7), 073407, 2005.

[127] S. Gibilisco, M. Di Vece, S. Palomba, G. Faraci and R. E. Palmer, "Pinning of size-selected Pd nanoclusters on graphite", *J. Chem. Phys.*, vol. 125 (8), 084704, 2006.

[128] E. Pop, V. Varshney and A. K. Roy, "Thermal properties of graphene: Fundamentals and applications", *MRS Bull.*, vol. 37 (12), pp. 1273–1281, 2012.

[129] B. L. Zink and F. Hellman, "Specific heat and thermal conductivity of low-stress amorphous Si-N membranes", *Solid State Commun.*, vol. 129 (3), pp. 199–204, 2004.

[130] A. Kiejna and K. F. Wojciechowski, "Metal Surface Electron Physics", Elsevier, 1996.

[131] M. Walter, J. Akola, O. Lopez-Acevedo, P.D. Jadzinsky, G. Calero, C.J. Ackerson, R.L. Whetten, H. Grönbeck and H. Häkkinen, "A unified view of ligand-protected gold clusters as superatom complexes", *Proc. Natl. Acad. Sci. U.S.A.*, vol. 105, (27), pp. 9157–9162, 2008.

[132] M. Zhou, C. Zeng, Y. Chen, S. Zhao, M.Y. Sfeir, M. Zhu and R. Jin, "Evolution from the plasmon to exciton state in ligand-protected atomically precise gold nanoparticles", *Nat. Commun.*, vol. 7, 13240, 2016.

[133] H. E. Sauceda, D. Mongin, P. Maioli, A. Crut, M. Pellarin, N. D. Fatti, F. Vallée and I. L. Garzón, "Vibrational properties of metal nanoparticles: Atomistic simulation and comparison with time-resolved investigation", *J. Phys. Chem. C*, vol. 116 (47), pp. 25147-25156, 2012.

[134] B. Roldan Cuenya, L. K. Ono, J. R. Croy, K. Paredis, A. Kara, H. Heinrich, J. Zhao, E. E. Alp, A. T. DelaRiva, A. Datye, E. A. Stach and W. Keune, "Size-dependent evolution of the atomic vibrational density of states and thermodynamic properties of isolated Fe nanoparticles", *Phys. Rev. B*, vol. 86 (16), 165406, 2012.

[135] H. Brune, "Thermal dynamics at surfaces", *Annalen der Physik (Leipzig)*, vol. 18 (10-11), pp. 675-698, 2009.

[136] P. Buffat and J.-P. Borel, "Size effect on the melting temperature of gold particles", *Phys. Rev. A*, vol. 13 (6), pp. 2287–2298, 1976.

[137] G. A. Breaux, C. M. Neal, B. Cao and M. F. Jarrold, "Melting, premelting, and structural transitions in size-selected aluminum clusters with around 55 atoms", *Phys. Rev. Lett.*, vol. 94 (17), 173401, 2005.

[138] Y. Y. Gafner, S. L. Gafner, I. S. Zamulin, L. V. Redel and V. S. Baidyshev, "Analysis of the heat capacity of nanoclusters of FCC metals on the example of Al, Ni, Cu, Pd, and Au", *Phys. Met. Metallogr.*, vol. 116 (6), pp. 568–575, 2015.

[139] H. E. Sauceda, F. Salazar, L. A. Pérez and I. L. Garzón, "Size and shape dependence of the vibrational spectrum and low-temperature specific heat of au nanoparticles", *J. Phys. Chem. C*, vol. 117 (47), pp. 25160-25168, 2013.

[140] P. A. Buffat, "Size-effect modifications of the Debye-Waller factor in small gold particles", *Solid State Commun.*, vol. 23 (8), pp. 547–550, 1977.

[141] C. Solliard, "Debye-Waller factor and melting temperature in small gold particles: related size effects", *Solid State Commun.*, vol. 51 (12), pp. 947–949, 1984.

[142] N. Manavizadeh, A. Khodayari and E. Asl-Soleimani, "An investigation of the properties of Silicon Nitride (SiNx) thin films prepared by sputtering for application in solar cell technology", *ISES Solar World Congress*, vol. 2, pp. 1120-1122, 2007.

[143] S. Tan, L. Liu, Y. Dai, J. Ren, J. Zhao and H. Petek, "Ultrafast plasmon-enhanced hot electron generation at Ag nanocluster/graphite heterojunctions", *J. Am. Chem. Soc.*, vol. 139 (17), pp 6160–6168, 2017.

[144] B. C. Gundrum, D. G. Cahill and R. S. Averback, "Thermal conductance of metal-metal interfaces", *Phys. Rev. B*, vol. 72 (24), 245426, 2005.

[145] H. K. Lyeo and D. G. Cahill, "Thermal conductance of interfaces between highly dissimilar materials", *Phys. Rev. B*, vol. 73 (14), 144301, 2006.

[146] A. J. Schmidt, K. C. Collins, A. J. Minnich and G. Chen, "Thermal conductance and phonon transmissivity of metal-graphite interfaces", *J. Appl. Phys.*, vol. 107 (10), 104907, 2010.

[147] A. Giri, J. T. Gaskins, B. F. Donovan, C. Szwejkowski, R. J. Warzoha, M. A. Rodriguez, J. Ihlefeld and P. E. Hopkins, "Mechanisms of nonequilibrium electron-phonon coupling and thermal conductance at interfaces," *J. Appl. Phys.*,

vol. 117 (10), 105105, 2015.

[148] R. Cheaito, J. T. Gaskins, M. E. Caplan, B. F. Donovan, B. M. Foley, A. Giri, J. C. Duda, C. J. Szwejkowski, C. Constantin, H. J. Brown-Shaklee, J. F. Ihlefeld and P. E. Hopkins, "Thermal boundary conductance accumulation and interfacial phonon transmission: Measurements and theory", *Phys. Rev. B*, vol. 91 (3), 035432, 2015.

[149] A. Hanisch, B. Krenzer, T. Pelka, S. Möllenbeck and M. Horn-Von Hoegen, "Thermal response of epitaxial thin Bi films on Si(001) upon femtosecond laser excitation studied by ultrafast electron diffraction", *Phys. Rev. B*, vol. 77 (12), 125410, 2008.

[150] D. A. Walko, Y. M. Sheu, M. Trigo and D. A. Reis, "Thermal transport in thin films measured by time-resolved, grazing incidence x-ray diffraction", *J. Appl. Phys.*, vol. 110 (10), 102203, 2011.

[151] G. Antonius, S. Poncé, E. Lantagne-Hurtubise, G. Auclair, X. Gonze and M. Côté, "Dynamical and anharmonic effects on the electron-phonon coupling and the zero-point renormalization of the electronic structure", *Phys. Rev. B*, vol. 92 (8), 085137, 2015.

[152] X. Chen and X. Wang, "Near-field thermal transport in a nanotip under laser irradiation", *Nanotechnology*, vol. 22 (7), 075204, 2011.

[153] A. A. Maradudin and P. A. Flinn, "Anharmonic contributions to the Debye-Waller factor", *Phys. Rev.*, vol. 129 (6), pp. 2529–2547, 1963.

[154] M. Perner, S. Gresillon, J. März, G. von Plessen and J. Feldmann, "Observation of hot-electron pressure in the vibration dynamics of metal nanoparticles", *Phys. Rev. Lett.*, vol. 85 (4), pp. 792–795, 2000.

[155] F. C. Nix and D. MacNair, "The thermal expansion of pure metals : Copper, gold, aluminium, nickel, and iron", *Phys. Rev.*, vol. 60 (8), pp. 597–605, 1941.

[156] A. Pinto, A. R. Pennisi, G. Faraci, G. D'Agostino, S. Mobilio and F. Boscherini, "Evidence for truncated octahedral structures in supported gold clusters", *Phys. Rev. B*, vol. 51 (8), pp. 5315–5321, 1995.

[157] J. T. Miller, A. J. Kropf, Y. Zha, J. R. Regalbuto, L.Delannoy, C. Louis, E. Bus and J. A. van Bokhoven, "The effect of gold particle size on Au-Au bond length

and reactivity toward oxygen in supported catalysts", *J. Catal.*, vol. 240 (2), pp. 222–234, 2006.

[158] T. Comaschi, A. Balerna and S. Mobilio, "Temperature dependence of the structural parameters of gold nanoparticles investigated with EXAFS", *Phys. Rev. B*, vol. 77 (7), 075432, 2008.

[159] B. Roldan Cuenya, A. I. Frenkel, S. Mostafa, F. Behafarid, J. R. Croy, L. K. Ono and Q. Wang, "Anomalous lattice dynamics and thermal properties of supported size- and shape-selected Pt nanoparticles", vol. 82 (15), 155450, 2010.

[160] A. Balerna, E. Bernieri, P. Picozzi, A. Reale, S. Santucci, E. Burattini and S. Mobilio, "A structural investigation on small gold clusters by EXAFS", *Surf. Sci.*, vol. 156 (part 1), pp. 206–213, 1985.

[161] P. Kluth, B. Johannessen, V. Giraud, A. Cheung, C. J. Glover and G. de M. Azevedo, "Bond length contraction in Au nanocrystals formed by ion implantation into thin SiO_2", *Appl. Phys. Lett.*, vol. 85(16), pp. 3561–3563, 2004.

[162] J. H. Hodak, A. Henglein and G. V. Hartland, "Electron-phonon coupling dynamics in very small (between 2 and 8 nm diameter) Au nanoparticles", *J. Chem. Phys.*, vol. 112 (13), pp. 5942–5947, 2000.

[163] D. A. Reis, M. F. DeCamp, P. H. Bucksbaum, R. Clarke, E. Dufresne, M. Hertlein, R. Merlin, R. Falcone, H. Kapteyn, M. M. Murnane, J. Larsson, Th. Missalla and J. S. Wark, "Probing impulsive strain propagation with X-ray pulses", *Phys. Rev. Lett.*, vol. 86 (14), 3072, 2001.

[164] R. Li, K. Sundqvist, J. Chen, H. E. Elsayed-Ali, J. Zhang and P. M. Rentzepis, "Transient lattice deformations of crystals studied by means of ultrafast time-resolved X-ray and electron diffraction", *Struct. Dyn.*, vol. 5 (4), 044501, 2018.

[165] R. Li, O. A. Ashour, J. Chen, H. E. Elsayed-Ali and P. M. Rentzepis, "Femtosecond laser induced structural dynamics and melting of Cu (111) single crystal. An ultrafast time-resolved x-ray diffraction study," *J. Appl. Phys.*, vol. 121 (5), 055102, 2017.

[166] A. R. Esmail, A. Bugayev, and H. E. Elsayed-Ali, "Electron diffraction studies of structural dynamics of Bismuth nanoparticles", *J. Phys. Chem. C*, vol. 117 (17), pp.

9035–9041, 2013.

[167] P. B. Johnson and R. W. Christy, “Optical constants of the noble metals”, *Phys. Rev. B*, vol. 6 (12), 4370, 1972.

[168] A. Plech, S. Grésillon, G. Von Plessen, K. Scheidt and G. Naylor, “Structural kinetics of laser-excited metal nanoparticles supported on a surface”, *Chem. Phys.*, vol. 299 (2-3), pp. 183–191, 2004.

[169] M. A. Van Dijk, M. Lippitz and M. Orrit, “Detection of acoustic oscillations of single gold nanospheres by time-resolved interferometry”, *Phys. Rev. Lett.*, vol. 95 (26), 267406, 2005.

[170] S. H. Yau, O. Varnavski and T. Goodson, “An ultrafast look at Au nanoclusters”, *Acc. Chem. Res.*, vol. 46 (7), pp. 1506–1516, 2013.

[171] J. N. Clark, L. Beitra, G. Xiong, D. M. Fritz, H. T. Lemke, D. Zhu, M. Chollet, G. J. Williams, M. M. Messerschmidt, B. Abbey, R. J. Harder, A. M. Korsunsky et al., “Imaging transient melting of a nanocrystal using an X-ray laser”, *Proc. Natl. Acad. Sci.*, vol. 112 (24), pp. 7444–7448, 2015.

[172] A. Plech, R. Cerna, V. Kotaidis, F. Hudert, A. Bartels and T. Dekorsy, “A surface phase transition of supported gold nanoparticles”, *Nano Lett.*, vol. 7 (4), pp. 1026–1031, 2007.

[173] A. Rousse, C. Rischel, S. Fourmaux, I. Uschmann, S. Sebban, G. Grillon, Ph. Balcou, E. Förster, J. P. Geindre, P. Audebert, J. C. Gauthier and D. Hulin, “Non-thermal melting in semiconductors measured at femtosecond resolution”, *Nature*, vol. 410 (6824), pp. 65–67, 2001.

[174] S. K. Sundaram and E. Mazur, “Inducing and probing non-thermal transitions in semiconductors using femtosecond laser pulses”, *Nat. Mater.*, vol. 1 (4), pp. 217–224, 2002.

[175] K. Sokolowski-Tinten, J. Bialkowski and D. Von Der Linde, “Ultrafast laser-induced order-disorder transitions in semiconductors”, *Phys. Rev. B*, vol. 51 (20), 14186, 1995.

[176] F. Bottin and G. Zérah, “Formation enthalpies of monovacancies in aluminum and gold under the condition of intense laser irradiation”, *Phys. Rev. B*, vol. 75 (17),

174114, 2007.

[177] M. Rapacioli, N. Tarrat and F. Spiegelman, “Melting of the Au_{20} gold cluster: Does charge matter? ”, *J. Phys. Chem. A*, vol. 122 (16), pp. 4092–4098, 2018.

[178] J. Cuny, N. Tarrat, F. Spiegelman, A. Huguenot and M. Rapacioli, “Density-functional tight-binding approach for metal clusters, nanoparticles, surfaces and bulk: Application to silver and gold”, *J. Phys. Condens. Matter*, vol. 30 (30), 303001, 2018.

[179] N. Memmel and E. Bertel, “Role of surface states for the epitaxial growth on metal surfaces”, *Phys. Rev. Lett.*, vol. 75 (3), pp. 485–488, 1995.

[180] P. Ruggerone, C. Ratsch and M. Scheffler, “Chapter 13 Density-functional theory of epitaxial growth of metals”, *Chem. Phys. Solid Surfaces*, vol. 8 (C), pp. 490–544, 1997.

[181] N. Memmel, “Monitoring and modifying properties of metal surfaces by electronic surface states”, *Surf. Sci. Rep.*, vol. 32 (3-4), pp. 91–163, 1998.

[182] N. Knorr, H. Brune, M. Epple, A. Hirstein, M. A. Schneider and K. Kern, “Long-range adsorbate interactions mediated by a two-dimensional electron gas”, *Phys. Rev. B*, vol. 65 (11), 115420, 2002.

[183] J. Repp, F. Moresco, G. Meyer, K. H. Rieder, P. Hyldgaard and M. Persson, “Substrate mediated long-range oscillatory interaction between adatoms: Cu/Cu(111)”, *Phys. Rev. Lett.*, vol. 85, 2981, 2000.

[184] P. Hyldgaard and T. L. Einstein, “Surface-state-mediated three-adsorbate interaction”, *Europhys. Lett.*, vol. 59 (2), pp. 265–271, 2002.

[185] J. Kliewer, R. Berndt, E. V. Chulkov, V. M. Silkin, P. M. Echenique and S. Crampin, “Dimensionality effects in the lifetime of surface states”, *Science*, vol. 288 (5470), pp. 1399–1402, 2000.

[186] M. Fuglsang Jensen, T. K. Kim, S. Bengió, I. Yu. Sklyadneva, A. Leonardo, S. V. Eremeev, E. V. Chulkov and Ph. Hofmann, “Thermally induced defects and the lifetime of electronic surface states”, *Phys. Rev. B*, vol. 75 (15), 153404, 2007.

[187] I. Yu. Sklyadneva, R. Heid, V. M. Silkin, A. Melzer, K. P. Bohnen, P. M.

Echenique, Th. Fauster and E. V. Chulkov, "Unusually weak electron-phonon coupling in the Shockley surface state on Pd(111)", *Phys. Rev. B*, vol. 80 (4), 045429, 2009.

[188] I. Barke and H. Hövel, "Confined Shockley surface states on the (111) facets of gold clusters", *Phys. Rev. Lett.*, vol. 90, 166801, 2003.

[189] L. Bürgi, N. Knorr, H. Brune, M. A. Schneider and K. Kern, "Two-dimensional electron gas at noble-metal surfaces", *Appl. Phys. A Mater. Sci. Process.*, vol. 75 (1), pp.141–145, 2002.

[190] M. Ternes, M. Pivetta, F. Patthey and W. D. Schneider, "Creation, electronic properties, disorder, and melting of two-dimensional surface-state-mediated adatom superlattices", *Prog. Surf. Sci*., vol. 85 (1-4), pp. 1–27, 2010.

[191] N. N. Negulyaev, V. S. Stepanyuk, L. Niebergall, P. Bruno, W. Hergert, J. Repp, K. H. Rieder and G. Meyer, "Direct evidence for the effect of quantum confinement of surface-state electrons on atomic diffusion" , *Phys. Rev. Lett.*, vol. 101 (22), 226601, 2008.

[192] V. Simic-Milosevic, M. Heyde, N. Nilius, M. Nowicki, H. P. Rust and H. J. Freund, "Substrate-mediated interaction and electron-induced diffusion of single lithium atoms on Ag(001)", *Phys. Rev. B*, vol. 75 (19), 195416, 2007.

[193] H. Petek, M. J. Weida, H. Nagano and S. Ogawa, "Real-time observation of adsorbate atom motion above a metal surface", *Science*, vol. 288 (5470), pp. 1402–1404, 2000.

[194] J. A. Misewich, T. F. Heinz and D. M. Newns, "Desorption induced by multiple electronic transitions", *Phys. Rev. Lett.*, vol. 68 (25), pp. 3737–3740, 1992.

[195] M. Mehlhorn, H. Gawronski and K. Morgenstern, "Diffusion and dimer formation of CO molecules induced by femtosecond laser pulses", vol. 104 (7), 076101, 2010.

[196] M. Brandbyge, P. Hedegård, T. F. Heinz, J. A. Misewich and D. M. Newns, "Electronically driven adsorbate excitation mechanism in femtosecond-pulse laser desorption", *Phys. Rev. B*, vol. 52 (8), pp. 6042–6056, 1995.

[197] R. Scholz, G. Floß, P. Saalfrank, G. Füchsel, I. Lončarić and J. I. Juaristi,

"Femtosecond-laser induced dynamics of CO on Ru (0001): Deep insights from a hot-electron friction model including surface motion", vol. 94 (16), 165447, 2016.

[198] T. L. Cocker, D. Peller, P. Yu, J. Repp and R. Huber, "Tracking the ultrafast motion of a single molecule by femtosecond orbital imaging", *Nature*, vol. 539 (7628), pp. 263–267, 2016.

[199] S. Plimpton, "Fast parallel algorithms for short-range molecular dynamics", *J. Comput. Phys.*, vol. 117 (1), pp. 1–19, 1995.

[200] H. Heinz, R. A. Vaia, B. L. Farmer and R. R. Naik, "Accurate simulation of surfaces and interfaces of face-centered cubic metals using 12-6 and 9-6 Lennard-Jones potentials", *J. Phys. Chem. C*, vol. 112 (44), pp. 17281–17290, 2008.

[201] S. L. Mayo, B. D. Olafson and W. A. Goddard, "DREIDING: A generic force field for molecular simulations", *J. Phys. Chem.*, vol. 94 (26), pp. 8897– 8909, 1990.

[202] M. Harb, H. Enquist, A. Jurgilaitis, F. T. Tuyakova, A. N. Obraztsov and J. Larsson, "Phonon-phonon interactions in photoexcited graphite studied by ultrafast electron diffraction", *Phys. Rev. B*, vol. 93 (10), p. 104104, 2016.

[203] C. H. Lui, K. F. Mak, J. Shan and T. F. Heinz, "Ultrafast photoluminescence from graphene", *Phys. Rev. Lett.*, vol. 105 (12), p. 127404, 2010.

[204] H. Yan, D. Song, K. F. Mak, I. Chatzakis, J. Maultzsch and T. F. Heinz, "Time-resolved Raman spectroscopy of optical phonons in graphite: Phonon anharmonic coupling and anomalous stiffening," *Phys. Rev. B*, vol. 80 (12), 121403, 2009.

[205] J. C. Duda, P. E. Hopkins, T. E. Beechem, J. L. Smoyer and P. M. Norris, "Inelastic phonon interactions at solid-graphite interfaces", *Superlattices Microstruct.*, vol. 47 (4), pp. 550–555, 2010.

[206] E. Panizon, R. Guerra and E. Tosatti, "Ballistic thermophoresis of adsorbates on free-standing graphene", *Proc. Natl. Acad. Sci.*, vol. 114 (34), pp. E7035– E7044, 2017.

[207] Y. Maruyama, "Temperature dependence of Lévy-type stick-slip diffusion of a gold nanocluster on graphite", *Phys. Rev. B*, vol. 69 (24), 245408, 2004.

[208] C. S. Allen, E. Liberti, J. S. Kim, Q. Xu, Y. Fan, K. He, A. W. Robertson, H. W.

Zandbergen, J. H. Warner and A. I. Kirkland, "Temperature dependence of atomic vibrations in mono-layer graphene", *J. Appl. Phys.*, vol. 118 (7), 074302, 2015.

[209] L. Lindsay, D. A. Broido and N. Mingo, "Flexural phonons and thermal transport in graphene", *Phys. Rev. B*, vol. 82 (11), 115427, 2010.

[210] Q. H. Wang, K. Kalantar-Zadeh, A. Kis, J. N. Coleman and M. S. Strano, "Electronics and optoelectronics of two-dimensional transition metal dichalcogenides", *Nat. Nanotechnol.*, vol. 7 (11), pp. 699– 712, 2012.

[211] A. K. Geim and I. V. Grigorieva, "Van der Waals heterostructures", *Nature*, vol. 499 (7459), pp. 419–425, 2013.

[212] K. S. Novoselov, A. Mishchenko, A. Carvalho and A. H. Castro Neto, "2D materials and van der Waals heterostructures", *Science*, vol. 353 (6298), aac9439, 2016.

[213] R. Bertoni, C. W. Nicholson, L. Waldecker, H. Hübener, C. Monney, U. De Giovannini, M. Puppin, M. Hoesch, E. Springate, R. T. Chapman, C. Cacho, M. Wolf, A. Rubio and R. Ernstorfer, "Generation and evolution of spin-, valley-, and layer-polarized excited carriers in inversion-symmetric WSe_2", *Phys. Rev. Lett.*, vol. 117, 277201, 2016.

[214] M. Puppin, "Time- and angle-resolved photoemission spectroscopy on bidimensional semiconductors with a 500 kHz extreme ultraviolet light source", PhD Dissertation, Freien Universität Berlin, 2016.

[215] R. F. Frindt, "The optical properties of single crystals of WSe_2 and $MoTe_2$", *J. Phys. Chem. Solids*, vol. 24 (9), pp. 1107–1108, 1963.

[216] H. Häkkinen, "The gold-sulfur interface at the nanoscale", *Nature Chemistry*, vol. 4 (6), pp. 443–455, 2012.

[217] K. O. Aruda, M. Tagliazucchi, C. M. Sweeney, D. C. Hannah, G. C. Schatz and E. A. Weiss, "Identification of parameters through which surface chemistry determines the lifetimes of hot electrons in small Au nanoparticles", *Proc. Natl. Acad. Sci. U. S. A.*, vol. 110 (11), pp. 4212–4217, 2013.

[218] M. E. Kleemann, R. Chikkaraddy, E. M. Alexeev, D. Kos, C. Carnegie, W. Deacon, A. C. de Pury, C. Große, B. de Nijs, J. Mertens, A. I. Tartakovskii and J.

J. Baumberg, "Strong-coupling of WSe_2 in ultra-compact plasmonic nanocavities at room temperature," *Nat. Commun.*, vol. 8 (1), 1296, 2017.

[219] M. Wang, A. Krasnok, T. Zhang, L. Scarabelli, H. Liu, Z. Wu, L. M. Liz-Marzán, M. Terrones, A. Alù and Y. Zheng, "Tunable Fano resonance and plasmon-exciton coupling in single Au nanotriangles on monolayer WS_2 at room temperature", *Adv. Mater.*, vol. 30 (22), 1705779, 2018.

[220] B. Mukherjee, W. S. Leong, Y. Li, H. Gong, L. Sun, Z. X. Shen, E. Simsek and J. T. L. Thong, "Raman analysis of gold on WSe_2 single crystal film", *Mater. Res. Express*, vol. 2, 065009, 2015.

[221] J. Y. Kim, J. Kim and J. Joo, "Surface-enhanced Raman scattering for 2-D WSe_2 hybridized with functionalized gold nanoparticles", *Opt. Express*, vol. 24(24), pp. 27546–27553, 2016.

[222] B. Radisavljevic, A. Radenovic, J. Brivio, V. Giacometti and A. Kis, "Single-layer MoS_2 transistors," *Nat. Nanotechnol.*, vol. 6, pp. 147–150, 2011.

[223] C. M. Smyth, R. Addou, S. McDonnell, C. L. Hinkle and R. M. Wallace, "WSe_2-contact metal interface chemistry and band alignment under high vacuum and ultra high vacuum deposition conditions", *2D Mater.*, vol. 4, 025084, 2017.

[224] M. Dendzik, M. Michiardi, C. Sanders, M. Bianchi, J.A. Miwa, S.S. Grønborg, J.V. Lauritsen, A. Bruix, B. Hammer and P. Hofmann,, "Growth and electronic structure of epitaxial single-layer WS_2 on Au(111)", *Phys. Rev. B*, vol. 92 (24), 245442, 2015.

[225] G. Nicolay, R. Claessen, F. Reinert, V. N. Strocov, S. Hüfner, H. Gao, U. Hartmann and E. Bucher, "Fast epitaxy of Au and Ag on WSe_2", *Surf. Sci.*, vol. 432 (1-2), pp. 95–100, 1999.

[226] A. C. Domask, K. A. Cooley, B. Kabius, M. Abraham and S. E. Mohney, "Room Temperature van der Waals Epitaxy of Metal Thin Films on Molybdenum Disulfide", *Cryst. Growth Des.*, vol. 18 (6), pp 3494–3501, 2018.

[227] N. Krane, C. Lotze and K. J. Franke, "Moiré structure of MoS_2 on Au(111): Local structural and electronic properties", *Surf. Sci.*, vol. 678, pp. 136–142, 2018.

[228] Y. Zhou, D. Kiriya, E. E. Haller, J. W. Ager, A. Javey and D. C. Chrzan,

"Compliant substrate epitaxy: Au on MoS_2", *Phys. Rev. B*, 93 (5), 054106, 2016.

[229] S. B. Desai, S. R. Madhvapathy, M. Amani, D. Kiriya, , M. Hettick, M. Tosun, Y. Zhou, M. Dubey , J. W. Ager, D. Chrzan and A. Javey, "Gold-mediated exfoliation of ultralarge optoelectronically-perfect monolayers", *Adv. Mater.*, vol. 28(21), pp. 4053–4058, 2016.

[230] A. Castellanos-Gomez, M. Buscema, R. Molenaar, V. Singh, L. Janssen, H. S. J. van der Zant and G. A. Steele, "Deterministic transfer of two-dimensional materials by all-dry viscoelastic stamping", *2D Mater.*, vol. 1 (1), 011002, 2014.

[231] D. Zahn, "Structural dynamics of transition metal dichalcogenide heterostructures studied by ultrafast high-energy electron diffraction", Master thesis, Freien Universität Berlin, 2017.

[232] Y. Liao, W. Cao, J. W. Connell, Z. Chen and Y. Lin, "Evolution of Moiré profiles from van der Waals superstructures of Boron Nitride nanosheets," *Sci. Rep.*, vol. 6, 26084, 2016.

[233] P. Zeller and S. Günther, "What are the possible moiré patterns of graphene on hexagonally packed surfaces? Universal solution for hexagonal coincidence lattices, derived by a geometric construction", *New J. Phys.*, vol. 16, 083028, 2014.

[234] D. Le, A. Barinov, E. Preciado, M. Isarraraz, I. Tanabe, T. Komesu, C. Troha, L. Bartels, T. S. Rahman and P. A. Dowben, "Spin-orbit coupling in the band structure of monolayer WSe_2", *J. Phys. Condens. Matter*, vol. 27, 182201, 2015.

[235] A. S. Bolgar, Z. A. Trofimova and A. A. Yanaki, "Thermodynamic properties of tungsten diselenide in a broad temperature range", *Sov. Powder Metall. Met. Ceram.*, vol. 29 (5), pp 382–385, 1990.

[236] S. H. El-Mahalawy and B. L. Evans, "The thermal expansion of 2*H*-MoS_2 , 2*H*-$MoSe_2$ and 2*H*-WSe_2 between 20 and 800°C", *J. Appl. Crystallogr.*, vol. 9 (5), 1976.

[237] A. G. Čabo, J. A. Miwa, S. S. Grønborg, J. M. Riley, J. C. Johannsen, C. Cacho, O. Alexander, R. T. Chapman, E. Springate, M.Grioni, J. V. Lauritsen, P. D. C. King *et al.*, "Observation of ultrafast free carrier dynamics in single layer MoS_2", *Nano Lett.*, vol. 115 (9), pp 5883–5887, 2015.

[238] H. Sun, M. Yu, G. Wang, X. Sun and J. Lian, "Temperature-dependent morphology evolution and surface plasmon absorption of ultrathin gold island films", *J. Phys. Chem. C*, 116 (16), pp 9000–9008, 2012.

Publications

Scientific publications within the scope of this PhD thesis:

1. Thomas Vasileiadis, Lutz Waldecker, Dawn Foster, Alessandra Da Silva, Daniela Zahn, Roman Bertoni, Richard E. Palmer, and Ralph Ernstorfer, *Ultrafast Heat Flow in Heterostructures of Au Nanoclusters on Thin Films: Atomic Disorder Induced by Hot Electrons*.
   Published in ACS Nano, vol. 12 (8), pp 7710–7720, 2018.
2. Thomas Vasileiadis, Emmanuel N. Skountzos, Dawn Foster, Shawn P. Coleman, Daniela Zahn, Faruk Krečinić, Vlasis G. Mavrantzas, Richard E. Palmer, and Ralph Ernstorfer, *Ultrafast rotational motions of supported nanoclusters probed by electron diffraction*.
   Accepted in Nanoscale Horizons.

Work in progress:

Thomas Vasileiadis and the group of Dr. Ralph Ernstorfer in collaboration with the groups of Dr. Laurenz Rettig (FHI Berlin) and Prof. Stephanie Reich (FU Berlin),
Ultrafast energy flow in 2D metal / 2D semiconductor heterostructures.

Additional publications:

1. Vasileiadis, T., Dracopoulos, V., Kollia, M., and Yannopoulos, S.N., *Laser-assisted growth of t-Te nanotubes and their controlled photo-induced unzipping to ultrathin core-Te/sheath-TeO_2 nanowires*.
   Scientific Reports, vol. 3, 1209, 2013 (**Master thesis**).
2. Vasileiadis, T. and Yannopoulos, S.N., *Photo-induced oxidation and amorphization of trigonal tellurium: A means to engineer hybrid nanostructures and explore glass structure under spatial confinement*.
   Journal of Applied Physics, vol. 116(10), 103510, 2014 (**Master thesis**).
3. Vasileiadis, T. and Yannopoulos, S.N., *Laser-assisted growth and processing of functional chalcogenide nanostructures*.
   NATO Science for Peace and Security Series A: Chemistry and Biology, 39, pp. 17-27, 2015 (**Master thesis**).

4. Christopoulou, P.-E., Papageorgiou, A., Vasileiadis, T., Tsantilas, S., *A holistic view of the W UMA type TY BOO*.
   Astronomical Journal, vol. 144 (5), 149, 2012 (**Diploma thesis**).
5. Ehberger, D, Mohler, K., Vasileiadis, T., Ernstorfer, R., Waldecker, L., and Baum, P., *Terahertz Compression of Electron Pulses at a Planar Mirror Membrane*. Physical Review Applied, vol. 11 (2), 024034, 2019.
6. Waldecker, L., Bertoni, R., Hübener, H., Brumme, T., Vasileiadis, T., Zahn, D., Rubio, A., Ernstorfer, R., *Momentum-resolved view of electron-phonon coupling in multilayer WSe_2*.
   Physical Review Letters, vol. 119 (3), 036803, 2017.
7. Waldecker, L., Vasileiadis, T., Bertoni, R., Ernstorfer, R., Zier, T., Valencia, F.H., Garcia, M.E., Zijlstra, E.S., *Coherent and incoherent structural dynamics in laser-excited antimony*.
   Physical Review B, vol. 95 (5), 054302, 2017.
8. Lewandowski, M., Scheibe, B., Vasileiadis, T., Michalak, N., Miłosz, Z., Ranecki, R., Mielcarek, S., Luciński, T., Jurga, S., *Raman spectroscopy indications of the Verwey transition in epitaxial Fe3 O4 (111) films on Pt(111) and Ru(0001)*. Surface and Coatings Technology, vol. 271, pp. 87-9, 2015.
9. Vlachos, K., Vasileiadis, T., Dracopoulos, V., Markos, C., Kakarantzas, G., and Yannopoulos, S.N., *Development of hybrid solid and hollow core photonic crystal fiber with soft glass deposition for infrared light manipulation*.
   International Conference on Transparent Optical Networks, 6876463, 2014.
10. Voleská, I., Akola, J., Jóvári, P., Gutwirth, J., Wágner, T., Vasileiadis, T., Yannopoulos, S.N., Jones, R.O., *Structure, electronic, and vibrational properties of glassy $Ga_{11}Ge_{11}Te_{78}$: Experimentally constrained density functional study*.
    Physical Review B, vol. 86 (9), 094108, 2012.

Acknowledgements

The author of this thesis wishes to express his gratitude to the following people:

First of all, I want to thank my supervisor Ralph Ernstorfer for the opportunity to work with him, the training, the overall support and everything I learned from him regarding nonequilibrium phenomena and pump-probe experiments. I am grateful that he trusted me and let me develop my own scientific interests and ideas and that he was always available for discussions. Outside work, Ralph and his family were always very friendly and hospitable with me and my colleagues and it was a pleasure to meet all of them!

Next, I want to thank my colleagues Lutz Waldecker, Roman Bertoni and Melanie Müller who have trained me when I arrived at the FHI. I am also thankful that they welcomed me in the group as a friend and supported me during the initial stage of my studies.

My colleagues, working with the FED setup, Daniela Zahn, Yingpeng Qi, Helene Seiler, Shuo Dong and Will Windsor. Being a colleague and a friend of yours was a pleasure!

Our Director, Professor Martin Wolf for the excellent working environment in the PC department and all the thoughtful comments and recommendations in the regular departmental meetings.

I also want to thank Professor Katharina Franke who accepted to be the second supervisor of my thesis.

Richard Palmer, Dawn Foster and Alessandra Da Silva for our collaboration with the size-selected metallic nanoclusters. I am very thankful to Richard Palmer for all the interesting discussions regarding the physics of nanoclusters.

I am thankful to Emmanuel Skountzos and Vlasis Mavrantzas for our collaboration with the MD simulations and to Shawn Coleman for his help with the electron diffraction simulations.

Tommaso Pincelli, Shuo Dong and Samuel Beaulieu and the group of Laurenz Rettig for our collaboration and the ARPES experiments.

The group of Professor Stephanie Reich, Niclas Müller and Yu Okamura for the optical spectroscopy experiments and Emmerson Coy for the electron microscopy images.

Manuel Krüger, Sven Kubala, Albrecht Ropers, Daniel Wegkamp, Marcel Krenz, Ines

Bressel, and all the people in the workshops, the administration and the library. The work of researchers would not be possible without their everyday support.

Last but not least, I want to express my gratitude to my family: Natalia Michalak, Grażyna Warszewska Michalak and Maciej Warszewsk, and, of course, Ελένη Παπαζαφειροπούλου, Ζωή Βασιλειάδου and Λάζαρος Βασιλειάδης. Thank you for your love and support!

In addition, I am thankful to all my new friends who made these years so pleasant (Martyna, Majkel, Magdalena, Mariusz, Mateusz, Weronika, Betty, Κωστής and my friends at the FHI) and all my friends from Greece (Νίκος, Σπύρος, Γιώργος, Γιάννης, Ανδρέας Δ., Ανδρέας Ρ., Πέτρος, Στράτος) who remember me and support me.

I want to close this thesis with special thanks to my wife Natalia Michalak. I am forever grateful for her love and her support in so many things, her patience, and her encouragement. Thank you Natalia!